The Applications of Interaction between light and chemical reactivity in molecular systems

by

Brahmjot Kaur

M.Sc. (Chemistry), Jamia Millia Islamia, 2014

B.Sc. (Hons.), University of Delhi, 2012

Thesis Submitted in Partial Fulfillment of the

Requirements for the Degree of

Doctor of Philosophy

in the

Department of Chemistry

Faculty of Science

SIMON FRASER UNIVERSITY

Summer 2021

Declaration of Committee

Name:	**Brahmjot Kaur**
Degree:	**Doctor of Philosophy**
Title:	**The Applications of Interaction between Light and Chemical reactivity in molecular systems**
Committee:	**Chair:** Corina Andreoiu Associate Professor, Chemistry
	Neil R. Branda Supervisor Professor, Chemistry
	Andrew J. Bennet Committee Member Professor, Chemistry
	Jeffrey J. Warren Committee Member Associate Professor, Chemistry
	Vance E. Williams Examiner Professor, Chemistry
	Belinda Heyne External Examiner Professor Department of Chemistry University of Calgary

Abstract

This thesis presents a series of scientific examples that provide further insight into the connection of light and chemical reactivity for applications in catalysis, targeted drug delivery, and detection. Small organic molecules based on 1,2-dithienylethenes (DTEs) and noble metal-based nano-assemblies were incorporated into the system to impart control over their physical and chemical properties, and activity. The light was used as an external stimulus to initiate chemical reactions by causing either a structural, electronic, or chemical change in the chromophore or energy transformation (such as heat) in the system.

In the first example (Chapter 2), light is employed to generate the variation in the activity of Karstedt's catalyst by introducing a DTE-based inhibitor. It is demonstrated that the electronic changes that occur during the light-assisted isomerization of dithienylethene lead to changes in the binding strength of the inhibitor to the catalyst's metal centre. This, in turn, leads to changes in the reaction progression of simple hydrosilylation reactions.

In the second example (Chapter 3), a novel dual-mode (colourimetric and fluorescent) optical probe based on photoresponsive dithienylethene is developed for fast and user-friendly detection and consumption of hydrazine in the vapour and solution phase. The molecule reacts with hydrazine to induce an irreversible structural change in the 1,3,5-hexatriene system leading to deactivation of photochromic activity by quenching effects and simultaneously generating an emissive response.

In the third example (Chapter 4), light is used as an external stimulus to indirectly gate the chemical reactivity for an on-demand release of therapeutics in aqueous environments by creating nanoassemblies based on gold nanoparticle core. The constructed nanoassemblies consist of the thermoresponsive Diels-Alder adducts of the molecules to be released close to gold nanoparticles enclosed in an amphiphilic polymer shell. The system uses the photothermal effect of gold nanoparticles to trigger thermo-responsive retro Diels-Alder reactions in the vicinity of nanoparticles to release therapeutic molecules in aqueous solutions.

Keywords: Photochromism; dithienylethenes; dual-mode detector; quenching effects; photothermal effect; thermoresponsive

To my grandfather, late Dr Gurbachan Singh Sohi, for being an endless inspiration

Acknowledgements

The journey of my graduate studies would remain incomplete without thanking everyone who helped me to navigate through. I would begin by expressing my sincere gratitude to Prof. Neil Branda for giving me the opportunity to develop a better sense of scientific reasoning and to mature as a researcher. He has been a perennial source of expert advice, encouragement, guidance, and patience throughout my degree.

I would further like to communicate my earnest appreciation to my supervisory committee, Prof. Andrew Bennet and Prof. Jeff Warren, for their valuable suggestions and feedback on my research projects. I would also like to thank Prof. Vance Williams for his heartening conversations and views about proceeding in chemistry, and science.

A progressive start-up to my lab experience would not have been possible without the recommendations and directions from Dr. Amir Asadirad, Dr. Khaled Arafeh, Dr. David Ester, Dr. Danielle Wilson, Dr. Tony Wu, Kailey Wright, Mitchell Stashick, and Scott Beaupre – I am very thankful for all your insights and expertise.

In the course of my degree, I strengthened my existing friendships and was fortunate enough to weave some new ones. A special thanks to Rameez Raza for his unwavering support for these many years, for being a refining critique, and for standing by during challenging times. My very first research partner, Daina Baker, made working in a completely new setting simpler and more fun. For that, I am extremely grateful. I would like to thank Carson Zellman for the wonderful collaboration and for helping me in my fluorescence and DSC experiments. One could not possibly ask for a better group to share lab space with. As a teaching assistant, I got to know and had a chance to work with Kelsy Yuan and Rana Faryad Ali. The experience would always remain memorable and most cherished. A special thanks to Scott Fang and Camille Valdez for the pleasant time in the lab.

I am also grateful to Dr. Farahnaz Nourmohammadian for giving certain intrinsic tips regarding photochemistry and for the collaboration. I would further like to acknowledge Dr. Eric Ye for his helpful discussion about Pt-NMR studies, Colin Zhang and Hongwen Chen for all the practical assistance required for NMR and MS experiments. I very much appreciate Nathalie Fournier, Leslie Butler, and Jen Jackson for their help with administrative and financial tasks. A special thanks to Dr. Saeid Kamal, the manager of

the LASIR facility at 4D Labs, for his help in setting up the laser experiments. I am thankful to Li Yang, Nanoimaging Facilities at 4D Labs, for training me for TEM experiments.

I am thankful to the Department of Chemistry and Simon Fraser University for the graduate fellowship and other forms of financial support.

I want to humbly thank my parents and my brother for playing a pivotal role in transforming and bringing the best out in me. Their faith and determination have always motivated me to dream on and achieve.

Finally, I am grateful to all my friends and family members for all their support and encouragement.

'La reconnaissance est la memoire du Coeur (Gratitude is the memory of the heart)'

~ Jean-Baptiste Massieu

Table of Contents

List of Tables

List of Figures

List of Schemes

List of Equations

List of Acronyms

λ	wavelength
Δ	heat
>	greater than
<	less than
~	approximately
%	per cent
$\bar{\upsilon}$	wavenumber
°C	degree Celsius
ϕ	quantum yield
δ	chemical shift
ε	molar extinction/absorptivity coefficient ($M^{-1}cm^{-1}$)
v	frequency
µL	microlitre
µm	micrometre
µg	microgram
ψ	molecular orbital
Å	angstrom
A	absorbance
acac	acetylacetonate
AcOH	acetic acid
AMF	alternating magnetic field
ATP	adenosine triphosphate
ATR	attenuated total reflection
a.u.	atomic units
Au	gold
AuNPs	gold nanoparticles
Ba^{2+}	barium
$BF_3.OEt_2$	boron trifluoride etherate
B3LYP	becke 3-parameter lee yang parr
BDD	boron-doped diamond
Bu_4NBr	tetrabutylammonium bromide
Ca^{2+}	calcium

CCl_4	carbon tetrachloride
$CDCl_3$	deuterated chloroform
$CHCl_3$	chloroform
CH_2Cl_2	dichloromethane
CoQ	Coenzyme Q
Cu^+	copper
d	doublet
dd	doublet of doublet
DASA	donor-acceptor Stenhouse adduct
DCTE	dicyanoethylene-thienylethene
DFT	density functional theory
DI	delocalization index
DLS	dynamic light scattering
DMF	*N,N*-dimethylformamide
DMSO	dimethylsulfoxide
DNA	deoxyribonucleic acid
Dox	doxorubicin
DTE	dithienylethene
E	*E*-isomer
EDTA	ethylenediaminetetraacetic acid
EGFR	epidermal growth factor receptor
EPA	environmental protection agency
Equiv.	equivalents
ES	excited-state
ESI	electrospray ionization
ESIPT	excited-state intramolecular proton transfer
EtOH	ethanol
Et_2O	diethyl ether
Et_3SiH	triethylsilane
etc.	et cetera
eV	electron volt
FET	field-effect transistors
FRET	Förster resonance energy transfer
FT-IR	Fourier-transform infrared

g	gram
GI	genotoxic impurity
GS	ground state
GNP	gold nanoparticles
H_2O_2	hydrogen peroxide
h	hour
$HAuCl_4$	chloroauric acid
hCAI	human carbonic anhydrase I
HCl	hydrochloric acid
HOMO	highest occupied molecular orbital
HRMS	high-resolution mass spectroscopy
Hz	hertz
ICT	intramolecular charge transfer
i.e.	Id est (that is)
J	coupling constant
k	rate constant
kJ/mol	kilojoule/mole
KOH	potassium hydroxide
LC/MS	liquid chromatography/mass spectrometry
ln	natural logarithm
LoD	limit of detection
LSPR	localized surface plasmon resonance
LUMO	lowest unoccupied molecular orbital
M	molar
MeOH	methanol
mg	milligram
Mg^{2+}	magnesium
$MgSO_4$	magnesium sulfate
MHz	mega hertz
min	minute
mJ	millijoule
mL	millilitre
mmol	millimole
mM	millimolar

MSNP	mesoporous silica nanoparticles
NBS	*N*-bromosuccinimide
n-BuLi	*n*-butyllithium
$NaBH_4$	sodium borohydride
NaCN	sodium cyanide
Na_2CO_3	sodium carbonate
$NaHCO_3$	sodium bicarbonate
NaOAc	sodium acetate
NaOH	sodium hydroxide
NH_2	amino functional group
N_2	nitrogen
N_2H_4	hydrazine
NMR	nuclear magnetic resonance
nm	nanometre
$^1O_2$	singlet oxygen
O_2	oxygen molecule
ODA	octadecylamine
OH	hydroxyl functional group
oop	out of plane
PBr_3	phosphorus tribromide
Pd	palladium
$Pd(PPh_3)_4$	*tetrakis*(triphenylphosphine)palladium(0)
PEG	polyethylene glycol
PET	photo-induced electron transfer
PFC	perfluorocarbon
Ph	phenyl
pK_a	negative logarithm of an acid dissociation constant
PLP	pyridoxal 5'-phosphate
ppb	parts-per-billion
ppm	parts-per-million
PSA	particle size analysis
PSMA	poly(styrene-*co*-maleic anhydride)
PSS	photostationary state
PS-β-CD-PEO-Fc	polystyrene-β-cyclodextrin-poly(ethylene oxide)-ferrocene

Pt	platinum
PTT	photothermal therapy
rpm	revolutions per minute
RPT	reverse proton transfer
RTK	receptor tyrosine kinases
s	singlet
s^{-1}	per second
$SnCl_4$	tin(IV) chloride
t	triplet
TCNE	tetracyanoethylene
TEM	transmission electron microscopy
T_g	glass transition temperature
TGA	thermogravimetric analysis
THF	tetrahydrofuran
TICT	twisted intramolecular charge transfer
TKI	tyrosine kinase inhibitor
TLC	thin-layer chromatography
TLV	threshold limit value
TOF	time of flight
UDMH	unsymmetrical dimethylhydrazine
UV	ultra-violet
UV-vis spectroscopy	ultra-violet visible spectroscopy
VOC	volatile organic compound
W/cm^2	watt per centimetre squared
w/v	weight/volume
w.r.t	with respect to
Z	*Z*-isomer
ZnO	zinc oxide

Chapter 1.

Introduction

This thesis aims to provide details about the dynamic relationship between light and chemistry in molecular systems. A common type of interaction between light and chemistry or chemical reactivity is when light is used to initiate certain chemical reactions (called gated reactivity). This light-gated reactivity was successfully demonstrated by using small photoresponsive molecules called dithienylethenes (DTEs) and noble metal-based nano-assemblies. The second type of interaction between light and chemistry is when an auxiliary external stimulus induces a photochemical response, for example, colour change or photochromism (called gated photochemistry). This objective was illustrated by developing modified dithienylethenes (DTEs) to create systems that respond to certain chemical reagents which alter or quench the photochemical response of the molecule.

1.1. Chemical transformations using light

"Chemistry is a central science that responds to societal needs"[1]

Controlling chemical reactions continues to be an objective that is central to the development of technologies that can convert abundant substances into useful materials. The chemical industries continually seek to improve these existing chemical processes, while proposing new ideas for the same.[2,3] As a result, there is a perpetual need for such innovations in various sectors like materials science, biomedicine, energy conversion, etc. Process and synthetic chemists make use of variables such as temperature,[4,5] pH,[6] redox,[7] pressure, or time, to control chemical reactions in industrial processes, with the temperature remaining the most common parameter used for controlling chemical reactions.[8] However, it remains a challenge to specifically control the location and time duration of temperature changes along with accounting for rapid heat dissipation.[9]

As technological advancements in the chemical industry become complex and elaborate, the corresponding methodologies also require greater accuracy. A stimulus that can enable the control over *when* and *where* the bond formation occurs, would provide the ultimate control over chemistry.[10]

Light, as an external stimulus, offers several distinct benefits to control molecular systems and chemical processes. Light provides superior temporal control over illumination down to the sub-femtosecond range and an improved spatial resolution through the use of multi-photon processes.[11] The external switching of the light source between the 'on' and 'off' state enables the ability to start and stop a chemical reaction on-demand.[3] The non-invasive character of light as a stimulus is beneficial in applications related to biomedicine and drug delivery. In addition, chemical reactions that demand specific wavelengths and intensities of light can be achieved by using modern optic technologies allowing to activate parallel processes. Chemical reactivity induced by light most commonly involves the excitation of molecules resulting in reactive excited-state species which can, then, react to give desired products (Figure 1.1 a)). The process of photosynthesis in plants, where visible light is used to drive an electron transport chain to produce energetic biological fuels, is one of the most notable examples of this approach. However, this approach has limited scope for molecular structure-property modifications due to the unpredictable nature of the excited states in terms of their reactivity and lifetime. Another strategy to use light for chemical transformations involves the use of dormant 'caged' species which become reactive once they are 'uncaged' upon photoexcitation (Figure 1.1 b)). This strategy is frequently employed in photolithography and involves the cleavage of a covalently bound protecting group that is responsive to light to generate the free molecule.[12] Such systems undergo irreversible photoreactions and are good for a single time activation/deactivation process.[9]

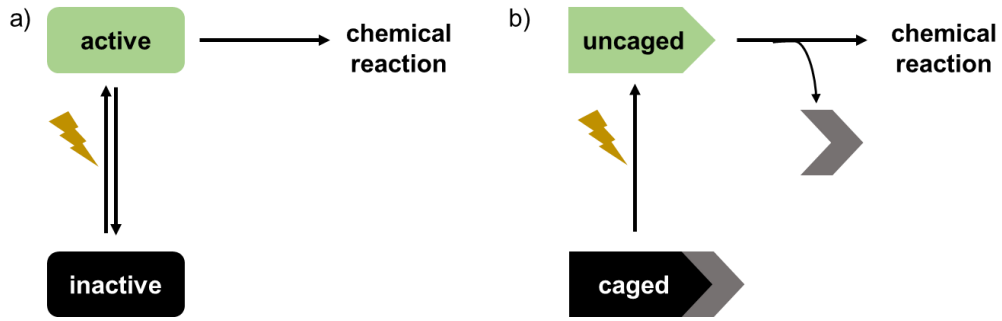

Figure 1.1: Schematic representation of light-assisted control of chemical reactivity[3]; a) where the reaction occurs using excited-state species, b) where the reaction occurs upon uncaging the reactive species

An alternate and attractive approach that can overcome the aforementioned issues is that of introducing a photoreversible "gate" based on small molecules called photochromes/photoswitches and the phenomenon itself is known as

photochromism/photoswitching, described in Section **1.2**. These molecules can toggle between two distinct isomers multiple times when exposed to the light of appropriate wavelengths. Systems incorporating such photoswitches can provide effective control over the entire chemical process using light, thereby, making them useful in applications ranging from optical devices to “smart” materials.[13]

1.2. Photochromism

The phenomenon of photochromism (or photoswitching) is defined as a light-induced reversible transformation of a molecule between two isomers that possess different absorption spectra (Figure 1.2).[14] Typically, there occurs a corresponding change in the colour of the system. The process of photochromism is generally assumed to be a unimolecular process involving interconversion between two molecular species.[15]

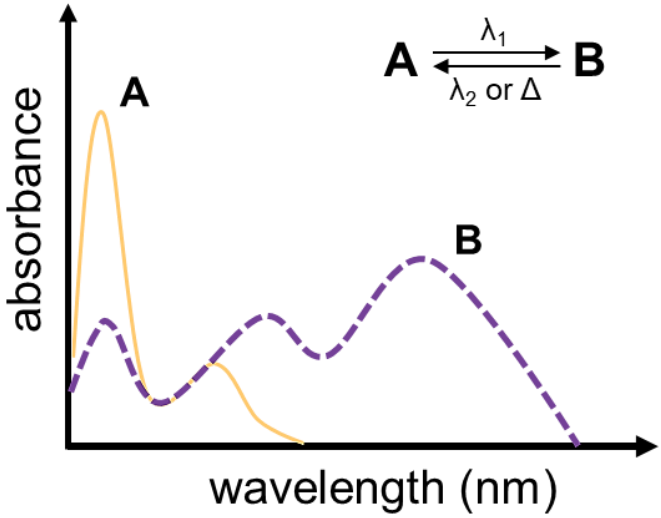

Figure 1.2: Representative absorption spectrum for the two isomers **A** and **B** for the reversible photoisomerization between **A** and **B**

As shown in scheme 1.1, when isomer **A** absorbs photons of wavelength λ_1, there occurs a photoisomerization reaction producing isomer **B**. The reverse reaction can be induced photochemically by irradiating with light of wavelength λ_2, a phenomenon called P-type photochromism; or thermally, a phenomenon called T-type photochromism, if the potential energy barrier between the two states is low.[16]

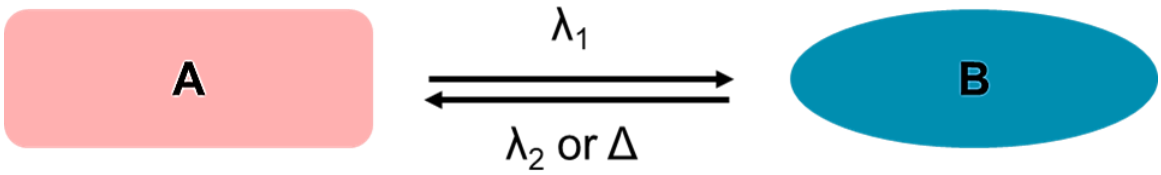

Scheme 1.1: Schematic representation of a photochromic reaction in which exposure of A with the light of wavelength λ_1 triggers photoisomerization to produce B. The reversion process can either be thermal, Δ (T-type), or photochemical (P-type) using the light of wavelength λ_2

Apart from the change in colour, marked differences in properties like chemical reactivity,[17,18] solubility,[19,20] refractive index,[21,22,23] conductivity,[24,25,26] dielectric properties,[27,28] shape & size[29,30] are observed upon interconversion due to the difference in geometry and electronic distribution of the two isomers.[31]

The dominant photochromic processes that occur when such molecules are irradiated with light are: cis/trans isomerization, ring-closing reaction, or photo-tautomerization.[32]

1.2.1. Thermal (T-type) photochromism

The common classes of organic molecules that belong to T-type systems include spiropyrans, spirooxazines, azo compounds, and donor-acceptor Stenhouse adducts (DASAs). Some examples of these T-type photochromic molecules are given in scheme 1.2.[15]

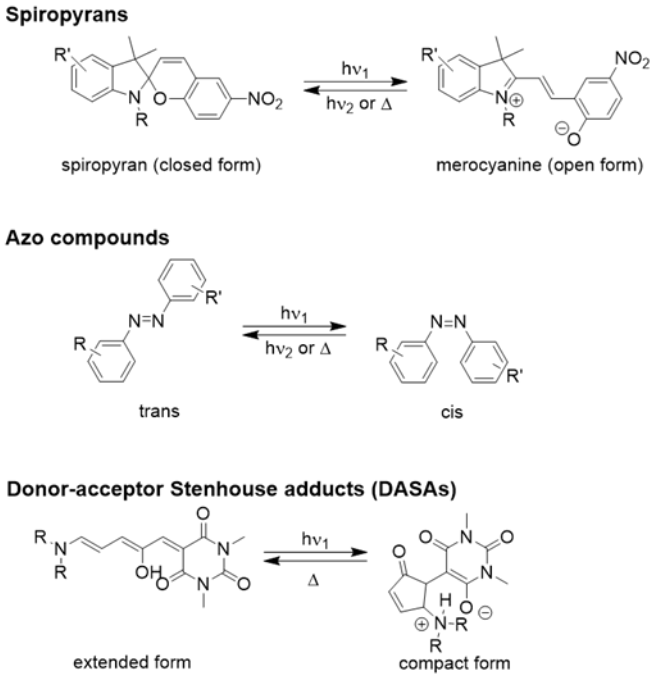

Scheme 1.2: Examples of photochromic molecules that exhibit T-type photochromism

Azobenzene derivatives have been used extensively as dyes and remain to be the most popular class of photochromic compounds that undergo cis/trans isomerization reaction upon irradiation with light of appropriate wavelength. The trans isomer has thermodynamic stability of 50 kJ/mol higher than the cis isomer.[33] Therefore, upon irradiation with UV light, the trans form will isomerize into the cis form, which, can spontaneously revert to the more stable trans form thermally in the dark, the rate of the reverse reaction depends on the chemical structure of the system and is generally slower than the photochemical reversion.[32] The rearrangement of the electronic structure of the molecule upon irradiation is not pronounced, as a result of which, only small changes in absorption spectra of the two isomers are observed. But, the rearrangement of the structure induces a significant change in the free volume of the molecule, and much of the azobenzene derivatives find applications that are related to the structural changes of the molecule.[16] For example, azobenzenophane-type crown ethers are capable of toggling between cis and trans isomers upon irradiation with light leading to an “all-or-nothing” change in their ion binding ability, wherein only the cis isomer can bind alkali metals.[34]

Spiropyrans, spirooxazines, and chromenes belong to the class of T-type photochromic molecules that involve the ring-opening/closing reaction together with double bond isomerization. Irradiation with the light of an appropriate wavelength generates the fully π-

conjugated and charged open isomer. This structural reorientation leads to changes in the dipole moment, polarizability, emission spectra along with the usual change in the absorption spectra.[35]

Generally, most classes of photochromic molecules require high-energy UV light to induce their photochemical reactions. This high-energy UV light can damage healthy cells and can cause the degradation of some macromolecular systems. Therefore, the photochromic systems involving UV light have limited applications in biomedicine and material science. A new class of T-type photochromic molecules called donor-acceptor Stenhouse adducts (DASAs) were designed to potentially overcome this limitation by using visible light to trigger the photochemical reaction. These molecules convert from the coloured and conjugated extended form to the compact ring-closed, colourless, zwitterionic form upon irradiation with visible light. The ring-closed isomer only reverts back thermally.[36]

1.2.2. Photochemical (P-type) photochromism

The class of organic molecules that exhibit P-type photochromism possess a bistable system with a large potential energy barrier between the two isomers leading to the absence of spontaneous thermal reversion. Therefore, no reverse reaction occurs in the absence of light.[16]

Two main families of P-type photochromic molecules are fulgides & fulgimides, and diarylethenes. The examples of these P-type photochromic molecules are given in scheme 1.3. These molecules possess a 1,3,5-hexatriene system that can undergo a 6π-electrocyclization reaction upon irradiation with UV light leading to a conjugated ring-closed isomer which is coloured. Cycloreversion to the ring-opened isomer occurs only upon irradiation with visible light.[15,37]

Fulgides & Fulgimides

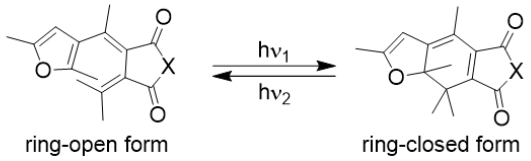

X = O; fulgide
X = NH; fulgimide

Diarylethenes

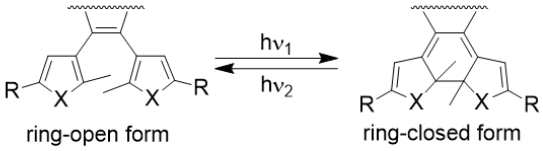

X = S, O, N

Scheme 1.3: Examples of photochromic molecules that exhibit P-type photochromism

Fulgides and fulgimides belong to the category of organic molecules whose core structural features include a basic skeleton of bismethylenesuccinic anhydride/succinimide and at least one aromatic ring/heterocycle directly attached to the methylene carbon atom. The ring-open isomer in the case of fulgides and fulgimides exists in *E*- and *Z*-geometries, and it is only the *E*-isomer that undergoes photocyclization reaction (Scheme 1.4). A competing cis-trans isomerization reaction of *E*-isomer to *Z*-isomer is regarded as an energy-wasting and a system complicating process.[38,39]

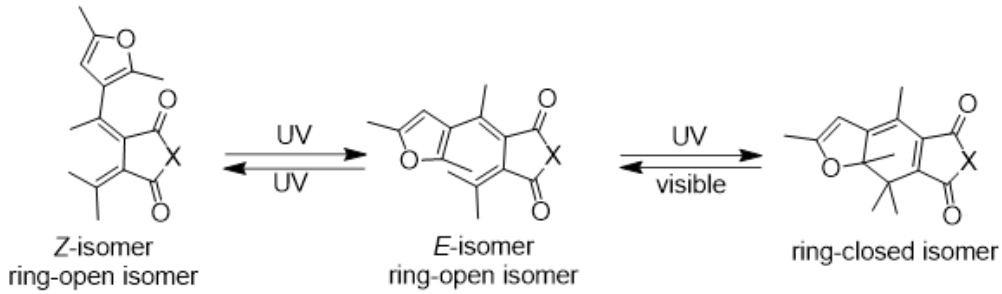

X = O; fulgide
X = NH; fulgimide

Scheme 1.4: Photoisomerization in fulgides and fulgimides

Photochromic diarylethene derivatives based on heterocyclic aryl groups were developed in the late 1980s and represent the most extensively studied category of P-type

photochromic compounds. The most striking features of this class of molecules include:[16,40,41,42]

1. high fatigue resistance of ring-closing and ring-opening photoreactions
2. the relative ease of synthesis
3. high bistable character, *i.e.*, the two isomers interconvert only in the presence of the light of appropriate wavelengths
4. both isomers possess distinct optical and electronic properties

1.3. Dithienylethene-based photoswitches

The research on 1,2-dithienylethene-based diarylethenes has received the most attention among all the heterocycles. The following sections will discuss this class in further detail.

1.3.1. Basic structure

Photoswitches based on dithienylethenes (DTEs) consists of a central alkene that connects two thiophene heterocycles at 3 and 3' positions (Figure 1.3). The arrangement generates the1,3,5-hexatriene system (Figure 1.3, indicated in bold yellow colour) required for photochemical ring closure. The thiophene ring-substituents, labelled R_1-R_6 in Figure 1.3, can be modified, thereby varying the optical and electronic properties of the two isomers based on the desired area of application.[43]

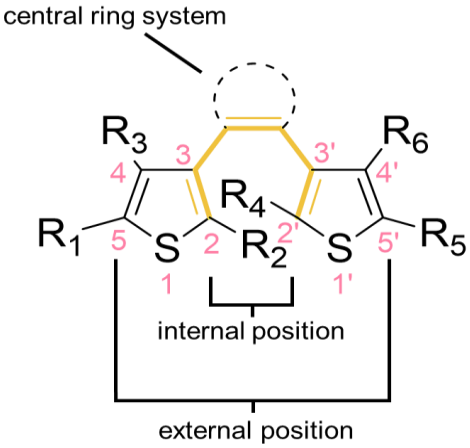

Figure 1.3: Basic structure of a dithienylethene photoswitch

The central alkene is often part of a ring system (central ring system in Figure 1.3), such as maleic anhydride, cyclopentene, hexafluorocyclopentene, etc. The ring system prevents the competing cis-trans isomerization reaction.[16] Substitution of alkyl groups at the internal 2 and 2' positions leads to stable and reversible systems that do not undergo oxidation reactions that form condensed rings.[44,45]

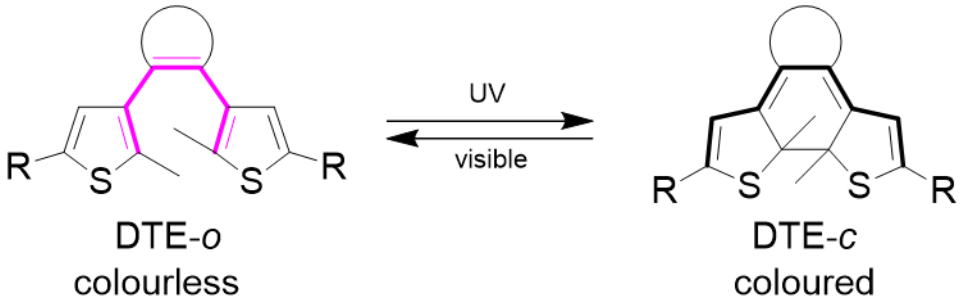

Scheme 1.5: Light-induced reversible cyclization of DTE derivatives between the colourless ring-open (DTE-*o*) and the coloured ring-closed (DTE-*c*) isomers upon irradiation with light of two appropriate wavelengths

The ring-open form of dithienylethene, DTE-*o*, is generally colourless as the π-electrons are localized on the two thiophenes and the alkene. Therefore, it can absorb light of a suitable wavelength (in most cases is in the UV region) and undergo the 6π-electrocyclization reaction to obtain a 1,3-cyclohexadiene structure, DTE-*c*. This ring-closed isomer, DTE-*c*, now has extended π conjugation along the backbone, thus, shifting the absorption spectrum into the visible region (Scheme 1.5).[44] Cycloreversion process of DTE-*c* can be triggered using light of this different wavelength, usually in the visible region, to regenerate the ring-open isomer, DTE-*o*. Figure 1.4 shows the typical change in the absorption spectrum of a dithienylethene when the light of wavelength λ_1 triggers ring closure of the system.

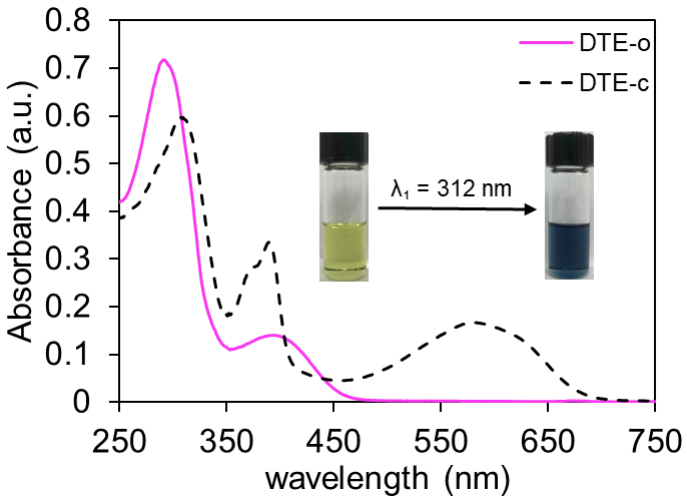

Figure 1.4: Typical changes in the UV-visible absorption spectrum of ring-open isomer DTE-o (pink line) when it is irradiated with light of wavelength λ_1 to produce ring-closed isomer DTE-c (black dotted line)

Frequently, the ring-closed isomers of dithienylethenes are considered to be thermally stable and do not spontaneously revert back to the ring-open isomer in dark under ambient conditions and at temperatures as high as 80°C.[42] This thermal stability of the ring-open and ring-closed isomers of DTE photoswitches is attributed to the change in aromaticity of thiophenes upon ring closure whose low value (aromatic stabilization energy difference for thiophene = 4.7 kcal/mol) reduces the energy barrier between the two isomers (relative ground-state energy difference between ring-open and ring-closed isomers = -3.3 kcal/mol) and makes the ring-closed isomer of DTE stable.[41,42,44,46] In addition, dithienylethenes are considered to undergo photochemical cyclization and cycloreversion reactions multiple times without suffering from any undesired side reactions (fatigue-resistance).[41] By employing clever design strategies, the resistance to unwanted side reactions and photodegradation can be minimized.[42]

1.3.2. Photochemical ring-closing and ring-opening reactions

In dithienylethene derivatives, the photochemical ring closure is dependent on the arrangement of the π-orbitals of the central 1,3,5-hexatriene system. In the ring-open isomer DTE-*o*, the two thiophene rings can rotate freely around the carbon-carbon single bond joining the heterocycle with the alkene. As a result of this free rotation, the ring-open isomer DTE-*o* exists as an equilibrium mixture of two different conformers (Scheme 1.6).

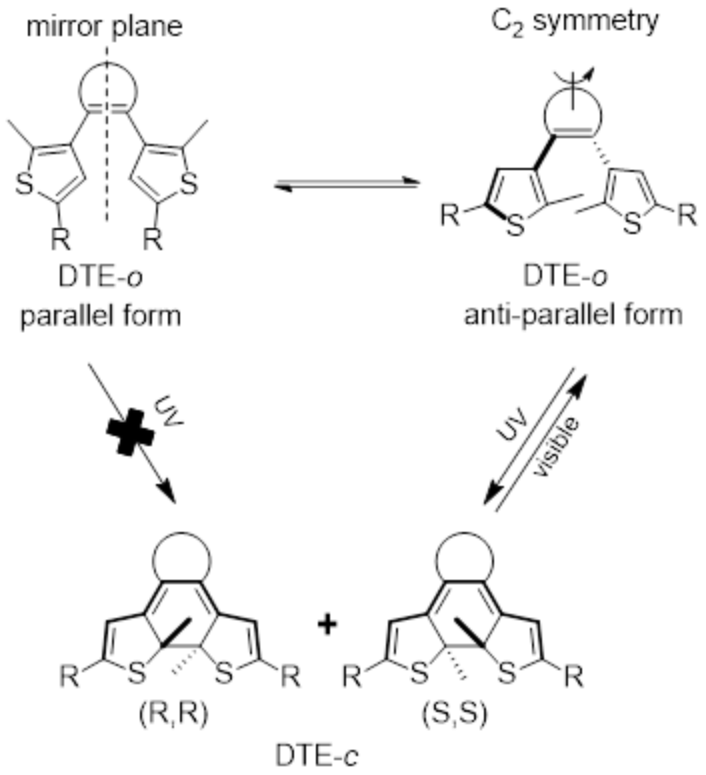

Scheme 1.6: The ring-open isomer of dithienylethene DTE-*o* can exist as *parallel* and *anti-parallel* conformations. The *parallel* conformation that has a mirror plane of symmetry is non-photoactive, while the *anti-parallel* conformer possesses a C_2 axis of symmetry and can undergo photoinduced electrocyclization reaction to generate a racemic mixture of two enantiomers of the ring-closed isomer DTE-*c*[46]

When the two thiophene groups are facing the same direction, they possess a mirror plane of symmetry and the conformation is known as *parallel* conformation (Scheme 1.6, parallel form). While, in the *anti-parallel* conformation of DTE-*o*, the two thiophene groups are oriented in the opposite direction with a C_2 axis of symmetry across the molecule (Scheme 1.6, anti-parallel form).[42,46] As described by Woodward-Hoffmann rules, the photochemically induced ring closure can only occur via a conrotatory electrocyclization of the *anti-parallel* conformer to conserve orbital symmetry.[47]

The photoresponsive dithienylethenes have a central 6π 1,3,5-hexatriene system. The photoisomerization reaction in such molecules occurs from the highest occupied molecular orbital (HOMO) of the excited state configuration ψ_4^* (which is the lowest unoccupied molecular orbital (LUMO) of the ground state configuration) by a conrotatory motion generating a new σ bond, which yields the 1,3-cyclohexadiene (Figure 1.5).[48]

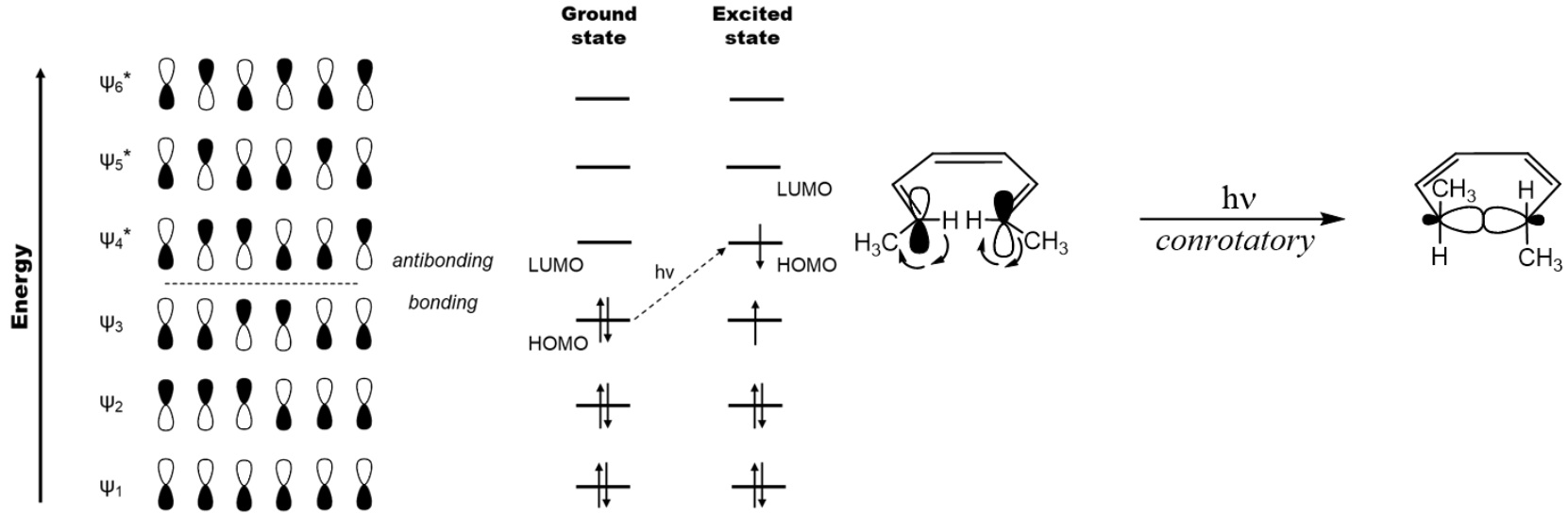

Figure 1.5: Typical π molecular orbital configuration of 1,3,5-hexatriene systems (left); conrotatory photochemical electrocyclization of the HOMO of the excited state ψ_4* (right)[49]

The thermally induced electrocyclization in the case of 1,3,5-hexatrienes occurs by the disrotatory motion of the ground state HOMO ψ_3 (Figure 1.5). This does not occur in the case of dithienylethenes due to the large activation energy barrier that is created by the steric hindrance of the internal methyl groups in DTE-*o*.[16,46]

The light-induced ring-opening reaction/cycloreversion of the ring-closed isomer DTE-*c* occurs in the conrotatory mode upon irradiation with light of a wavelength in the visible region due to their extended π-conjugated systems (Scheme 1.5).[46]

1.3.3. Quantum yield and photostationary state

Quantum yield (φ) and photostationary state (PSS) are used to determine the photochromic performance of DTE systems. The quantum yield (φ) of a photochemical reaction describes the product yield of the reaction.[15] Mathematically, it is defined at a certain wavelength as the ratio of the amount of product formed, which in the case of DTEs are the number of molecules that are isomerized, to the total number of photons absorbed (Equation 1.1).[14]

$$\varphi(\lambda) = \frac{number\ of\ isomerized\ molecules}{total\ number\ of\ photons\ absorbed}$$

Equation 1.1: Mathematical representation of quantum yield (φ) at a given wavelength (λ)

Quantum yield of photocyclization and cycloreversion reactions provides a measure for the efficiencies of these reactions for a DTE molecule. Theoretically, the maximum value of φ can be 1, but, in practice, the values are lower due to the presence of a non-photoactive *parallel* isomer or any side reactions.[37,42,43]

The photostationary state (PSS) of a photochemical reaction, reported as a percentage describes the relative yield of photocyclization reaction under a specific set of conditions (wavelength, temperature, solvent) (Equation 1.2).

$$PSS = \left(\frac{number\ of\ isomerized\ molecules}{total\ number\ of\ molecules}\right) * 100\%$$

Equation 1.2: Mathematical representation of the photostationary state

A photochemical reaction is said to reach its photostationary state, a steady state at which the rate of ring-closing reaction becomes equal to the rate of ring-opening reaction.[14] The photostationary state of a system depends upon the intensity of the incident light, molar absorption coefficients of the two isomers at a given wavelength, quantum yields of the forward and back reactions, and the rate of thermal back-reaction.[15,16]

PSS for most DTE systems is never 100% as some of the ring-closed isomers tend to revert to the ring-open isomer during irradiation with UV light.[49] Although, multiple DTE systems have been developed where PSS → 100%.[50,51] Throughout this thesis, the PSS of DTEs will refer to the ring-closing reactions of the ring-open isomers until no further changes in ^{1}H NMR spectra and UV-visible absorption spectra are observed. In contrast, the cycloreversion reaction is quantitative (PSS = 100%) as only the ring-closed isomers absorb the visible light while the ring-open isomers remain unchanged.[42]

1.3.4. Photodegradation and by-products

In most cases, dithienylethene-based photochromic compounds are fatigue-resistant and thermally irreversible. Nonetheless, some dithienylethenes can undergo certain irreversible photochemical reactions that lead to products that are non-photochromic, thus diminishing the photoresponsive properties of dithienylethenes. Irradiation with UV light in the presence of oxygen degrades the ring-closed isomer DTE-*c* and leads to the formation of oxidized products like endo-peroxides (Scheme 1.7, **II** & **III**).[52,53] Even in the absence of oxygen, exposure of ring-closed isomer DTE-*c* to UV light for an extended period of time causes rearrangement into a non-photochromic fused system **I** (Scheme 1.7).[53,54]

When dithienylethene molecules are designed with a non-cyclic alkene backbone connecting the two thiophene heterocycles, the ring-open isomer of such systems can undergo *Z* → *E* isomerization upon irradiation with UV light (Scheme 1.7).[44] The DTE-*E* (Scheme 1.7) isomer that is produced is non-photochromic.

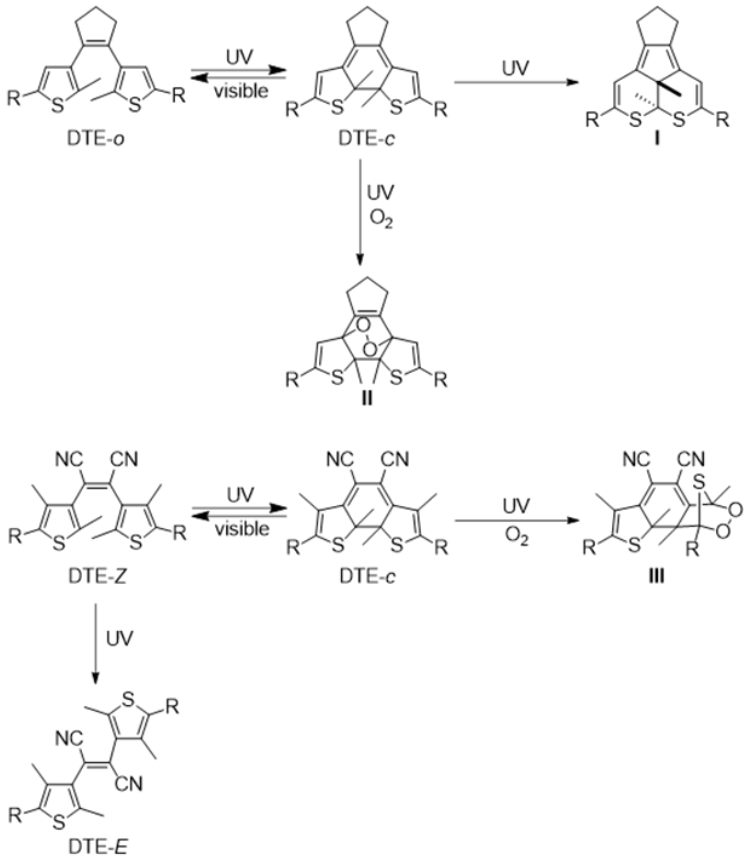

Scheme 1.7: Side reactions of dithienylethenes upon prolonged UV exposure

Several synthetic modifications of DTE structures tend to reduce these degradation processes:

1. employing ring systems as part of the central alkene prevents the *Z* → *E* isomerization

2. protecting the 4 and 4' positions of the thiophene rings by substitution (*e.g.* methyl groups) or annelation (*e.g.* benzothiophenes) hinders the ring-oxidation, and rearrangement of the ring-closed isomer to form a polyene[55]

1.3.5. Synthetic and functional diversity

The dithienylethenes molecules are considered amenable to synthetic and functional modifications depending on the end-use application. The DTE architecture is, in general, compliant with a variety of chemistries. Most often, these alterations are made on the 5- or "external" positions of the thiophene rings (Figure 1.6).[43,54,56] The 2- or "internal"

positions on thiophene rings are, typically, substituted with methyl groups (Figure 1.6). Although, these internal positions can also be tailored to induce changes in the optical and electronic properties of DTEs.[40,57,58] Moreover, the “top” or “central” ring systems (Figure 1.6) of much of the reported literature is limited to cyclopentene or hexafluorocyclopentene units. More recently, there have been reports where the “top” or “central” ring has been modified to expand the areas of application of DTEs.[59,60,61,62]

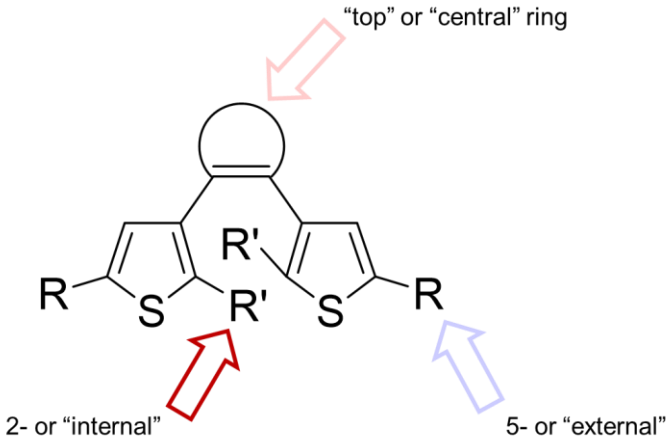

Figure 1.6: Synthetic tailoring of DTEs can be achieved by modifications on 5- or “external” positions or 2- or “internal” positions of the thiophene rings; or the “top” or “central” ring system

1.3.6. Steric differences between ring-open and ring-closed isomers

The ring-open isomers of DTEs are comparatively more flexible than their ring-closed isomers. Consequently, the ring-open isomer can rotate freely around the carbon-carbon single bonds that connect the thiophene rings to the central alkene (details in Section 1.3.2). This structural flexibility results in the interconversion between *parallel* and *anti-parallel* conformers and allows for the convergence of the functionalities located at internal or external positions of the thiophene rings (Figure 1.7).[37,41,42]

The ring-closed isomers of DTEs are considerably more rigid due to the formation of a tricyclic structure upon photocyclization. As a result, the functional groups on thiophene rings are forced to diverge from each other. Irradiation with visible light regenerates the structurally flexible ring-open isomer.

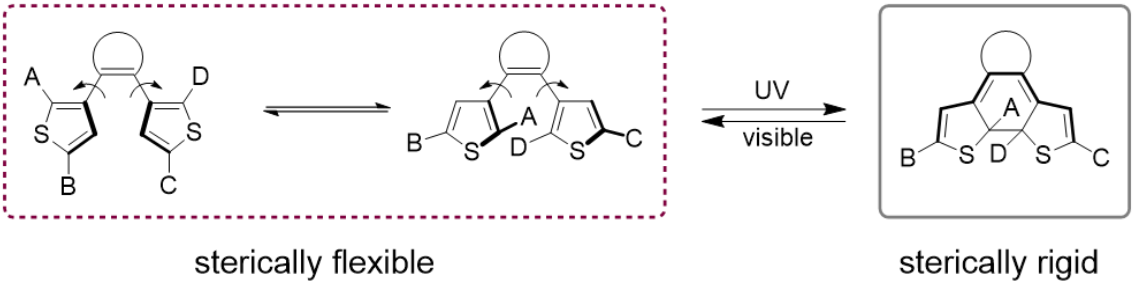

Figure 1.7: Geometrical changes in DTE derivatives upon photocyclization. In the ring-open isomer, the thiophene rings can freely rotate resulting in the convergence of functional groups at internal (A and D) or external (B and C) positions; while in the ring-closed isomer, the rings are locked such that the functional groups diverge from each other

1.3.7. Electronic differences between ring-open and ring-closed isomers

Upon irradiation with UV light, the photocyclization reaction induces changes in the bond configuration of the two isomers leading to dramatic electronic changes upon ring closure. In the ring-open form of DTE, the π-systems are localized on the two thiophene rings making them electronically isolated from each other. This electronic isolation is a direct consequence of the steric hindrance of the functional groups at internal positions leading to the thiophene rings being not in the same plane. Additionally, the functional groups on the thiophene rings, A and B; C and D, are electronically connected via the π-system of the thiophene rings (Figure 1.8). Upon ring closure, the bond rearrangement leads to a linear π-conjugated system across the DTE backbone. This extended π-conjugation shifts the absorption spectrum of the ring-closed isomer into the visible region, thus making the solution appear coloured in most cases. Furthermore, active electronic communication is enabled between the external groups, B and C, on the two thiophene rings thereby allowing them to identify their electronic character (Figure 1.8). In contrast, the groups, A and B; C and D, now become electronically insulated from each other as a result of the generation of sp^3 centres between them.[37,41,42,43,63,64]

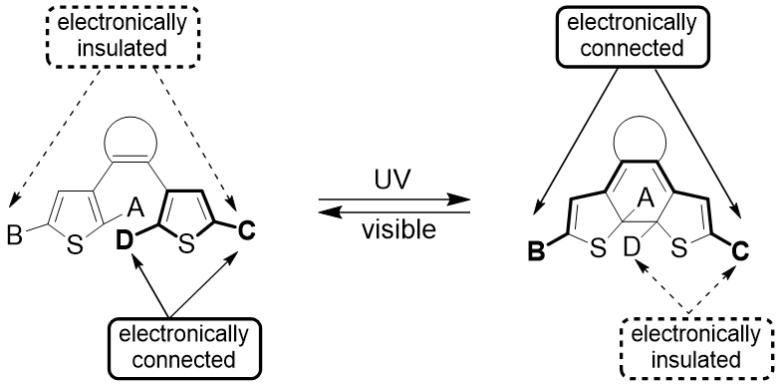

Figure 1.8: Electronic differences between the ring-open and the ring-closed isomers of DTEs. In the ring-open isomer, the π-electrons are localized on the thiophene rings making the functional groups A, B, and C, D electronically connected to each other, while, an inter-ring connection between the external groups B, C is electronically insulated. Ring closure generates a π-system which is delocalized thus making B and C electronically connected while electronically insulating the connections between A, B, and C, D

1.4. Integration of photochromism and chemical reactivity

Section 1.1 of this thesis describes the significance of the relationship between light and chemistry. This integration of photoactivity of DTEs and chemical reactivity can potentially create new technologies that can prove to be advantageous in materials science, biomedicine, analytical chemistry. The synergy between light and the photoresponsive DTEs is recognized in the following two ways:

1. *gated reactivity* (*i.e.* photochemistry happens first) – when the structural and electronic differences in the two isomers of DTEs influence the chemical reactivity in a markedly different manner. Further details about this photochromic modulation of chemistry will be presented in section 1.5.

2. *gated photochemistry* (*i.e.* chemistry happens first) – when a chemical reaction regulates the photoresponsive behaviour of precisely designed DTE molecules. Section 1.6 provides details about this approach.

The outline of the thesis, in section 1.7, eventually correlates these strategies to different areas of application.

1.5. Gated reactivity approach

The steric and electronic variations that occur in DTE molecules upon photoisomerization can be used to influence the interaction of the DTE molecules with other substrates. Such modulated systems can be employed in areas of catalysis, as reagents for drug delivery, etc. The following sections (1.5.1 and 1.5.2) provide representative examples from the literature that utilizes these differences to integrate light and chemical reactivity.

1.5.1. Controlling chemical reactivity using steric/geometric differences

Harnessing the steric differences of the DTE systems that occur upon photoisomerization, Irie *et al.* synthesized DTEs functionalized with boronic acid groups at the external positions of the benzothiophene rings (Scheme 1.8 a)). In the ring-open isomer, the boronic acid groups can converge towards each other, due to the rotation of the carbon-carbon single bond connecting the heterocyclic rings to the central alkene, to reversibly bind saccharides in the parallel conformer. The carbohydrate bound DTE would no longer undergo a ring-closing reaction. Only the anti-parallel ring-open isomer would undergo ring closure upon irradiation with UV light to produce the rigid ring closed isomer which has the boronic acid groups diverging away from each other leading to a structure that would be unable to bind any carbohydrates.[65]

Based on the same concept, DTE systems modified with heterocyclic crown ethers were developed by Irie *et al.*[66,67,68] and Kawai *et al.*[69] to bind alkali-metal cations (Scheme 1.8 b)). The flexible ring-open isomer of the system is able to bind larger cations like rubidium and caesium owing to the cooperative interactions of the convergent crown ether functionalities. In contrast, the rigid ring-closed isomer has both the crown ether functionalities diverging away from each other thereby acting as independent, single crown ether units that could now only bind smaller cations like sodium and potassium.

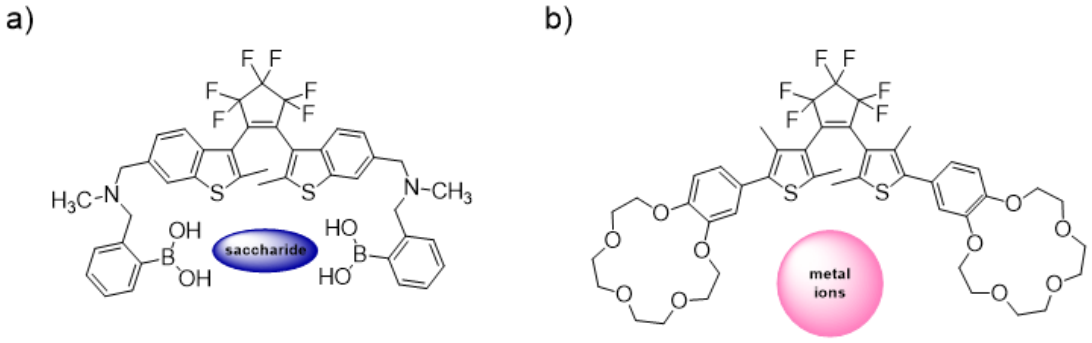

Scheme 1.8: DTEs as photoswitchable hosts for a) carbohydrates[65]; b) metal ions[69]

Branda *et al.* have successfully demonstrated that the geometric differences between the ring-open and ring-closed isomers of tailormade DTE systems can effectively control metal-catalyzed reactions.[18] Their system consisted of oxazoline rings tethered to the internal positions of the DTE backbone. The flexible ring-open isomer can chelate with metals such as Cu(I). The chelated Cu^{+} is forced to reside in a C_2-chiral environment consequently acting as a chiral catalyst for the cyclopropanation reaction of styrene with ethyldiazoacetate. In the presence of the ring-open isomer, the reaction is both diastereo- and enantioselective. The rigid ring-closed isomer that is generated upon irradiation with UV light has the two oxazoline rings inappropriately positioned for metal binding, thus reducing the stereoselectivity of the reaction (Scheme 1.9).

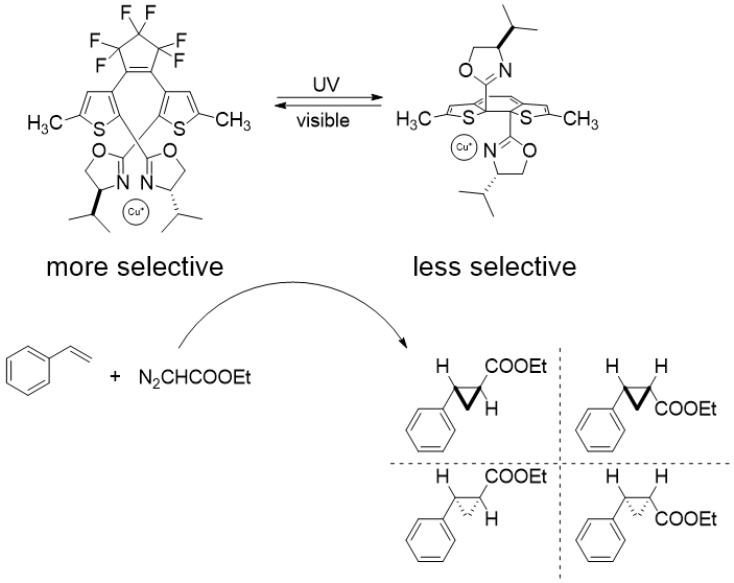

Scheme 1.9: Chiral bis(oxazoline) based DTE system with geometry difference in the two photoisomers can chelate with Cu(I) centre only in the ring-open isomer, thus varying the diastereo-and enantioselectivity of the Cu-catalyzed cyclopropanation reaction[18]

The geometric changes in DTE systems that affect their binding properties can also be augmented to biochemical systems. A DTE backbone with modifications on external positions has been designed to alter the enzymatic activity of human carbonic anhydrase I (hCAI) depending upon which photoisomer is present (Scheme 1.10).[70] The flexible ring-open isomer can acquire a conformation where the sulfanilamide and copper iminodiacetate are at a suitable distance to simultaneously bind at the active site of the enzyme. Irradiation with UV light generates the rigid ring-closed isomer which has the two binding groups farther apart such that only the sulfonamide group binds with the active site of the enzyme thereby decreasing the inhibition effect.

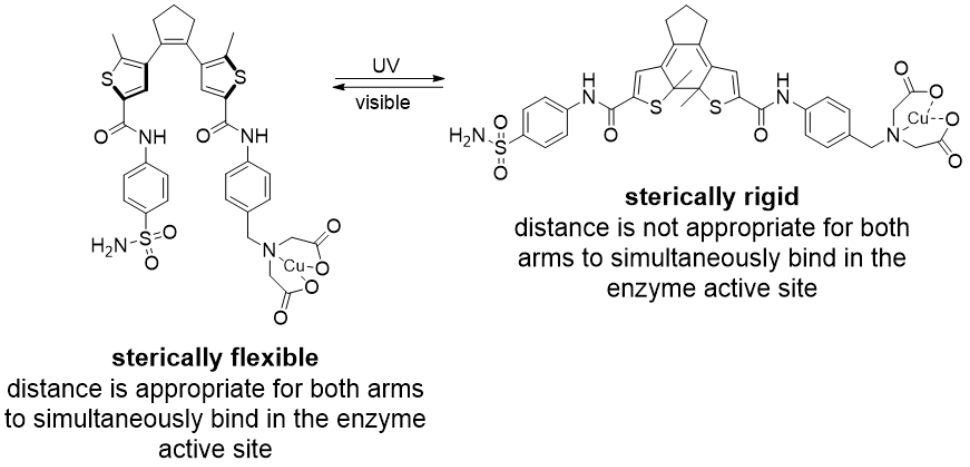

Scheme 1.10: Variations in enzyme activity of hCAI due to the steric differences between the ring-open and the ring-closed isomers of the DTE backbone[70]

1.5.2. Controlling chemical reactivity using electronic differences

Photoisomerization of the ring-open isomer of DTE systems to their ring-closed counterparts also changes the electron distribution of all the DTE backbones. This difference in electronic communication for ring-open and ring-closed isomers of DTE systems was successfully demonstrated by Lehn *et al.* the changes in the acidity of the external phenol groups of unsymmetrical DTE photochromes with light.[71] The phenol group and the pyridinium groups are electronically insulated in the ring-open isomer, while, in the ring-closed isomer, due to the π-system delocalization, electronic communication is established between the two functional groups leading to a decrease in pK_a value upon photoisomerization (Scheme 1.11 a)).

Similarly, localization of π-electrons in the ring-open isomer enables the electronic communication between the functional groups on the internal and external positions of each thiophene ring. Ring closure disrupts this localization and leads to a break in communication between these groups. Irie *et al.* illustrated this by functionalizing the internal position with a phenol moiety and external position with the pyridinium group on one of the thiophene rings.[72] The pK_a of the phenol group is higher for the ring-open isomer due to the interaction between the pyridinium and phenol groups through the localized π-system of the thiophene ring. Irradiation with UV light breaks this conjugation thereby disrupting the communication between the pyridinium and phenol groups, thus, leading to an increase in the value of pK_a of the phenol for ring-closed isomer (Scheme 1.11 b)).

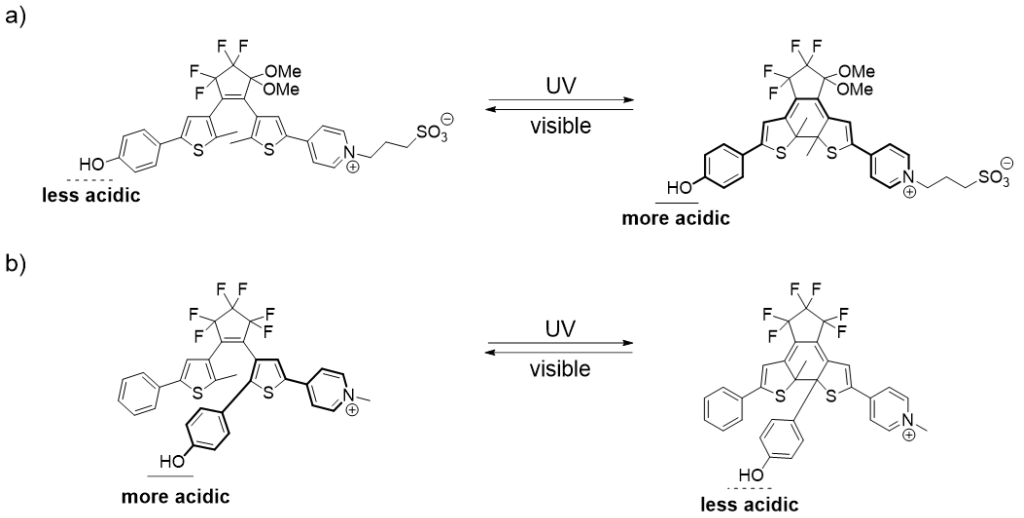

Scheme 1.11: a) Increase in the acidity of the phenol group on the DTE upon ring closure as a result of enhanced electronic communication (highlighted in bold) between the pyridinium and phenol groups[71]; b) Decrease in the acidity of the phenol group on the DTE upon ring closure caused by the disruption in electronic communication (highlighted in bold) between pyridinium and phenol groups[72]

Lapouyade *et al.* successfully applied the electronic difference between the ring-open and ring-closed isomers of an azacrown DTE to bind and release cations.[73] In the ring-open isomer, the azacrown ether complexes with metal cations like calcium (Ca^{2+}), thus acting as an effective ionophore. Irradiation with UV light generates the ring-closed isomer which now has a delocalized π-system allowing the ionophore to communicate with the electron-withdrawing aldehyde group on the other thiophene ring (Scheme 1.12). The net result is a decrease in the binding affinity of the azacrown ether by 4 orders of magnitude and the release of the bound cation upon photocyclization.

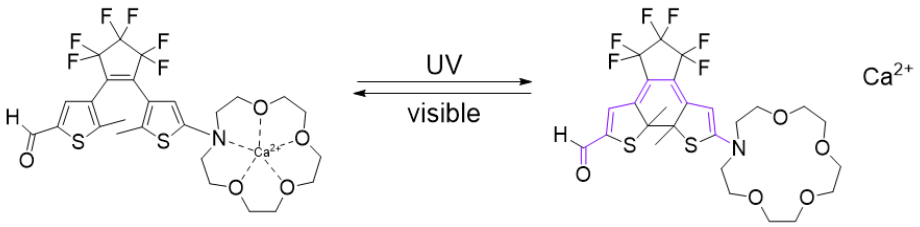

Scheme 1.12: Ring closure by UV light establishes an electronic communication pathway between the electron-withdrawing aldehyde group and the azacrown ether ionophore (highlighted in purple) resulting in the decrease in the density of nucleophilic lone-pair electrons on the nitrogen atom in the azacrown ether ring leading to the release of Ca^{2+} ions[73]

Branda *et al.* have applied the variations in electronic communications for ring-open and ring-closed isomers of specially designed DTE systems to regulate and monitor different types of chemical reactions (Scheme 1.13).[74,75,76]

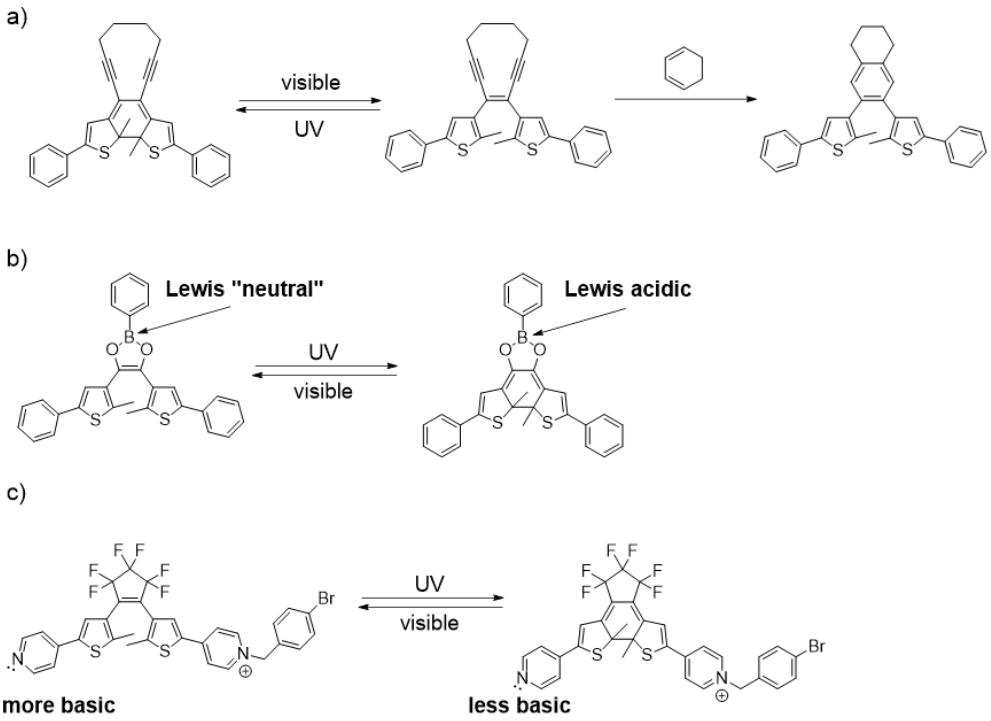

Scheme 1.13: Modulation of chemical reactivity using the electronic differences between the ring-open and ring-closed isomers of various DTE systems designed to a) photoregulate Bergman cyclization[74]; b) adjust Lewis acidity of Boron using light[76]; c) modulate the coordination behaviour of nitrogen's lone-pair of electrons with light[75]

The changes in the electronic pathways within the DTE backbone upon irradiation with light can also be applied in biochemical reactions. For example, Branda *et al.* have

successfully presented that a DTE-based pyridoxal 5'-phosphate (PLP) can act as a light-controlled catalyst.[51] The ring-open isomer of the photoresponsive PLP mimic has the aldehyde and pyridinium groups electronically insulated from each other and cannot catalyze the racemization of amino acid. Irradiation with UV light facilitates the interaction between aldehyde and pyridinium groups by creating the extended π-system across the DTE backbone which now acts as the catalyst for racemization (Scheme 1.14).

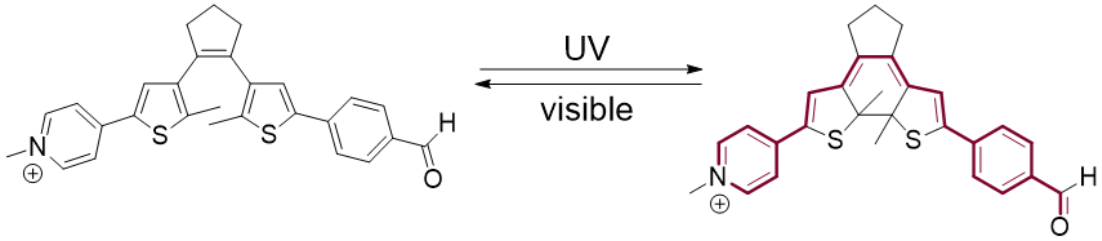

Scheme 1.14: Photoresponsive PLP mimic DTE system in the ring-closed form has the desired extended π-conjugation (highlighted in bold purple) that allows the aldehyde and pyridinium groups to communicate and thus catalyze the racemization of amino acid[51]

More recently, Branda *et al.* successfully reported the spontaneous release of small molecules from a 'masked' DTE system containing amine and carbonated groups on the external positions of the two thiophene rings.[77] In the ring-open isomer, amine and carbonate groups are electronically insulated from each other and no spontaneous release occurs. Exposure to UV light generates the ring-closed isomer with an electronic pathway consisting of the lone-pair of electrons on the amine group to push into the conjugated backbone, thereby, stimulating the spontaneous breakdown of the carbonate to release *tert*-butylcarbonate anion (Scheme 1.15).

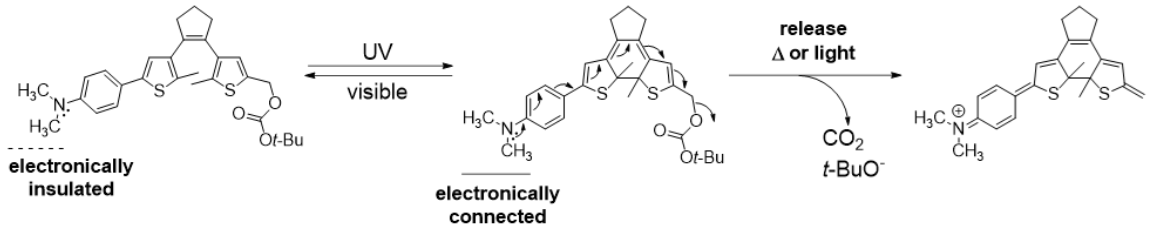

Scheme 1.15: UV light exposure creates the desired electronic pathway for fast spontaneous fragmentation of carbonate group to release tert-butylcarbonate anion from a 'masked' DTE system[77]

1.6. Gated photochemistry approach

The approach of 'gated photochemistry' involves the use of an additional external stimulus such as heat, solvation, electricity, or chemicals to induce the photochromic behaviour of the system (Scheme 1.16).[37,78] In most cases, the DTE systems are designed such that the central hexatriene ring that is essential for the photocyclization reaction is absent until the additional stimulus spontaneously generates it.[40]

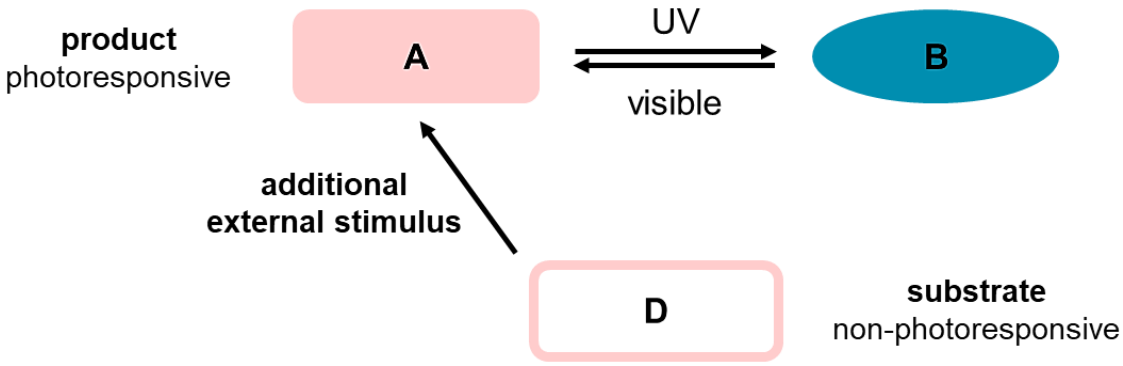

Scheme 1.16: Pictorial representation of the 'gated photochemistry' approach

The strategies involved to chemically gate photochromism frequently involve the following strategies:

1. 'gated' photochromism based on *geometric* effects of DTEs
2. *electronic* effects of DTE systems for 'gating' photochromic properties
3. 'gating' based on *quenching* effects
4. 'gated' photochromism via *chemical reagents* to generate the hexatriene ring

Sections 1.6.1 to 1.6.4 provide examples from literature to further discuss each of the strategies in detail.

1.6.1. Geometric effects of DTEs to 'gate' photochromism

The flexible nature of the ring-open isomer of DTE systems allows them to exist as *parallel* and *anti-parallel* conformers (details in section 1.3.2). Only the *anti-parallel* conformers can undergo the ring-closing reaction. The systems that 'gate' photochromic properties of

DTEs via the differences in their geometries do so by locking, both intramolecular and intermolecular, the DTEs in their *parallel* conformations.

Irie *et al.* demonstrated the phenomenon of intramolecular locking of the two arms of DTEs by modifying the external positions of the two benzothiophene heterocycles with carboxylic acid and thiol functional groups.[78] The DTE system functionalized with carboxylic acid groups at the external positions were locked in their *parallel* conformation by strong intramolecular hydrogen bonds between the two arms which is responsible for the 'gating'. The system was unlocked and became photoactive only upon the addition of a solvent, like ethanol, that can compete for the hydrogen bonds (Scheme 1.17 a)). While the DTE system decorated with thiol groups could reversibly be locked in their *parallel* conformation by oxidation of thiols to produce disulphide linkages. The addition of a reducing agent unlocks the photochromism of the system (Scheme 1.17b)).

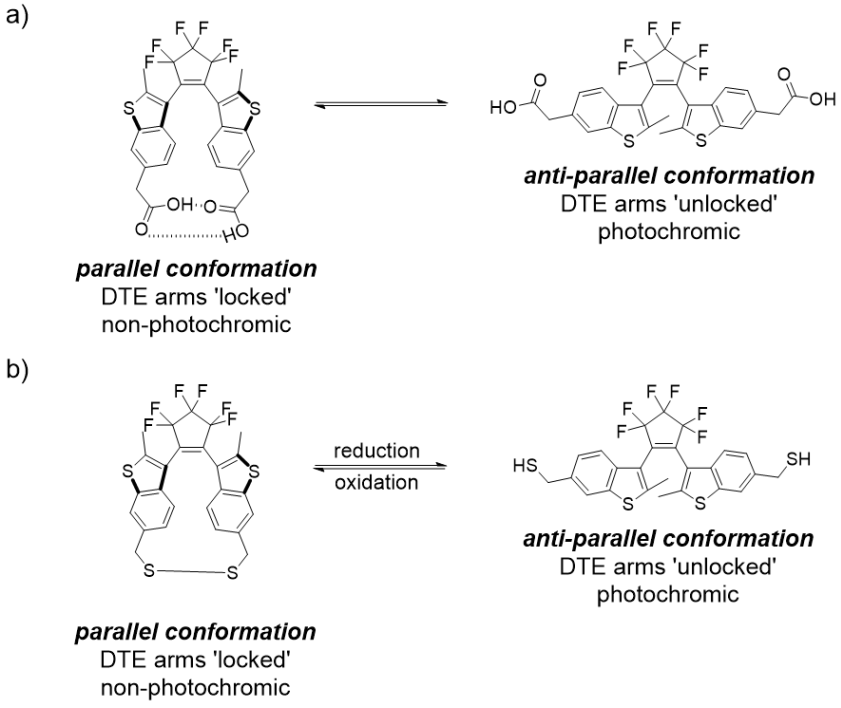

Scheme 1.17: Intramolecular locking of DTEs in their parallel conformations[78] via a) hydrogen bonding; b) disulphide linkages

Intramolecular locking of the DTE arms in *parallel* conformation can also be achieved by modifying the systems such that the functionalities can chelate with metal ions and lock the system. Tian *et al.* synthesized a DTE system tethered with piperazine moieties on the external positions.[79] Cu (II) ions were added as molecular 'lock' to make the system non-

photoresponsive by metal coordination. The addition of EDTA to the complex reverts the system to the *anti-parallel* conformation and regenerates the photoactivity (Scheme 1.18).

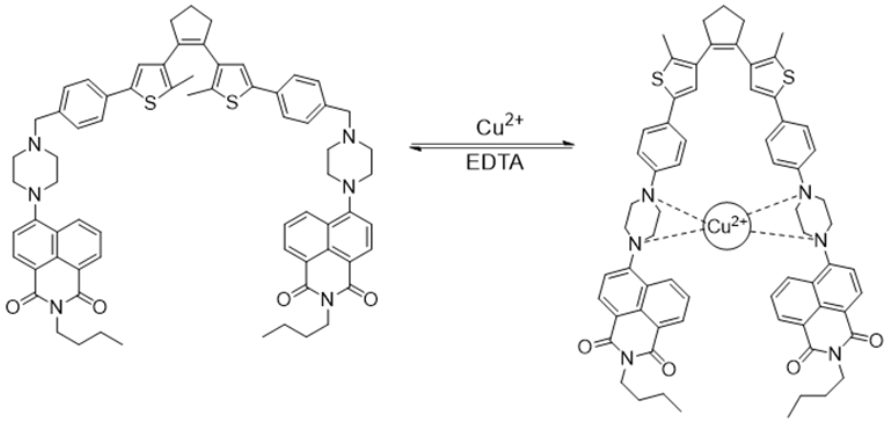

Scheme 1.18: Chelation of Cu (II) ions with the piperazine groups locks the DTE system in its *parallel*, non-photoactive conformer[79]

More recently, Yi *et al.* synthesized a DTE system modified with Thiazole orange dye (Figure 1.9; top).[80] In aqueous solutions, the system was locked in its *parallel* conformation due to the strong intramolecular interactions of the Thiazole orange. The photochromic behaviour of the molecule is unlocked upon binding with DNA (Figure 1.9; bottom).

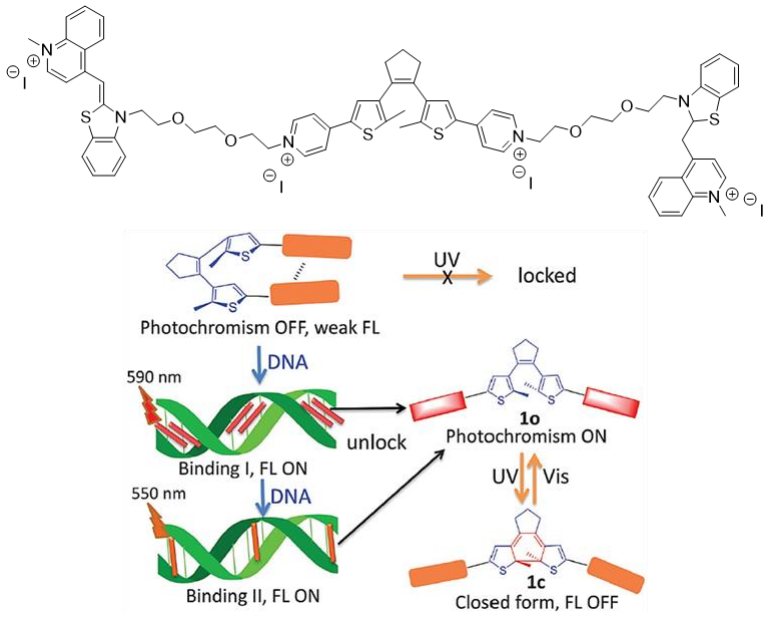

Figure 1.9: Structure of the Thiazole orange modified DTE system (top); DNA-gated photoresponsive behaviour of the molecule (bottom). Reproduced with permission from ref. 80. © 2014 Royal Society of Chemistry [80]

1.6.2. Electronic effects of DTEs to 'gate' photochromism

The electronic differences between the ring-open and ring-closed isomers of DTE systems can be employed to control chemically the photoresponsive properties of these systems. Lehn *et al.* have designed bis(phenol) based DTE molecules whose photoactivity is gated by the redox chemistry of the photoisomer that is present.[81,82] The ring-open isomer of the bis(phenol) DTE is electrochemically stable and can undergo ring closure upon irradiation with UV light. In the ring-closed isomer, both the external phenol groups can interact with each other via the π-conjugated pathway and undergo reversible electrochemical oxidation to generate the non-photoactive quinoid form (Scheme 1.19). Reduction of the quinoid form to the bis(phenol) compound re-establishes the photochromism in the molecule.

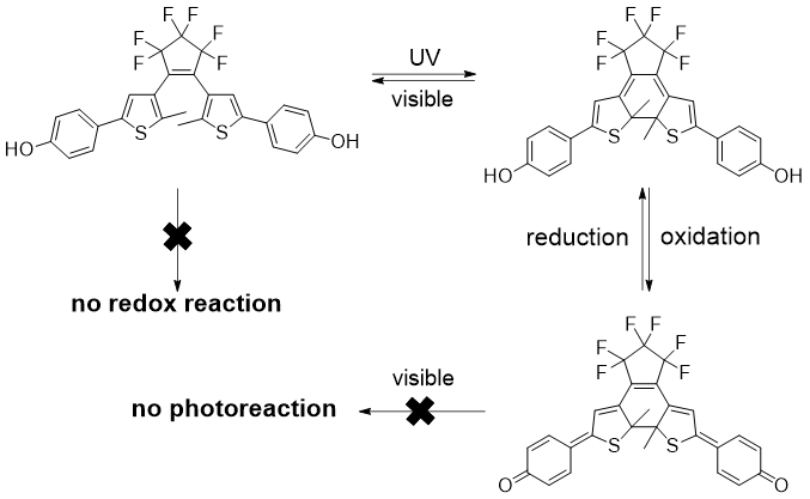

Scheme 1.19: Electronically gating photochromism of bis(phenol) DTE which can oxidize to its quinoid form only in its ring-closed form due to the extended conjugation in the system[81]

This redox reaction-based gating of photochromic properties of DTE systems for biologically relevant systems was utilized by König *et al.* who synthesized a photoresponsive mimic for Coenzyme Q (CoQ) based on a DTE structure that was redox-active only in its ring-open form.[83] In the ring-closed isomer, the double bond in the benzoquinone group is delocalized over the DTE backbone, thus making the system redox inactive (Scheme 1.20).

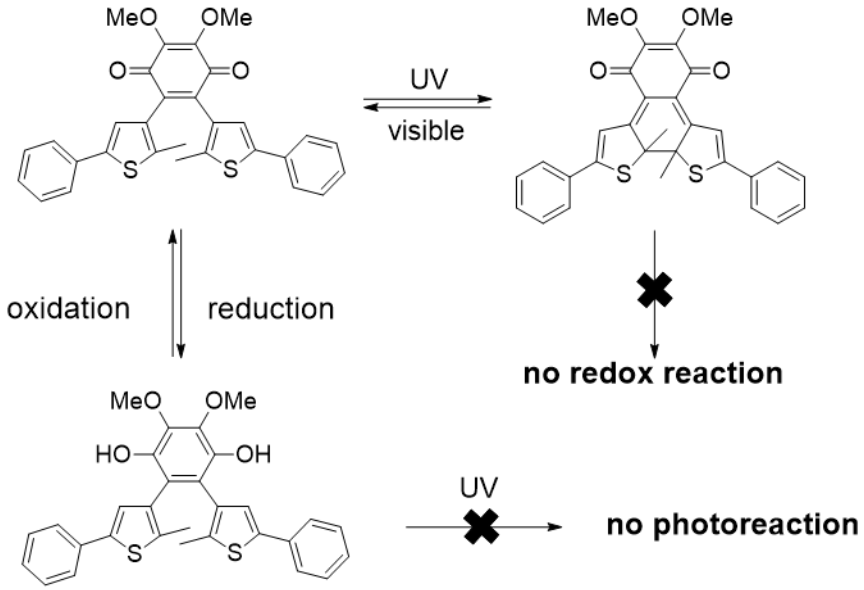

Scheme 1.20: Descriptive outline of redox switchable photoresponsive CoQ mimic[83]

1.6.3. Gating photochromism of DTEs based on quenching effects

In general, for DTE derivatives, irradiation with UV light promotes them to an excited state eventually leading to ring closure of the molecule. Nonetheless, there are systems specifically designed such that there occur certain competing processes, like intramolecular charge transfer (ICT), excited-state intramolecular proton transfer (ESIPT), or twisted intramolecular charge transfer (TICT) excited state, that can effectively quench the excited state to prevent photocyclization. Irie *et al.* developed one such system in which the presence or absence of the phenol -OH group significantly affected the outcome of the excited-state.[84] Upon irradiation with UV light, the presence of phenol -OH group leads to intramolecular proton transfer to one of the carbonyl groups of the maleimide backbone in the excited state at a rate much faster than photocyclization. Therefore, no ring-closed isomer is observed. Simple acylation of the phenol disrupts the quenching mechanism and makes the system photoresponsive. Hydrolysis of the ester re-establishes the quenching effect, thus, making the system photoinactive (Scheme 1.21 a)).

Branda *et al.* applied the principle of quenching via excited-state intramolecular proton transfer to design a DTE system that can detect volatile toxic organophosphorus nerve agents (Scheme 1.21 b)).[85]

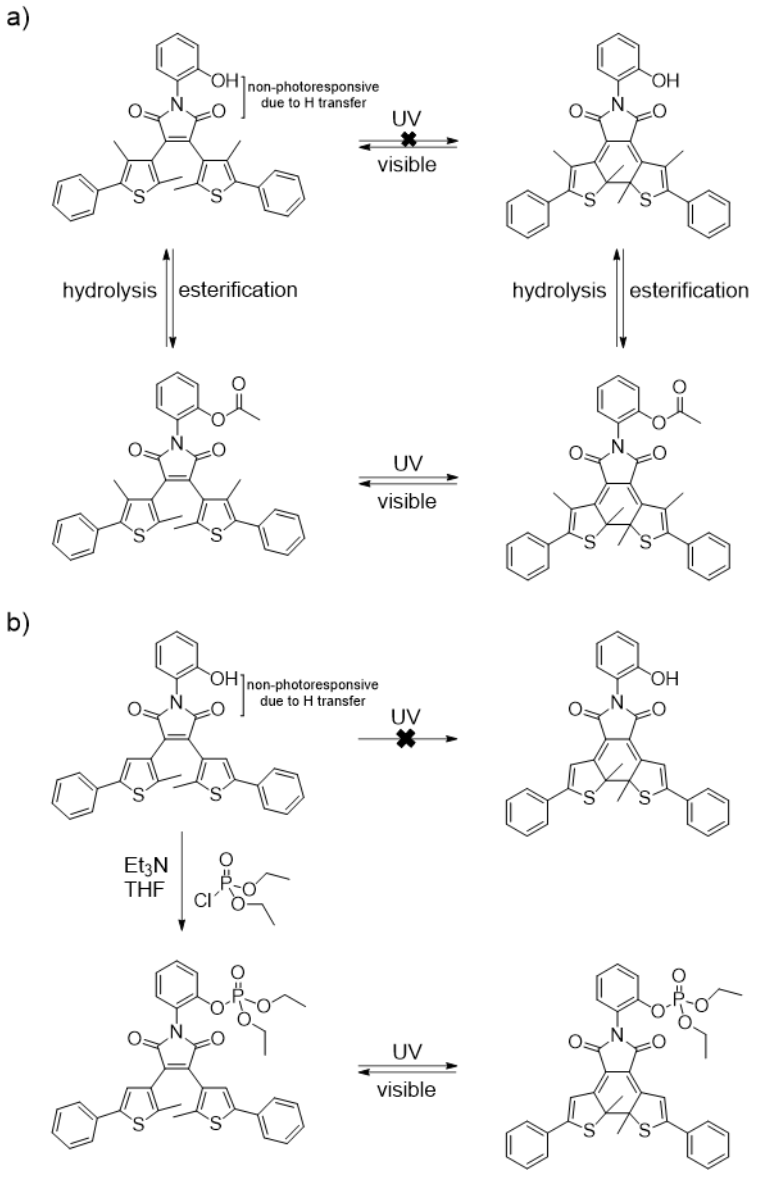

Scheme 1.21: Examples of DTE systems that possess functionalities to effectively quench their photochromism via intramolecular proton transfer in the excited state. The photochromic behaviour is induced only upon a) acylation of the phenol[84]; b) phosphorylation of the phenol[85]

Zhang *et al.* have synthesized DTE systems that exhibit photoresponsive behaviour only under acidic conditions.[86] Upon deprotonation, the photochromism of the DTE system is switched 'off' due to the formation of zwitterionic pyridinium betaine moiety by intramolecular charge transfer phenomenon (Scheme 1.22).

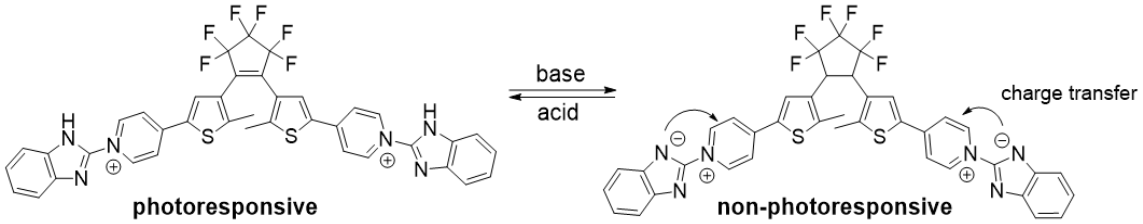

Scheme 1.22: Modified DTE system whose photoresponsive behaviour can be reversibly quenched upon deprotonation via intramolecular charge transfer in the excited state[86]

Similar 'gated' photochromic activity of DTE systems utilizing deprotonation/protonation reaction was demonstrated by Irie *et al.*[87] Only the protonated form of the DTE system exhibits photochromic behaviour. Upon deprotonation with a base, the N, N-diethylamino groups suppress the photocyclization reaction. This quenching effect is attributed to the twisted intramolecular charge transfer (TICT) phenomenon (Scheme 1.23).

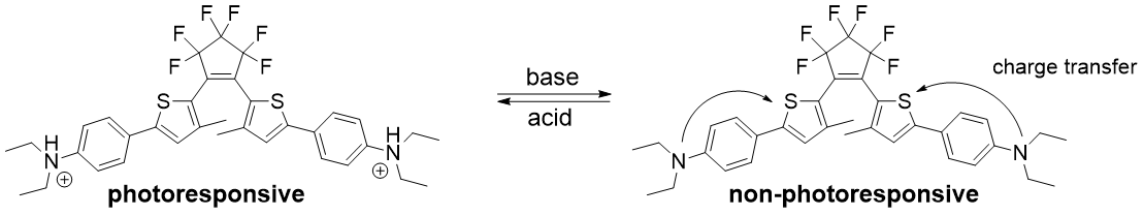

Scheme 1.23: The electron-donating N, N-diethylamino groups on the DTE introduce the twisted intramolecular charge transfer (TICT) based quenching of the excited-state leads to inhibition of photocyclization. Protonation of the DTE re-establishes the photochromism[87]

Another example of 'reactivity-gated' photochromism by chemical protection/deprotection was demonstrated by Belser *et al.* using a cyclobutene-1,2-dione modified DTE system.[88] Despite the system possessing the required 1,3,5-hexatriene arrangement for photocyclization, ring closure does not occur upon irradiation with UV light. A faster competing photochemical ring-opening reaction to yield 1,2-bisketenes relieves the system from ring strain. The net result being quenched photochromism. Protection of one of the ketone groups as a cyclic acetal does not induce any photochromism. Protecting both the ketone groups as cyclic acetals shuts down the competing ring-opening reaction, thus making the molecule photoresponsive (Scheme 1.24). Deprotection of the ketones by acids can influence and 'gate' the photochromic properties of such DTE systems.

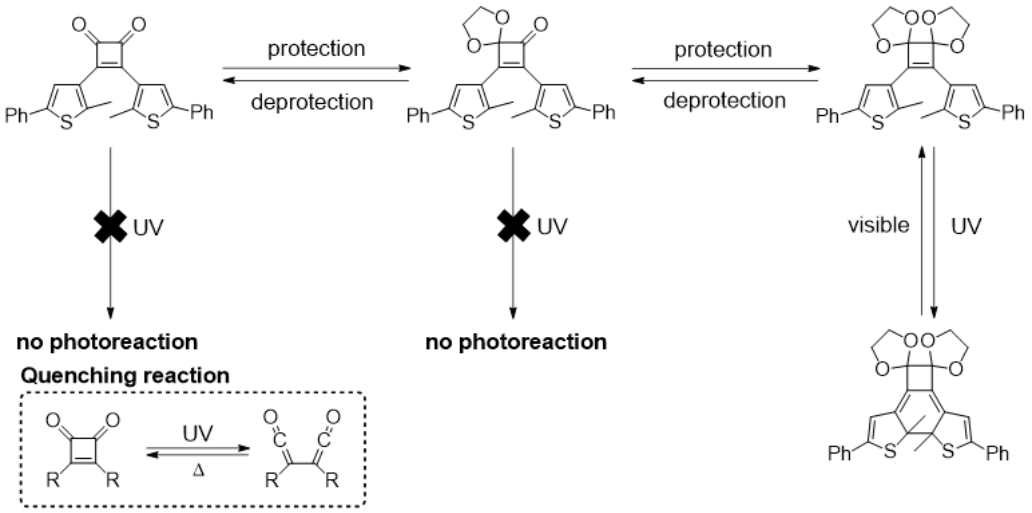

Scheme 1.24: Reversible protection of the ketone groups on cyclobutene-1,2-dione generates the protected structure that can undergo photocyclization upon irradiation with UV light. The unprotected ketone groups undergo a faster ring-opening reaction that effectively quenches the photochromic properties of cyclobutene-1,2-dione modified DTE[88]

Branda *et al.* have created modified DTE systems with one thiophene ring replaced by trisubstituted alkenes that retain the 1,3,5-hexatriene ring system and thus the photochromic properties.[89,90] One such system with dicyanomethylene-thienylethene backbone substituted with pyridine can coordinate with ruthenium tetraphenyl porphyrin in both ring-open and ring-closed forms. Upon coordination, the photochromism of the complex is turned 'off' (Scheme 1.25).[91] The authors predict this inhibition to be related to energy transfer involving triplet states.[40]

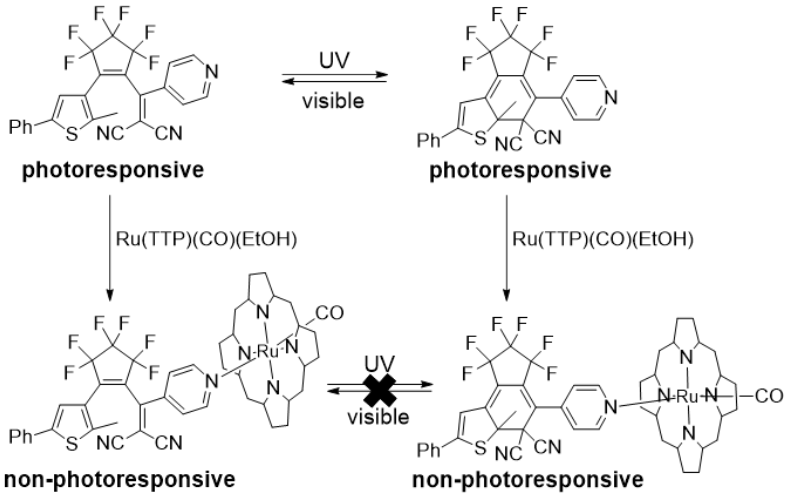

Scheme 1.25: Coordination of a pyridine substituted dicyanoacetylene-thienylethene can turn 'off' the photoresponsive behaviour of both the isomers[91]

1.6.4. Chemically gated photochromism

This approach is rather recent and involves modification of the top ring such that a chemical reaction generates the 1,3,5-hexatriene system on top thereby turning the photochromism of the system 'on'. Branda *et al.* did some pioneering work in this 'reactivity-gated' photochromism strategy. In the first example, Branda *et al.* reported that a Diels-Alder reaction of the hexadiene ring bridging the thiophene heterocycles with maleic anhydride as a dienophile generated the intended 1,3,5-hexatriene system, consequently unlocking the photochromism of the molecule (Scheme 1.26).[92]

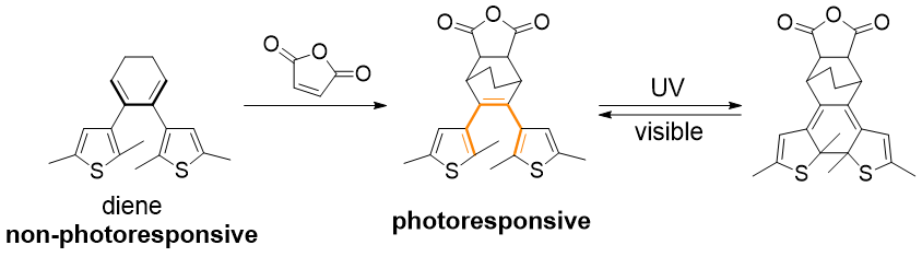

Scheme 1.26: Diels-Alder reaction between the cyclohexadiene and maleic anhydride to generate the photoresponsive DTE system (highlighted in orange)[92]

Branda *et al.* further applied this approach to selectively and sequentially release small molecules from a concealed DTE system.[93] Such systems can potentially be used for photodelivery applications. The non-photoresponsive diene was based on dithienylfulvene structure. This diene could undergo a thermal Diels-Alder reaction with dicyanofumarate to generate a racemic mixture of a photoresponsive DTE. Upon irradiation with UV light, the DTE molecule underwent the π-bond rearrangement to generate the ring-closed isomer, which was thermally stable, *i.e.*, the *retro*-Diels-Alder reaction cannot take place. The thermal reaction was regenerated only upon exposure to visible light (Scheme 1.27).

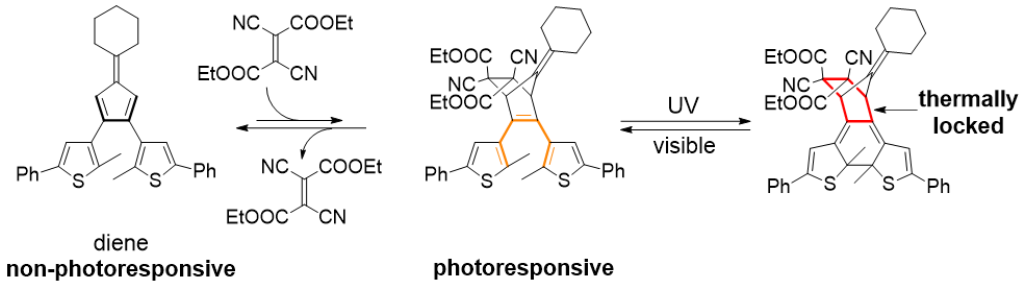

Scheme 1.27: Dithienyl fulvene undergoes a thermal Diels-Alder reaction to form a photoresponsive DTE (highlighted in orange) which upon ring closure is thermally locked (highlighted in red)[93]

More recently, Branda *et al.* designed polymers whose “self-healing” properties can be controlled with light.[94] The polymer backbone consisted of non-photoresponsive dithienylfuran moieties which were crosslinked by thermal Diels-Alder reaction with maleimide-terminated monomers. The resultant polymer was photoresponsive that would undergo ring closure. The resultant polymer in the ring-closed form displayed better adhesive properties than the ring-open counterpart due to the locking of the thermal reverse reaction in the ring-closed form (Scheme 1.28).

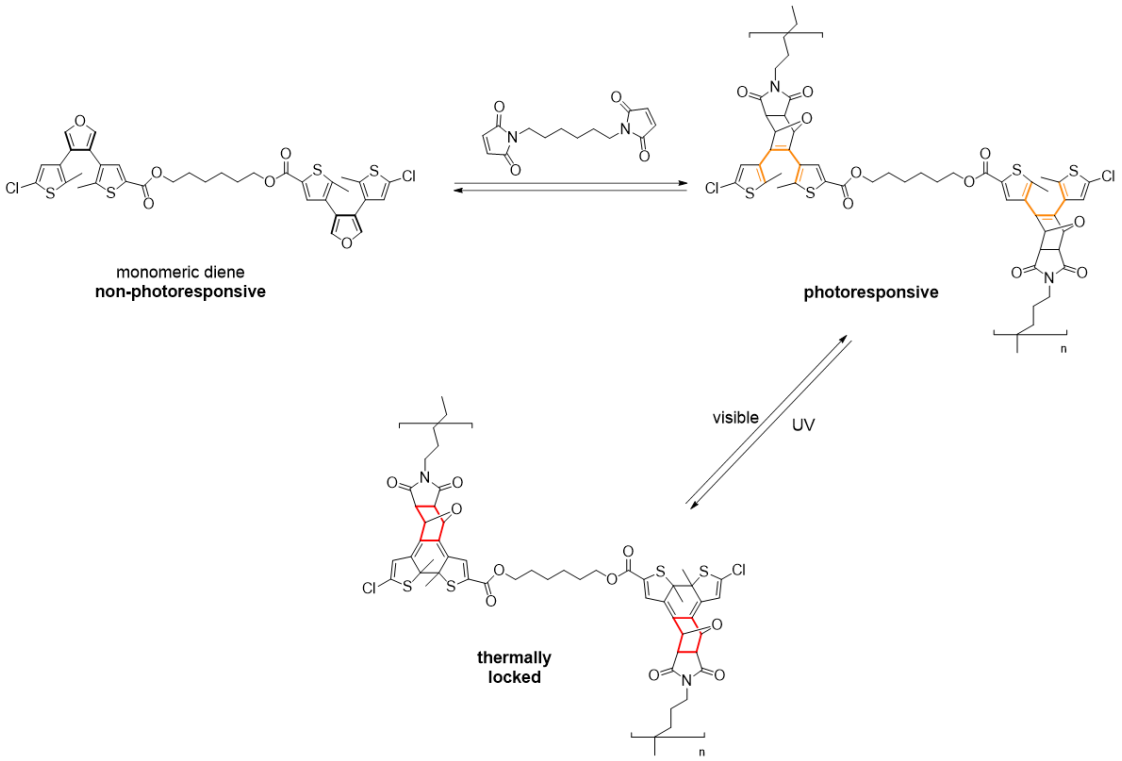

Scheme 1.28: Thermal Diels-Alder reaction between non-photoresponsive dithienylfuran and maleimide monomers produces polymers that are photoresponsive (highlighted in orange). Ring closure locks the thermal reverse reaction (highlighted in red) thereby altering the adhesive properties of the polymers[94]

1.7. Incorporation of light and chemical reactivity to regulate chemical reactions – Goal of this thesis

Sections 1.5 and 1.6 elaborately discuss the numerous methods and strategies for regulating the chemical reactions using photoresponsive DTE derivatives and modulating the photoresponsive nature of the DTE molecules via chemical reactions. The objective

of this thesis is to further discuss this connection of chemical reactivity and photochromism for applications in catalysis, drug delivery, and sensing.

Regardless of its better spatial and temporal control, the use of light as an external stimulus to prompt chemistry remains to be limited. This lack of widespread use is primarily due to the extra cost that is generated for designing starting materials that can respond to light and the use of sophisticated equipment such as modern optical devices (LASERs). As a result, most industries still employ heat as a source for driving chemical reactions to develop new materials.

Herein, the difference in properties of specifically designed DTE molecules will be utilized to control chemical activity in different areas of application. 'Gated photochemistry' approach to alter the 1,3,5-hexatriene system will be used for sensing and detection purposes. Incorporating noble metal nanoparticles that are also responsive to light for drug delivery applications will also be demonstrated.

1.8. Thesis overview

In *Chapter 2*, the difference in electronic properties of the ring-open and ring-closed isomers of DTE systems are employed for controlling the catalytic activity of Karstedt's catalyst used in the industrial hydrosilylation reaction with light. The synthesis of this small molecule photoresponsive inhibitor is described. The design of the photoresponsive inhibitor is based on electron-deficient alkene being part of the 1,3,5-hexatriene system (Scheme 1.29). The coordinating ability of the two photoisomers with the metal centre of Karstedt's catalyst is also studied with the aim that both isomers will have different binding strengths. The difference in the inhibition ability of the two photoisomers in a model hydrosilylation reaction is also monitored.[95]

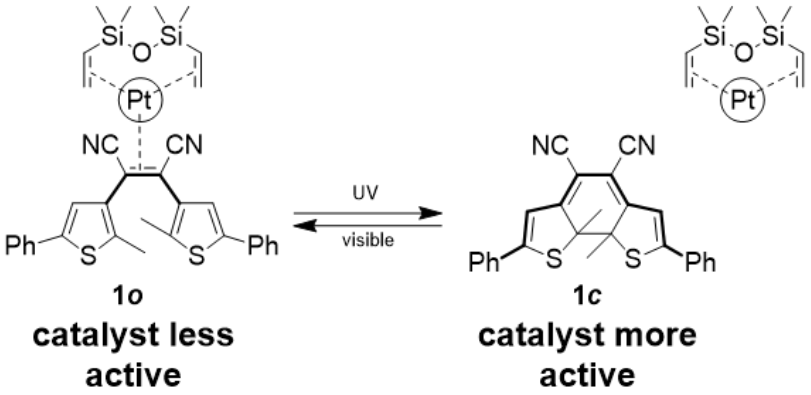

Scheme 1.29: The photoresponsive inhibitor for Karstedt's catalyst described in *Chapter 2*. Light is used to turn the inhibition of the small molecule 'off', thereby, activating the catalyst[95]

Chapter 3 provides an example of a unique way of detecting hydrazine vapour by 'gating' the photochromic activity of a DTE system by quenching effects. Both the ring-open and ring-closed isomers of this small photoresponsive molecule can react with hydrazine and becomes non-photoresponsive (Scheme 1.30). The reaction of hydrazine with the ring-closed isomer results in decolourization of the solution and the formation of a product that does not respond to light. Additionally, the ring-open isomer reacts with hydrazine to yield an emissive response. Such a system can be useful for a dual-mode visual detection of toxins.

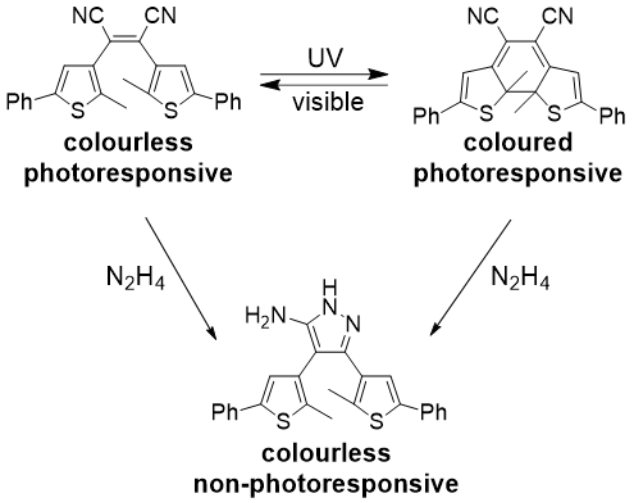

Scheme 1.30: Reaction with hydrazine can turn 'off' the photochromic behaviour of both the isomers of the small molecule photoresponsive detector is demonstrated in *Chapter 3*

In *Chapter 4*, the release of biologically relevant molecules from encapsulated nanoassemblies containing gold nanoparticles and masked forms of biologically relevant molecules is described (Figure 1.10). Light acts as an indirect stimulus to induce the photothermal effect of the gold nanoparticles inside the nanoassemblies to generate localized heat around their surface that activates the retro-Diels-Alder reaction to release the desired molecule. Furthermore, two different encapsulation strategies are presented. The thermoresponsive Diels-Alder adducts of the molecules to be released are trapped in the vicinity of gold nanoparticles using an amphiphilic polymer shell. The amphiphilic polymer provides the advantage of releasing the molecules directly in aqueous environments.

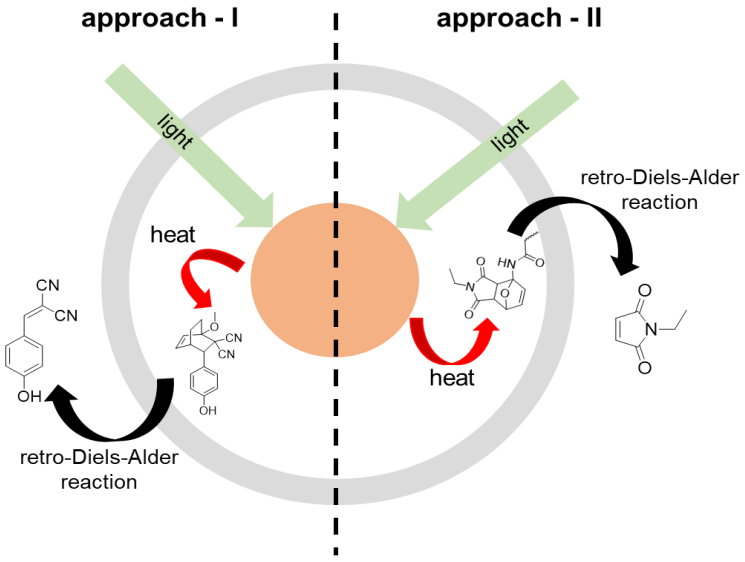

Figure 1.10: Photothermally assisted release of biologically relevant molecules from gold nanoassemblies in which the masked forms of the molecules to be released can be encapsulated by two approaches as described in *Chapter 4*

Chapter 2.

Using light to control inhibition of Karstedt's catalyst

2.1. Permission of reprint and contributions

The research work presented in this chapter has been published as a communication in Organic Chemistry Frontiers and is being reproduced in its entirety with permission from the journal (B.Kaur, R.Raza, M.J.Stashick, N.R.Branda. *Org. Chem. Front.* **2019**, *6*, 1253-1256). The project was designed by Dr Neil R. Branda. The synthesis and characterization of all organic precursors were carried out by B. Kaur. All photochemistry experiments on the final organic molecule were done by B. Kaur. ^{195}Pt-NMR studies were conducted by B. Kaur. The model reaction experiment was designed by B. Kaur and R. Raza based on the results from previous experiments performed by M.J. Stashick. ^{1}H-NMR based kinetic experiments were carried by B. Kaur together with the help of Dr E. Ye and Mr Y. Zhang. B. Kaur wrote the first draft of the manuscript. It was later edited by R. Raza and finally by Dr N.R. Branda. The authors thank Dr E. Ye for his guidance and help to carry out ^{195}Pt-NMR studies.

2.2. Graphical abstract

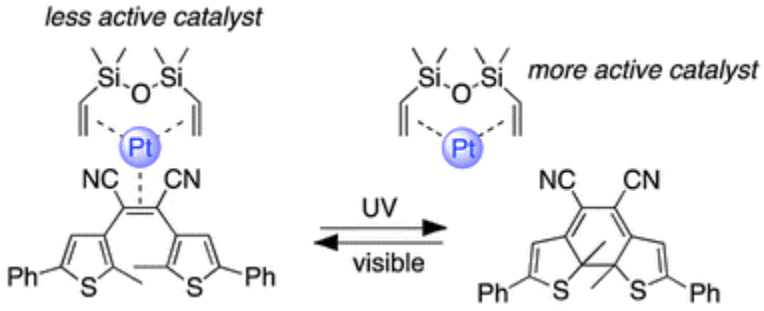

2.3. Abstract

Hydrosilylation reactions are commonly used in the coating industry but the high activity of the platinum catalysts diminishes the 'pot-life' of the reagents which poses a serious industrial problem. Herein, we illustrate a method for controlling the activity of one of these

catalysts by using light as an external stimulant to turn ‘off’ a small molecule inhibitor, thereby turning ‘on’ and activating the catalyst.

2.4. Introduction

The use of light to turn ‘on’ catalysts would provide a higher level of control over chemical processes and put into the hands of the user the ability to decide when and where reactions take place. The approach of using light here differs from other photochemical reactions. Here, light has to be ‘on’ for the brief period of time needed to activate the catalyst; conventionally, the light would require to be ‘on’ for the entire process chemistry. Only a few examples of small photoresponsive molecules that act as catalysts after being exposed to light have been reported.[9,96,97,18,98] This chapter describes our approach towards the problem of light-controlled catalysis and inhibition by developing a photoresponsive compound based on a dithienylethene backbone that acts as an inhibitor of Karstedt’s catalyst by coordinating to the platinum centre until it is exposed to UV light. This exposure triggers a structural change in the compound rendering it a poor metal ligand and activating the catalyst for hydrosilylation reactions. The release coatings produced using hydrosilylation reactions will be described in detail in section **2.4.1**.

2.4.1. Release coatings and Hydrosilylation reaction

Tag and label industry across the world manufacture polymer-based release coatings which are used as thin non-stick layers for labels, stamps, and envelopes, designed to provide for their facile removal from a surface without any loss in adhesive properties (Figure 2.1).[99,100,101]

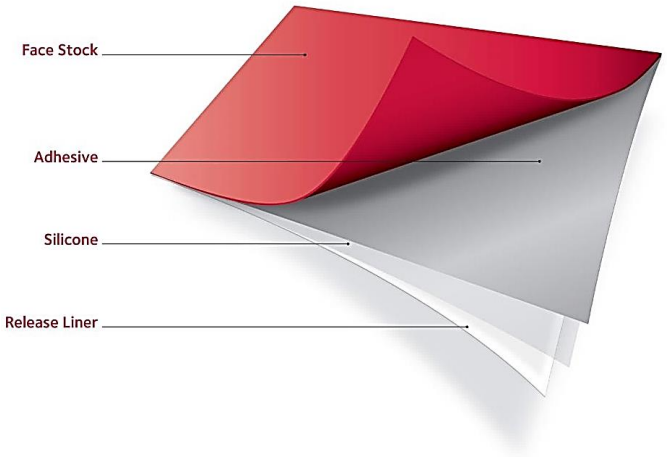

Figure 2.1: A typical release coating is applied to label backing paper (release liner) to facilitate removal of self-adhesive labels[102]

Silicone/polysiloxane based release coatings have become an integral part of this world-wide industry and most major chemical manufacturers, like Evonik Industries, Dow Corning, Shin-Etsu, etc. have dedicated release coating fabrication units.[103] These coatings have proved to be a class of dependable release agents owing to their unique physical and chemical properties.

Polysiloxanes, polymers containing siloxane (-Si-O-Si-) linkage in the main chain, are an important class of inorganic polymers because of their high flexibility and temperature resistance (Scheme 2.1). These polymers are known to show good low-temperature flexibility because of their low T_g values. The long Si-O bond and wide Si-O-Si bond angles provide for the remarkable flexibility of the Si-O-Si bond, which, in turn, imparts the desired low release force, necessary in the release applications. In addition, the greater strength of the Si-O bond, compared to the C-C bond, leads to polymers that are stable at high temperatures, and are resistant to any chemical, physical or biological degradation.[104]

Scheme 2.1: Representative siloxane polymer containing Si-O bond in the backbone with R groups = alkyl, aryl

Industrially, these highly crosslinked polymers are synthesized by the hydrosilylation reaction, which involves the addition of a silane group across an unsaturated carbon-carbon bond (Scheme 2.2 i)).[105] Hydrosilylation reactions are catalyzed by highly active low-valent platinum complexes. The most common ones are Speier's catalyst, Karstedt's catalyst and Markó's catalyst (Scheme 2.2 ii)).[106] Karstedt's catalyst is a complex with Pt (0) centre coordinated to both bridging and chelating siloxane ligands and remains to be the most used catalyst industrially.

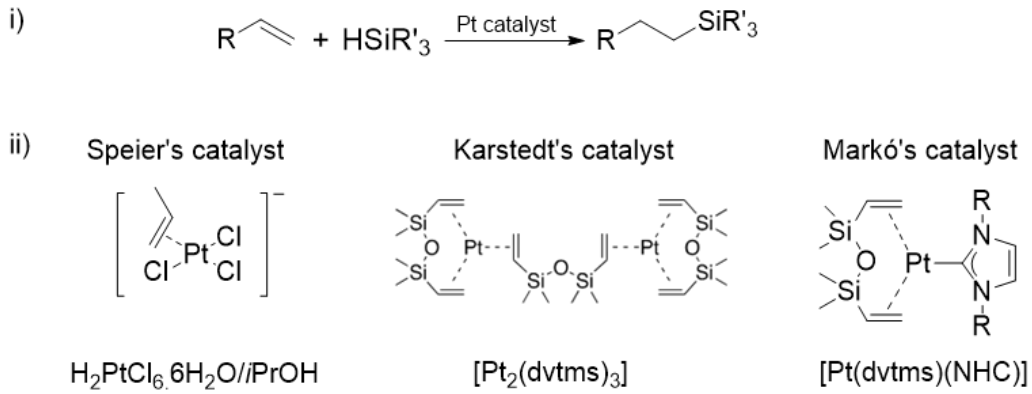

Scheme 2.2: i) A general hydrosilylation reaction between an alkene and an alkylsilane catalyzed by soluble Pt catalyst; ii) Molecular structures of Speier's catalyst, Karstedt's catalyst and Markó's catalyst

The catalytic cycle that governs all hydrosilylation reactions were studied in 1965 by Chalk and Harrod and continues to be acknowledged in platinum catalysis (Scheme 2.3). The Chalk-Harrod catalytic cycle includes four basic steps: Step *I;* oxidative addition of the hydrosilane to the metal centre which generates a Pt (II) species. Coordination of the olefin occurs in Step *II*. This is followed by the migratory insertion of an olefin into the Pt-H bond in Step *III*; and finally, in Step *IV*, occurs the reductive elimination of the product.[106,107]

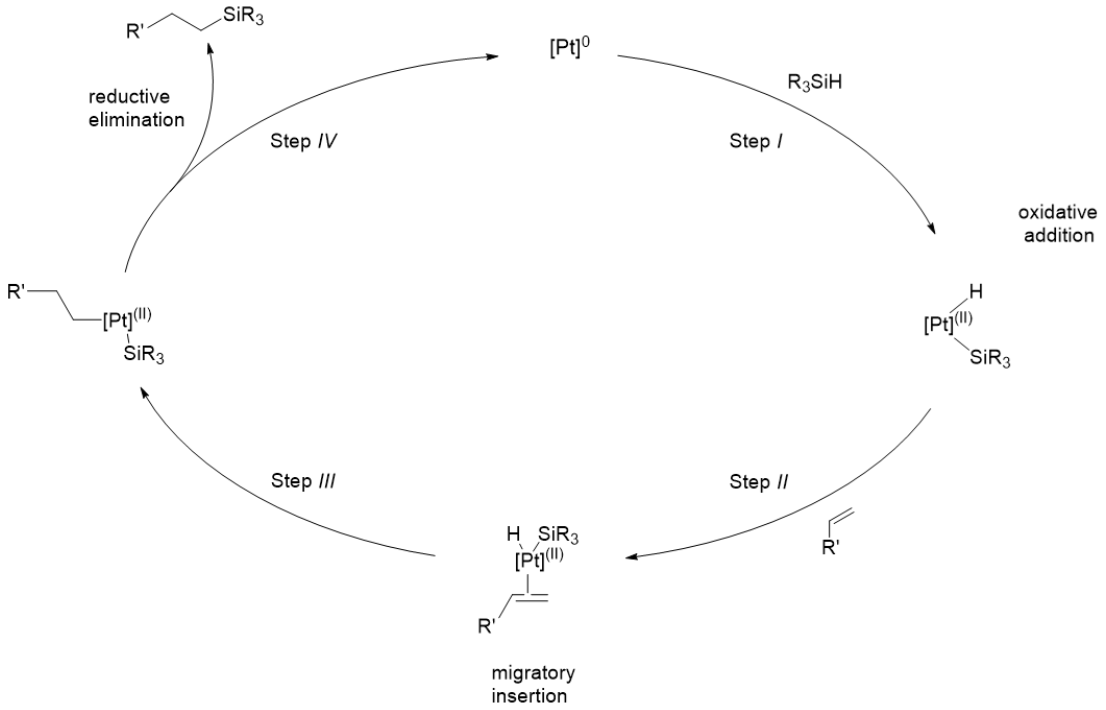

Scheme 2.3: Chalk-Harrod mechanism for hydrosilylation of olefins using platinum metal catalysts

Platinum catalyzed hydrosilylation reactions are usually fast at ambient conditions even with very small amounts (less than 10 ppm) of platinum.[108,109] Significant crosslinking can be obtained for silicones within an hour of curing time at room temperature with platinum concentration ~2-5 ppm. Coatings with a high elastic modulus (greater than 10^4 Pa) require higher platinum concentrations.[110] However, such high concentrations cause premature curing of polymers that causes difficulty in resin processing, storage and transportation, and reduces the shelf life of a precured resin batch under ambient conditions.[109,111] To avoid the issues caused by premature curing of polymers, inhibitors are added to the processing mixture to hinder or reduce the catalytic activity of Karstedt's catalyst.[111]

Inhibitor ligands are, generally, electron-deficient alkenes, e.g. tetracyanoethylene (TCNE), naphthoquinone, dimethyl maleate, dimethyl fumarate, etc., which are capable of coordinating with platinum, thus, competing with added reactant for a site on the active platinum catalyst (Scheme 2.4).[109,112] These electron-deficient alkenes bond directly with the metal centre by a co-planar η^2 -alkene interaction such that the anti-bonding π* orbitals of the inhibiting alkene (Inh) are in the same plane as the complex.[113]

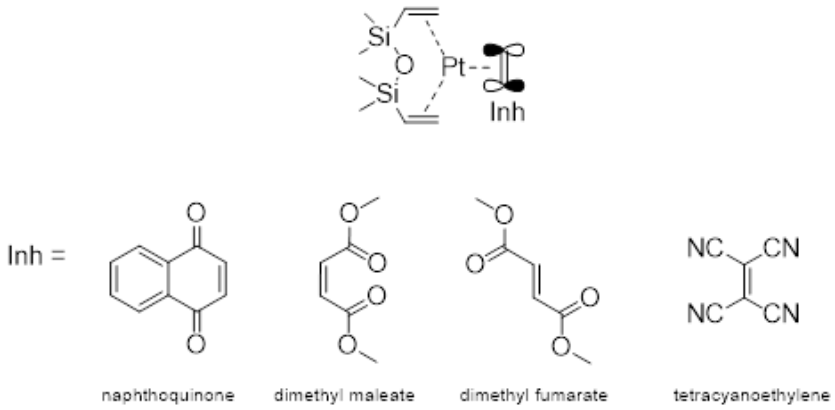

Scheme 2.4: Types of inhibitors and mode of inhibition

In zero-valent platinum complexes, the electronic configuration of the metal is d^{10} and the π-back-donation from the electron-rich metal centre to the alkene is the most important contributor to the strength of the Pt-C bond.[114] Backbonding occurs when the electrons from n*d*-orbitals of the metal are donated to the empty π*-orbitals of the ligand (Scheme 2.5). The greater is the electron deficiency of the inhibiting alkene, the stronger its coordination with the metal centre (stronger π-back-donation) and the higher will be the degree of its inhibition. Tetracyanoethylene, being highly electron-deficient, coordinates to the metal centre strongly enough to completely poison the catalyst making the catalyst ineffective for use in curing processes.

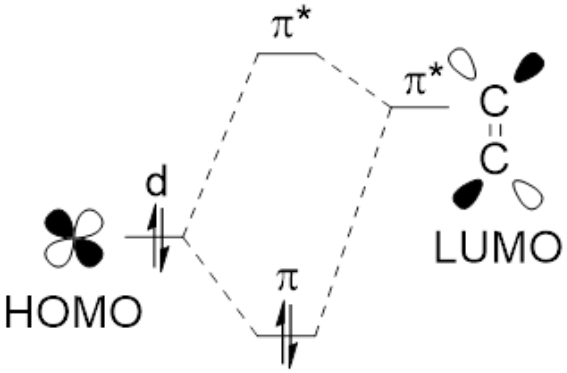

Scheme 2.5: Molecular Orbital (MO) diagram for π-back-donation of electrons from filled d-orbitals of Pt metal to the empty π* anti-bonding orbitals of alkene

Industrially, the selection of inhibitors is based on two conditions: i) strength of ligand is enough to inhibit the catalyst completely at room temperature; ii) catalyst can still be activated on heating.[115] The most commonly used inhibitors for thermal curing processes in industry, owing to their high-temperature volatility, are maleates and fumarates.[109]

Consequently, manufacturers must balance the temperature and time for the effective thermal curing of silicones (Figure 2.2). Higher temperatures would more quickly remove the inhibitor, catalyzing the reaction in the process, but such temperatures would damage the finished coatings. Lower temperatures (~60 °C) are sufficiently low as to not damage the final coating but are slower to remove the inhibitor, resulting in increased operating times prompting higher energy costs. Furthermore, heating also causes the generation of volatile organic compounds (VOCs) which pose great environmental concerns.

As an alternative to thermal curing, industry, at present, uses ultraviolet (UV) light or electron beam, *i.e.*, radiation-assisted curing. These techniques make use of initiators that generate reactive radicals upon irradiation and require specific functional groups to be attached to the siloxane backbone. While the curing efficiency for these methods is higher than thermal curing, a limited range of products is available in the market.[116]

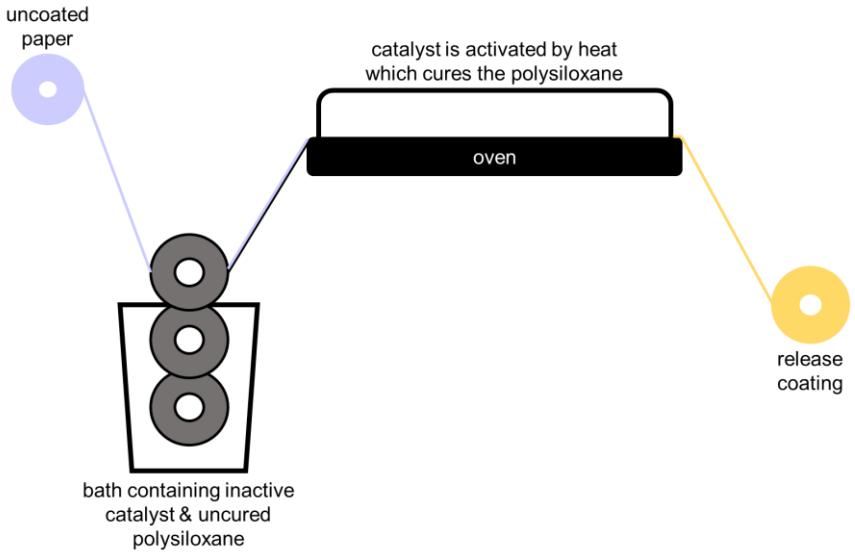

Figure 2.2: Schematic representation of the manufacturing process of silicone-based release coatings

Therefore, an ideal approach would be to combine the effective features of both heat-assisted curing and radiation-assisted curing to create a system that would involve the direct interaction of light/radiation with the inhibitor-catalyst pair. Such a 'light-initiated' system would prove to be advantageous over the conventional radiation-based methods in that the radiation source is used only once to permanently activate the catalyst, reducing the effective radiation time involved. The need for radical initiators and photoactive functional groups in reactants would also be avoided. Additionally, the selection of

inhibitors of intermediate strength would no longer be a limitation as such a system would completely lose inhibition as soon as it responds to light. The specific class of photoresponsive compounds based on dithienylethenes, owing to their ease of functionalization, greater thermal stability and difference in electronic properties of the two isomers, can prove to be appropriate for such light-initiated systems.

Peters *et al.* have previously published systems that demonstrate the facile synthesis of 1,2-dithienylethenes with one thiophene ring replaced by a substituted olefin (Scheme 2.6). This novel molecular structure provides enhanced feasibility of incorporating versatile functional groups onto the photoresponsive systems without restricting their photochromic behaviour.[89] Wüstenberg *et al.* further customized the framework by incorporating nitrile groups to the alkene to create D-π-A systems called dicyanoethylene-thienylethene (DCTE) (Scheme 2.6).[90]

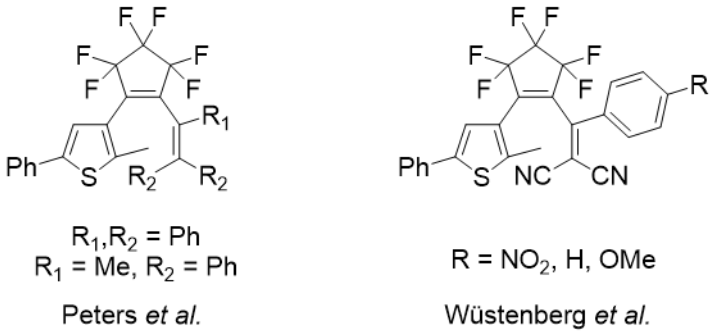

Scheme 2.6: Previously synthesized photoresponsive compounds with modified thienylcyclopentene backbone

DCTE design is of particular interest corresponding to the electron-deficient character of the alkene that can act as an inhibitor to Karstedt's catalyst Scheme 2.7).

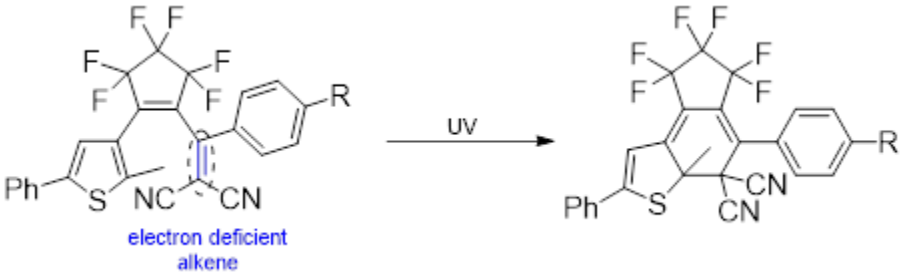

Scheme 2.7: Ring-open form of DCTE possesses the electron-deficient double bond that can coordinate with the metal centre to inhibit the catalyst, which is lost upon ring closure by UV irradiation

These hexatriene systems have been employed by the Branda group[117] as potential photoresponsive inhibitor ligands for Karstedt's catalyst, but, with little success. The lack of inhibition by the DCTE was attributed to the additional steric bulk of the hexafluoro ring connected to the alkene.

2.4.2. Our system

The molecular design chosen contains an electron-deficient alkene connecting two nitrile groups and two thiophene heterocycles (Scheme 2.8). Like all dithienylethenes, compound **1*o*** possesses a photoreactive hexatriene that undergoes a ring-closing reaction when exposed to UV light and produces its isomer **1*c*** that no longer contains an electron-deficient alkene.[42]

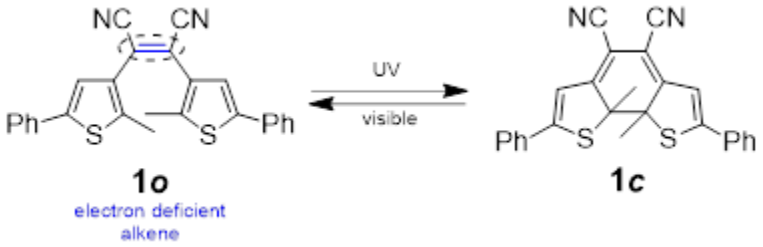

Scheme 2.8: Only in its ring-open form can dithienylethene **1*o*** bind to the metal centre of Karstedt's catalyst. UV light triggers the ring-closing reaction, removes the electron-deficient alkene and turns the inhibitor 'off'

It was expected that the ring-open isomer, **1*o***, will preferentially coordinate to the catalyst under ambient conditions to displace the bridging siloxane ligand and form a complex with a platinum metal centre (catalyst.**1*o***). Thus, **1*o*** will act as an inhibitor for Karstedt's catalyst. And upon irradiation with light of suitable wavelength, ring-closure will occur via rearrangement of π-system leading to the loss of coordination site with the generation of active catalyst and **1*c*** (Scheme 2.9) (inhibition turned 'off').

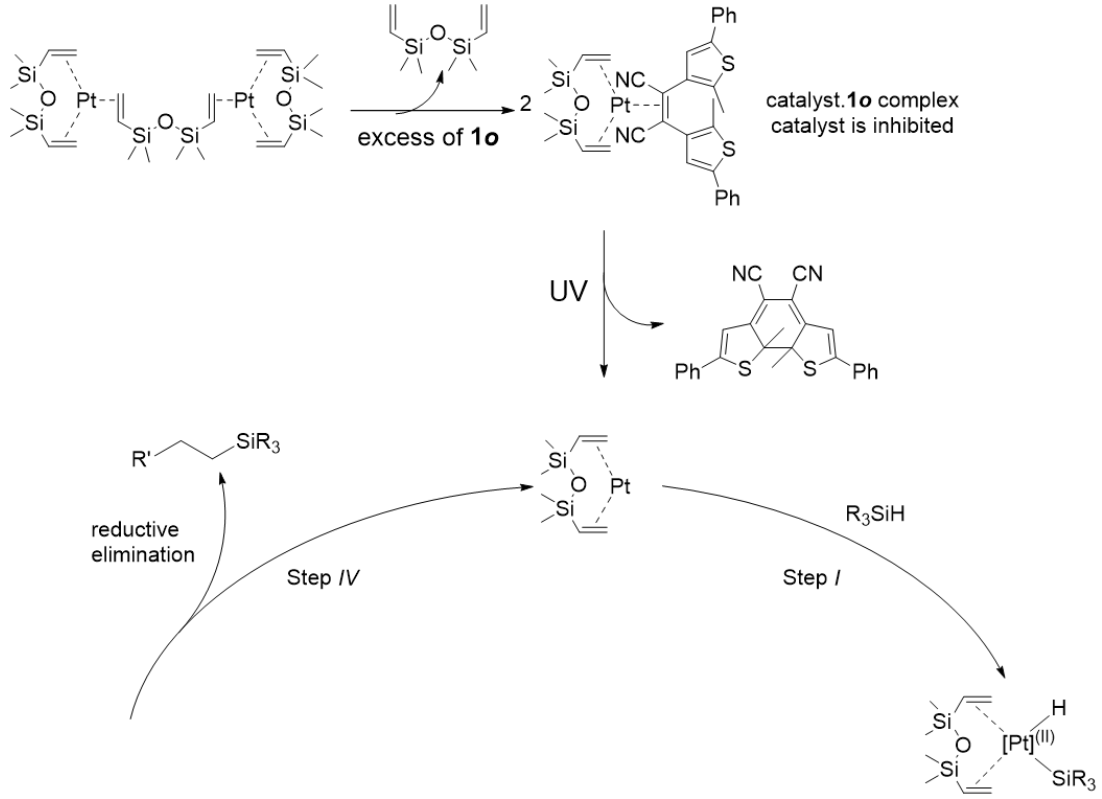

Scheme 2.9: Proposed mechanism for inhibition of Karstedt's catalyst by **1*o*** and catalyst activation upon UV exposure

Alternatively, a solution containing Karstedt's catalyst and **1*c*** would continue to catalyze a hydrosilylation reaction until irradiated with light of a suitable wavelength. This would lead to the conversion of **1*c*** to **1*o*** that can now bind with the metal centre of the catalyst and inhibit its activity (inhibition turned 'on').

2.5. Results and Discussion

2.5.1. Synthesis

The photoresponsive inhibitor (**1*o***) was synthesized in seven steps from commercially available 2-methylthiophene as described in the literature (Scheme 2.10). Starting with 2-methylthiophene, the 3- and 5-positions on the thiophene were brominated using N-bromosuccinimide in acetic acid to give **2** in excellent yield, whose structure was confirmed by the appearance of a singlet for 1H at δ = 6.85 ppm for thiophene in the ^{1}H NMR spectrum.[118] A subsequent Suzuki cross-coupling reaction with phenylboronic acid yielded **3**, as established by the emergence of four peak pattern in the aromatic region of the ^{1}H

NMR spectrum.[119] Insertion of aldehyde group was achieved through treatment of **3** with n-butyllithium followed by quenching with DMF and acidification to yield **4** as was seen by the appearance of a singlet for 1H at δ = 10.01 ppm, characteristic of aldehyde protons.[51] A one-pot reduction of aldehyde **4** by sodium borohydride in methanol followed by substitution with phosphorus tribromide to form alkyl bromide **5** almost quantitatively, as seen from the disappearance of aldehyde proton at δ = 10.01 ppm and appearance of a peak at δ4.46 for 2H for methylene group.[120] Installation of nitrile group was done by a substitution reaction of **5** with sodium cyanide in water.[121] The presence of the nitrile group was confirmed by the appearance of a peak at δ =117.20 ppm in the ^{13}C NMR spectrum. The desired α,β-unsaturated nitrile, **1*o***, was prepared by coupling reaction of **6** in aqueous sodium hydroxide and carbon tetrachloride with tetrabutylammonium bromide as a phase-transfer agent and was obtained as a cis-isomer in modest yield.[84] Experimental details and characterizations of all compounds are provided in Section 2.7.

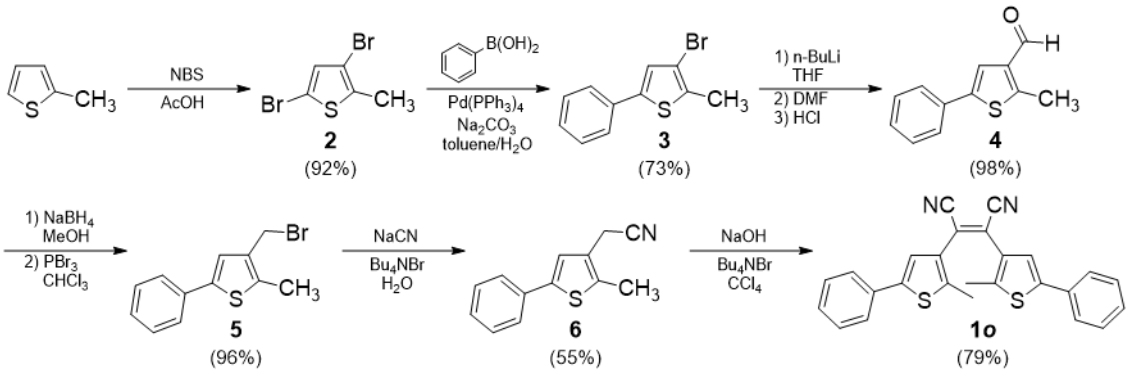

Scheme 2.10: Synthesis of photoresponsive inhibitor (**1*o***) used to control the activity of Karstedt's catalyst. The electron-deficient alkene is shown as *cis*-isomer

2.5.2. Photoresponsive behaviour of 1*o*

2.5.2.1. UV-visible Absorption spectroscopy

Light-induced ring-closing of the photoresponsive inhibitor **1*o*** was evaluated by UV-visible Absorption spectroscopy and ^{1}H-NMR spectroscopy. When a solution of **1*o*** (1.05×10^{-5} M) in chloroform, is irradiated with light of wavelength around 312 nm, an intense and relatively broad band centred at 580 nm appeared in the visible region of the spectrum implying conversion to ring-closed isomer, **1*c*** (Figure 2.3 b)). A corresponding decrease in intensity in the high energy band at 290 nm for **1*o*** was observed. This change is typical for dithienylethenes, which upon ring closure undergo rearrangement, thus, creating an

extended π-conjugated system that shifts the absorption to the visible region. A parallel change in the colour of the solution occurs from pale yellow to blue (Figure 2.3 a)). Two isosbestic points at 404 nm and 436 nm indicate that ring closure occurs with minimal degradation or side reactions.

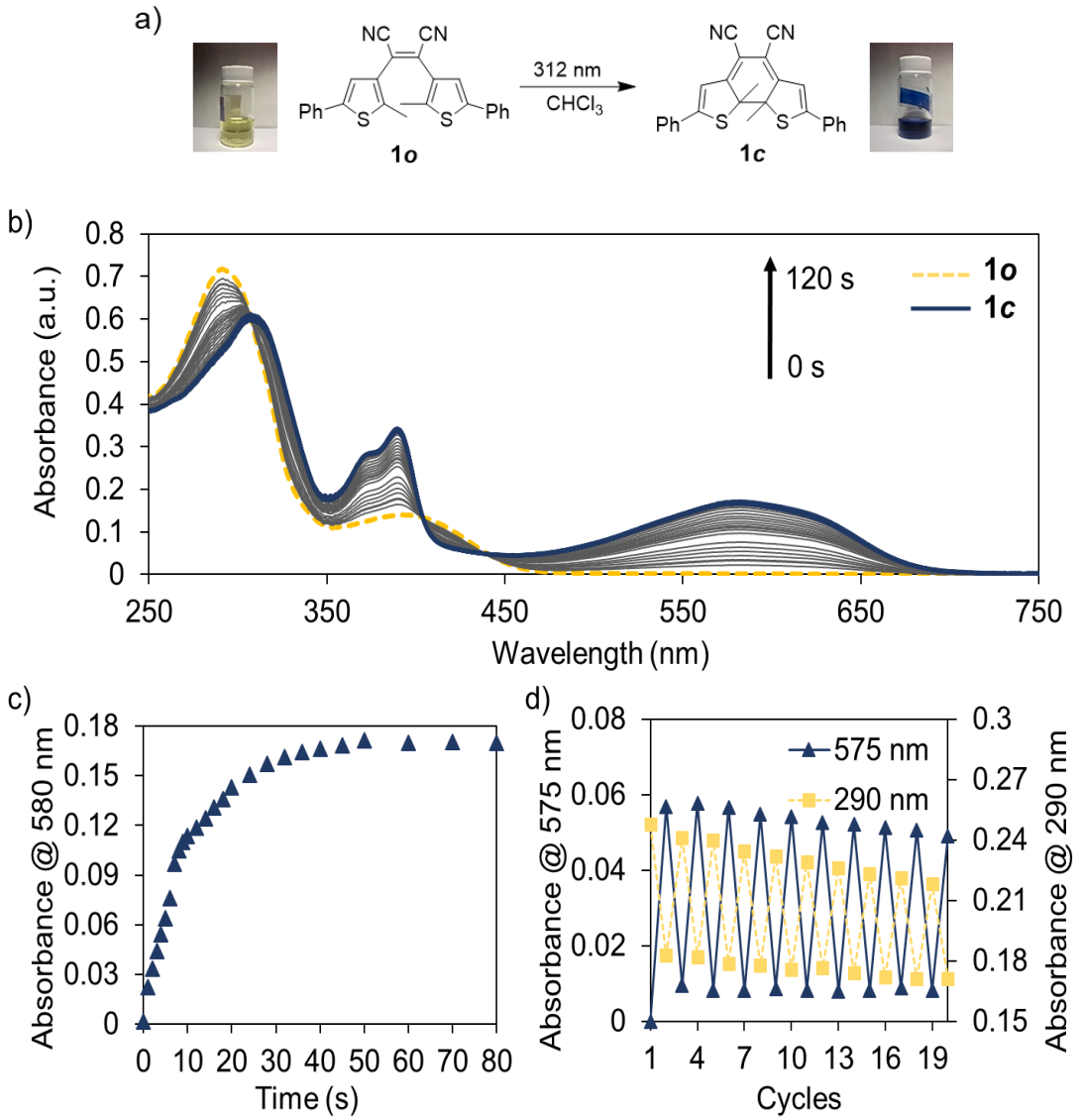

Figure 2.3: a) Irradiation of a solution of **1*o*** in $CHCl_3$ with 312 nm light produces ring-closed isomer, **1*c***, along with a colour change from pale yellow to blue; b) Changes in UV-vis absorption spectrum when a $CHCl_3$ solution of **1*o*** (1.05×10^{-5} M) was exposed to 312 nm light for 120 s; c) Kinetic plot summarizing the changes in the absorbance value at λ_{max} = 580 nm as the concentration of **1*c*** increases over time; d) Modulated absorption at 290 nm corresponding to absorbances for ring-open isomer (**1*o***) and at 575 nm corresponding to absorbances for ring-closed isomer (**1*c***) during alternating irradiation at 312 nm (30 s) and >435 nm (60 s)

The ring-closed isomer (**1*c***) is stable in the dark under ambient conditions and can be reverted to the ring-open isomer with exposure to light >435 nm. The reversible nature of the photoswitching process was analyzed by alternating the ring-closing reaction and ring-opening reaction, by exposing the solution of **1*o*** to UV light (312 nm) for 30 s followed by visible light (>435 nm) for 60 s for a total of 20 cycles (Figure 2.3 d)). A slight degradation of the photoresponsive compound is observed as evident from the decrease in intensity of the absorbances at 290 nm and 575 nm upon consecutive cycling. Fortunately, this degradation should not be considered a limitation as it is unlikely that the photoresponsive inhibitor system will be subjected to more than one or two cycles in the final curing operation.

2.5.2.2. NMR spectroscopy

Quantification of the ring-closing reaction of **1*o*** and the structure confirmation of **1*c*** was assessed by ^{1}H-NMR spectroscopy. A solution of ring-open isomer **1*o*** (5.00×10^{-3} M) in deuterated chloroform in a glass NMR tube was irradiated with 312 nm light until no further changes were observed in the ^{1}H NMR spectrum (Figure 2.4). After 120 min the photostationary state was reached at this concentration. In the ring-open isomer **1*o***, the methine protons (H^{a}) are attached to aromatic thiophene rings and appeared in the aromatic region (downfield) at δ = 6.91 ppm. The ring closure upon irradiation led to the distortion of the aromaticity of π-system of thiophene units upon rearrangement and formation of a conjugated polyene **1*c***. As a result, the methine protons (H^{b}) in **1*c*** appeared in the alkene region (upfield) at δ = 6.72 ppm.

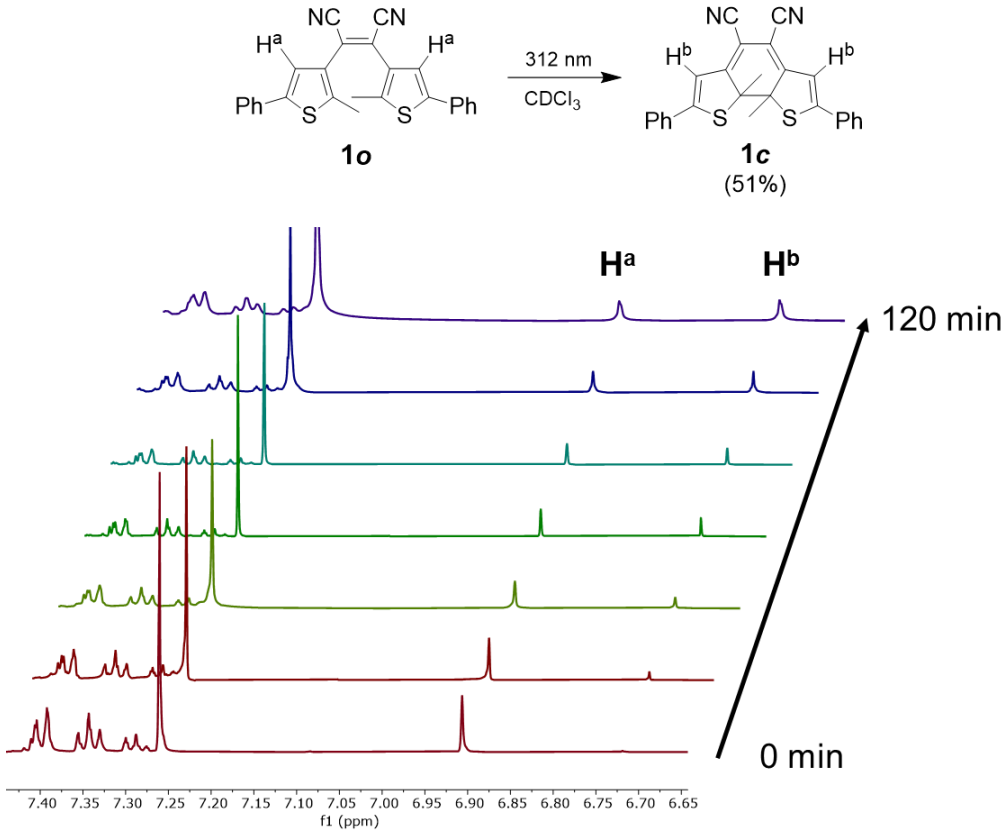

Figure 2.4: Partial ^{1}H-NMR spectra (600 MHz) of a $CDCl_3$ solution of **1*o*** (5.00×10^{-3} M) showing the spectral changes when the solution is irradiated with 312 nm light for a total of 120 min

The yield for the photoconversion reaction was determined by comparing the relative integrations of the independent chemical shifts of ring-open isomer **1*o*** and ring-closed isomer **1*c*** in the ^{1}H-NMR spectrum of the photostationary state mixture. At the photostationary state condition, the mixture was estimated to be ~ 51% of **1*c*** (Figure 2.5).

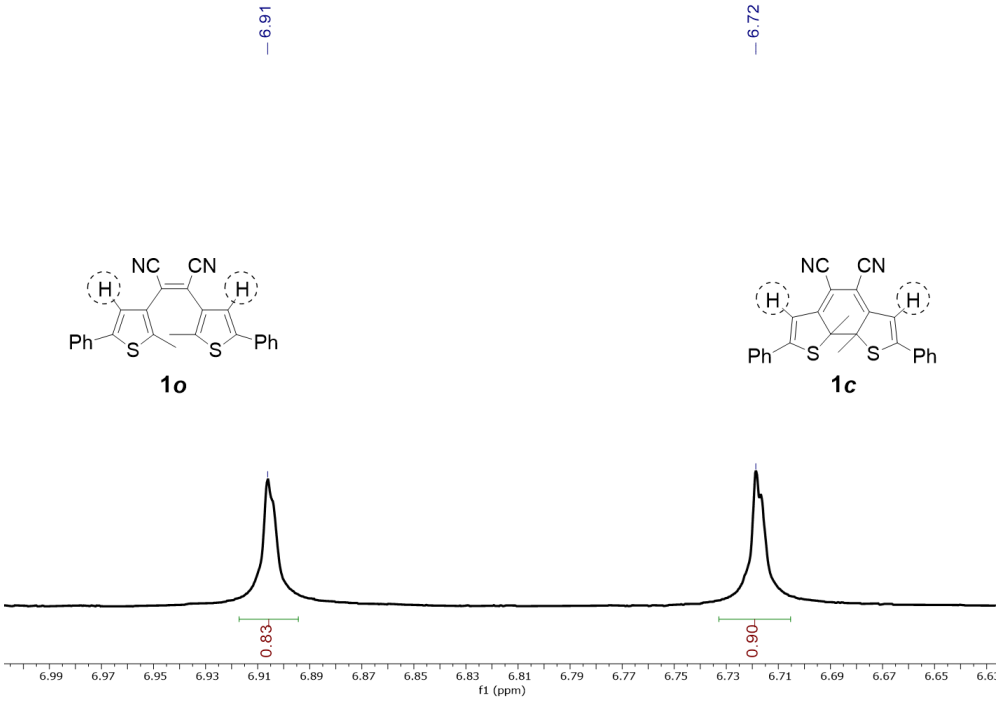

Figure 2.5: Partial ^{1}H-NMR spectrum (600 MHz) of $CDCl_3$ solution of photostationary state mixture obtained from irradiation of **1*o*** with 312 nm light for 120 min. Using the relative integrals of thiophene protons for **1*o*** and **1*c*** the photostationary state was determined to be ~51%

2.5.3. Coordination behaviour of metal with photoresponsive inhibitor ligand

The reactivity of hydrosilylation reaction is influenced by the ability of the alkene to coordinate to the Pt metal centre. Upon addition of alkene, the resultant complex replaces the bridging 1,3-divinyl-1,1,3,3-tetramethyldisiloxane (dvtms) group of Karstedt's catalyst.[109] Depending upon the π-acidic nature of the alkene, the coordination of the alkene to the metal could be weak or strong.[106,113] The strongly π-acidic (electron-deficient) nature of **1*o*** suggests strong coordination with the platinum centre (Scheme 2.8). This hypothesis of different coordination behaviour of the metal with the two isomeric forms of the photoresponsive ligand was demonstrated by comparing the ^{195}Pt NMR spectra of Karstedt's catalyst in presence of **1*o*** and **1*c*** separately (Figure 2.6).

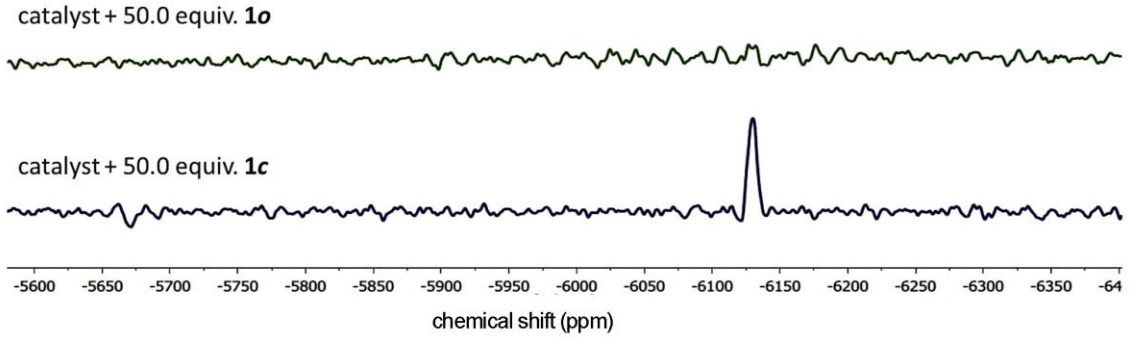

Figure 2.6: The ^{195}Pt NMR spectra for solutions of Karstedt's catalyst (0.015 mL) in toluene-d_8 (0.50 mL) at 25°C in the presence of an excess of ring-open isomer (**1*o***) (top) and ring-closed isomer (**1*c***) (bottom)

A solution of Karstedt's catalyst (0.015 mL) in toluene-d_8 (0.50 mL) was taken in an NMR tube and was allowed to incubate for 60 min at 25°C. The solution of Karstedt's catalyst is a complex solution containing Pt(0)-1,3-divinyl-1,1,3,3-tetramethyldisiloxane in xylenes with approx. 2% Pt metal content and was used as supplied. The spectrum of the catalyst by itself has a peak for Pt metal at δ = -6130 ppm, common for low-valent platinum alkene complexes.[106,122]

In order to facilitate a complete ligand exchange, **1*o*** and **1*c*** were used in excess (50 equivalents) to the catalyst and the solutions were incubated for 60 min at 25°C. Ideally, a downfield shift in signal is expected when metal coordinates with an electron-deficient alkene indicating that there is less electron density at the metal centre.[123] However, in the presence of ligand **1*o***, no new signal was observed in the downfield region. This absence of a signal can be attributed to the fact that our ligand, used in excess for complete ligand exchange, contains nitrile groups with ^{14}N atoms (I = 1 and 99.6% abundance) in close proximity to the metal centre. The quadrupolar ^{14}N relaxation is slow enough to couple with the ^{195}Pt signal, resulting in peak broadening leading to a very weak (if any) signal.[124] The spectrum obtained in the presence of ring-closed isomer, **1*c***, on the other hand, has a clear peak at δ = -6130 ppm, which is in the region of the pure Karstedt's catalyst. No new peaks were observed in the case of **1*c***, which is expected since the ring-closed isomer no longer possesses the electron-deficient alkene to coordinate with the metal. No observable change in the optical properties was observed after incubation as the photoresponsive inhibitor was used in excess.

2.5.4. Testing for Inhibition

2.5.4.1. Model inhibitor

The effect of the inhibitor on Karstedt's catalyst was evaluated by monitoring the progress of a model hydrosilylation reaction (Scheme 2.11).

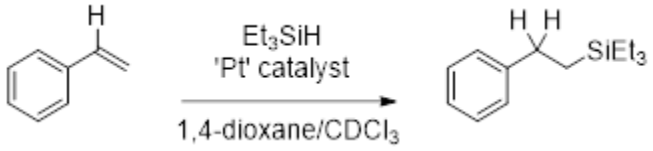

Scheme 2.11: Model hydrosilylation reaction between Styrene and Triethylsilane to analyze inhibition of Karstedt's catalyst ('Pt' catalyst)

An equimolar solution of styrene (0.00108 mol) and triethylsilane (0.00108 mol) in $CDCl_3$ was charged with Karstedt's catalyst (1.31×10^{-6} mol of Pt, 0.12% catalyst) in a sealed NMR tube at 30°C and 1,4-dioxane was added as an internal standard. Reaction progress was evaluated using ^1H NMR spectroscopy by monitoring the disappearance of styrene and the appearance of the hydrosilylated product. After acquiring an immediate ^1H NMR spectrum for the initial mixture, the tube was heated at 30°C for 4 h with ^1H NMR spectra being recorded every hour. The areas under the peaks corresponding to styrene proton (δ = 5.82 ppm) and the protons of the product (δ = 2.72 ppm) were measured and compared to the internal standard to monitor the progress of the reaction (Figure 2.7).

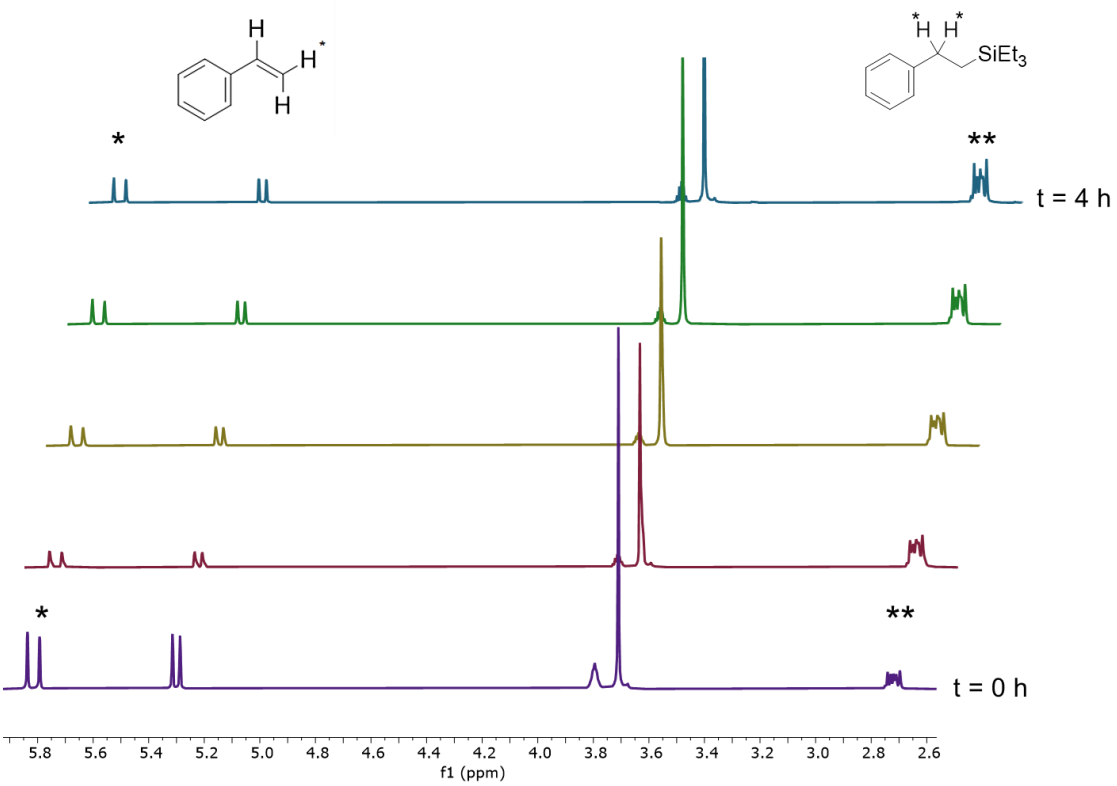

Figure 2.7: Changes in ^{1}H NMR spectrum corresponding to styrene proton (δ = 5.82 ppm) and the protons of the product (δ = 2.72 ppm) when a $CDCl_3$ solution of styrene, triethylsilane and dioxane (as an internal standard) was treated with Karstedt's catalyst for 4 h at 30°C without inhibitor

A similar reaction was carried out in the presence of model inhibitor, tetracyanoethylene (TCNE) in our case, 3.30 x 10^{-6} mol, 2.5 equivalents compared to Pt.[125] The ratio of 2.5 equivalents of the inhibitor in comparison to Pt was experimentally determined to be the minimum amount of TCNE that can be added to the reaction mixture without having any negative impact on the ability of the catalyst. While, at lower equivalent ratios, no observable inhibition was observed. Reaction progress was, again, evaluated using ^{1}H NMR spectroscopy by monitoring the disappearance of styrene and the appearance of hydrosilylated product. After acquiring an immediate ^{1}H NMR spectrum for the initial mixture, the tube was heated at 30°C for 4 h with a ^{1}H NMR spectrum being recorded every hour (Figure 2.8).

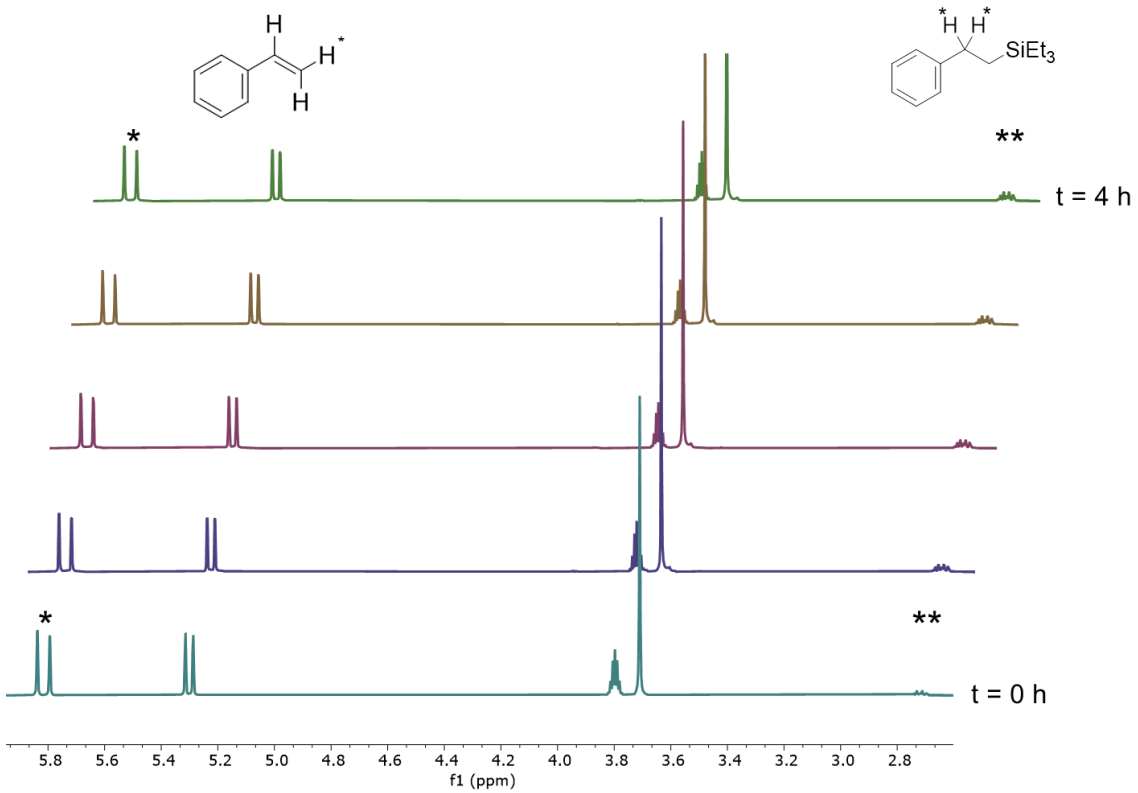

Figure 2.8: Changes in ^{1}H NMR spectrum corresponding to styrene proton (δ = 5.82 ppm) and the protons of the product (δ = 2.72 ppm) when a $CDCl_3$ solution of styrene, triethylsilane and dioxane (as an internal standard) was treated with Karstedt's catalyst for 4 h at 30°C with TCNE

In the absence of an inhibitor, the hydrosilylation reaction began instantaneously under ambient conditions, with about 12 % of product formation, after the first ^{1}H NMR spectrum acquisition. The reaction progress increased significantly within the first 60 minutes of heating the reaction mixture at 30°C with nearly 50 % product formation. Upon further heating, only a slow increase in product formation was observed that plateaued to about 64% after a total of 240 minutes of heating. In contrast, only 6% of the product was formed in the presence of tetracyanoethylene that increased to about 18% after a total of 240 minutes of heating at 30°C. The results of the experiments are outlined in Table 2.1 and Figure 2.9.

Reaction time (min)	Without inhibitor		% completion	With TCNE		% completion
	styrene proton (δ = 5.82 ppm)	product proton (δ = 2.72 ppm)		styrene proton (δ = 5.82 ppm)	product proton (δ = 2.72 ppm)	
0	0.92	0.12	11.96	1	0.07	6.54
60	0.49	0.48	49.74	0.81	0.14	15.18
90	0.44	0.65	59.63	0.79	0.16	16.84
180	0.42	0.71	62.83	0.78	0.17	17.89
240	0.41	0.72	63.71	0.77	0.17	18.08

Table 2.1: Results for reaction progress in the absence of an inhibitor and the presence of TCNE (model inhibitor)

The percent completion of the reaction in both cases, that is, without inhibitor and with tetracyanoethylene, was determined by comparing the changes in the integration of signals in ^{1}H NMR spectrum of styrene proton (δ = 5.82 ppm) and the protons of the product (δ = 2.72 ppm) with respect to the internal standard (dioxane) over a period of 4 h and was found to be 64% and 18% respectively (Figure 2.9). The symmetry of plots for reactant disappearance and product appearance in both cases suggests the absence of any side reactions, and the inactivity of the catalyst (as observed from the change of solution colour from yellow to golden brown and platinum metal deposition on NMR tube walls) could be the predominant reason for the incomplete conversion.

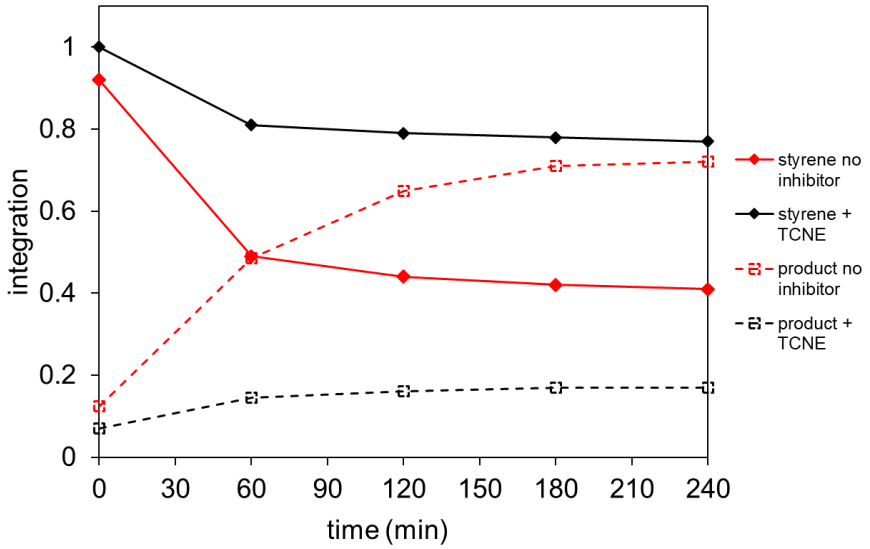

Figure 2.9: Changes in the integration of the signals in the ^{1}H NMR spectrum corresponding to the protons highlighted in Figure 2.8 when a $CDCl_3$ solution of styrene, triethylsilane and dioxane (as an internal standard) was treated with Karstedt's catalyst for 4 h at 30°C without inhibitor and with TCNE

2.5.4.2. Photoresponsive inhibitor

Model hydrosilylation reaction from Scheme 2.11 was used to determine the effect of the photoresponsive inhibitor in both its isomeric forms on Karstedt's catalyst. When an equimolar solution of styrene (0.00108 mol) and triethylsilane (0.00108 mol) in $CDCl_3$ charged with Karstedt's catalyst (1.31×10^{-6} mol of Pt, 0.12% catalyst) in a sealed NMR tube at 30°C with 1,4-dioxane as an internal standard was treated with 2.5 molar equivalents of ring-open isomer, **1*o***, the progress of the reaction was similar to the reaction progress observed when 2.5 molar equivalents of tetracyanoethylene were used as an inhibitor. The results suggest that the ring-open isomer, **1*o***, behaves as an inhibitor to Karstedt's catalyst, but, is not as potent an inhibitor as tetracyanoethylene.

Upon replacing, ring-open isomer, **1*o***, with isolated ring-closed isomer, **1*c***, the progress of the reaction, now appeared to resemble the reaction without any inhibitor (Figure 2.10).

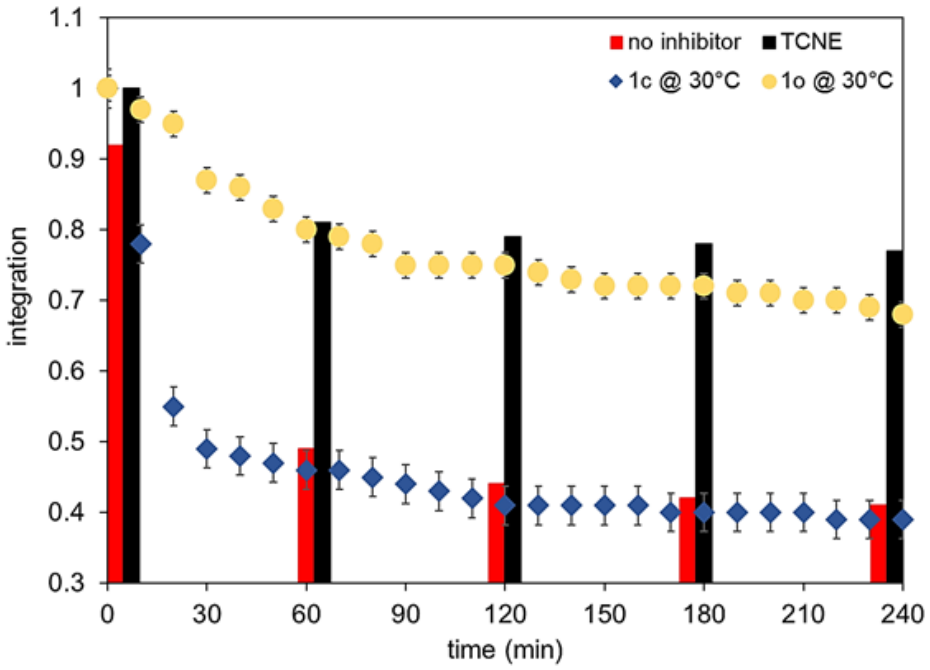

Figure 2.10: Changes in the integration of the signals in the ^1H NMR spectrum corresponding to the protons highlighted in Figure 2.8 when a $CDCl_3$ solution of styrene, triethylsilane and dioxane (as an internal standard) was treated with Karstedt's catalyst for 4 h at 30°C with **1*o*** (yellow circles) and **1*c*** (blue diamonds). The same reaction at 30°C without any inhibitor (red) and TCNE (black) are shown in the bars. The error bars are the result of three runs at 30°C

The percent completion of the reaction for **1*o*** and **1*c*** was determined by comparing the changes in the integration of signals in ^{1}H NMR spectrum of styrene proton (δ = 5.82 ppm) and the protons of the product (δ = 2.72 ppm) w.r.t the internal standard (dioxane) over a period of 4 h and was found to be 32% and 61% respectively. These observations clearly demonstrate how the ring-open isomer acts as an effective inhibitor for Karstedt's catalyst, while its ring-closed counterpart does not.

The reaction progresses at a slower rate and with a more complex reaction profile when the temperature of the hydrosilylation reaction is lowered to 20°C, but, the effects of **1*o*** and **1*c*** on Karstedt's catalyst remain relatively the same (Figure 2.11). At 20°C, the reaction progresses with a more observable short induction period due to the oxidative addition of triethylsilane to generate the active Pt (II) form of the catalyst. This period is then followed by a rapid decrease in the amount of styrene as seen in Figure 2.11 from 60 to 120 min and is indicative of the mechanistic step of migratory insertion of styrene into Pt-H bonds and reductive elimination of the hydrosilylated product. This also suggests that the hydrosilylation reaction occurs only in a small portion of the total reaction time. [126,106] The reaction reaches equilibrium after 120 min with the incomplete conversion of styrene. This incomplete conversion can be attributed to one or some combination of the following reasons:

a) formation of stable, unreactive metal colloidal species in the reaction[105]
b) formation of side products in the reaction[127]
c) the fact that electron-donating ethyl groups on Et_3SiH have a low rate of addition to styrene[128]

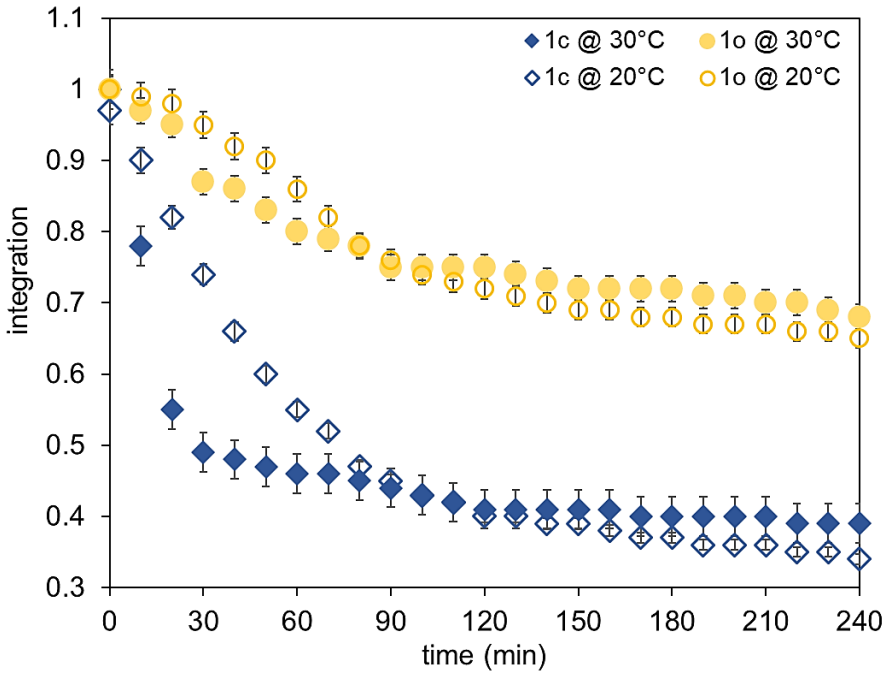

Figure 2.11: Changes in the integration of the signals in the ^{1}H NMR spectrum corresponding to the protons highlighted in Figure 2.8 when a $CDCl_3$ solution of styrene, triethylsilane, and dioxane (as an internal standard) was treated with Karstedt's catalyst for 4 at 30°C with **1*o*** (yellow solid circles) and **1*c*** (blue solid diamonds) and at 20°C with **1*o*** (yellow hollow circles) and **1*c*** (blue hollow diamonds). The error bars are the result of three runs at 30°C and 20°C

2.5.5. Reversibility of Photoresponsive inhibitor

The reversible nature of the inhibition mechanism of the photoresponsive inhibitor was also determined using ^{1}H NMR spectroscopy. Starting with an equimolar deuterated chloroform solution of styrene and triethylsilane containing Karstedt's catalyst (1.31×10^{-6} mol Pt) and **1*o*** (2.5 molar equivalents), and incubating at 20°C for 30 min, the reaction progress appears to be slow, as expected. Then, upon irradiation of the solution for 30 min with 312 nm light, no significant change in consumption of styrene was observed and the reaction progress was almost identical to the experiment using pure ring-open isomer, **1*o*** and no UV light (Figure 2.12).

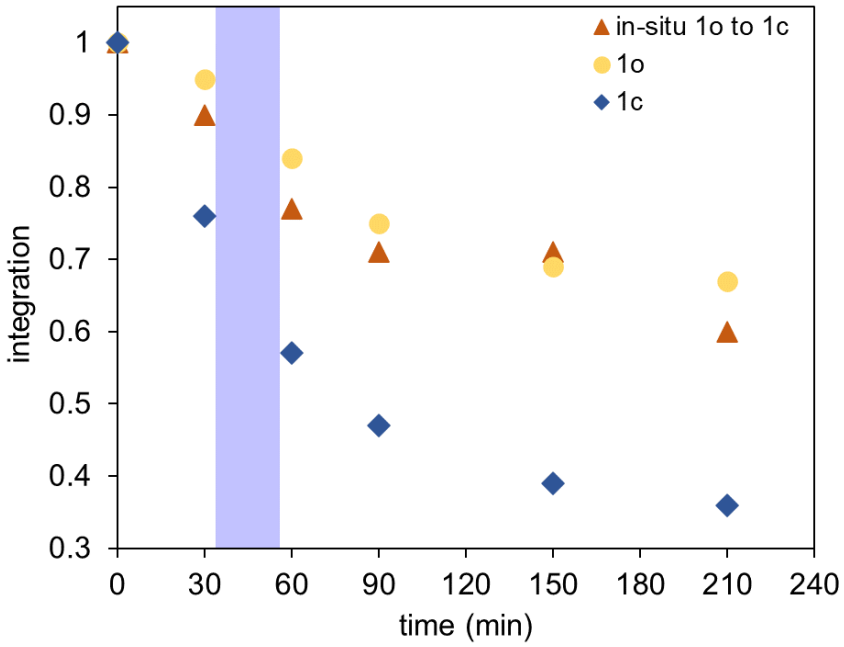

Figure 2.12: Changes in the integration of the signals in the ^{1}H NMR spectrum corresponding to the vinylic protons of styrene when a $CDCl_3$ solution of it is treated with triethylsilane, **1*o*** was treated with Karstedt's catalyst at 20 °C for 30 minutes (brown triangles) followed by irradiation with 312 nm UV light for 30 minutes (violet shaded area), and further incubation at 20 °C for 210 minutes. The results are compared with corresponding reactions of isolated forms **1*o*** (yellow circles) and **1*c*** (blue diamonds)

The lack of difference in consumption of styrene upon exposure to 312 nm light can be attributed to the fact that the photostationary state contains almost equal amounts of ring-open, **1*o***, and ring-closed, **1*c***, isomers. It is unlikely that the lack of change in consumption of styrene was due to the remaining ring-open isomer (~1.25 equivalents compared to the metal) in the photostationary state still acting as an effective inhibitor making it difficult to turn the inhibitor completely 'off'. Instead, we ascribe it to the presence of metal slowing the conversion of **1*o*** to its ring-closed counterpart, while any ligand not bound to metal results in the solution turning dark blue. The overlap of thiophene protons for **1*c*** and styrene protons in the δ = 6.70 to 6.90 ppm region makes the estimation of the photostationary state of the complex catalyst mixture difficult. Reducing the amount of **1*o*** to 1.74 equivalents resulted in no observable inhibition. This absence of inhibition at low equivalents of **1*o*** suggests that the ligand exchange in the catalyst with **1*o*** is not sufficient to reduce the lower the activity of the catalyst and enough coordination sites are available for the hydrosilylation reaction to proceed.

In contrast, if **1*c*** is used instead of **1*o*** in an analogous experiment, it was evident that the inhibition turned 'on' (Figure 2.13). This is a valid observation as the conversion of the 'inactive' ring-closed isomer to the 'active' ring-open isomer is quantitative when solutions are exposed to visible light. As seen from the progress of the reaction, there is a rapid consumption of styrene in the initial 30 min of the reaction with a slope of decrease in styrene being -7.30 x 10^{-3} min^{-1}, which is similar to that for experiment with **1*c*** whose slope is calculated to be -6.90 x 10^{-3} min^{-1}. After 35 minutes, the solution was exposed to light of wavelengths greater than 435 nm for 2 min, the blue colour of the solution disappeared and a corresponding decrease in consumption of styrene was observed. Reaction progression after exposure is seen to slow down with the slope of decrease in styrene becoming –3.10 x 10^{-3} min^{-1} which is the same as when pure **1*o*** was used, the slope of decrease in styrene was -3.00 x 10^{-3} min^{-1}).

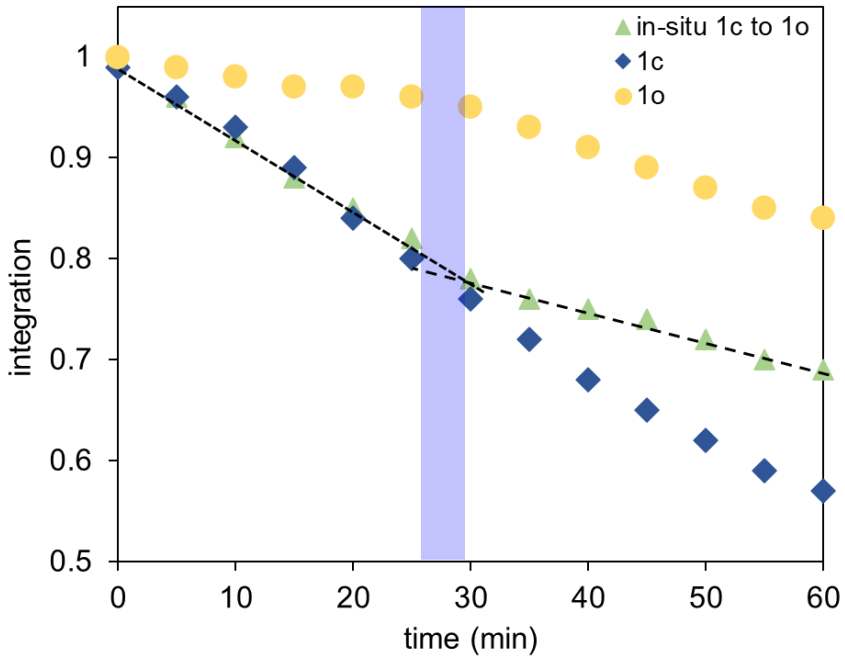

Figure 2.13: Changes in the integration of the peaks in the ^{1}H NMR spectra corresponding to the vinylic hydrogen on styrene when a $CDCl_3$ solution of it is treated with triethylsilane and **1*c*** at 20 °C (green triangles) followed by exposing the solution to visible light (greater than 435 nm for 2 minutes) after 35 minutes. The violet vertical line shows the time of visible light irradiation. Dashed lines are the fits for each reaction

2.6. Conclusion and Future prospects

2.6.1. Summary

The concept of light-controlled catalysis using small molecules was reported successfully in this chapter. The synthesis of **1*o*** was presented. As anticipated, ring-open isomer,**1*o***, bound to the platinum metal centre in the catalyst to slow/inhibit the hydrosilylation reaction. Ring-closed isomer, **1*c***, did not bind to the metal centre at all, which was expected, due to the loss of the electron-deficient double bond. The behaviour of both isomers towards metal coordination was also assessed. The photochromic system presented was capable of acting as a light-triggered "off" control to deactivate Karstedt's catalyst. The desired two-way "on-off" inhibition system was not successful currently.

2.6.2. Future prospects

As can be seen from the photoinhibitor, **1*o***, the twin nitrile groups on the alkene make it sufficiently electron-deficient to bind to the platinum metal centre. The two main limitations of our system are: 1) the conversion to ring-closed isomer is low; 2) the metal coordination is strong enough to reduce the ring-closing efficiency of our system which prevents the desired two-way "on-off". A potential solution to this can be obtained by modifying the molecular scaffold that is presented in this chapter with different functional groups on the outer thiophene units (Scheme 2.12). The percent conversion of the suggested ring-open isomers to their corresponding ring-closed isomers is listed in Table 2.2.[129] This can lead to a range of such inhibitors having different abilities to coordinate to platinum and more ring-closed isomers in the photostationary states. The inhibitor system containing fluorenyl groups is seen to have a much higher conversion ratio to ring-closed isomer (94%) since the fluorenyl groups are electron-rich and have larger π conjugation. It is proposed that the inhibitor-containing bulky fluorenyl groups on the thiophene units would be able to inhibit Karstedt's catalyst in its' ring-open form. It is also proposed that the electron-rich character of the fluorenyl groups would lead to weaker coordination to the metal centre, which can increase the ring-closing efficiency of the system either partially or entirely. The inhibitor system containing pyridyl groups, on the other hand, would not be recommended as the pyridyl groups themselves are known to bind to platinum-based metal centres strongly.

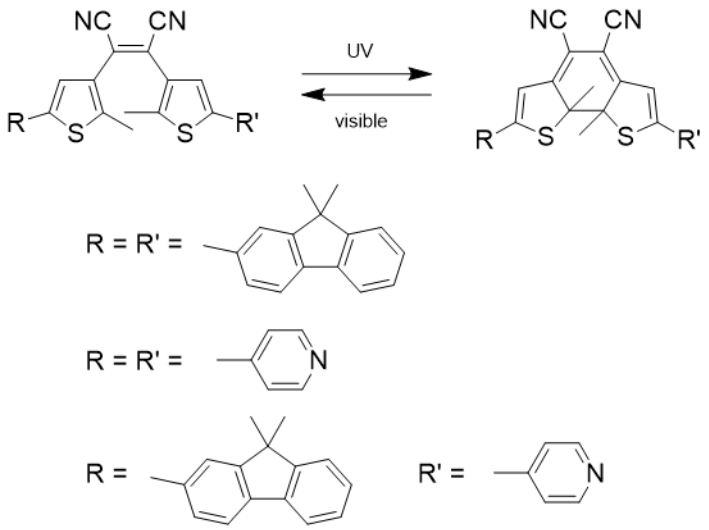

Scheme 2.12: Potential photo-inhibitors of Karstedt's catalyst with bulky R groups[129]

R	R'	photostationary state
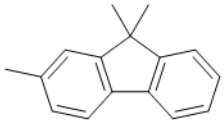	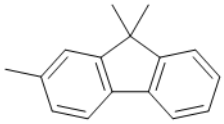	94%
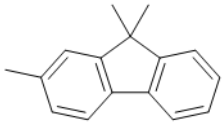	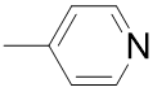	78%
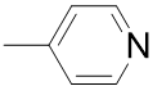	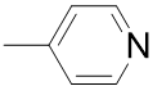	60%

Table 2.2: Percent conversion of ring-open isomers to ring-closed isomers with different R groups[129]

To obtain better conversion yields for hydrosilylation reaction, more reactive silanes, such as trichlorosilane (Cl_3SiH), can be used along with different alkene substrates, such as norbornene, cyclohexene, etc. Using aliphatic alkene substrates can also help in avoiding the competing absorption of the alkenes at the excitation wavelength in the experiments involving turning the inhibition "off" *in-situ* in the presence of the photoinhibitor.

2.7. Experimental

2.7.1. General

All solvents and reagents used for synthesis, chromatography, UV-vis spectroscopy and photochemical studies were purchased from Aldrich, Anachemia, Caledon Labs, Fisher Scientific or Alfa Aesar, and used as received. Solvents used for metal-halogen exchange reactions were dried and degassed by passing them through steel columns containing activated alumina under nitrogen using an MBraun solvent purification system. Solvents for NMR analysis were purchased from Cambridge Isotope Laboratories and used as received. Column chromatography was performed using silica gel 60 (230–400 mesh) from Silicycle Inc. Karstedt's catalyst used for all hydrosilylation experiments was purchased from Aldrich and was used as received. According to the company, it is a complex solution containing Pt(0)-1,3-divinyl-1,1,3,3-tetramethyldisiloxane in xylenes with approx. 2% metal content. The structure of the complex in solution consists of both bridging and chelating divinyl ligands (shown in the figure below).

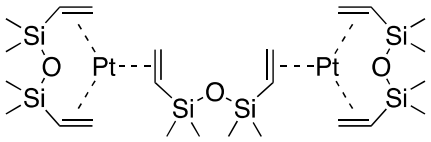

2.7.2. Instrumentation

^{1}H and ^{13}C NMR characterizations were performed on a Bruker Avance-400 instrument with a 5 mm inverse probe operating at 400.13 MHz for ^{1}H NMR and 100.61 MHz for ^{13}C NMR. ^{195}Pt NMR characterizations were performed on a Bruker Avance-400 Solids and Microimaging instrument. Chemical shifts (δ) are reported in parts per million (ppm) relative to tetramethylsilane using the residual solvent peak as a reference. Coupling constants (J) are reported in Hertz. UV-visible absorption spectra were recorded on a Varian Cary 300 Bio-spectrophotometer. High-Resolution Mass Spectroscopy (HRMS) measurements were performed using an Agilent 6210 TOF LC/MS in ESI-(+) mode. Melting points were measured using a Gallenkamp melting point apparatus and are uncorrected.

2.7.3. Photochemistry

All the ring-closing reactions were carried out using the light source from a lamp used for visualizing TLC plates at 312 nm (Spectroline E series, 470 W/cm^2). The ring-opening reactions were carried out using the light of a 150 W halogen photo-optic source passed through a 435 nm cut-off filter to eliminate higher energy light.

2.7.4. Synthesis

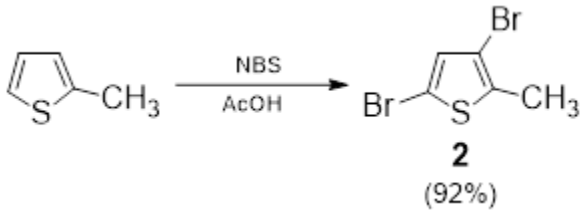

2
(92%)

Synthesis of 3,5-dibromo-2-methylthiophene (2). A solution of 2-methylthiophene (20.0 g, 0.200 mol) in glacial acetic acid (200 mL) was slowly treated with N-bromosuccinimide (72.5 g, 0.400 mol) while stirring at room temperature. After stirring for an additional 90 min, the reaction was neutralized by the addition of aqueous NaOH (8% w/v). The mixture was extracted with dichloromethane (3 × 100 mL), the combined organic extracts were washed with saturated aqueous sodium thiosulphate (100 mL) to remove any unreacted bromine, dried over anhydrous $MgSO_4$, filtered and concentrated under reduced pressure. Purification by vacuum distillation afforded 18.5 g (92%) of 3,5-dibromo-2-methylthiophene (2) as a colourless oil.

^{1}H NMR (400 MHz, $CDCl_3$): δ 6.85 (s, 1H), 2.34 (s, 3H).

^{13}C NMR (101 MHz, $CDCl_3$): δ 135.7, 131.7, 108.5, 108.3, 14.6.

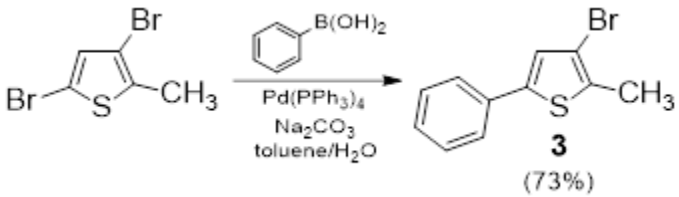

3
(73%)

Synthesis of 3-bromo-2-methyl-5-phenylthiophene (3). A bi-phasic mixture of a solution of 3,5-dibromo-2-methylthiophene (2) (15.0 g, 0.0586 mol) in toluene (100 mL)

and aqueous Na_2CO_3 (100 mL, 1M) in a 250 mL 3-necked round-bottom flask equipped with a reflux condenser was deoxygenated by bubbling N_2 through it for 60 min. The mixture was then treated with a solution of phenylboronic acid (7.2 g, 0.0586 mol) in EtOH (50 mL). The resulting mixture was heated to 80°C for 30 min, followed by the addition of $Pd(PPh_3)_4$ (0.6 g, 0.0005 mol) in one portion. The reaction contents were heated at reflux for 16 h under an N_2 atmosphere. The heat source was removed and the mixture was allowed to cool to room temperature, at which time it was extracted with diethyl ether (3 × 100 mL). The combined organic extracts were washed with brine (100 mL), dried over anhydrous $MgSO_4$, filtered and concentrated under reduced pressure. Purification by column chromatography using silica gel (hexanes) afforded 11.0 g (73%) of 3-bromo-2-methyl-5-phenylthiophene (3) as a white solid.

^{1}H NMR (400 MHz, $CDCl_3$): δ 7.53 (d, J = 7.3 Hz, 2H), 7.38 (d, J = 7.9 Hz, 2H), 7.31 (d, J = 7.3 Hz, 1H), 7.13 (s, 1H), 2.44 (s, 3H).

^{13}C NMR (101 MHz, $CDCl_3$): δ 140.9, 133.4, 133.3, 128.7, 127.5, 125.33, 125.1, 109.6, 14.6.

Melting point: 60-61 °C.

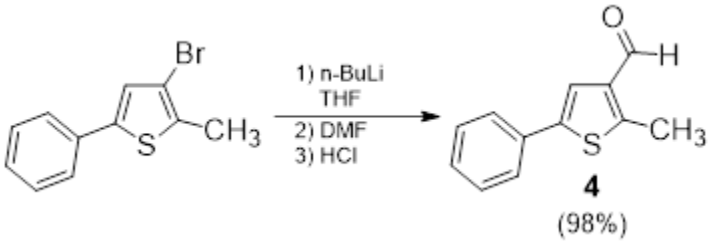

Synthesis of 2-methyl-5-phenylthiophene-3-carbaldehyde (4). A solution of 3-bromo-2-methyl-5-phenylthiophene (3) (0.356 g, 0.00141 mol) in anhydrous THF (50 mL) in a flame dried 3-necked round bottom flask equipped with a mechanical stirrer was cooled to -60°C (dry ice/acetone bath) under N_2 atmosphere. The solution was treated with n-butyllithium (2.5 M in hexanes, 0.58 mL, 0.00145 mol) dropwise over a period of 15 min. The mixture was stirred for a further 10 min at -60°C and the reaction progress was monitored by TLC (20:1 hexanes/ethyl acetate). After all the starting material was consumed, anhydrous dimethylformamide (0.22 mL, 0.00285 mol) was added to the reaction mixture. After stirring for 1 h at -60°C, the cooling bath was removed and the

reaction contents were allowed to warm to room temperature and were left to stir for 16 h under an N_2 atmosphere. The mixture was poured into 1M HCl (50 mL) and extracted with diethyl ether. The organic layer was washed with saturated sodium bicarbonate (2 × 50 mL), followed by brine (2 × 50 mL), dried over $MgSO_4$, filtered and concentrated under reduced pressure. Purification by column chromatography using silica gel (20:1 hexanes/ethyl acetate) afforded 0.35 g (98%) of 2-methyl-5-phenylthiophene-3-carbaldehyde (4) as a white solid.

^{1}H NMR (400 MHz, $CDCl_3$): δ 10.01 (s, 1H), 7.55 (s, 1H), 7.54 (d, J = 7.1 Hz, 2H), 7.37 (d, J = 7.8 Hz, 2H), 7.31 (d, J = 7.8 Hz, 1H), 2.77 (s, 3H).

^{13}C NMR (101 MHz, $CDCl_3$): δ 184.6, 151.4, 141.4, 138.1, 133.3, 129.2, 128.16, 125.9, 122.2, 13.8.

Melting point: 78-79 °C.

HRMS (ESI): m/z (M+H) calculated for $C_{12}H_{11}OS$: 203.052512, found: 203.052572.

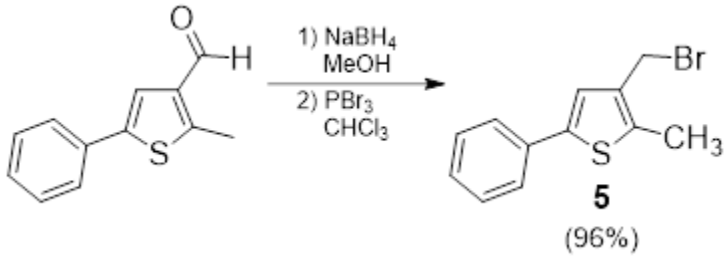

5

(96%)

Synthesis of 3-(bromomethyl)-2-methyl-5-phenylthiophene (5). A solution of 2-methyl-5-phenylthiophene-3-carbaldehyde (4) (1.6 g, 0.0078 mol) in methanol (50 mL) was cooled to 0 °C in an ice bath and treated with sodium borohydride (0.59 g, 0.0156 mol). The reaction was stirred at 0 °C for 1 h and the reaction progress was monitored by TLC (20:1 hexanes/ethyl acetate). On completion, the reaction mixture was washed with 5% HCl and extracted with diethyl ether (2 × 50 mL). The combined organic layers were dried over $MgSO_4$, filtered and concentrated under reduced pressure at low temperature. The crude alcohol was dissolved in chloroform (50 mL) and slowly treated with a solution of phosphorus tribromide (1M in dichloromethane, 15.6 mL, 0.0156 mol). The reaction mixture was allowed to stir for 2.5 h at room temperature while monitoring the reaction using TLC (3:1 hexanes/ethyl acetate). Upon completion, the contents were washed with

saturated sodium bicarbonate (50 mL), followed by brine (50 mL), dried over $MgSO_4$, filtered and concentrated under reduced pressure to afford 1.51 g (96%) of 3-(bromomethyl)-2-methyl-5-phenylthiophene (5) as a yellow solid, which was used without further purification.

^{1}H NMR (400 MHz, $CDCl_3$): δ 7.54 (d, J = 7.1 Hz, 2H), 7.36 (d, J = 7.8 Hz, 2H), 7.28 (d, J = 7.4 Hz, 1H), 7.18 (s, 1H), 4.46 (s, 2H), 2.46 (s, 3H).

^{13}C NMR (101 MHz, $CDCl_3$): δ 140.8, 137.9, 134.4, 129.0, 127.6, 125.6, 124.6, 26.3, 13.2.

Melting point: 70-71 °C

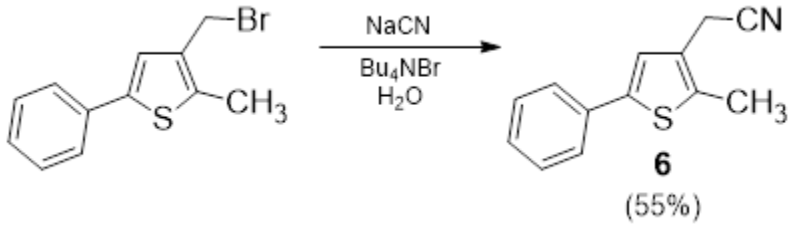

6

(55%)

Synthesis of 2-(2-methyl-5-phenylthiophen-3-yl) acetonitrile (6). A mixture of 3-(bromomethyl)-2-methyl-5-phenylthiophene (5) (0.53 g, 0.002 mol), tetrabutylammonium bromide (0.31 g, 0.001 mol) and sodium cyanide (0.56 g, 0.0114 mol) in water (10 mL) was heated at reflux for 3 h. After complete consumption of reactant 5 as monitored by TLC (4:1 hexanes/ethyl acetate), the reaction was cooled to room temperature and extracted with diethyl ether (3 × 20 mL). The combined organic layers were dried over $MgSO_4$, filtered and concentrated under reduced pressure. Purification by column chromatography using silica gel (4:1 hexanes/ethyl acetate) afforded 0.29 g (55%) of 2-(2-methyl-5-phenylthiophen-3-yl) acetonitrile (6) as a yellow solid.

^{1}H NMR (400 MHz, $CDCl_3$): δ 7.53 (d, J = 7.2 Hz, 3H), 7.36 (d, J = 7.8 Hz, 2H), 7.29 (d, J = 7.4 Hz, 1H), 7.15 (s, 1H), 3.59 (s, 2H), 2.43 (s, 3H).

^{13}C NMR (101 MHz, $CDCl_3$): δ 141.1, 135.2, 133.6, 128.8, 127.4, 125.3, 123.5, 117.2, 16.8, 13.0.

Melting point: 58-59 °C.

HRMS (ESI): m/z (M+Na) calculated for $C_{13}H_{11}NNaS$: 236.050441, found: 236.050476.

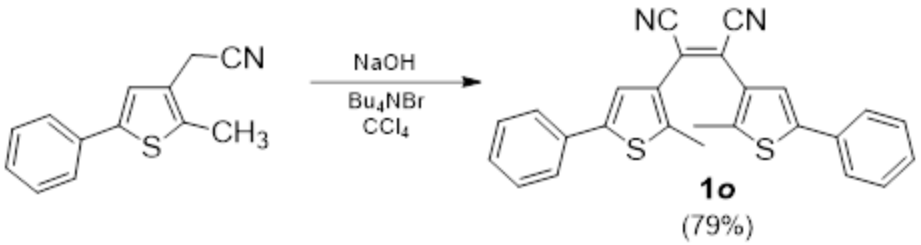

Synthesis of 2,3-bis(2-methyl-5-phenylthiophen-3-yl) maleonitrile (1*o*). A solution of 2-(2-methyl-5-phenylthiophen-3-yl) acetonitrile (6) (0.93 g, 0.0022 mol) in carbon tetrachloride (5 mL) was added to a stirring solution of 50% aqueous sodium hydroxide (5 mL) containing tetrabutylammonium bromide (0.035 g, 0.00011 mol) at room temperature. The mixture was stirred at 50°C for 1.5 h and the reaction progress was monitored by TLC (10:1 hexanes/ethyl acetate). Upon completion, the reaction mixture was poured into water and extracted with chloroform (2 × 10 mL), dried over $MgSO_4$, filtered and concentrated under reduced pressure. Purification by column chromatography using silica gel (10:1 hexanes/ethyl acetate) afforded 0.74 g (79%) of 2,3-bis(2-methyl-5-phenylthiophen-3-yl) maleonitrile (1*o*) as a yellow-green solid.

^{1}H NMR (400 MHz, $CDCl_3$): δ 7.40 (d, J = 8.1 Hz, 3H), 7.33 (d, J = 7.2 Hz, 2H), 7.29 (d, J = 7.1 Hz, 1H), 6.91 (s, 1H), 2.31 (s, 3H).

^{13}C NMR (101 MHz, $CDCl_3$): δ 142.4, 133.1, 131.8, 129.4, 128.6, 127.5, 126.2, 126.0, 121.1, 116.4, 15.0.

Melting point: 132-133 °C.

HRMS (ESI): m/z (M+H) calculated for $C_{26}H_{18}N_2S_2$: 423.098417, found: 423.097986.

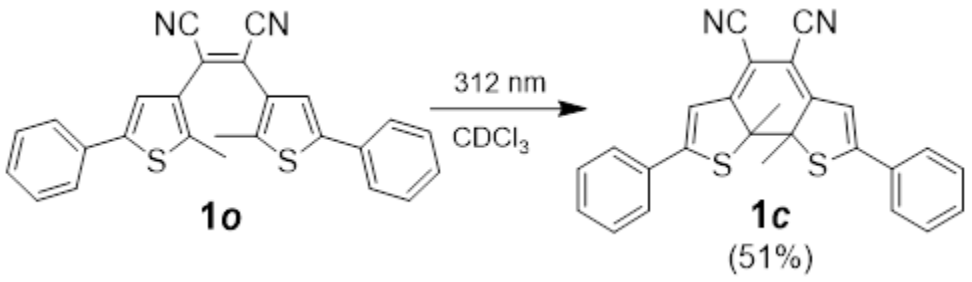

Photochemical synthesis of 1*c*. A deuterated chloroform solution of compound **1*o*** (5.00 × 10^{-3} M) in an NMR tube was irradiated with 312 nm light until no further changes were

observed in the ^{1}H NMR spectrum. After 120 min the photostationary state was reached at this concentration, which contained 51% of the ring-closed isomer **1*c*** as measured by comparing relative integrals for chemical shifts for **1*o*** and **1*c***. The ring-closed isomer **1*c*** was isolated by column chromatography using silica gel (2:1 dichloromethane/hexanes).

^{1}H NMR (400 MHz, $CDCl_3$): δ 7.58 (d, J = 6.8 Hz, 2H), 7.46 (d, J = 6.8 Hz, 2H), 7.44 (d, J = 6.7 Hz, 1H), 6.72 (s, 1H), 2.17 (s, 3H).

^{13}C NMR (101 MHz, $CDCl_3$): δ 170.72, 144.69, 130.82, 129.20, 127.25, 115.62, 108.90, 99.58, 53.22, 29.87.

Model reaction 1: hydrosilylation without an inhibitor. A solution of styrene (0.124 mL, 0.00108 mol) and 1,4-dioxane (0.020 mL) as an internal standard in $CDCl_3$ (0.500 mL) in an NMR tube was treated with Karstedt's catalyst (0.015 mL solution (approx. 2% metal content in xylene), 1.31 x 10^{-6} mol of Pt, 0.12% catalyst) followed by triethylsilane (0.172 mL, 0.00108 mol). An initial ^{1}H NMR spectrum was immediately acquired. The NMR tube was heated at 30 °C for 4 h while ^{1}H NMR spectra were recorded every hour. The areas under the peaks corresponding to styrene proton (δ = 5.82 ppm) and the protons of the product (δ = 2.72 ppm) were measured and compared to the internal standard to monitor the progress of the reaction. These results are shown in Figures 2.7 and 2.9.

Model reaction 2: hydrosilylation with tetracyanoethylene (TCNE) as an inhibitor. A solution of styrene (0.124 mL, 0.00108 mol) and 1,4-dioxane (0.020 mL) as an internal standard in $CDCl_3$ (0.500 mL) in an NMR tube was treated with Karstedt's catalyst (0.015 mL solution (approx. 2% metal content in xylene), 1.31 x 10^{-6} mol of Pt, 0.12% catalyst) followed by tetracyanoethylene (4.00 x 10^{-4} g, 3.30 x 10^{-6} mol, 2.5 equivalents compared to Pt) and finally triethylsilane (0.172 mL, 0.00108 mol). An initial ^{1}H NMR spectrum was immediately acquired. The NMR tube was heated at 30°C for 4 h while ^{1}H NMR spectra were recorded every hour. The areas under the peaks corresponding to styrene proton (δ = 5.82 ppm) and the protons of the product (δ = 2.72 ppm) were measured and compared to the internal standard to monitor the progress of the reaction. These results are shown in Figures 2.8 and 2.9.

Hydrosilylation with ring-open isomer 1*o* as an inhibitor. A solution of styrene (0.124 mL, 0.00108 mol) and 1,4-dioxane (0.020 mL) as an internal standard in $CDCl_3$ (0.500 mL) in an NMR tube was treated with Karstedt's catalyst (0.015 mL solution (approx. 2%

metal content in xylene), 1.31 x 10^{-6} mol of Pt, 0.12% catalyst) followed by compound 1*o* (1.40 x 10^{-3} g, 3.30 x 10^{-6} mol, 2.5 equivalents compared to Pt) and triethylsilane (0.172 mL, 0.00108 mol). An initial ^{1}H NMR spectrum was immediately acquired. The NMR tube was heated at 30 °C for 4 h while ^{1}H NMR spectra were recorded every 10 min. The areas under the peaks corresponding to styrene proton (δ = 5.82 ppm) and the protons of the product (δ = 2.72 ppm) were measured and compared to the internal standard to monitor the progress of the reaction. These results are shown in Figures 2.10 and 2.11.

Hydrosilylation with ring-closed isomer 1*c* as an inhibitor. A solution of styrene (0.124 mL, 0.00108 mol) and 1,4-dioxane (0.020 mL) as an internal standard in $CDCl_3$ (0.500 mL) in an NMR tube was treated with Karstedt's catalyst (0.015 mL solution (approx. 2% metal content in xylene), 1.31 x 10^{-6} mol of Pt, 0.12% catalyst) followed by isolated compound 1*c* (1.40 x 10^{-3} g, 3.30 x 10^{-6} mol, 2.5 equivalents compared to Pt) and triethylsilane (0.172 mL, 0.00108 mol). An initial ^{1}H NMR spectrum was immediately acquired. The NMR tube was heated at 30°C for 4 h while ^{1}H NMR spectra were recorded every 10 min. The areas under the peaks corresponding to styrene proton (δ = 5.82 ppm) and the protons of the product (δ = 2.72 ppm) were measured and compared to the internal standard to monitor the progress of the reaction. These results are shown in Figure S5. The reaction was repeated at 20°C and the results are shown in Figures 2.10 and 2.11.

In situ experiments

A solution of styrene (0.124 mL, 0.00108 mol) and 1,4-dioxane (0.020 mL) as an internal standard in $CDCl_3$ (0.500 mL) in an NMR tube was treated with Karstedt's catalyst (0.015 mL solution (approx. 2% metal content in xylene), 1.31 x 10^{-6} mol of Pt, 0.12% catalyst) followed by compound 1*o* (1.40 x 10^{-3} g, 3.30 x 10^{-6} mol, 2.5 equivalents compared to Pt) and triethylsilane (0.172 mL, 0.00108 mol). An initial ^{1}H NMR spectrum was immediately acquired. The NMR tube was kept in a water bath at 20 °C for 30 min followed by the acquisition of another ^{1}H NMR spectrum. The contents of the tube were then irradiated with 312 nm light for 5 minutes to induce the ring-closing reaction. The colour changed from colourless to blue indicating the reaction was successful. A ^{1}H NMR spectrum for this coloured solution was immediately acquired. The tube was kept in a water bath at 20 °C for another 150 minutes with ^{1}H NMR spectra being acquired every 30 min. The areas under the peaks corresponding to styrene proton (δ = 5.82 ppm) were measured and

compared to the internal standard to monitor the progress of the reaction before and after irradiation. These results are shown in Figures 2.12 and 2.13.

Chapter 3.

A Dual-mode Visual Detector for Toxic Hydrazine

The research work presented in this chapter has been published as a paper in Organic RSC Advances and is being reproduced in its entirety with permission from the journal (B. Kaur, R. Raza, N.R. Branda, *RSC Adv.*, **2021**, *11*, 22835-22841). The project was designed by Brahmjot Kaur and Dr Neil R. Branda. The synthesis and characterization of all organic precursors were carried out by B. Kaur. All photochemistry experiments on the final organic molecule were done by B. Kaur and R. Raza. ^{13}C NMR based experiments were carried by B. Kaur. All detection experiments were carried out by B. Kaur and R. Raza. The DFT calculations were carried out by B. Kaur using Compute Canada Database (CCDB). B. Kaur wrote the first draft of the manuscript. It was later edited by R. Raza and finally by Dr N.R. Branda.

3.1. Graphical abstract

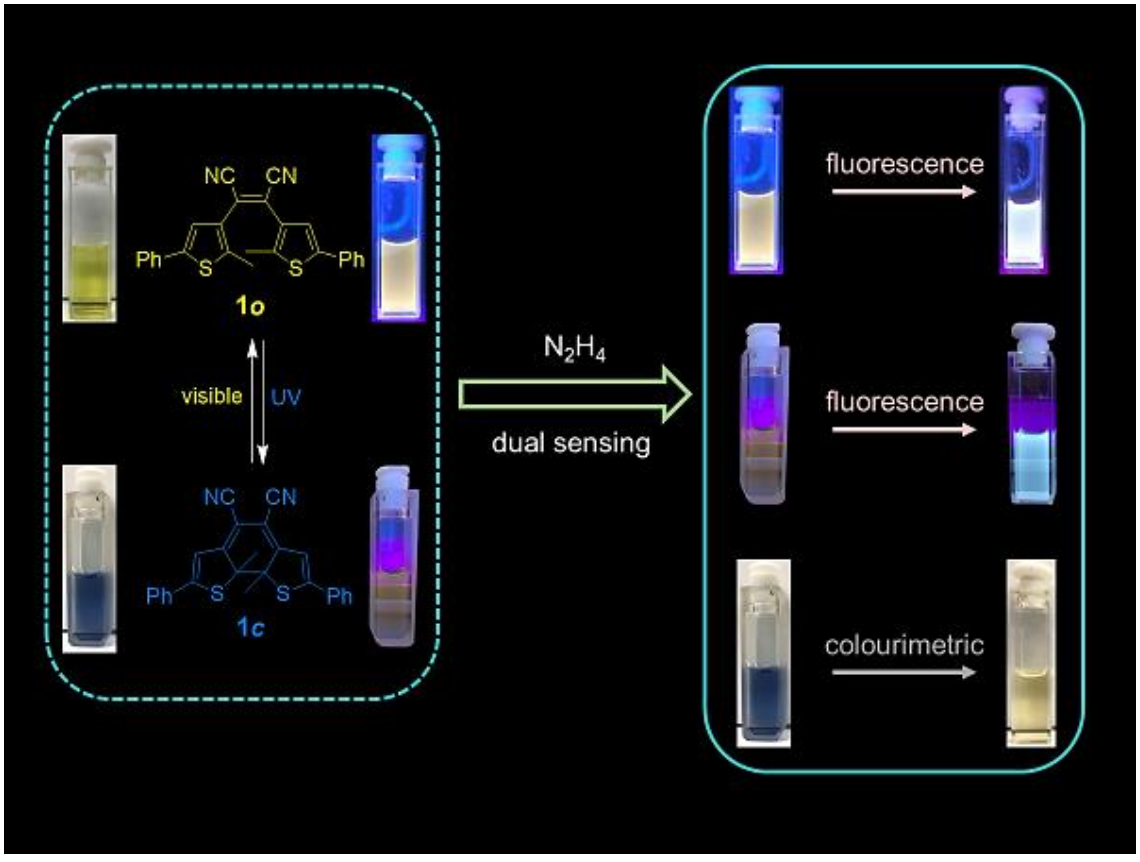

3.2. Abstract

Hydrazine (N_2H_4) is one of the commonly used chemical reagents in numerous industries and applications but its toxicity to humans poses a need to develop simple detection methods. Herein, we demonstrate a novel dual-sensing system for detecting hydrazine in vapour and solution form by using a small photoresponsive molecule that has altered optical response (both colourimetric and fluorescent) after reacting with hydrazine.

3.3. Introduction

The development of simple and inexpensive ways for sensing environmentally significant substances continues to be a crucial area of research.[130,131] Detectors are being designed for toxic gases and vapours such as those used in chemical warfare agents, as substrates in industries and as pesticides.[132] Hydrazine (N_2H_4) is one such extensively used industrial substrate. As a result of its high enthalpy of combustion, hydrazine is used as a rocket fuel propellant and in fuel cells.[133,134] Hydrazine acts as a strong base and a highly reactive reducing agent, and is thus, considered an important substrate for the production of pharmaceuticals, textile dyes, pesticides, among others.[135,136] Current worldwide production of hydrazine stands at about 200,000 tons[137] and is likely to increase as the areas of its application across industries increase.[138,139] But hydrazine is regarded as a possible carcinogen and toxic for the liver, kidneys and central nervous system of humans.[135,140,141] This has led to the development of highly sensitive and selective methods to detect hydrazine. Current technologies employed for the detection of hydrazine in vapour and solution form is further described in Section **3.3.1**.

In this chapter, a small photoresponsive compound is discussed whose structure is based on the dithienylethene backbone and has altered optical properties upon reaction with hydrazine. The reaction causes an irreversible structural change in the compound that can, now, no longer display the light assisted ring-opening/ring-closing reaction that leads to permanent shutting “off” of photochromism of the molecule.

3.3.1. Detection methods for hydrazine

Hydrazine is an extensively used synthetic intermediate in the production of important pharmaceutical drugs like nifuroxazide, hydralazine, isoniazid, etc. Salts of hydrazine, like

hydrazine sulphate, have been employed for the treatment of tuberculosis, sickle cell anaemia, etc.[142] Reports also suggest that hydrazine is the main by-product of the hydrolytic degradation of the anti-tuberculosis drug, isoniazid (Scheme 3.1).[143] It is also known to occur naturally as a by-product of the metabolism of yeasts and bacteria.[144]

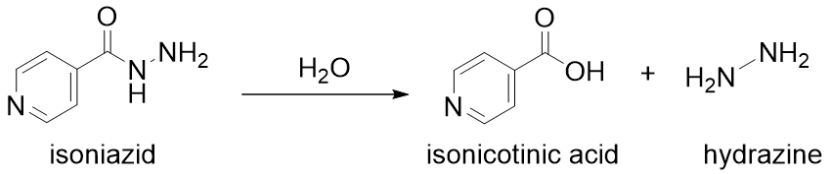

isoniazid isonicotinic acid hydrazine

Scheme 3.1: Hydrolytic degradation of anti-tuberculosis drug, isoniazid to generate hydrazine[143]

In 2017, residual rocket fuel-based debris containing unsymmetrical dimethylhydrazine (UDMH) launched by Russia for the European Space Agency led to international concerns over its significant environmental and health impact in arctic Canada.[145]

Despite being a relevant chemical for applications in a variety of fields, hydrazine is considered a genotoxic impurity (GI) that requires safe levels of use as active ingredients for pharmaceutical drugs.[142] Humans can be exposed to this toxic substance by inhaling the vapours or ingesting contaminated water.[135] Hydrazine and its derivatives decompose and metabolize to produce reactive intermediates that can form methyl adducts with DNA bases that can lead to DNA damage and gene mutations.[146,147] Chronic exposure to hydrazine can lead to symptoms like irritation of eyes, nose, and throat, dizziness and nausea among others, while, acute exposure can also lead to severe damage to the liver, kidneys and central nervous system.[140] All these severe effects have led the US Environmental Protection Agency (EPA) to suggest its threshold limit value to be low, ~0.01 ppm.[141] The increase in supply and demand of hydrazine has necessitated the need for the development of highly sensitive and selective methods to detect hydrazine.

Some of the early methods to detect hydrazine have involved electrochemical techniques such as potentiometry, ion-selective electrodes, capillary electrophoresis. Stetter *et al.* had successfully demonstrated the use of a gold-catalyzed Teflon-bonded diffusion electrode to detect hydrazine and methylhydrazine via electrooxidation on gold at all potentials in the range of detection.[148] Liu *et al.* were able to simultaneously detect hydrazine, methylhydrazine, and isoniazid by designing a palladium particle-modified carbon fibre microdisk array electrode that had excellent stability and displayed high catalytic activity

towards hydrazine and its derivatives. The developed electrode was employed in end-column capillary electrophoresis electrochemical detection.[149] Batchelor-McAuley *et al.* compared a random distribution of palladium nanoparticles supported on a boron-doped diamond (BDD) electrode and a palladium plated BDD microelectrode array as sensing platforms for detecting hydrazine via electrocatalytic oxidation occurring on the palladium centres (Figure 3.1).[150]

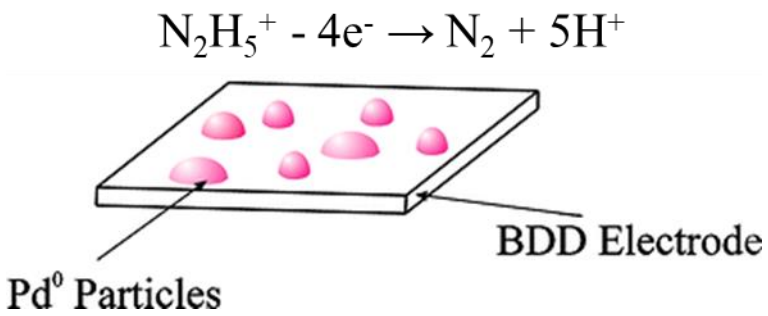

Figure 3.1: Schematic representation of Pd nanoparticle supported BBD electrode. Reproduced with permission from ref. 150 © 2005 Royal Society of Chemistry [150]

Nanostructures based on ZnO have also been fabricated as electrodes that are capable of detecting hydrazine by electrochemical detection.[151,152] While these techniques would enable cost-effective, quick detection methodologies, their fabrication process is tedious and requires the electroactive material to be fastened onto glassy carbon or precious metal (Au, Ag, Pt, Pd and Rh) electrodes that are immobilized using Nafion.[152] Also, the electrodes suffer from large overpotentials in presence of hydrazines, limiting amperometric detection methods.[149] The chemically modified electrodes undergo desorption of mediators from the electrode substrates that compromises the long-term stability of such electrodes and need to be regenerated for a reproducible response.[150,152]

Therefore, the multitude of detection techniques based on chromatography (gas chromatography, high-performance liquid chromatography, ion chromatography) have evolved as an alternative.[142,153] Most of these techniques are employed by pharmaceutical companies and involve chemical derivatization of hydrazine and methylated hydrazines as the molecules by themselves are low molecular weight, volatile, and highly polar, making direct analysis complex.[142] Sun *et al.* have devised an *in-situ* derivatization-headspace GC-MS technique for determining hydrazine content in various drug formulations. The general method of detection requires the reaction of acetone, acting as

a derivatizing agent, with hydrazine and detection of the reaction product acetone azine by headspace GC-MS (Scheme 3.2).[154]

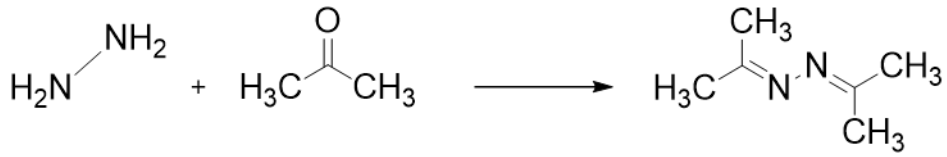

Scheme 3.2: An example of derivatization reaction of hydrazine using acetone to give acetone azine[154]

Fundamental problems associated with most of these methods are those of sophisticated equipment (such as columns with specific internal diameters, the specific particle size of the stationary phase)[155] and experiment design (such as nature of the analyte, the selectivity of sorbents), long processing times and greater equipment costs among others. All these issues limit their extensive use in public places.

In contrast, an optical read-out signal, both colour change, and change in emission offer to be cost-effective and more convenient. Conventionally, small molecule-based fluorescent probes detect hydrazine via a “turn-on” or “turn-off” mechanism which is caused by a chemical reaction.[156] The sensing mechanisms involved mostly include:

1. Photo-induced electron transfer (PET)
2. Internal charge transfer (ICT)
3. Excited-state intramolecular proton transfer (ESIPT)
4. Forster resonance energy transfer (FRET)
5. Aggregation-induced emission (AIE)
6. C=N isomerization

Most of these detection mechanisms utilize the strong nucleophilic character of hydrazine, which, upon reaction with the detecting species, gives the desired response. General detection strategies for fluorescence-based sensors for hydrazine can be divided into the following categories:[136]

1. deprotection of the fluorophore by hydrazine that triggers changes in fluorescence properties
2. the reaction of β-diketo group-functionalized fluorophores with hydrazine to generate pyrazole heterocycles that have a different fluorescent response

3. dicyano- or monocyanovinyl groups on fluorophores can specifically react with hydrazine to form hydrazones which alter the optical readout

The most extensively used strategy to develop fluorescent probes for detection of hydrazine involves the protection of the fluorophore with a leaving group like acetyl, phthalimide, 4-bromobutylryl, levulinate, etc. which can be cleaved readily upon reaction with hydrazine leading to variation in the fluorescent response of the fluorophore (Scheme 3.3).[157,158]

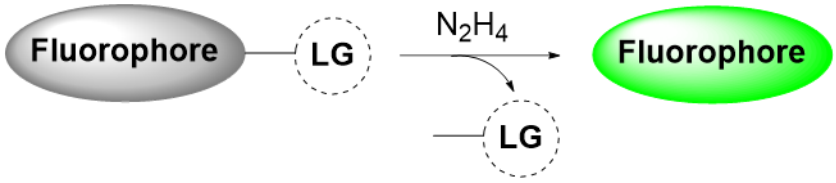

Scheme 3.3: Common deprotection of a fluorescent probe with a leaving group (LG) attached upon reaction with hydrazine leading to enhanced fluorescence

Jin *et al.* synthesized a fluorescent flavone dye which is functionalized with a bromoester leaving group. The reaction with hydrazine leads to the elimination of the bromoester group thereby turning the ESIPT emission “on”. Also, they were able to demonstrate the use of this probe to visualize hydrazine in living cells (Figure 3.2).[159]

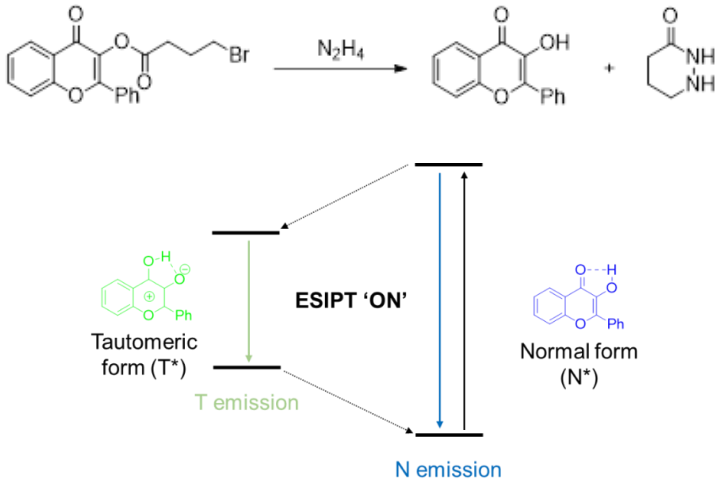

Figure 3.2: Hydrazine induced deprotection of a bromoester functionalized flavone dye to turn on ESIPT emission[159]

Cui *et al.* have designed a unique tri-output optical probe (colourimetric, ratiometric, and chemiluminometric) for the detection of hydrazine. The structure of the probe (CF) is based on an amino coumarin (AMC) that is protected by a phthalic anhydride group. When

the probe reacts with hydrazine, it generates the amino coumarin which has a high fluorescence quantum yield and luminol which displays chemiluminescence (Figure 3.3).[134]

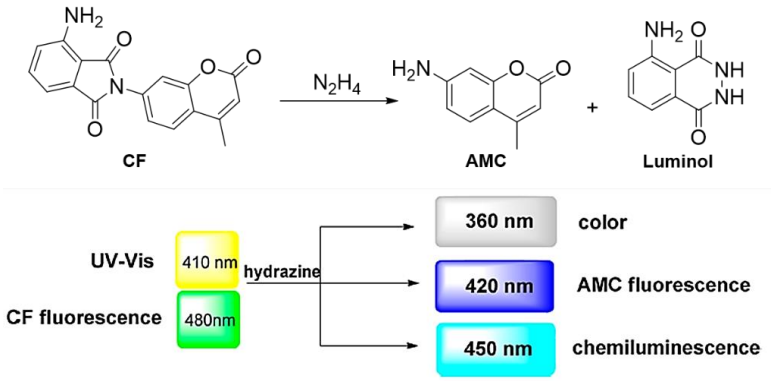

Figure 3.3: Schematic representation of the design of the probe that has a tri-output optical response upon reaction with hydrazine. Reproduced with permission from ref. 134 © 2014 American Chemical Society [134]

Numerous research groups have utilized the specific reaction occurring between hydrazine and dicyano- or monocyanovinyl groups to yield hydrazones. Incorporating these functional groups onto fluorescent dye molecules resulted in either enhanced fluorescent response or ratiometric fluorescent response (Figure 3.4).[160,161,162, 163]

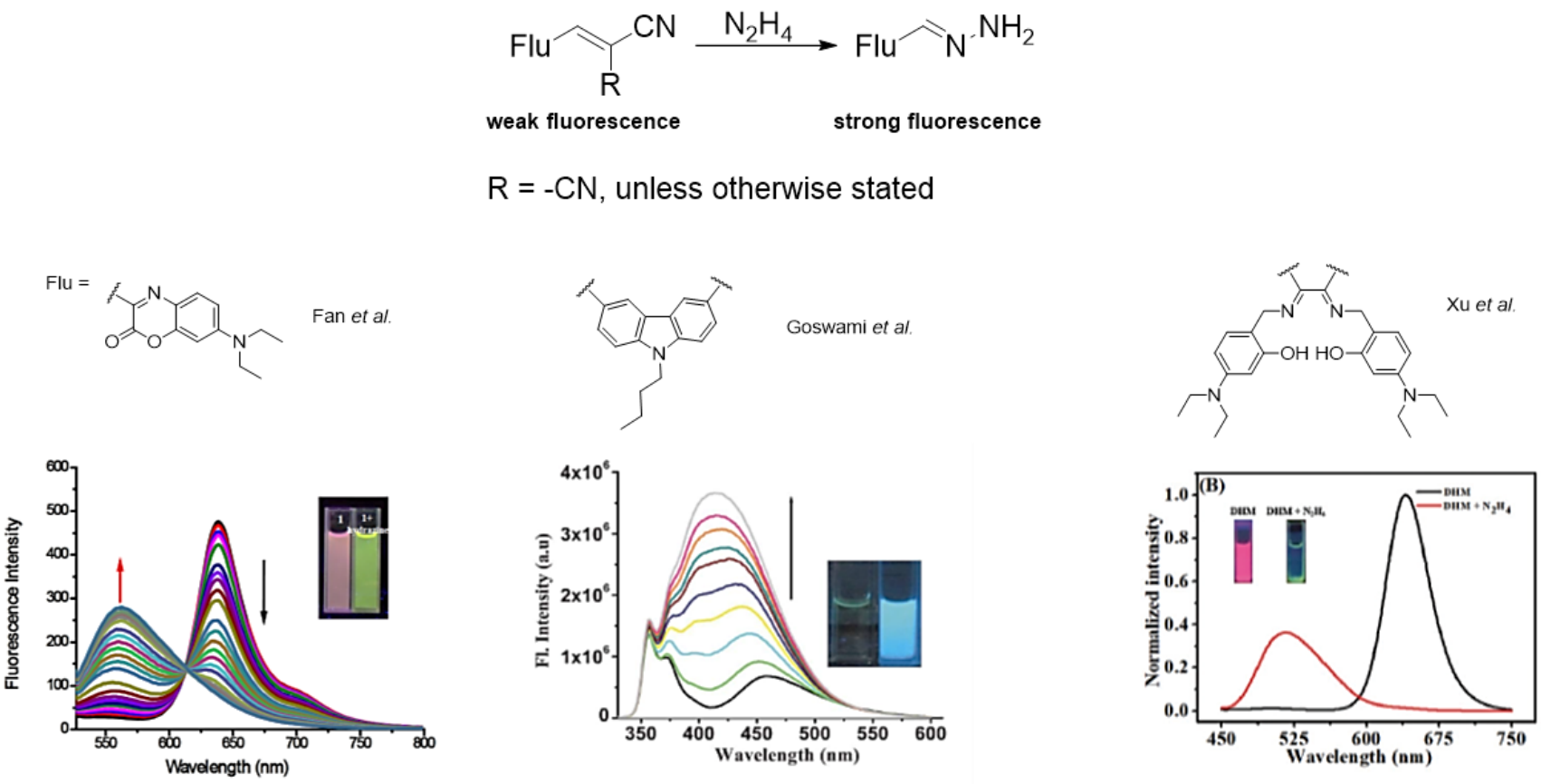

Figure 3.4: General reaction of dicyano- and monocyanovinyl groups with hydrazine along with some examples. Reproduced with permission from ref. 161 © 2012 Royal Society of Chemistry, 162 © 2013 Royal Society of Chemistry, 163 © 2018 Royal Society of Chemistry [161, 162, 163]

The reaction of β-diketo-substituted fluorescent molecules with hydrazine to generate pyrazole rings have also been employed by some research groups to develop chemodosimetric probes for the detection of hydrazine (Figure 3.5).[164,165]

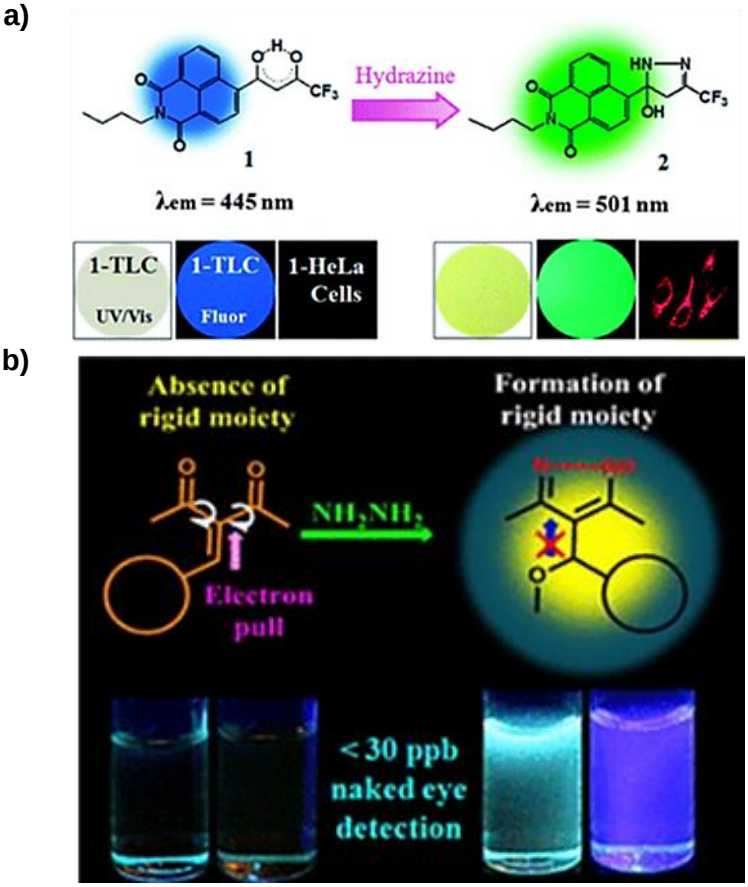

Figure 3.5: a) Naphthalimide trifluoroacetyl acetonate based probe for hydrazine detection. Reproduced with permission from ref. 164 © 2013 Royal Society of Chemistry [164]; b) Conjugated 1,3-diketo probes for sub-ppm detection of hydrazine. Reproduced with permission from ref. 165 © 2017 American Chemical Society [165]

Swager *et al.* have successfully synthesized fluorescent polymers based on poly(phenylene ethylene) backbone that displayed an enhancement in fluorescence upon exposure to hydrazine (Figure 3.6 a)).[166] Nandi *et al.* have formulated a unique modified merocyanine dye that becomes colourless upon reaction with hydrazine (Figure 3.6 b)).[167]

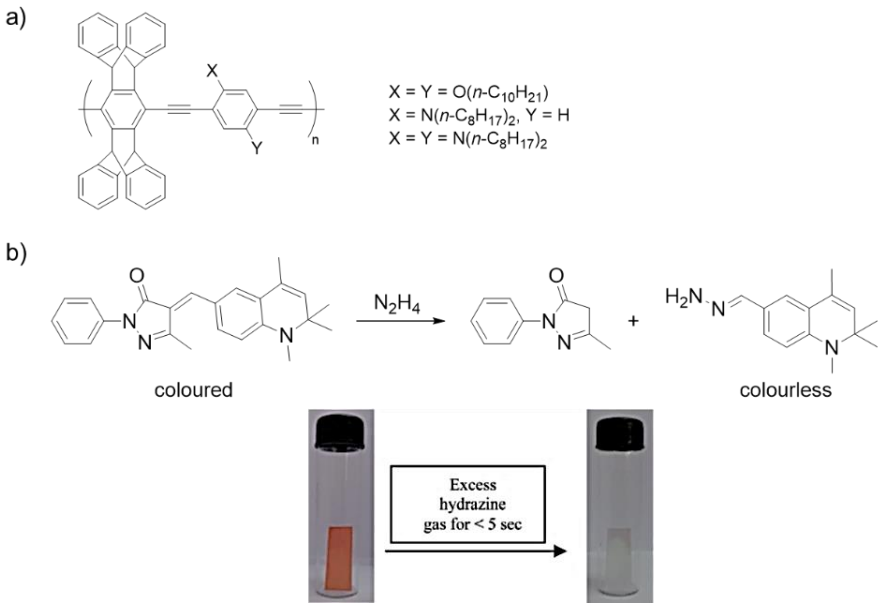

Figure 3.6: a) Structure of poly(phenylene ethylene) based polymers used to detect hydrazine[166]; b) Reaction of hydrazine with modified merocyanine dye. Reproduced with permission from ref. 167 © 2014 Royal Society of Chemistry [167]

While fluorescence-based methods are highly sensitive (detection limits ranging from 1 to 10 ppb), a response based on a change in the colour of material can be more suitable for primary visual detection that can be easily recognized. A detection method that can combine both these techniques would be simple and sensitive concurrently.[168] Recently, Liu *et al.* have designed such a dual-responsive system based on a nonaromatic fluorophore that goes from red to colourless in the presence of hydrazine along with a change in fluorescence.[169] Such material can easily be used as a surface coating and would not require any additional electronic controls.

3.3.2. Our system

The molecular design chosen was inspired by the specific reaction of the nitrile groups with hydrazine combined with the photoresponsive behaviour of dithienylethenes (DTEs).[162,170] Our system contains a disubstituted alkene connecting two nitrile groups and two thiophene heterocycles (Scheme 3.4). Like all dithienylethenes, compound **1*o*** possesses a photoreactive hexatriene that undergoes a ring-closing reaction when exposed to UV light and produces its isomer **1*c*** which is coloured.[42] Apart from the colour change, the photoisomerization process also causes changes in the electronic structure

of the molecule that can, in turn, influence the luminescence/fluorescence of **1*o*** and **1*c***.[171] Unlike most DTE molecules, which are non-fluorescent in both ring-open and ring-closed isomers, compound **1*o***, was expected to be fluorescent due to a localized donor-acceptor intramolecular charge transfer from electron-rich thiophenes to strongly electron-poor nitrile groups.[172,173] On the other hand, ring-closed isomer **1*c***, which is generated upon irradiation with UV light, has π-electrons delocalized over the entire molecule and was predicted to be non-fluorescent.[174,175]

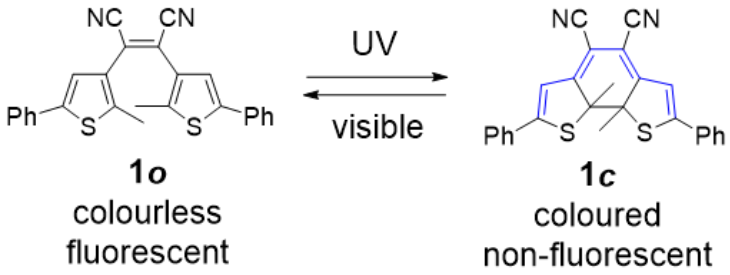

Scheme 3.4: Colourless ring-open form of dithienylethene **1*o*** is fluorescent which upon exposure to UV light isomerizes into coloured ring-closed form **1*c***, which now becomes non-fluorescent

It was anticipated that the molecular probe **1*o*** would act as a two-output optical probe (fluorescence, colourimetric) for sensing hydrazine in both the solution and vapour phase (Scheme 3.5). The reaction of ring-open isomer, **1*o***, with hydrazine would generate a cyclic product, **2*o***, along with a change in its fluorescence output. The compound **1*o***, upon irradiation with UV light, isomerizes to generate its ring-closed isomer, **1*c***, which can also react with hydrazine to generate the cyclic product ***2*o**, with a double output signal consisting of a change in both the colour and fluorescence of the solution. This **2*o*** is missing the desired 1,3,5-hexatriene system that is responsible for the ring-opening/ring-closing reaction via rearrangement of the π system. The photochromic behaviour of the system is, thus, completely shut “off” and the luminescent response is altered after reaction with hydrazine.[176]

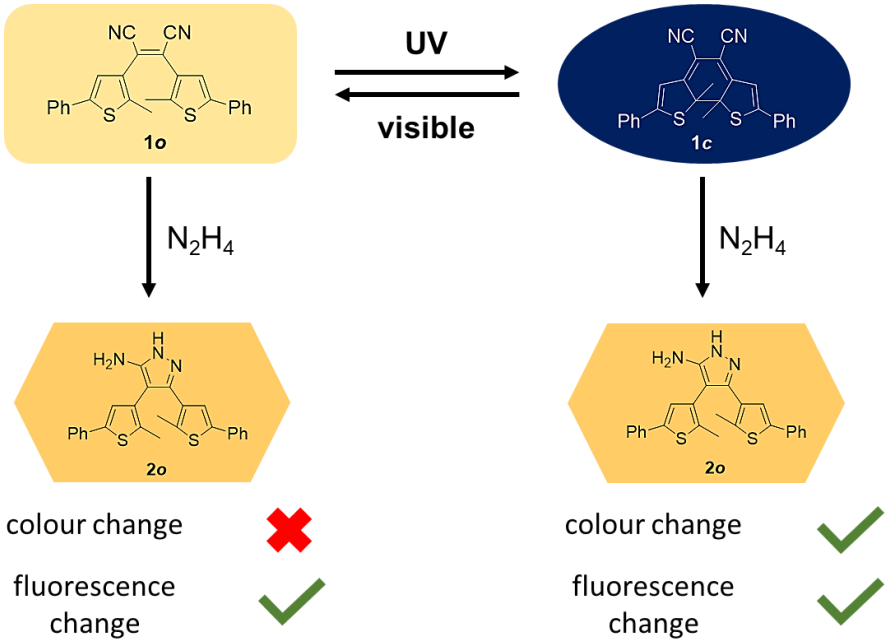

Scheme 3.5: Proposed triple sensing mechanism of **1*o*** and **1*c*** upon reaction with hydrazine leading to a non-photoresponsive product **2*o*** (Ph = phenyl)

One of the main advantages of our system lies in the photoresponsive nature of our probe molecule **1*o***, which can reversibly change its recognition form to **1*c*** upon interacting with UV light. This leads to multiple output signals upon reaction with the target analyte, hydrazine, thereby, providing greater sensing information for the analysis.

3.4. Results and Discussion

3.4.1. Synthesis

The photoresponsive dithienylethene (**1*o***) was synthesized in seven steps from commercially available 2-methylthiophene as described in Section **2.5.1** of *Chapter 2* (Scheme 3.6).[95] Experimental details and characterizations of all compounds are provided in Section **2.7**.

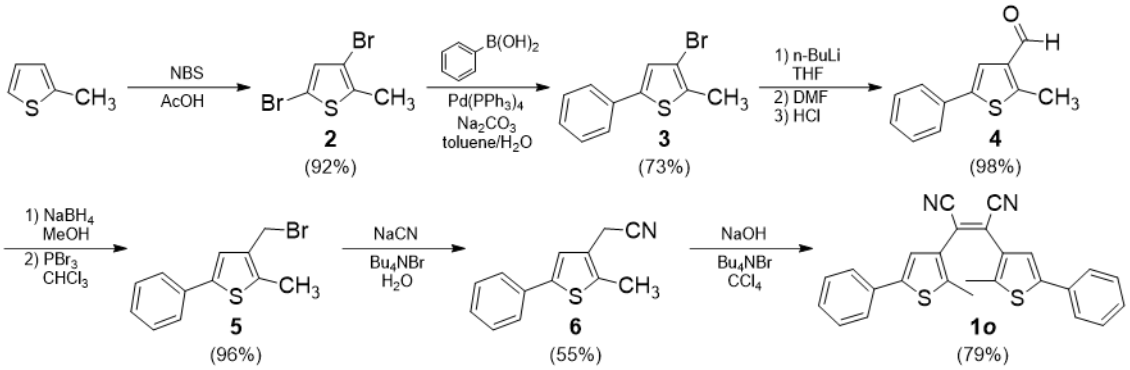

Scheme 3.6: Synthesis of photoresponsive dithienylethene (**1*o***)[39,40]

The photochemical synthesis of the ring-closed isomer (**1*c***) was carried out by irradiating a chloroform solution of **1*o*** with 312 nm UV light and was obtained in modest yield as described in Section **3.7** (Scheme 3.7).

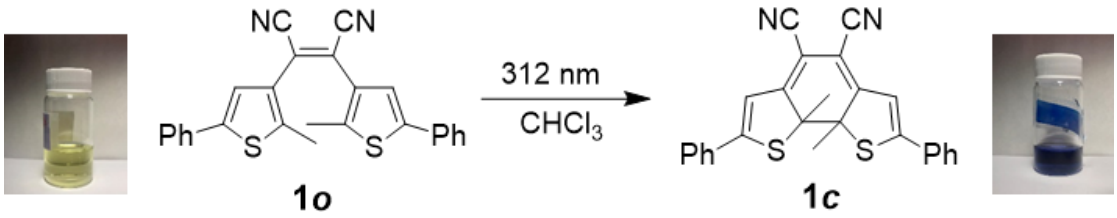

Scheme 3.7: Photochemical synthesis of the ring-closed isomer (**1*c***)

3.4.2. Structure prediction of the cyclic product upon reaction with hydrazine

The cyclic product obtained after the reaction of **1*c*** or **1*o*** with hydrazine can exist as two tautomers, **2*o*** and **3*o***, that can further exist as parallel and anti-parallel conformations (Scheme 3.8).

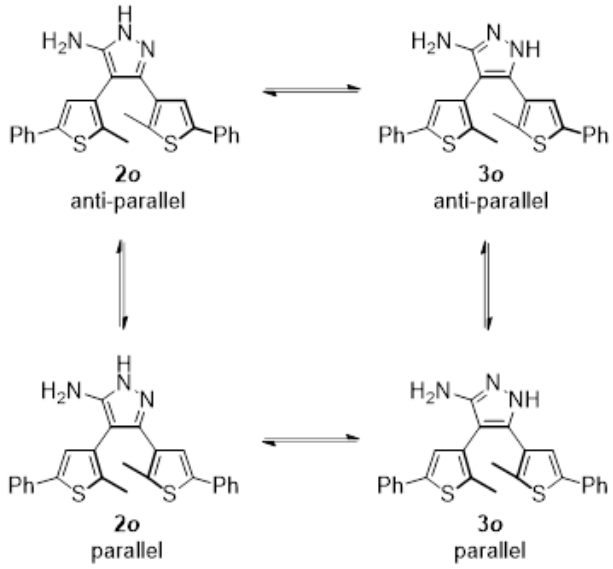

Scheme 3.8: Possible structures of the cyclic product obtained upon the reaction of hydrazine with **1*c*** or **1*o***

Theoretical calculations were carried out for the total energy of parallel and anti-parallel forms of the product, **2*o,*** and **3*o***, to determine the correct possible structure and its conformation, relative stability, and predominance of either of the isomers. The theoretical value for the relative energy between the parallel and anti-parallel isomers of **2*o*** and **3*o*** was determined using the computational method based on density functional theory (DFT) to analyze the electronic or nuclear structure of the molecule in its ground state.[177] The method utilizing B3LYP as the hybrid functional and 6-31G (d) basis set to calculate all the relative energy values was developed in Gaussian 09 software.[177,178,179,180] Hybrid functional and the basis set used for present calculations have been traditionally reported in the literature for energy calculations in a similar class of molecules.[181] The energy values were obtained in atomic units, a.u. (1 a.u. = 1 Hartree = 2625.4996 kJ/mol).[182] Based on the results of energy calculations, the anti-parallel conformers for both **2*o*** and **3*o*** were found to have lower energies than their corresponding parallel conformers (Figure 3.7). The difference in energy between parallel and anti-parallel conformers of **3*o*** is quite

low suggesting that both forms can exist in equal proportions in the solution, as can been seen for most DTE systems. While an unusually high energy difference was determined between the parallel and anti-parallel conformers of ***2o*** suggesting that ***2o*** would most likely exist in anti-parallel conformation exclusively. Furthermore, the energy difference between the optimized geometries of ***2o*** (anti-parallel) and ***3o*** (anti-parallel) was estimated to be 14.703 kJ/mol. The calculated energy barrier between ***2o*** and ***3o*** suggests that isomer ***2o*** has slightly lower energy, but, the difference is fairly low such that the two forms may coexist in a dynamic equilibrium in the same medium.[183,184] The greater stability of ***2o*** can be attributed to the presence of electron-donating -NH_2 group at C-5 position whose lone-pair of electrons are incorporated in the plane perpendicular to the pyrazole ring leading to significant changes in the π-electron distribution in the top 5-amino pyrazole ring.[184,185,186] The lack of photochromic behaviour of the reaction product further verify the structure of the product to be ***2o***.[176]

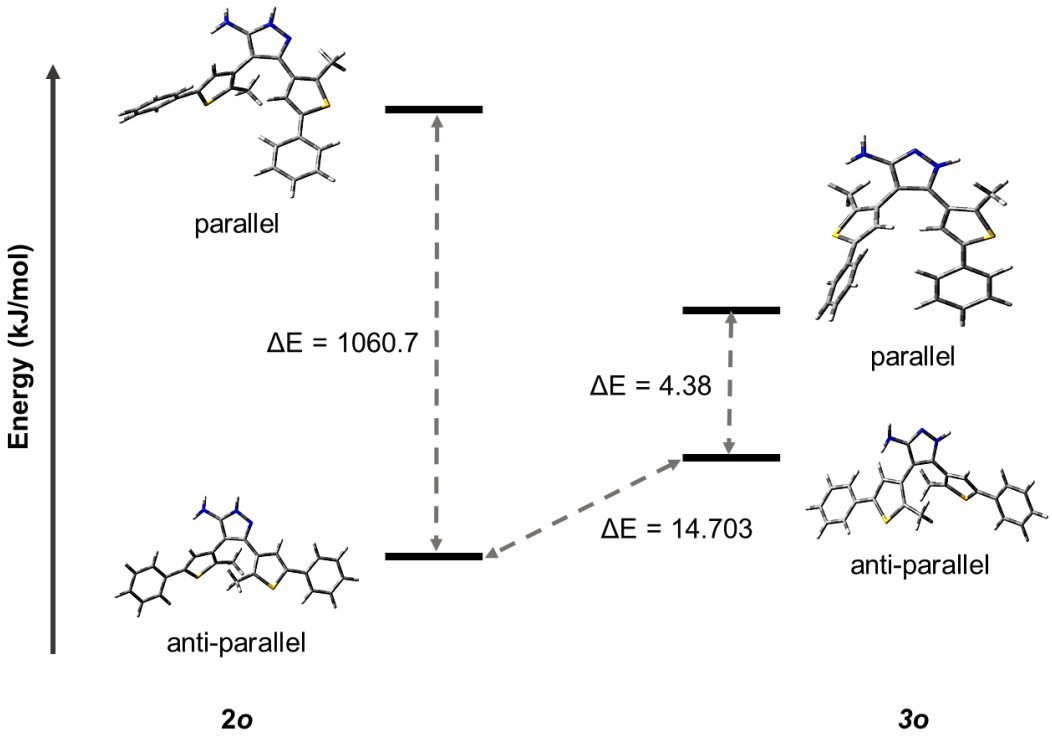

Figure 3.7: Energy diagram of calculated total energies for both isomers of the product along with the optimized geometries in both parallel and anti-parallel conformations (blue: nitrogen, yellow: sulfur, white: hydrogen, grey: carbon)

3.4.3. Detection of hydrazine in solution

3.4.3.1. Reaction with ring-closed isomer 1*c*

The reaction of hydrazine with ring-closed isomer **1*c*** was assessed by incremental addition of hydrazine monohydrate ($N_2H_4.H_2O$) to a 4.80 x 10^{-5} M solution of **1*c*** in DMSO (Scheme 3.9).

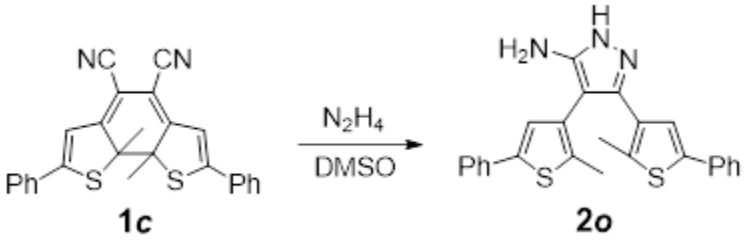

Scheme 3.9: Reaction of ring-closed isomer **1*c*** with hydrazine (Ph = phenyl)

The reaction progress was evaluated using UV-visible absorption spectroscopy (Figure 3.8) and fluorescence spectroscopy (Figure 3.9). After acquiring an initial spectrum of 0.7 mL solution of **1*c***, hydrazine monohydrate ($N_2H_4.H_2O$) was added in increments of 0.50 x 10^{-3} mL (0.01 M N_2H_4 in each increment) for a total added volume of 4.00 x 10^{-3} mL (0.083 M of total added N_2H_4) with spectra being acquired after each addition. After the addition of 0.50 x 10^{-3} mL of hydrazine monohydrate, the broad band at 580 nm for **1*c*** began to decrease in intensity (Figure 3.8 a)). A new band was also observed at 260 nm which continues to increase in intensity with the addition of hydrazine monohydrate. The band at 580 nm disappears completely after the addition of 4.00 x 10^{-3} mL (0.083 M of total added N_2H_4) of hydrazine monohydrate (Figure 3.8 a)). Observance of the band at 260 nm is considered to be the general region of absorbance for pyrazoles.[187,188] The decrease in absorbance at 580 nm and the increase in the absorbance at 260 nm are symmetric indicating that **1*c*** reacts with hydrazine to give **2*o*** without any other side reactions and the rates of both reactant disappearance and product formation are the same (Figure 3.8 b)).

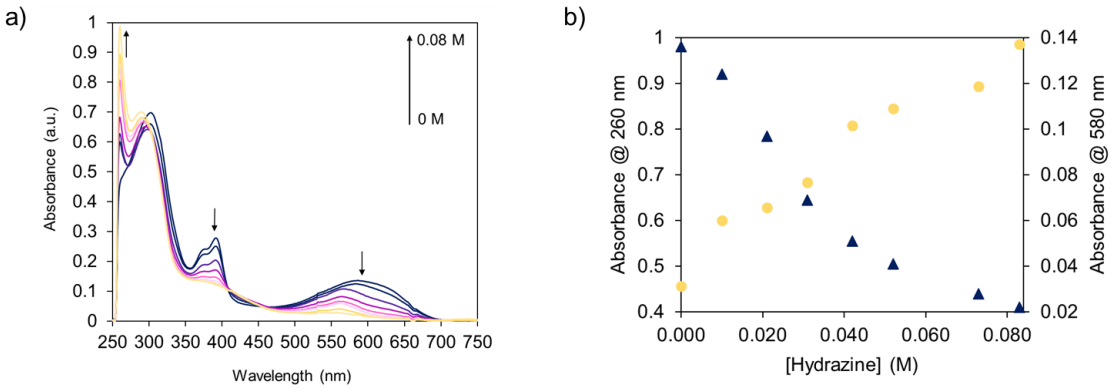

Figure 3.8: a) Changes in UV-vis absorption spectrum of a solution of **1*c*** (4.80×10^{-5} M) in DMSO upon addition of hydrazine monohydrate in 0.50×10^{-3} mL increments; b) Modulated absorption at 260 nm for **2*o*** and 580 nm for **1*c*** during the addition of hydrazine monohydrate

Similar results were observed when the reaction progress was assessed by fluorescence spectroscopy. Upon acquiring an initial emission spectrum for 2 mL solution of **1*c*** at an excitation wavelength of 365 nm, hydrazine monohydrate ($N_2H_4.H_2O$) was added in increments of 1.00×10^{-3} mL (0.01 M N_2H_4 in each increment) for a total added volume of 6.00×10^{-3} mL (0.052 M of total added N_2H_4) with spectra being acquired after each addition. Following the addition of 1.00×10^{-3} mL of hydrazine monohydrate, a broad band at 490 nm appeared and gradually began to increase in intensity with increasing hydrazine concentration (Figure 3.9 a)). A maximum in the intensity was observed upon the addition of 5.00×10^{-3} mL hydrazine monohydrate after which the intensity began to decrease (Figure 3.9 b)). Correspondingly, the solution began to decolourize from blue to golden-yellow (Figure 3.9 c)) and display a bright blue-white fluorescence emission upon the addition of hydrazine monohydrate (Figure 3.9 d)). This increase in fluorescence response of **2*o*** at 490 nm is typical of such substituted pyrazoles.[189]

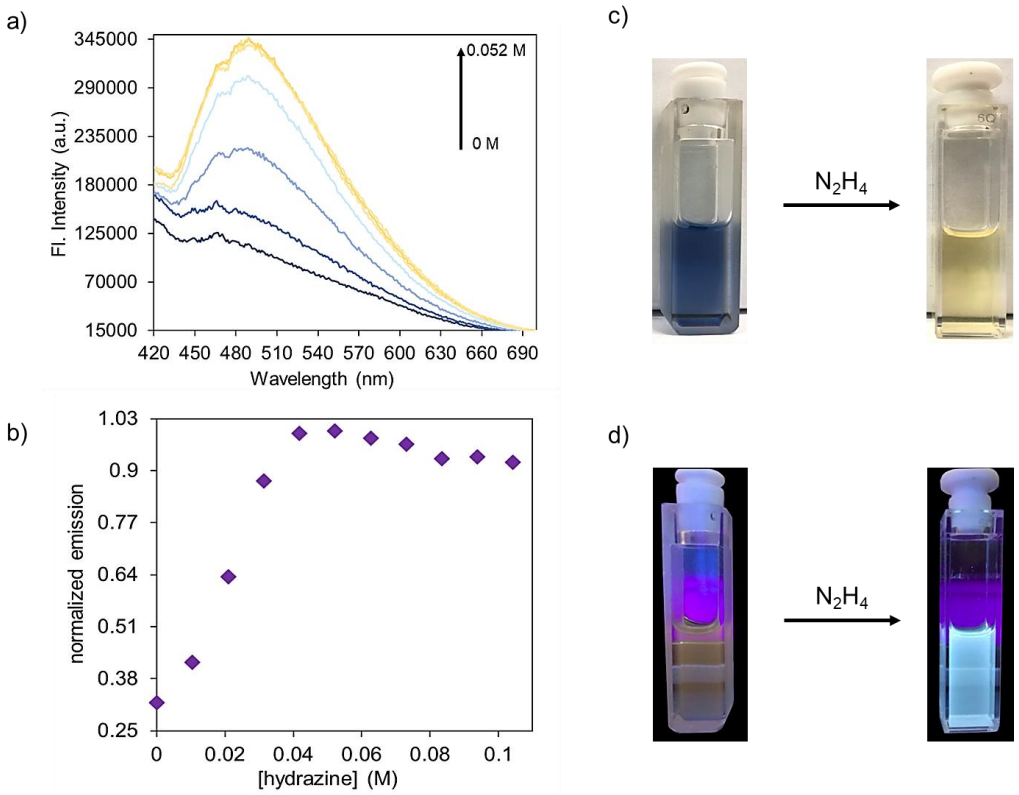

Figure 3.9: a) Changes in the fluorescence emission of a solution of **1*c*** (4.80 x 10^{-5} M) in DMSO upon addition of hydrazine monohydrate in 1.00 x 10^{-3} mL increments; b) Normalized fluorescence emission at 490 nm for **2*o*** upon addition of hydrazine monohydrate; c) Turning 'off' of photochromism after addition of hydrazine monohydrate; d) turning 'on' of bright blue-green fluorescence emission after addition of hydrazine monohydrate

The changes in the optical response of the ring-closed isomer **1*c*** and the reaction product **2*o*** were further analyzed theoretically using the density functional theory (DFT) (Figure 3.10). The method utilizing B3LYP as the hybrid functional and 6-31G (d) basis set to calculate all the relative energy values was developed in Gaussian 09 software.[190,178,179,180] The energy values were obtained in atomic units, a.u. (1 a.u. = 1 Hartree = 27.2114 eV).[182] The energy gap between the HOMO and LUMO of **1*c*** was calculated to be 2.46 eV (504 nm) with the electron distribution delocalized over the entire DTE backbone. In contrast, the HOMO and LUMO for the product **2*o*** were localized over the two thiophene rings and the resultant energy gap was calculated to be 4.19 eV (295 nm). This significantly high value of energy gap for **2*o*** directly corresponds to the observation of a significant blue-shift in the absorbance of the product.

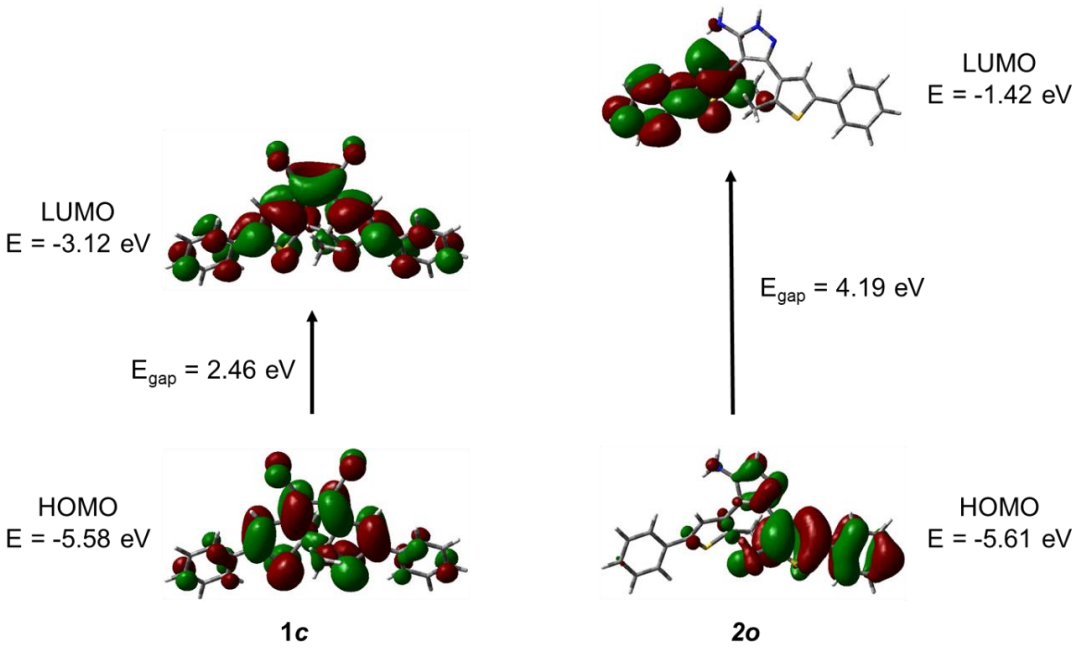

Figure 3.10: Interfacial plots of HOMO and LUMO energy levels for probe **1*c*** and **2*o*** and their corresponding energy gaps

The solution colour also changed from blue to pale yellow/colourless upon the addition of 5.00 x 10^{-3} mL (0.104 M of total added N_2H_4) of hydrazine monohydrate to a 2.40 x 10^{-4} M solution of **1*c*** (Figure 3.11).[176] The corresponding visual detection limit for **1*c*** was estimated to be 3 x 10^3 ppm.

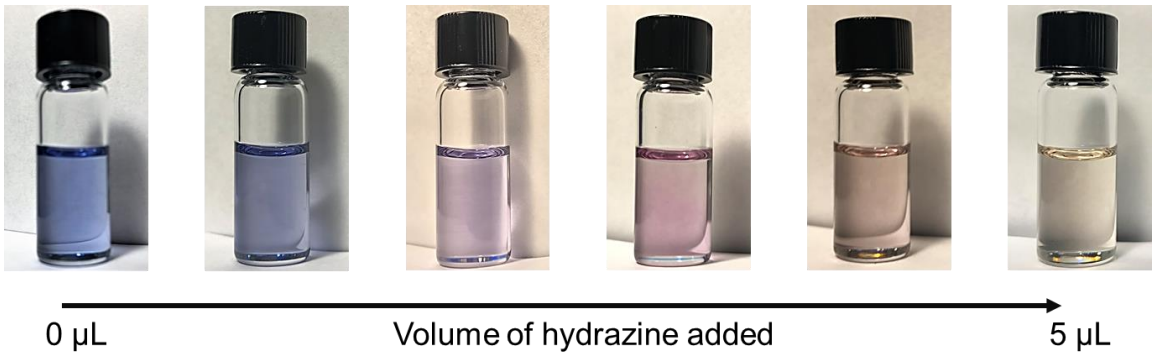

Figure 3.11: Change in colour of the solution of **1*c*** (2.40 x 10^{-4} M) in DMSO upon addition of hydrazine monohydrate in increments on 1.00 x 10^{-3} mL for a total of 5.00 x 10^{-3} mL (0.104 M of total added N_2H_4)

The reaction of hydrazine with tetracyanoethylene and other substituted cyanoethylenes has been used to synthesize pyrazoles.[170,187,191] The general mechanism involves the attack of hydrazine and replace a nitrile group which then cyclizes to give the product

pyrazole.[170,187] We expected similar results when hydrazine reacted with ring-closed isomer **1*c***. Ring-opening reaction/cycloreversion is an extremely facile process[42] and the highly reactive character of hydrazine can quickly ring-open **1*c*** followed by the reaction to yield **2*o*** (Scheme 3.10). The by-product generated from this reaction, HCN, can be trapped using solid adsorbents with small pore sizes such as molecular sieves[192], activated charcoal[193], and micro-fibreglass filters[194].

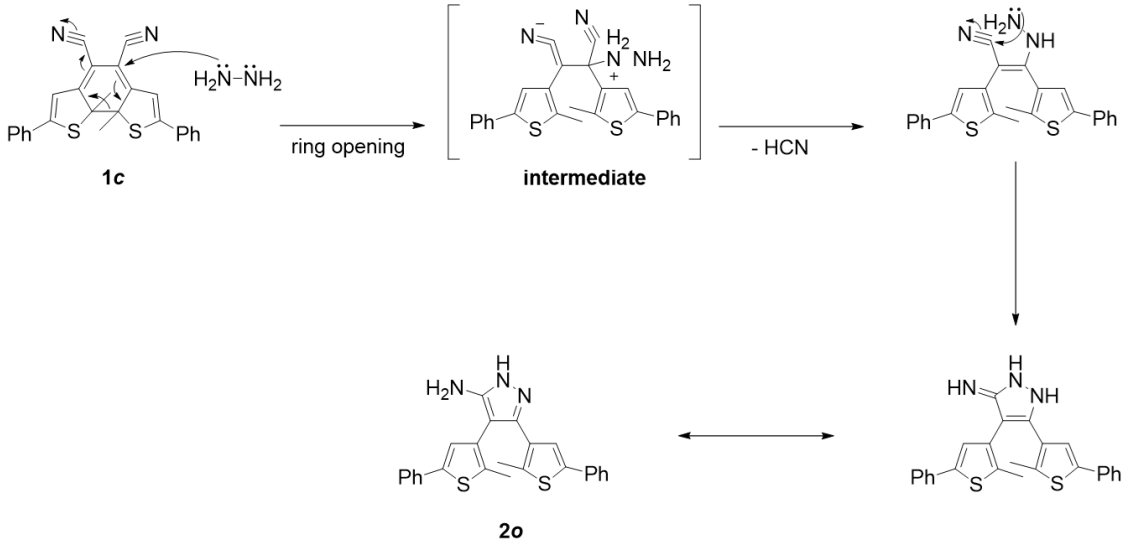

Scheme 3.10: Proposed mechanism of ring opening of **1*c*** upon reaction with hydrazine (Ph = phenyl)

The formation of **2*o*** was confirmed experimentally by ^{1}H- & ^{13}C-NMR spectroscopy and FT-IR spectroscopy. Upon comparison of the FT-IR spectra of the reactant, **1*c*** and the product, **2*o***, the band corresponding to C≡N stretching at $\bar{\upsilon}$ = 2210 cm^{-1} in **1*c*** disappears and a new set of bands for N-H stretching for primary and secondary amine in the region $\bar{\upsilon}$ = 3319-3076 cm^{-1}, N-H bending at $\bar{\upsilon}$ = 1625 cm^{-1}, C-N stretching at $\bar{\upsilon}$ = 1160 cm^{-1} for the product, **2*o*** (Figure 3.12).[195] In the case of ^{1}H-NMR spectroscopy, the peak for thiophene protons of **1*c*** shifted downfield from δ = 6.72 ppm to δ = 7.10 ppm for **2*o*** suggesting the restoration of aromaticity of the thiophene π-system by the opening of the 1,3,5-hexatriene system after reaction with hydrazine. Furthermore, ^{13}C-NMR results show the disappearance of the peak at δ = 115.62 ppm corresponding to the carbon atoms of -CN groups and appearance of peaks at δ = 117.81 ppm for the bridging carbons of central pyrazole ring and δ = 153.24 ppm for carbon atom connected to the NH_2 group.

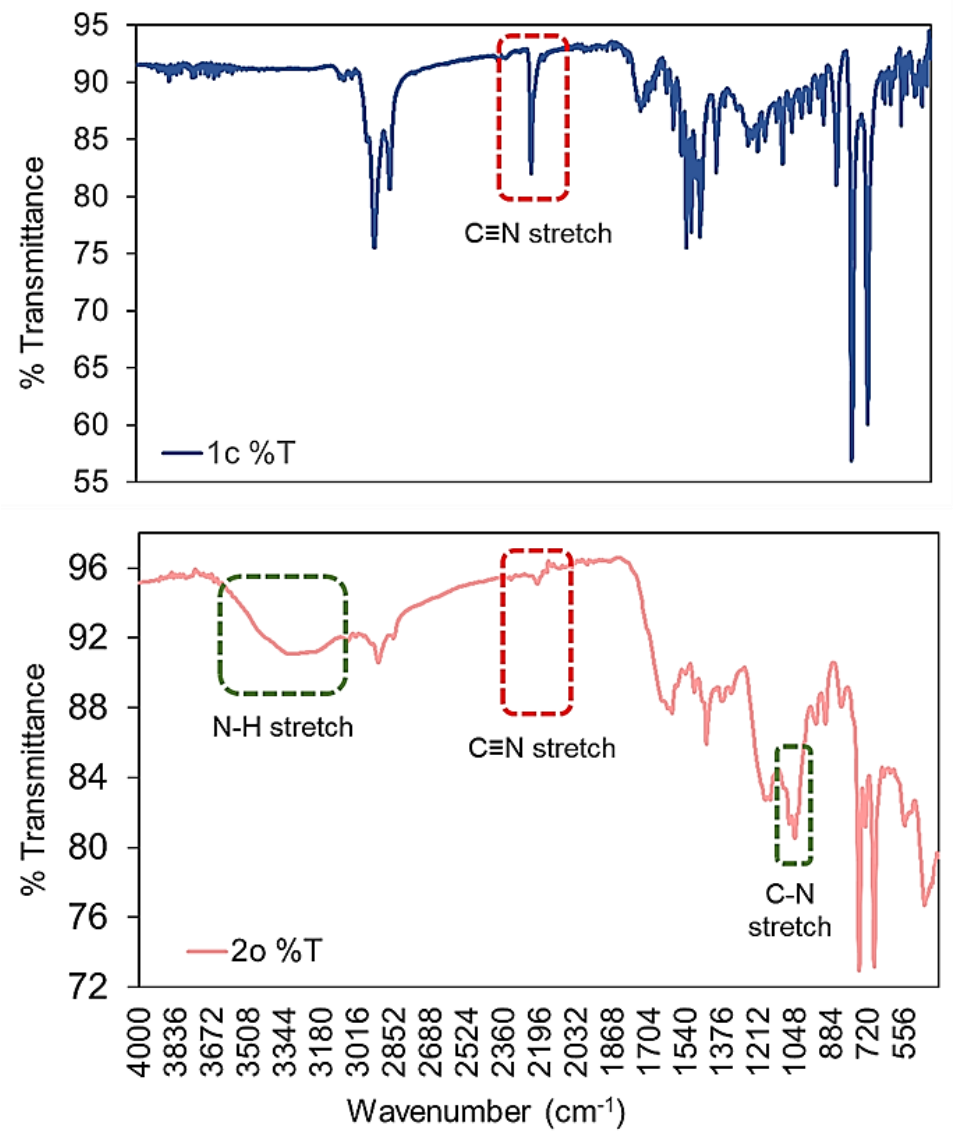

Figure 3.12: FT-IR spectra of **1*c*** and **2*o***

The rate constant for the reaction of **1*c*** with hydrazine monohydrate was evaluated by UV-visible absorption spectroscopy by monitoring the disappearance of **1*c*** after the addition of 4.00 x 10^{-3} mL of hydrazine monohydrate (0.08 M of total added N_2H_4) over 400 seconds. A 4.80 x 10^{-5} M solution of **1*c*** in DMSO was charged with 4.00 x 10^{-3} mL of hydrazine monohydrate (0.08 M of total added N_2H_4) in a sealed cuvette. After acquiring an immediate UV-visible absorption spectrum of the initial mixture, the cuvette was kept at room temperature in dark for 400 seconds, with spectra being recorded every 20 seconds. The decrease in the intensity of the band centred at 580 nm for **1*c*** was measured over the entire course of the reaction (Figure 3.13 a)).

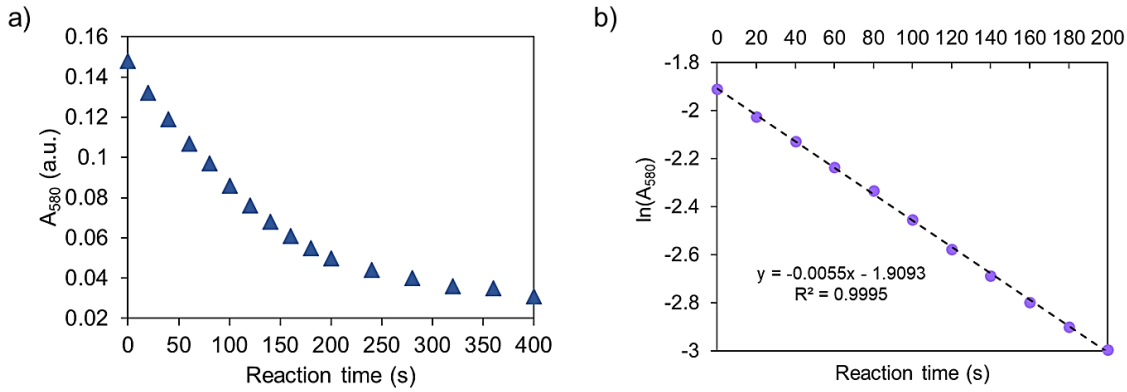

Figure 3.13: a) Decrease in the absorbance value at 580 nm for **1*c*** after addition of hydrazine monohydrate (0.08 M of total added N_2H_4) over the reaction period of 400 s; b) Reaction kinetics of the solution of **1*c*** (4.80 x 10^{-5} M) in DMSO upon reaction with hydrazine monohydrate (0.08 M of total added N_2H_4)

The value of the rate constant, *k*, was determined with respect to the change in concentration of **1*c*** and was calculated using the initial slope method for the recorded data until the intensity of band in the visible region (580 nm) decreased ~ 60% to avoid errors due to higher signal/noise ratio at the end of the kinetic experiment.[196] The rate constant, *k*, was calculated to be 0.0055 s^{-1} using equation 3.1 considering the changes in absorbance band centred at 580 nm (Figure 3.13 b)).

$$ln[A]_t = -kt + ln[A]_0$$

Equation 3.1: First-order rate equation to determine the rate constant

The rate of formation of the product was determined by fluorescence spectroscopy by monitoring the increase in the fluorescence emission at 490 nm of **2*o*** after the addition of 6.00 x 10^{-3} mL (0.052 M of total added hydrazine) of hydrazine monohydrate over 1200 s. A 4.80 x 10^{-5} M solution of **1*c*** in DMSO was charged with 6.00 x 10^{-3} mL of hydrazine monohydrate (0.052 M of total added N_2H_4) in a sealed cuvette. After acquiring an immediate emission spectrum of the initial mixture, the cuvette was kept at room temperature in dark for 1200 seconds, with spectra being recorded every 60 seconds. The increase in the intensity of the band centred at 490 nm for **2*o*** was measured over the entire course of the reaction (Figure 3.14 a)). The rate constant, *k*, for the formation of the product was also calculated using equation 3.1 and was determined to be 0.00047 s^{-1} considering the increase in fluorescence emission of the band centred at 490 nm (Figure 3.14 b)). The lower value of the rate constant for product formation suggests that the

formation of the top pyrazole ring in product **2*o*** is slower as compared to the ring-opening of reactant **1*c***.

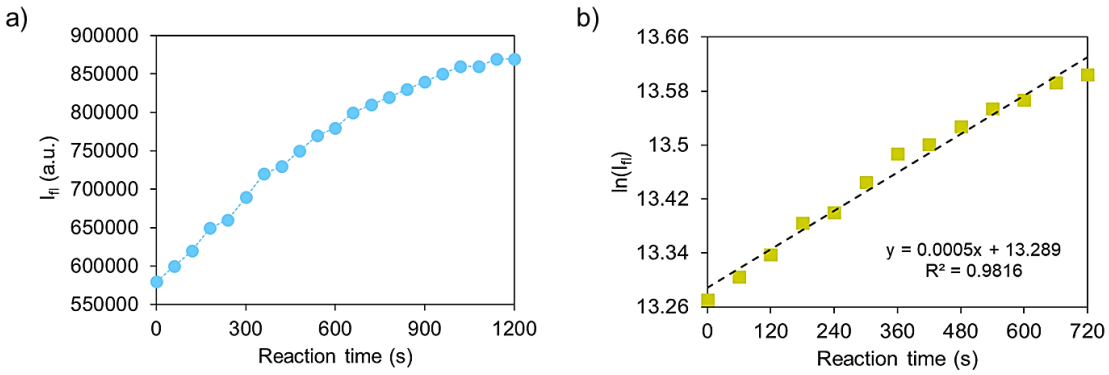

Figure 3.14: a) Increase in the fluorescence emission at 490 nm for **2*o*** after addition of hydrazine monohydrate (0.052 M of total added N_2H_4) over the reaction period of 1200 s; b) Reaction kinetics of the solution of **2*o*** in DMSO upon reaction with hydrazine monohydrate (0.052 M of total added N_2H_4)

3.4.3.2. Reaction with ring-open isomer 1*o*

The reaction of hydrazine with ring-open isomer **1*o*** was assessed by incremental addition of hydrazine monohydrate ($N_2H_4.H_2O$) to a 9.60 x 10^{-6} M solution of **1*o*** in DMSO (Scheme 3.11).

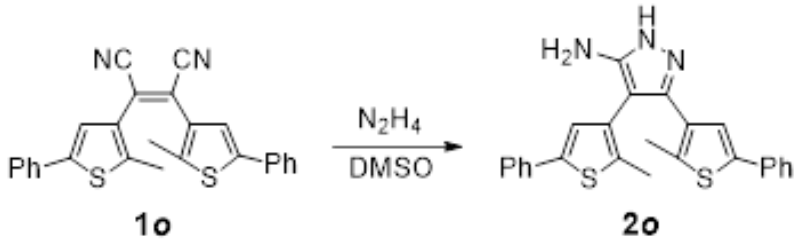

Scheme 3.11: Reaction of ring-closed isomer **1*o*** with hydrazine (Ph = phenyl)

The reaction progress was evaluated using UV-visible absorption spectroscopy (Figure 3.15 a)). After acquiring an initial spectrum of 0.7 mL solution of **1*o***, hydrazine monohydrate ($N_2H_4.H_2O$) was added in increments of 0.50 x 10^{-3} mL (0.01 M N_2H_4 in each increment) for a total added volume of 0.01 mL (0.207 M of total added N_2H_4) with spectra being acquired after each addition. After the addition of 0.50 x 10^{-3} mL of hydrazine monohydrate, the broad band at 298 nm for **1*o*** began to decrease in intensity. A new band was also observed at 260 nm which continues to increase in intensity with the addition of hydrazine monohydrate. The band at 298 nm shifts to 293 nm after the addition of 0.01

mL of hydrazine monohydrate (Figure 3.15b)). This blue shift in wavelength was also observable in the case of ring-closed isomer **1*c*** is considered to be the region of absorbance for pyrazoles.[187,188]

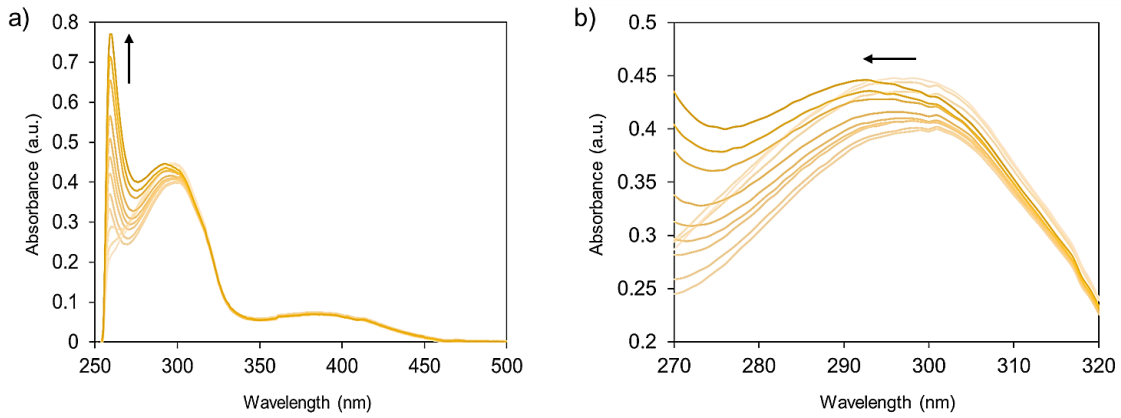

Figure 3.15: a) Changes in UV-vis absorption spectrum of a solution of **1*o*** (9.60 x 10^{-6} M) in DMSO upon addition of hydrazine monohydrate in 0.5 x 10^{-3} mL increments; b) Section of absorption spectrum from 270 nm to 320 nm showing the shift in the band for **1*o*** at 298 nm to 293 nm for **2*o*** upon addition of hydrazine monohydrate

The reaction progress was also assessed by fluorescence spectroscopy. Upon acquiring an initial emission spectrum for 2 mL solution of **1*o*** at an excitation wavelength of 365 nm, hydrazine monohydrate ($N_2H_4.H_2O$) was added in increments of 1.00 x 10^{-3} mL (0.01 M N_2H_4 in each increment) for a total added volume of 6.00 x 10^{-3} mL (0.063 M of total added N_2H_4) with spectra being acquired after each addition. Before the addition of hydrazine monohydrate, the solution of **1*o*** displayed bright yellow fluorescence with a broad band centred at 580 nm. Following the addition of 1.00 x 10^{-3} mL of hydrazine monohydrate, the band centred at 580 nm began to broaden and shift towards lower wavelengths with increasing hydrazine concentration (Figure 3.16 a)). A shoulder band began to appear at 490 nm after adding 3.00 x 10^{-3} mL of hydrazine monohydrate. A maximum in the intensity was observed upon the addition of 6.00 x 10^{-3} mL hydrazine monohydrate after which the intensity began to decrease. Correspondingly, the fluorescence emission of the solution shifted from bright yellow to bright blue-white upon the addition of hydrazine monohydrate (Figure 3.16 b)) which was similar to that observed for **2*o***.

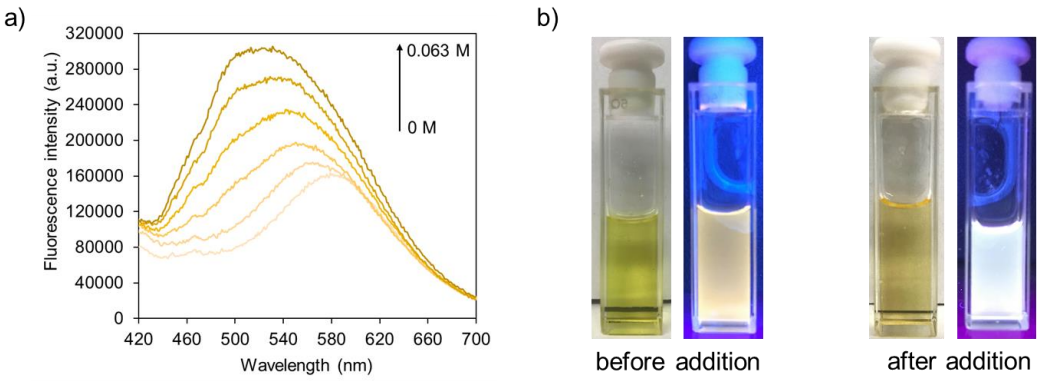

Figure 3.16: a) Changes in the fluorescence emission of a solution of **1*o*** (9.60×10^{-6} M) in DMSO upon addition of hydrazine monohydrate in 1.00×10^{-3} mL increments; b) Changes in colour and fluorescence emission of **1*o*** before (left) and after (right) addition of hydrazine monohydrate

The changes in the optical response of the ring-open isomer **1*o*** and the reaction product **2*o*** were also analyzed theoretically using the density functional theory (DFT) (Figure 3.17). The method utilizing B3LYP as the hybrid functional and 6-31G (d) basis set to calculate all the relative energy values was developed in Gaussian 09 software.[190,178,179,180] The energy values were obtained in atomic units, a.u. (1 a.u. = 1 Hartree = 27.2114 eV).[182] The energy gap between the HOMO and LUMO of **1*o*** was calculated to be 3.29 eV (376 nm) with the electron density being redistributed from the thiophene rings towards the nitrile groups. By comparison, the HOMO and LUMO for the product **2*o*** were localized over the two thiophene rings and the resultant energy gap was calculated to be 4.19 eV (295 nm). Furthermore, the energy gap from HOMO to LUMO for **2*o*** was only slightly larger than **1*o***, which was in accordance with the modest hypsochromic shift in the absorbance of the product.

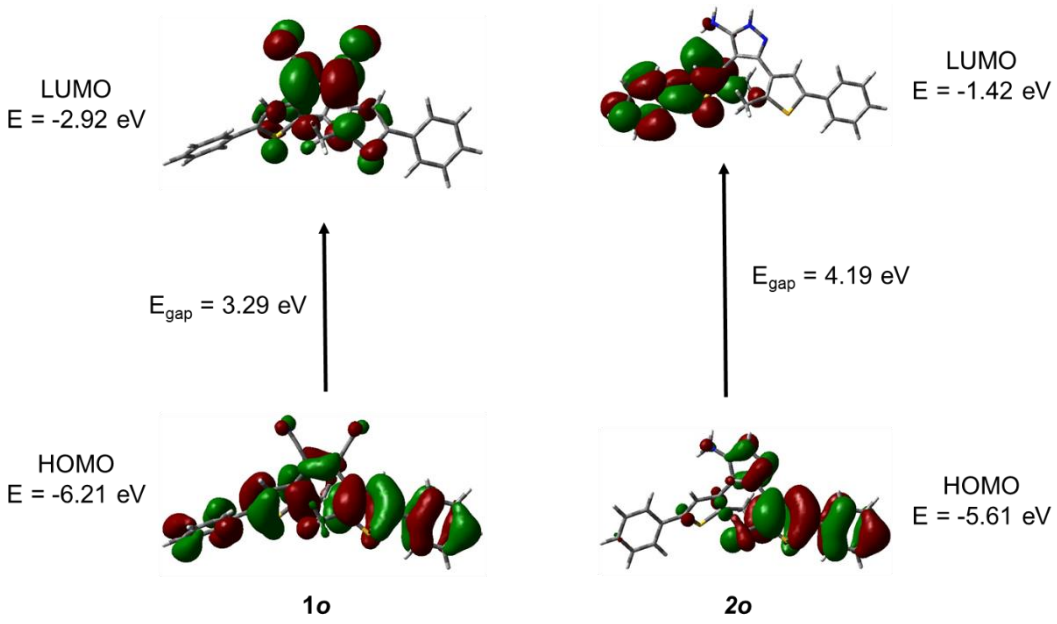

Figure 3.17: Interfacial plots of HOMO and LUMO energy levels for probe **1*o*** and **2*o*** and their corresponding energy gaps

While a visible change in colour was observed for the reaction of **1*c*** with hydrazine monohydrate, the solution colour change was not observable in the case of **1*o*** because the ring-open dithienylethenes are generally colourless. However, upon addition of hydrazine monohydrate in 1.00 x 10^{-3} mL increments for a total of 5.00 x 10^{-3} mL (0.12 M N_2H_4) to the 2.40 x 10^{-4} M solution of **1*o*** in DMSO, there was still a change in colour upon irradiation with 312nm light. When this solution was irradiated with light of wavelength >435 nm, the solution became colourless. It was only after the addition of a total of 8.00 x 10^{-3} mL (0.16 M) of hydrazine monohydrate that the solution became non-photoresponsive (Figure 3.18).

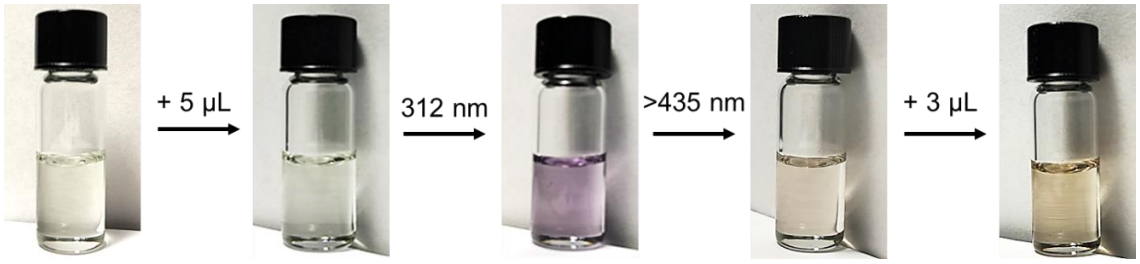

Figure 3.18: Change in colour of the solution of **1*o*** (2.40 x 10^{-4} M) in DMSO upon addition of hydrazine monohydrate in increments on 1.00 x 10^{-3} mL for a total of 8.00 x 10^{-3} mL (0.16 M N_2H_4)

The formation of **2*o*** was also confirmed experimentally by FT-IR spectroscopy and the product was found to be the same as in the case of reaction with **1*c***. Upon comparison of the FT-IR spectra of the reactant, **1*o*** and the product, **2*o***, the band corresponding to C≡N stretching at $\bar{\upsilon}$ = 2210 cm^{-1} in **1*o*** disappears and a new set of bands for N-H stretching for primary and secondary amine in the region $\bar{\upsilon}$ = 3319-3076 cm^{-1}, N-H bending at $\bar{\upsilon}$ = 1625 cm^{-1}, C-N stretching at $\bar{\upsilon}$ = 1160 cm^{-1} for the product, **2*o*** (Figure 3.19).[195]

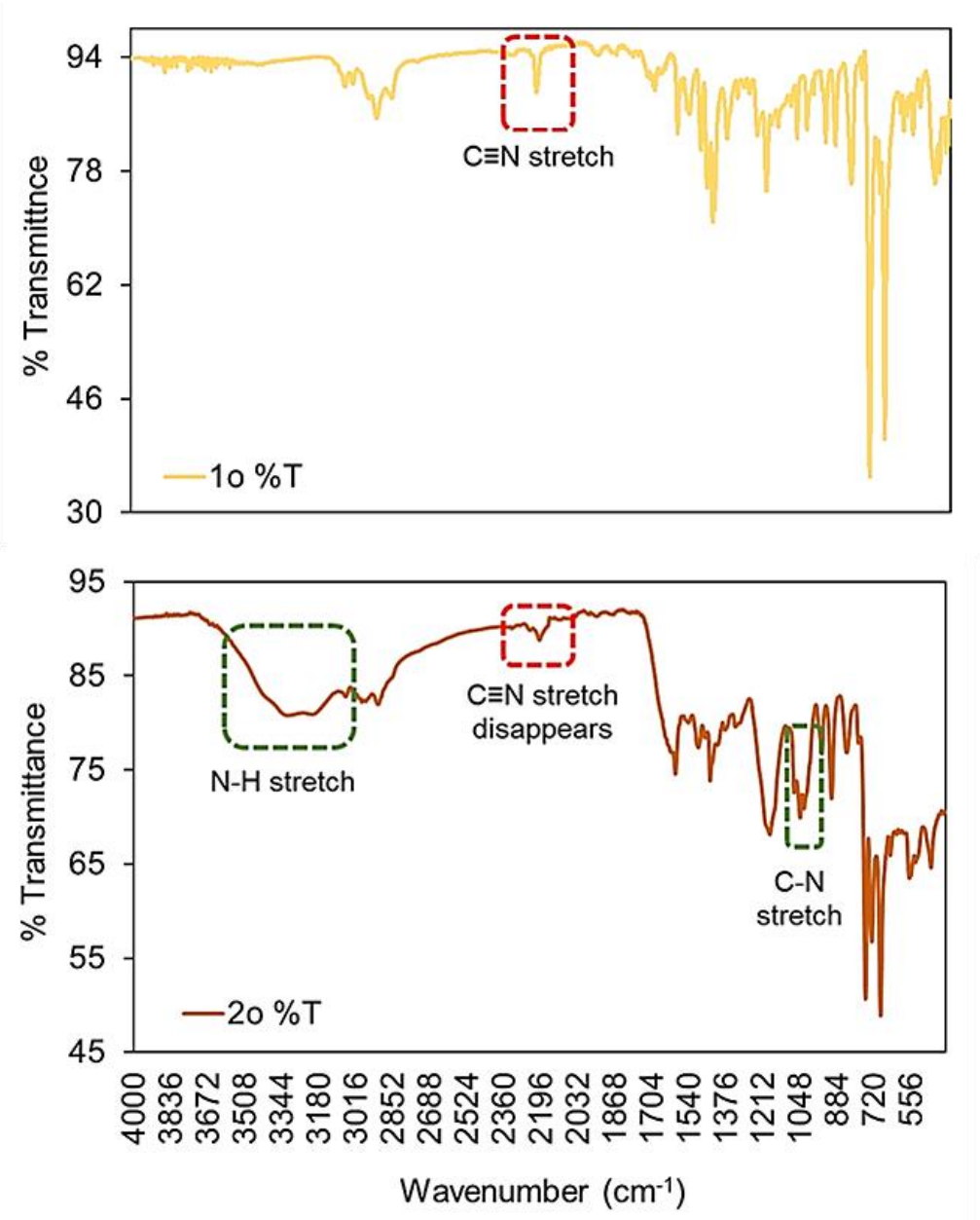

Figure 3.19: FT-IR spectra of **1*o*** and **2*o***

3.4.4. Detection of hydrazine in the vapour phase

Visual detection of hydrazine vapour was demonstrated by exposing a piece of filter paper soaked with **1*c*** to vapours of hydrazine. The filter paper was treated with a few drops of a solution of **1*c*** (0.001 g) dissolved in 0.10 mL of DMSO. The treated piece of filter paper was dried in the vacuum oven overnight to remove all the solvent. The dried filter paper (blue and non-fluorescent) was then placed elevated in a vial containing 20 drops of hydrazine monohydrate ($N_2H_4.H_2O$) that was placed at the bottom of the vial. The vial was heated at ~40°C to generate hydrazine vapour. The blue filter paper decolourized after a few minutes of exposure to the vapour showing that the vapours of hydrazine reacted with **1*c*** to generate **2*o*** which was colourless/pale yellow (Figure 3.20). Upon exposure with UV light of wavelength 312 nm, the filter paper remained pale yellow. The decolourized filter paper also displayed strong blue-white fluorescence emission under UV light of wavelength 365 nm. The results of this test indicate that upon reaction with hydrazine, the photoresponsive behaviour of our system completely stops while the system begins to fluoresce brightly in dark.

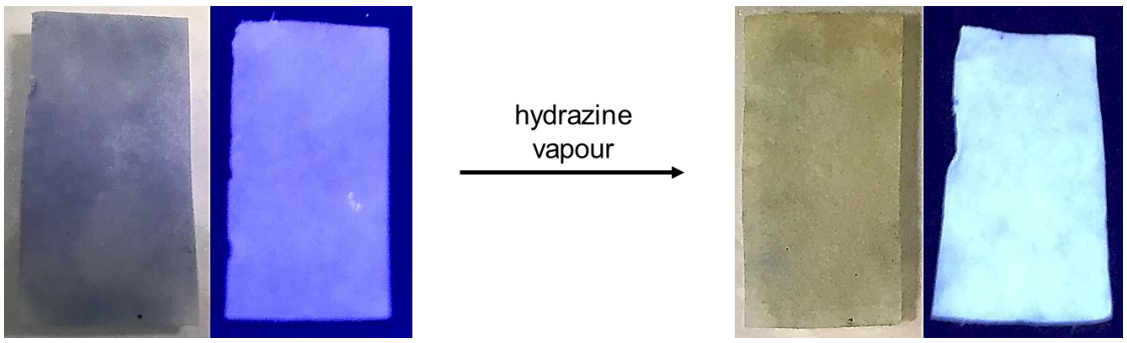

Figure 3.20: Visual changes in the colour and fluorescence emission of a piece of filter paper treated with a solution of **1*c*** (0.024 M) and vacuum-dried (blue and non-fluorescent; left) after exposure to hydrazine (N_2H_4) vapour (pale yellow and fluorescent; right)

3.4.5. Determination of the Limit of Detection (LoD)

The limit of detection is defined by IUPAC as the smallest concentration measure that can be detected with reasonable certainty for a given analytical method.[14] For a given analytical analysis, the limit of detection can be calculated by two commonly employed methods:

1. As per the formula recommended by IUPAC[197] and other agencies[198,199,200]:

$$Limit\ of\ detection, DL = 3 * \frac{\sigma}{m}$$

where, σ – standard error of the y-intercept of the regression line; m – slope of the calibration curve

Equation 3.2: Formula for the limit of detection

The minimum concentration for hydrazine in a solution of **1*c*** was evaluated using UV-visible absorption spectroscopy by observing the variation in the absorbance of **1*c*** at 580 nm for the concentration of hydrazine between 0.84 x 10^{-6} M and 2.00 x 10^{-5} M. Stock solutions of hydrazine (1.68 x 10^{-4} M) were prepared in DMSO. After acquiring an initial spectrum of **1*c*** (4.80 x 10^{-5} M) in DMSO, hydrazine was added from the stock solution in the increments of 5.00 x 10^{-3} mL (8.33 x 10^{-7} M N_2H_4 in each increment) for a total added volume of 0.12 mL (1.79 x 10^{-5} M for total added N_2H_4) with spectra being acquired after each addition. A linear regression curve was obtained for this concentration range with a correlation coefficient, R^2 = 0.9913 (Figure 3.21, left). The limit of detection, according to equation 3.2, was determined to 8.91 x 10^{-7} M using the slope and the standard error of y-intercept obtained from the regression line (Figure 3.21, right).

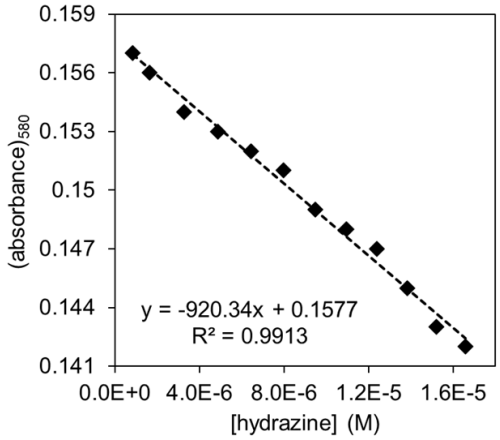

y = -920.34x + 0.1577	
slope	-920.3
intercept	0.1577
R^2	0.9913
standard error of intercept	2.73 x 10^{-4}

Figure 3.21: A plot of change in absorbance of **1*c*** (4.80 x 10^{-5} M) with the low concentration of hydrazine

2. Based on the plot of normalized absorbance against the log[hydrazine] as reported in literature[165,201,202,203]

The minimum concentration for hydrazine in a solution of **1*c*** was evaluated using UV-visible absorption spectroscopy by observing the variation in the absorbance of **1*c*** at 580 nm for the concentration of hydrazine between 8.33 x 10^{-7} M and 7.97 x 10^{-6} M. Stock solutions of hydrazine (1.68 x 10^{-4} M) were prepared in DMSO. After acquiring an initial

spectrum of **1*c*** (4.80 x 10^{-5} M) in DMSO, hydrazine was added from the stock solution in increments of 5.00 x 10^{-3} mL (8.33 x 10^{-7} M N_2H_4 in each increment) for a total added volume of 0.05 mL (7.97 x 10^{-6} M for total added N_2H_4) with spectra being acquired after each addition. A linear regression curve was obtained between this hydrazine concentration range with correlation coefficient, R^2 = 0.9761 when the normalized absorbance data was plotted against the log[hydrazine] and the intercept on the x-axis was considered as the detection limit (Figure 3.22). The limit of detection was determined to 6.92 x 10^{-7} M.

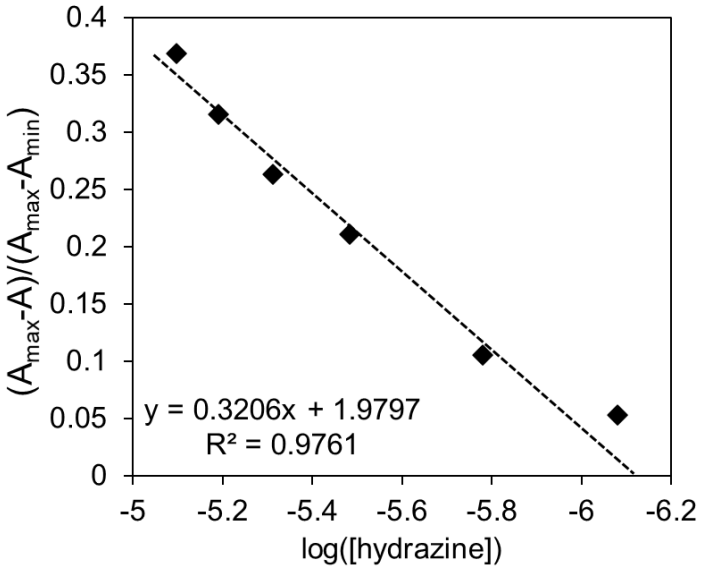

Figure 3.22: The plot of normalized absorbance of a DMSO solution of **1*c*** (4.8 x 10^{-5} M) upon treatment with low concentrations of hydrazine

The mean limit of detection value, based on both methods, was determined to be 7.91 x 10^{-7} M (0.025 ppm). The value of the limit of detection obtained for probe **1*c*** was lower than the permissible exposure limit (PEL) for hydrazine determined by the federal Occupational Safety and Health Administration (OSHA) (1.00 ppm, 8 h time-weighted average)[141], the ceiling recommended exposure limit (REL) advised by National Institute for Occupational Safety and Health (NIOSH) (0.03 ppm, 2 h exposure)[204], and the non-disabling and transient acute exposure guideline level (AEGL-1) established by US EPA (0.10 ppm, 8 h time-weighted average)[205]. However, the value obtained remains higher than the TLV recommended by the American Conference of Governmental Industrial Hygienists (ACGIH) (0.01 ppm, 8 h time-weighted average).[205]

3.4.6. The selectivity of the probe

The selectivity of the probe **1*c*** towards hydrazine (HY) over other possible interfering analytes such as cations (K^+, Ca^{2+}, Zn^{2+}, Na^+, Mg^{2+}, NH_4^+), anions (I^-, Br^-, CO_3^{2-}, OAc^-, Cl^-, SO_4^{2-}), triethylamine (TEA), phenylhydrazine (PhHY) was established by carrying out parallel UV-visible absorption experiments. Stock solutions of hydrazine and all interfering analytes (1.00 x 10^{-3} M) were prepared in ultrapure water. After acquiring an initial spectrum of **1*c*** (5.00 x 10^{-5} M) in DMSO, 20 molar equivalents of each analyte were added, and the solutions were incubated in dark at 24°C for 30 min to ensure reaction completion after which spectrum was acquired for each solution. As a comparison, 20 equivalents of hydrazine (HY) was used. No observable change in the absorbance of **1*c*** at 585 nm was observed after the addition of the interfering analytes (Figure 3.23 a)). In contrast, the intensity of the peak at λ_{max} = 585 nm decreased by ~50% after the addition of hydrazine. Correspondingly, the solutions of **1*c*** diluted with all other analytes appeared faintly blue, while the solution containing hydrazine became colourless (Figure 3.23 b)). The photoresponsive probe was found to be selective towards hydrazine.

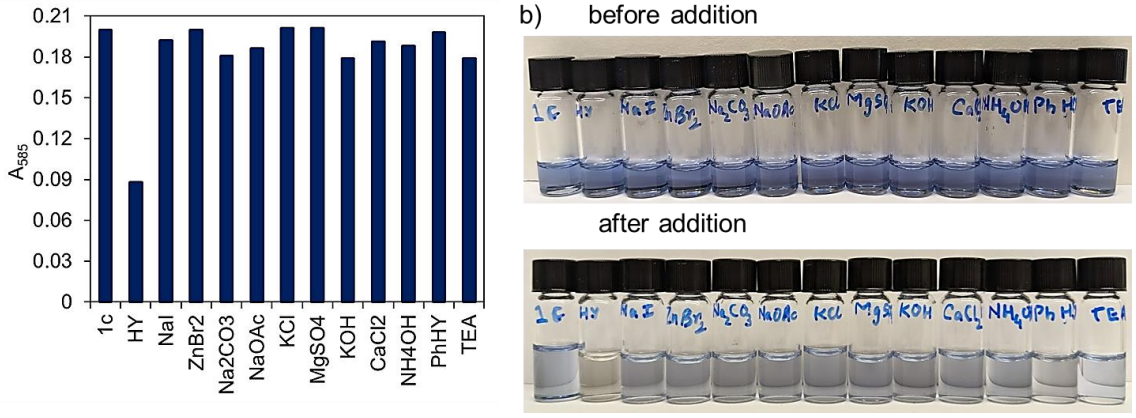

Figure 3.23: a) Comparative absorption spectra of **1*c*** (5.00 x 10^{-5} M) in the presence of hydrazine and other interfering analytes; b) Changes in the colour of the solution of **1*c*** (1.00 x 10^{-4} M) before and after addition of hydrazine and other analytes

In a similar experiment, 20 molar equivalents of each analyte and hydrazine were added to a solution of **1*o*** (1.00 x 10^{-4} M) in DMSO, and the solutions were incubated in dark at 24°C for 30 min to ensure reaction completion. The colour of solutions of **1*o*** diluted with all other analytes appeared bright yellow while the solution containing hydrazine decolourized. Upon irradiating all solutions with UV light of wavelength 312 nm for 1 min,

all solutions turned blue while the solution containing hydrazine remained colourless (Figure 3.24).

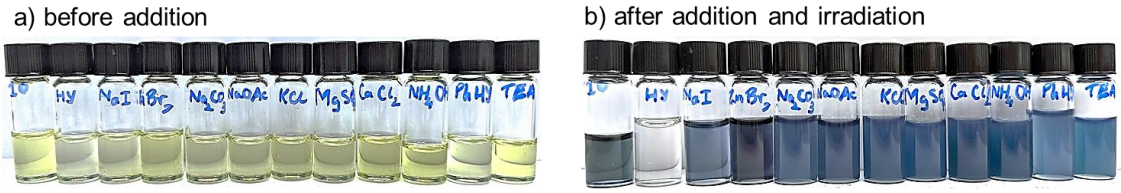

Figure 3.24: Changes in the colour of the solution of **1*o*** (1.00×10^{-4} M): a) before the addition of hydrazine and other analytes; b) after irradiation of incubated solutions containing hydrazine and other analytes

3.5. Conclusion and Future prospects

3.5.1. Summary

This chapter described a unique two-way output method for detecting hydrazine in both vapour and solution form by using a small photoresponsive molecule whose photochromism is turned 'off' and luminescence is modified upon reaction with hydrazine. The reaction led to an irreversible structural change in the dithienylethene backbone and the product molecule did not display the light assisted ring-opening/ring-closing reaction. The detection results were achieved via changes in fluorescence when ring-open (**1*o***) isomer reacted with hydrazine. In the case of ring-closed (**1*c***) isomer, however, a two-fold optical readout was observed that resulted in the change in both colour and fluorescence of the solution upon reaction with hydrazine. All the output signals of the system were visually evident in both solution and vapour phases.

3.5.2. Future prospects

The simple photoresponsive system based on **1*o*** conveniently and selectively detected hydrazine in both solution and vapour phase. The applicability of the system can be further improved by testing the reactivity of the probe in solutions containing both hydrazine and interfering analytes to determine whether the presence of other analytes leads to a difference in the reactivity of the probe with hydrazine. Similar experiments can be carried out in the vapour phase. Furthermore, the theoretical calculations based on TD-DFT (Time-Dependent Density Functional Theory) for the optical probe (**1*o*** and **1*c***) and the product (**2*o***) for the excited states using a basis set of 6-31 G(+) may provide useful

information related to diffuse functions such as long-range interactions like hydrogen bonds.

3.6. Limitations

While, the small photoresponsive molecular probe, **1*o***, could successfully visually detect hydrazine in both solution and vapour phase, it has certain drawbacks over some of the probes reported in the literature. Based on the results obtained for the reaction kinetics and the value of the rate constant, the reaction between our probe and hydrazine is quite slow. Additionally, high concentrations of hydrazine are required in order to obtain a decent optical response. Moreover, the current framework suffers from a lack of selectivity as both photoisomers undergo a reaction with hydrazine.

3.7. Experimental

3.7.1. General

All solvents and reagents used for synthesis, chromatography, UV-vis spectroscopy, and photochemical studies were purchased from Aldrich, Anachemia, Caledon Labs, Fisher Scientific, or Alfa Aesar, and used as received. Solvents used for metal-halogen exchange reactions were dried and degassed by passing them through steel columns containing activated alumina under nitrogen using an MBraun solvent purification system. Hydrazine monohydrate (64-65% hydrazine) was obtained from Aldrich and was as received. Solvents for NMR analysis were purchased from Cambridge Isotope Laboratories and used as received. Column chromatography was performed using silica gel 60 (230–400 mesh) from Silicycle Inc.

*warning: Hydrazine vapours are toxic upon ingestion or inhalation. Extreme caution must be exercised while handling.

3.7.2. Instrumentation

^{1}H and ^{13}C NMR characterizations were performed on a Bruker Avance-400 instrument with a 5 mm inverse probe operating at 400.13 MHz for ^{1}H NMR and 100.61 MHz for ^{13}C NMR unless stated otherwise. Chemical shifts (δ) are reported in parts per million (ppm)

relative to tetramethylsilane using the residual solvent peak as a reference. Coupling constants (J) are reported in Hertz. UV-visible absorption spectra were recorded on a Shimadzu UV-3600 Plus spectrophotometer. Fluorescence measurements were performed on a PTI Quantamaster spectrofluorometer. A JDS Uniphase 980 nm laser diode (device type L4-9897510-100M) coupled to a 105 um (core) fibre was employed as the excitation source. The output of the diode laser was collimated and directed on the 110 samples using a Newport F-91-C1-T Multimode Fiber Coupler. The visible emissions were collected from the samples at π/2 from the incident beam in the plane of the spectrometer. All of the samples were held in a square quartz cuvette (path length of 1 cm). All spectra were corrected for instrument sensitivity. IR spectroscopy measurements were conducted on a PerkinElmer Spectrum Two™ IR spectrometer equipped with a universal ATR accessory with a 9-bounce diamond top-plate. High-Resolution Mass Spectroscopy (HRMS) measurements were performed using an Agilent 6210 TOF LC/MS in ESI-(+) mode. Microanalysis (C, H, N) was carried out using a Carlo Erba EA 1110 CHN Elemental Analyzer. Melting points were measured using a Gallenkamp melting point apparatus and are uncorrected.

3.7.3. Photochemistry

All the ring-closing reactions were carried out using the light source from a lamp used for visualizing TLC plates at 312 nm (Spectroline E series, 470 W/cm^2). The ring-opening reactions were carried out using the light of a 150 W halogen photo-optic source passed through a 435 nm cut-off filter to eliminate higher energy light.

3.7.4. Synthesis

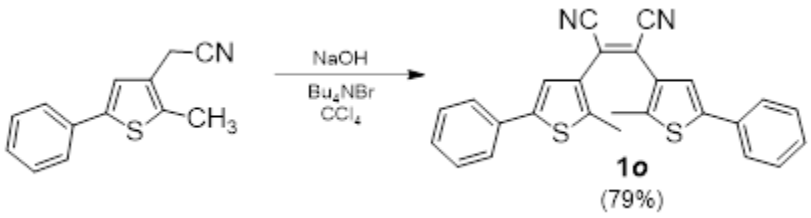

Synthesis of 2,3-bis(2-methyl-5-phenylthiophen-3-yl) maleonitrile (1*o*). A solution of 2-(2-methyl-5-phenylthiophen-3-yl) acetonitrile (6) (0.93 g, 0.0022 mol) in carbon tetrachloride (5 mL) was added to a stirring solution of 50% aqueous sodium hydroxide (5

mL) containing tetrabutylammonium bromide (0.035 g, 0.00011 mol) at room temperature. The mixture was stirred at 50°C for 1.5 h and the reaction progress was monitored by TLC (10:1 hexanes/ethyl acetate). Upon completion, the reaction mixture was poured into water and extracted with chloroform (2 × 10 mL), dried over $MgSO_4$, filtered, and concentrated under reduced pressure. Purification by column chromatography using silica gel (10:1 hexanes/ethyl acetate) afforded 0.74 g (79%) of 2,3-bis(2-methyl-5-phenylthiophen-3-yl) maleonitrile (**1*o***) as a yellow-green solid.

^{1}H NMR (400 MHz, $CDCl_3$): δ 7.40 (d, J = 8.1 Hz, 3H), 7.33 (d, J = 7.2 Hz, 2H), 7.29 (d, J = 7.1 Hz, 1H), 6.91 (s, 1H), 2.31 (s, 3H).

^{13}C NMR (101 MHz, $CDCl_3$): δ 142.4, 133.1, 131.8, 129.4, 128.6, 127.5, 126.0, 121.1, 116.4, 15.0.

FT-IR (diamond ATR): $\tilde{\upsilon}$ (cm^{-1}) 2924-2851 (C-H stretch, aromatic), 2210 (C≡N stretch), 1445 (C-C stretch, aromatic), 755 (C-H bend, oop), 690 (C-S stretch, thiophene).

Melting point: 132-133 °C.

HRMS (ESI): m/z (M+H) calculated for $C_{26}H_{18}N_2S_2$: 423.098417, found: 423.097986.

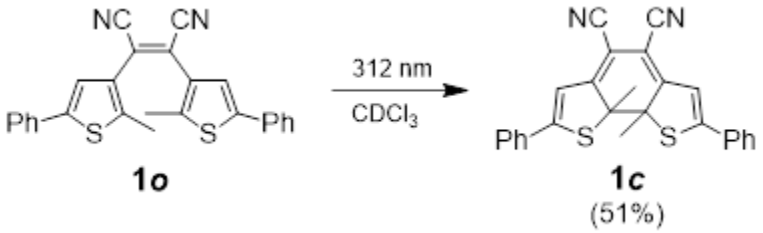

1*o* **1*c***
(51%)

Photochemical synthesis of 1*c*. A deuterated chloroform solution of compound **1*o*** (5.00 × 10^{-3} M) in an NMR tube was irradiated with 312 nm light until no further changes were observed in the ^{1}H NMR spectrum. After 120 min the photostationary state was reached at this concentration, which contained 51% of the ring-closed isomer **1*c*** as measured by comparing relative integrals for chemical shifts for **1*o*** and **1*c***. The ring-closed isomer **1*c*** was isolated by column chromatography using silica gel (2:1 dichloromethane/hexanes).

^{1}H NMR (400 MHz, $CDCl_3$): δ 7.58 (d, J = 6.8 Hz, 2H), 7.46 (d, J = 6.8 Hz, 2H), 7.44 (d, J = 6.7 Hz, 1H), 6.72 (s, 1H), 2.17 (s, 3H).

^{13}C NMR (101 MHz, $CDCl_3$): δ 170.72, 144.69, 130.82, 129.20, 127.25, 115.62, 108.90, 99.58, 57.19, 29.87.

FT-IR (diamond ATR): $\bar{\upsilon}$ (cm^{-1}) 2924-2851 (C-H stretch, aromatic), 2210 (C≡N stretch), 1445 (C-C stretch, aromatic), 755 (C-H bend, oop), 690 (C-S stretch, thiophene).

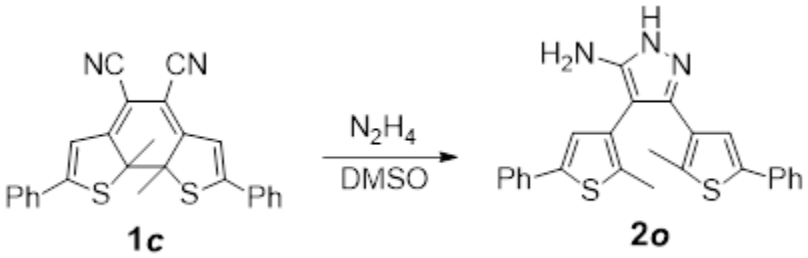

Synthesis of 3,4-bis(2-methyl-5-phenylthiophen-3-yl)-1H-pyrazol-5-amine (2*o*). A solution of **1*c*** (0.005 g, 1.2 x 10^{-5} mol) in DMSO (20 mL) was treated with $N_2H_4.H_2O$ (2 mL, 0.021 mol N_2H_4, excess). The reaction mixture was stirred at room temperature for 16 h and reaction progress was monitored by TLC (15% ethyl acetate in hexanes). Upon completion, the contents were washed with brine and extracted with ethyl acetate (2 x 20 mL) dried over $MgSO_4$, filtered, and concentrated under reduced pressure. Purification by column chromatography using silica gel (15% ethyl acetate in hexanes) afforded 0.004 g (78% yield) of 3,4-bis(2-methyl-5-phenylthiophen-3-yl)-1H-pyrazol-5-amine (**2*o***) as a yellow-brown solid.

^{1}H NMR (600 MHz, $CDCl_3$): δ 7.68-7.64 (m, 2H), 7.42 (d, J = 9.0 MHz, 3H), 7.29 (s, 1H), 2.11 (s, 3H).

^{13} NMR (151 MHz, $CDCl_3$): δ 153.24, 133.77, 132.27, 129.14, 129.07, 128.71, 128.62, 127.87, 125.75, 125.60,117.81, 14.72.

FT-IR (diamond ATR): $\bar{\upsilon}$ (cm^{-1}) 3319-3076 (N-H stretch), 2924 (C-H stretch, aromatic), 1625 (N-H bend), 1445 (C-C stretch, aromatic), 1160 (C-N stretch), 755 (C-H bend, oop), 690 (C-S stretch, thiophene).

Melting point: 110-113°C

Elemental Analysis: C = 68.22%, H = 5.32%, N = 8.84%, S = 14.47 %

The reaction of hydrazine with ring-closed isomer 1*c* in solution. A solution of **1*c*** in DMSO (0.7 mL, 4.80 x 10^{-5} M) was charged with a total of 5.00 x 10^{-3} mL of hydrazine monohydrate in increments of 0.5 x 10^{-3} mL. The UV-visible absorption spectrum was acquired after each addition. These results are shown in Figures 3.8 and 3.11.

A solution of **1*c*** in DMSO (2 mL, 4.80 x 10^{-5} M) was charged with a total of 6.00 x 10^{-3} mL of hydrazine monohydrate in increments of 1.00 x 10^{-3} mL. The fluorescence emission spectrum was acquired after each addition. These results are shown in Figure 3.9.

The reaction of hydrazine with ring-open isomer 1*o* in solution. A solution of **1*o*** in DMSO (0.7 mL, 9.60 x 10^{-6} M) was charged with a total of 10 x 10^{-3} mL of hydrazine monohydrate in increments of 0.01 mL. The UV-visible absorption spectrum was acquired after each addition. These results are shown in Figures 3.15 and 3.18.

A solution of **1*o*** in DMSO (2 mL, 9.60 x 10^{-6} M) was charged with a total of 6.00 x 10^{-3} mL of hydrazine monohydrate in increments of 1.00 x 10^{-3} mL. The fluorescence emission spectrum was acquired after each addition. These results are shown in Figure 3.16.

The reaction of hydrazine with ring-closed isomer 1*c* in the vapour phase. A filter paper soaked with a solution of **1*c*** (0.001 g) dissolved in 0.10 mL of DMSO was vacuum dried and exposed to hydrazine vapour (10 drops). Images were acquired before and after exposure. These results are shown in Figure 3.20.

The reaction of ring-closed isomer 1*c* with hydrazine and competing analytes in solution. A solution of **1*c*** in DMSO (0.7 mL, 5.00 x 10^{-5} M) was charged with a total of 1.00 mL of aqueous solutions of hydrazine monohydrate (1.00 x 10^{-3} M stock), phenyl hydrazine (1.00 x 10^{-3} M stock), triethylamine (1.00 x 10^{-3} M stock), sodium iodide (1.00 x 10^{-3} M stock), zinc bromide (1.00 x 10^{-3} M stock), sodium carbonate (1.00 x 10^{-3} M stock), sodium acetate (1.00 x 10^{-3} M stock), potassium chloride (1.00 x 10^{-3} M stock), magnesium sulfate (1.00 x 10^{-3} M stock), potassium hydroxide (1.00 x 10^{-3} M stock), calcium chloride (1.00 x 10^{-3} M stock), ammonium hydroxide (1.00 x 10^{-3} M stock) and incubated in dark at 24°C for 30 min. The UV-visible absorption spectrum was acquired after incubation. These results are shown in Figure 3.23.

The reaction of ring-open isomer 1*o* with hydrazine and competing analytes in solution. A solution of **1*o*** in DMSO (0.7 mL, 1.00 x 10^{-4} M) was charged with a total of

2.00 mL of aqueous solutions of hydrazine monohydrate (1 x 10^{-3} M stock), phenyl hydrazine (1.00 x 10^{-3} M stock), triethylamine (1.00 x 10^{-3} M stock), sodium iodide (1.00 x 10^{-3} M stock), zinc bromide (1.00 x 10^{-3} M stock), sodium carbonate (1.00 x 10^{-3} M stock), sodium acetate (1.00 x 10^{-3} M stock), potassium chloride (1.00 x 10^{-3} M stock), magnesium sulfate (1.00 x 10^{-3} M stock), potassium hydroxide (1.00 x 10^{-3} M stock), calcium chloride (1.00 x 10^{-3} M stock), ammonium hydroxide (1.00 x 10^{-3} M stock) and incubated in dark at 24°C for 30 min. The solutions were irradiated with a light of wavelength 312 nm after incubation. These results are shown in Figure 3.24.

3.7.5. Theoretical calculations

The computational method based on density functional theory (DFT) was employed to analyze the electronic structure of the optical probe (**1*o*** and **1*c***) and product (**2*o***) in their ground state and determine theoretical values for energies, and absorbances. In contrast to the calculation of individual electronic wave functions (as in ab initio methods), DFT measures the electron density of the entire molecule. The method utilizing B3LYP as the hybrid functional and 6-31 G (d) basis set to calculate all the relative energy values was developed in Gaussian 09 software. Hybrid functional and the basis set used for present calculations have been traditionally reported in the literature for energy calculations in a similar class of molecules. The energy values were obtained in atomic units, a.u. (1 a.u. = 1 Hartree = 2625.4996 kJ/mol). Geometry optimizations were conducted for all three molecules to determine the minimum energy configuration for each molecule prior to all energy calculations. The optimized geometries were then submitted for energy calculations. All calculations were submitted on Westgrid, the regional partner for Compute canada, which is a high computing power facility for the use of research in western Canada. The results for the calculations are shown in Figures 3.7, 3.10 and 3.17.

Chapter 4.

Using light and decorated gold nanoparticles for activation and 'on-command' release of small molecules

The research work presented in section 4.2 of this chapter has been recently published as a communication in Nanoscale Advances and is being reproduced in its entirety with permission from the journal (B. Kaur, D. Baker, K. Arafeh, A. Asadirad, R. Raza, N. R. Branda, *Nanoscale Adv.*, **2021**, accepted manuscript). The synthesis and characterization of the nanoparticles, polymers and nano-assemblies for Strategy II were conducted by Brahmjot Kaur. The nano-assemblies for Strategy I were prepared by Daina Baker. The characterization of the polymer assemblies and nanoparticles for Strategy I was conducted by Brahmjot Kaur. Thermal release studies were done by Brahmjot Kaur and Daina Baker. Laser-assisted experiments were conducted by M. Khaled Arafeh. The laser-assisted release studies were done by Brahmjot Kaur and Daina Baker. Neil R. Branda and Amir Asadirad co-designed the project concept.

4.1. Introduction

The application of light as an external stimulus to control chemical reactions is desired in fields related to drug delivery.[206,207] The scientific and medical communities continue to create and improve approaches to develop pharmaceutical drugs that can differentiate between healthy and diseased cells. With a growing increase in the global population of both elderly and children, the demand for such targeted and controlled drug delivery systems in the market is projected to grow at an annual rate of 7.8% by the year 2027.[208] The targeted release processes provide increased regulation as to when and where the drugs are delivered. Section **4.1.1** describes briefly such targeted drug delivery systems.

Some popular delivery systems are based on nanoparticles, such as liposomes, polymer micelles, and metal nanoparticles. These systems have been designed and are continually being optimized to accurately deliver therapeutic materials at specific sites within the body. These systems offer three notable advantages over conventional drug delivery systems: i) easier control over the dose release rate; ii) enhanced curative effect of the material for

improved drug efficacy and reduced administration frequency of the drug; and iii) low toxic side effects.[207,209] Such a stimuli-controlled release is required to achieve the maximum therapeutic effect. Discussion on nanomaterials as drug delivery systems can be found in section **4.1.2**.

Among the metal nanoparticles, gold nanoparticles are being regarded as potential candidates for the effective release of molecules in diverse biological systems owing to their relatively inert nature and biocompatibility.[210,211, 212] Their unique ability to convert light of specific wavelength into localized heat called the photothermal effect and their ease of synthesis and functionalization will be discussed in greater detail in section **4.1.3** of this chapter.

Different types of chemical reactions can be applied to load various drugs onto the gold nanoparticles. One of these is the reversible Diels-Alder reaction, which can provide a suitable approach for binding and releasing molecules from nanoparticles. Section **4.1.4** describes Diels-Alder chemistry and its applications regarding nanoparticle-based drug delivery.

Section **4.1.5** of this chapter briefly discusses the polymer-based encapsulation method to create robust nano-assemblies that can be used in biological environments. Discussion about our systems begins in section **4.2**.

4.1.1. Controlled drug delivery

Research in the field of drug delivery systems continues to improve health and extended life across the globe; developing technologies to deliver drugs to their site of action for the desired therapeutic effect has been the main driving force for this change.[213] The utility of such a system is in that a drug can be released in a controlled manner and this often minimizes systemic side effects. Such a system is also capable of providing greater control over the release time and/or release rate of the drug.[214] Furthermore, this system will better enable the drug to cross physiological barriers, protect the drug from premature elimination from the body, and significantly increase its compatibility with the patient's body.[215] Work on controlled drug delivery systems began in the early 1950s and focused mostly on understanding the various drug release mechanisms like osmosis, dissolution, diffusion, and ion-exchange. Development of twice-a-day and once-a-day oral delivery

systems; and once-a-day and once-a-week transdermal patches also happened by the 1980s.[216]

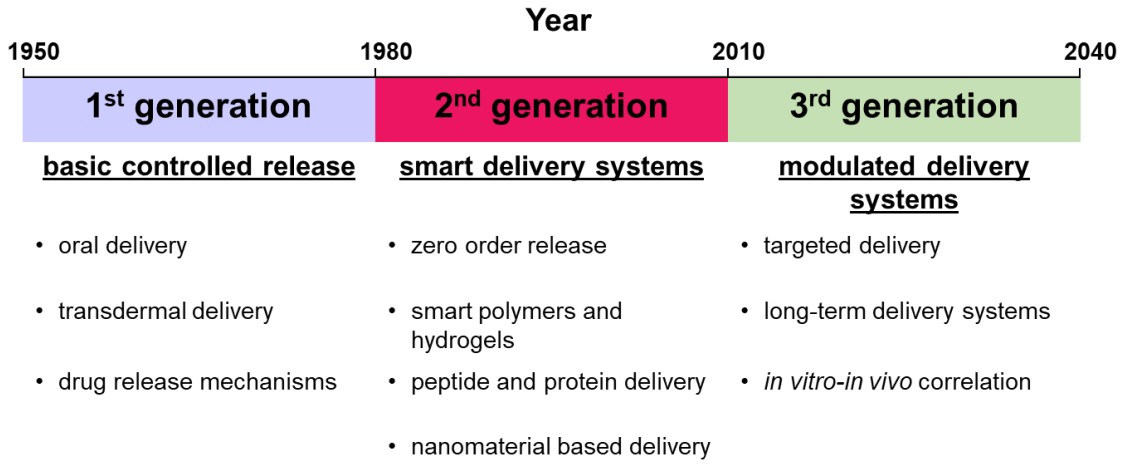

Scheme 4.1: Progression of controlled drug delivery systems over time[216]

Research work that was done during the development of the 2nd generation of controlled drug delivery systems mostly focused on systems that could provide zero-order drug release (Scheme 4.1).[216]

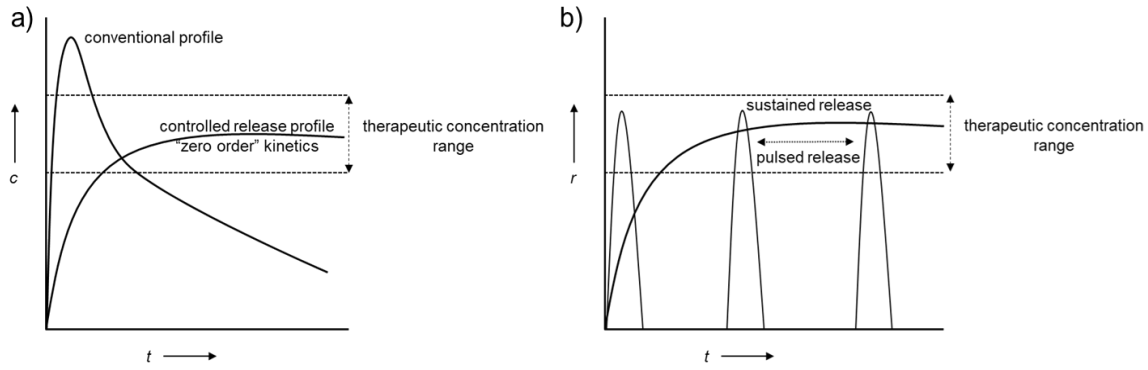

Figure 4.1: a) schematic concentration (c) vs. time (t) profiles for conventional and controlled release systems; b) schematic release rate (r) vs. time (t) for sustained and pulsatile release systems[214]

Zero-order or sustained drug release aims at maintaining the concentration of the drug in the bloodstream within an optimum range – the therapeutic concentration range - where maximum therapeutic benefits can be obtained with minimal side effects (Figure 4.1 a)). Conventional drug delivery systems such as tablets or injections allow the concentration of the drug to increase sharply well above the therapeutic range and are not able to

maintain therapeutic concentrations. The development of polymer coatings to encapsulate drugs were the major focus of this original research.[217] The purpose of the coating was to release the drug at a nearly constant rate via the process of diffusion or by the degradation of the polymer over time.[214]

However, such a continuous release of drugs is not always considered to be an ideal method of delivery. Sometimes, it is even undesirable to have a constant level of concentration in the bloodstream as in the case of insulin, pituitary gland hormones, and nitroglycerin.[216] Alternatively, an optimal concentration of drug being delivered as a pulse at variable intervals of time is preferred (Figure 4.1 b)). Such pulsatile release is advantageous in that it mimics the release mechanism for some compounds naturally produced by the human body.[214] Pulsatile release systems require materials, mostly polymers, and nanomaterials, that can respond to specific external or internal stimuli; like changes in pH inside the cells[218], changes in temperature[219], molecules present in the human body[220], enzymes[221], ultrasound[222], light[223], electric or magnetic fields[224]. Representative examples of stimuli-responsive pulsatile release systems are shown in Figure 4.2.

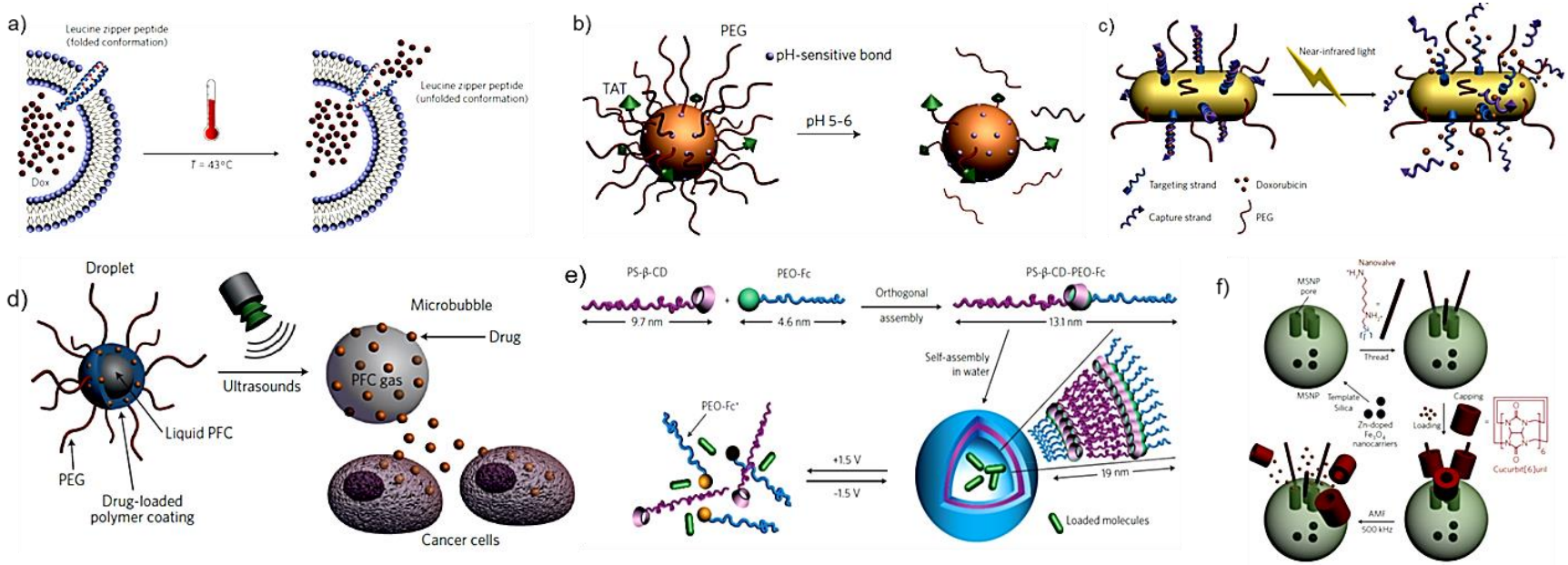

Figure 4.2: Examples of stimuli-responsive pulsatile release of therapeutics; a) release of doxorubicin (Dox) by unfolding of leucine peptide zipper inserted in the membrane of liposome carrying doxorubicin (Dox) triggered by temperature. Reproduced with permission from ref. 225 © 2012 American Chemical Society[225], b) pH-sensitive hydrolyzable PEG shells for efficient transactivating regulatory protein (TAT)-peptide sequence exposure. Reproduced with permission from ref. 226 © 2012 Elsevier B.V. [226], c) near IR triggered the release of doxorubicin by dehybridization of DNA conjugated at the surface of gold nanorods. Reproduced with permission from ref. 227 © 2012 WILEY-VCH Verlag GmbH & Co. KGaA [227], d) ultrasound-assisted drug delivery from perfluorocarbon (PFC)-containing nanoemulsions. Reproduced with permission from ref. 228 © 2009 Elsevier B.V. [228], e) assembly and disassembly of polystyrene-β-cyclodextrin-poly(ethylene oxide)-ferrocene (PS-β-CD-PEO-Fc) supramolecular vesicles by applying voltage. Reproduced with permission from ref. 229 © 2010 American Chemical Society [229], f) application of alternating magnetic field (AMF) for the release of cucurbit[6]uril from Fe_2O_3 doped mesoporous silica nanoparticles (MSNP). Reproduced with permission from ref. 230 © 2010 American Chemical Society [230]

4.1.2. Nanomaterials as drug delivery payloads

Nanomaterials emerged as an important topic of research in targeted drug delivery in the last two decades.[231] Most of the research was focused on the modification of properties of these nanomaterials to improve targeted drug delivery to tumours and for gene therapy/delivery.[216] Nanomaterials are a class of materials with sizes in the range of 1 nm to 100 nm.[232] Owing to the variations in size, these materials have found themselves at the centre stage of applications relating to fields such as biosensors, drug delivery, and tissue engineering.[233] For drug delivery applications, nanomaterials are loaded with inactive, masked drug molecules that can be released, when required, in the desired area of interest in the body.[234] These nano-sized carriers are retained for a long time by the blood circulatory system to facilitate the required dose release of the drug, thus, leading to fewer dosages. Moreover, the small size of these materials, in comparison with cells, provides for easy penetration in the tissue which, in turn, aids the process of drug uptake by cells to ensure site-specific and efficient drug release.[233] The biocompatibility of nanomaterials, the ease of large-scale synthesis, reliability, and reproducibility of nanomaterials, and the ability of nanomaterials to be target-specific while releasing the drug are some of the critical requirements taken into consideration when designing such nanomaterials.[235]

Significant advancements in the field of materials science and pharmaceutics have led to the preparation of nanomaterials with diverse sizes, architecture, and surface properties.[236] These broadly include liposomes, dendrimers, polymer-based micelles, and inorganic nanoparticles based on metals, metal oxides, quantum dots (Figure 4.3).

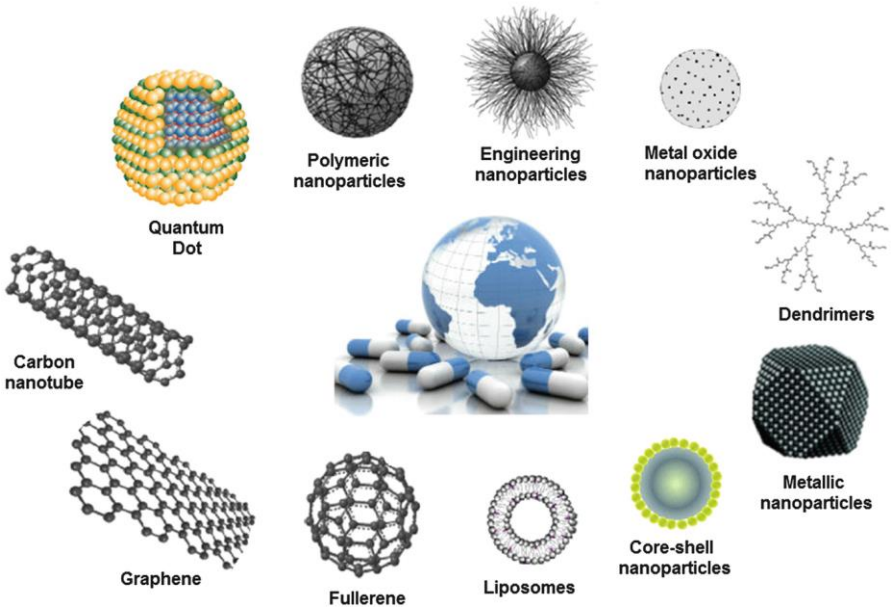

Figure 4.3: Types of nanomaterials developed for drug delivery applications. Reproduced with permission from ref. 232. © 2017, Springer International Publishing AG [232]

Liposome based nanomaterials are one of the most common classes of nanomaterials in the field of drug delivery. Liposomes consist of vesicles that are formed by natural or synthetic phospho-based lipids. Presently, a wide range of clinically approved anti-cancer drug formulations are based on liposomal nanomaterials broadly due to their low toxicity, hydrophilic/hydrophobic character, biocompatibility, and straightforward size modulation.[237] However, the concerns regarding their low blood circulation half-life and their immunogenic nature have restricted the use of liposomes as drug delivery vehicles.[233]

Dendrimers are three-dimensional, nano-sized radially symmetric, hyperbranched macromolecules that are designed for drug delivery purposes.[238] Dendrimers encapsulate the drug within their branches and release the drug after enzyme-based degradation or with changes in a physical environment like pH. However, the presence of positively charged amino groups as the surface end groups makes the dendrimers toxic, thereby, limiting their clinical applications.[233]

Polymer-based micelles are another class of nanomaterials that are used as drug delivery systems.[239] These micelles are obtained by self-assembly of amphiphilic block copolymers to form a core-shell structure in aqueous environments. The core of this system is hydrophobic and can be loaded with hydrophobic drug molecules which can then be

released in the target area.[237] Limited stability of these nanomaterials can lead to premature hydrolysis and drug leakage during transportation to targeted areas and consequently has limited their use in delivery applications.[240]

Inorganic nanoparticles consist of nanoparticles based on metals like gold, silver, copper; metal oxides like iron oxide; and quantum dots. Based on their core material, inorganic nanoparticles tend to possess different properties such as high electron density and strong optical absorption (e.g.: gold nanoparticles), fluorescence (e.g.: semiconductor quantum dots), or magnetic moment (e.g.: iron oxide nanoparticles). Upon desired surface modification, these nanoparticles can be employed as drug delivery vehicles.[241]

4.1.3. Gold nanoparticles as drug delivery systems

Recently, extensive research in the field of nanoscience has led to the development of drug delivery systems based on gold nanoparticles. Owing to their unique electronic, optical, and catalytic properties, gold nanoparticles have emerged as tools for theranostic applications, which involve the use of gold nanoparticles for both diagnostic and therapeutic purposes (Figure 4.4).[242]

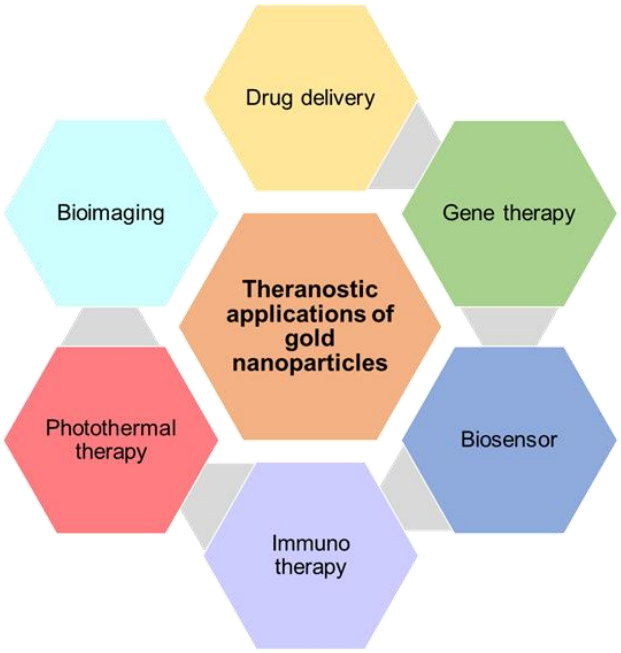

Figure 4.4: Theranostic applications of gold nanoparticles[242]

Some of the extraordinary features and advantages of gold nanoparticles are:

- *high level of chemical inertness*: gold nanoparticles remain unoxidized in biological environments and are taken up by liver cells for removal from the body[210, 243]
- *facile synthesis*: monodisperse gold nanoparticles of sizes ranging from 1 nm to 150 nm and with various shapes can be synthesized[244]
- *ease of surface functionalization*: gold nanoparticles can be decorated with diverse targeting ligands like small organic molecules, peptides, antibodies and oligosaccharides[245]
- *noncytotoxic*: gold nanoparticles, depending upon their size, surface charge, and surface functionalization, have shown to not cause any detrimental effects to cells[246]
- *photoresponsive*: gold nanoparticles can absorb light of a specific wavelength and efficiently convert it into heat for targeted drug release[247]

The first and still the most common method to synthesize gold nanoparticles was developed in 1951 by John Turkevich. The original procedure simply involved the reduction of $HAuCl_4$ in water using trisodium citrate; the resulting nanoparticles were about 20 nm in diameter.[248] Further modification in the synthetic procedure has led to the formation of gold nanoparticles with predefined sizes.[249] The resulting nanostructure consists of a loose shell of ligands around a gold core which can act as a precursor to developing various gold nanoparticle-based materials.[250]

The most commonly used types of gold nanoparticles for drug delivery applications are nanospheres, nanorods, nanoshells, and nanocages (Figure 4.5). This difference in shape and size of nanoparticles accounts for their distinctive electronic and optical properties.[244]

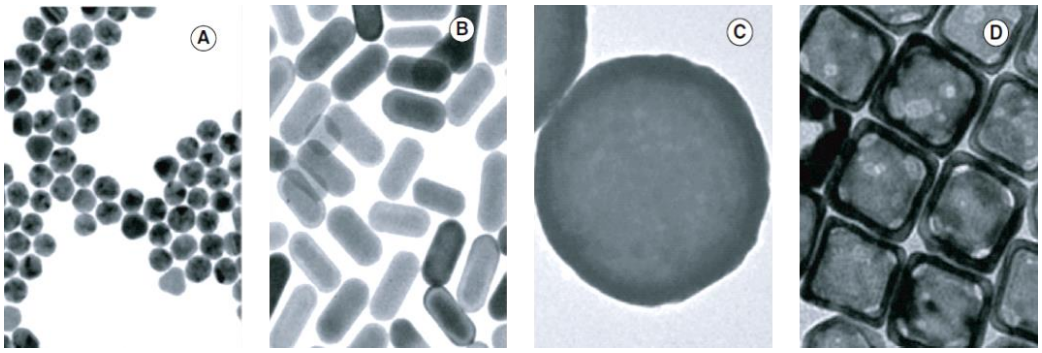

Figure 4.5: TEM images of most commonly used gold nanoparticles: (A) Gold nanospheres (~ 15 nm)[251]; (B) Gold nanorods (~ 20 x 45 nm)[251]; (C) Gold nanoshells (~ 100 nm)[252]; (D) Gold nanocages (~ 60 nm)[253]. Reproduced with permission from ref. 251 © 2010 WILEY-VCH Verlag GmbH & Co. KGaA, ref 252 © 2007 American Chemical Society

Noble metal nanoparticles such as gold and silver possess an interesting optical property called Localized surface plasmon resonance (LSPR). Surface plasmon resonance refers to the collective oscillation of the delocalized conduction electrons of the metal upon interaction with the light of appropriate wavelength (Figure 4.6 a)), which in the case of metallic nanoparticles is very well localized.[254,255]

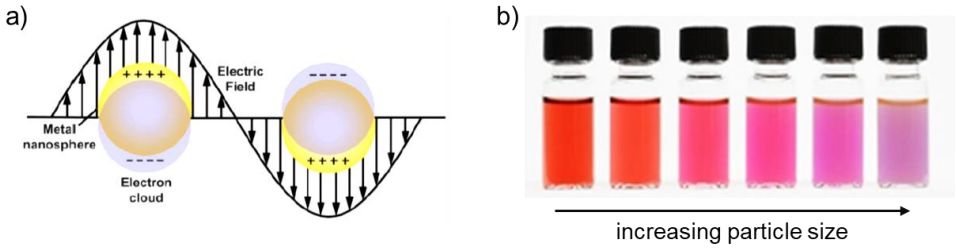

Figure 4.6: a) Schematic representation of LSPR in gold nanospheres. Reproduced with permission from ref. 254 © 2008 Royal Society of Chemistry[254]; b) Colours of monodispersed gold nanoparticles of different sizes

This absorbed light can then either be scattered giving them the distinct colour (Figure 4.6 b)) or converted into lattice vibrations (*i.e.* phonons) in the form of heat. Depending upon the size and shape of the nanoparticles, the position of the absorption maximum is shifted.[255] Upon increasing the size of the particles, the absorption maximum can be shifted from the visible to the near-IR region (bathochromic shift). The absorption in the near-IR regions is desired for biomedical applications as this light can penetrate deeply into the tissue (Figure 4.7).[254]

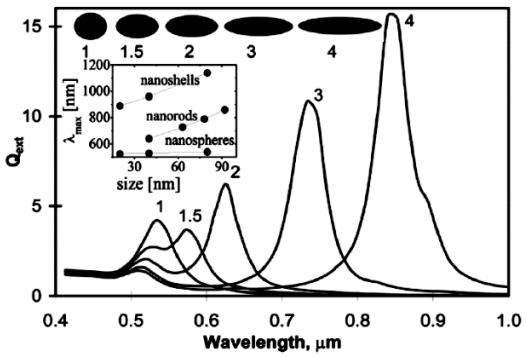

Figure 4.7: Calculated effect of the geometry of gold nanorods on the optical properties, with different aspect ratios but equal volumes and an effective radius of 20 nm. The inset shows the variation of surface plasmon extinction maximum λ_{max} as a function of particle size for gold nanospheres, gold nanorods, and gold nanoshells. Reproduced with permission from ref. 256. © 2006 Wiley-VCH Verlag GmbH Co. and ref. 244. © 2012 Royal Society of Chemistry. [244, 256]

The photothermal effect of gold nanoparticles is the phenomenon in which upon irradiation with visible (or near-IR), the absorbed light energy is converted into heat (Figure 4.8 a)).[257] The absorbed photons cause crystal lattice vibrations which rapidly relax leading to an increase in temperature and generating localized heat.[255,258] This photothermal effect has been widely used in the treatment of cancer in a process known as photothermal therapy (PTT) in which hyperthermia is used directly to kill the tumour cells.[245] Upon suitable functionalization with target molecules, the increase in temperature can also lead to photothermally triggered drug delivery (Figure 4.8 b)).

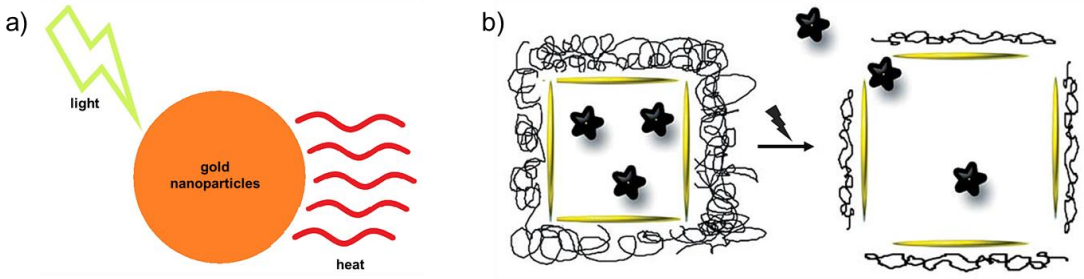

Figure 4.8: a) Schematic representation of the photothermal effect of gold nanoparticles; b) Heat-induced release of therapeutic molecules from loaded gold nanocages upon irradiation with near-IR LASER. Reproduced with permission from ref. 244. © 2012 Royal Society of Chemistry [244]

Drug delivery systems based on gold nanoparticles that make use of the photothermal effect can be designed using diverse approaches. These can be classified into three major categories[244,255]:

1. gold nanoparticles are surrounded by a polymer matrix containing the drug molecules. The localized heat induces a structural change in the polymer that releases the drug
2. gold nanoparticles and drug molecules are embedded in liposomes, which break down upon heating to release the drug
3. drug molecules are directly attached to the gold nanoparticle surface via spacer molecules. Local heat that is generated is enough to break this bond and release the drug

4.1.4. Photothermally triggered drug delivery systems

Targeted drug delivery systems that make use of the heat generated at the surface of gold nanoparticles during the photothermal effect requires decoration of the nanoparticle

surface with thermally responsive systems. Such thermally responsive systems involve chemical reactions that are temperature sensitive and reversible. The Diels-Alder reaction is one such type of well-studied chemical reaction that is thermally responsive. The Diels-Alder reaction is a reversible [4+2] cycloaddition of a diene and a dienophile used to make a six-membered ring, in a regio- and stereo-controlled manner (Scheme 4.2).[259] Altering the structure of the two components (diene and dienophile) adjusts the temperature at which the retro/reverse reaction is activated.

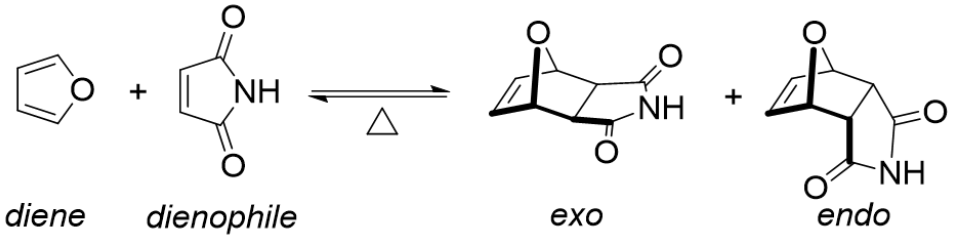

Scheme 4.2: Diels-Alder reaction between Furan and Maleimide

Among the early examples of employing Diels-Alder adducts onto gold nanoparticles were developed by Bakhtiari *et al.* in 2009. This system involved a furan terminated fluorescein dye that was attached via Diels-Alder reaction with the maleimide component that was anchored onto the silica-gold core-shell nanoparticles through Au-S bonds (Figure 4.9). The change in fluorescence emission from the dye molecule before and after stimulation was used to monitor the photothermally induced release process.[247]

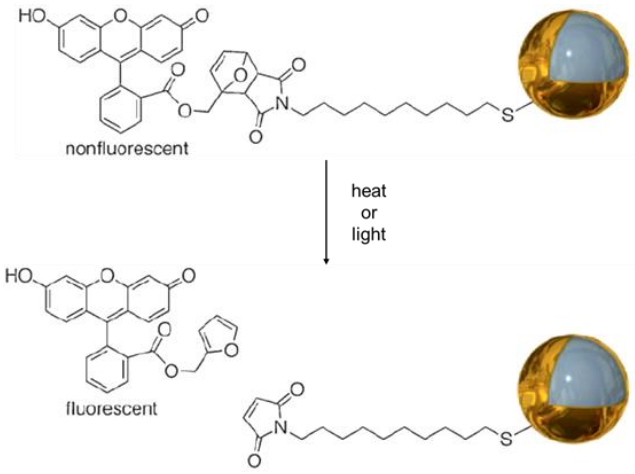

Figure 4.9: Photothermally triggered the release of the fluorescein dye from the surface of silica-gold core-shell nanoparticles by inducing retro-Diels-Alder reaction of anchored 7-oxa-bicyclo-[2.2.1]hept-5-ene-2,3-dicarboxylic imide derivative. Reproduced with permission from ref. 247 © 2009 WILEY-VCH Verlag GmbH & Co. KGaA [247]

Similar work was done by Yamashita *et al.* who designed and modified gold nanorods with polyethylene glycol (PEG) terminated with maleimide through Diels-Alder reaction with the furan side tethered to the gold nanorod surface by Au-S bonds. The release mechanism involved the retro-Diels-Alder reaction of the Diels-Alder adduct induced by the photothermal effect of gold nanorods (Figure 4.10).[257]

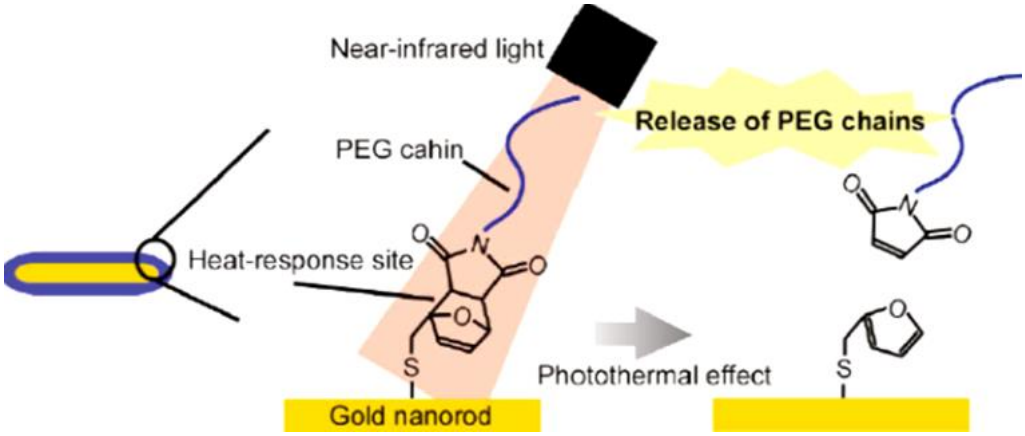

Figure 4.10: Photothermal release of PEG chain from the surface of gold nanorods modified with PEG-based Diels-Alder adduct. Reproduced with permission from ref. 257 © 2011 American Chemical Society [257]

In one of the recent examples, Asadirad *et al.* developed a system that could provide an ultimate "on-command" control over the photothermal release process of nanoparticles. The system consisted of a photoresponsive dithienylethene based chromophore which was synthesized as a Diels-Alder adduct of maleimide and dithienylfuran. This was then linked to silica-gold core-shell nanoparticles by Au-S linkages. While the chromophore is in its ring-closed isomer, it did not undergo any retro-Diels-Alder reaction upon irradiation with near-IR light to trigger the photothermal effect due to the absence of the cyclohexene ring. The intended release of dithienylfuran was only observed when the system was irradiated with visible light, to generate the ring-open isomer of the Diels-Alder adduct, and near-IR light to, then, activate the retro-Diels-Alder reaction by the photothermal effect (Figure 4.11).[260]

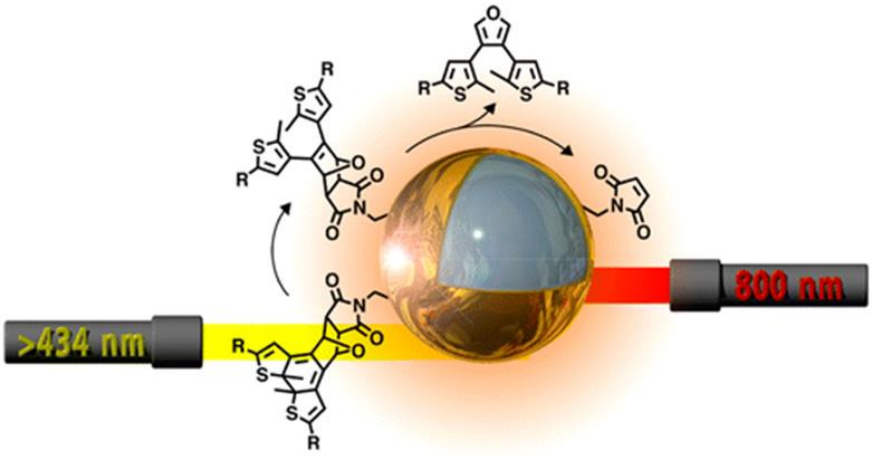

Figure 4.11: Two input stimuli, visible and near-IR light, are required to bring about the bond-breaking and release of the desired product. Reproduced with permission from ref. 260 © 2015 American Chemical Society [260]

The research reported so far has involved the release of a molecule that is directly linked to the gold nanoparticle surface. While direct tethering of the molecule onto the nanoparticle surface is straightforward, there are some disadvantages to this approach of direct binding and release:

1. easy desorption of ligands from the gold nanoparticle surface leading to decreased stability of the gold nanoparticles, thereby, increasing the chances of their aggregation, *i.e.*, small ligand molecules on the gold nanoparticle surface undergo dynamic binding and unbinding process that can cause the ligand to fall off by excessive washing[261]
2. the selective nature of the core material towards certain ligands which limits the choice of molecules that can be bound, *i.e.*, gold nanoparticles (soft acids) preferentially interact with large anionic or neutral ligands (soft bases) to form stable soft-soft interactions[241]
3. the release approach, in most cases, involves breaking of Au-S bond that releases free thiols which are detrimental to living cells[262]

An alternative strategy to avoid the above issues would be to incorporate an additional molecular coating layer that can provide for the desired release in biological environments while trapping the less desirable elements.

4.1.5. Polymer coatings to create stable nano-assemblies

Decorating the gold nanoparticles with amphiphilic polymers would be a desirable approach to create nano-assemblies that can be dispersed in water without compromising

their physical and chemical properties. Amphiphilic polymers are defined as macromolecules that are composed of both hydrophilic and hydrophobic components (Scheme 4.3). In aqueous conditions, these polymers create a core-shell structure with a hydrophobic interior and a hydrophilic exterior.[263]

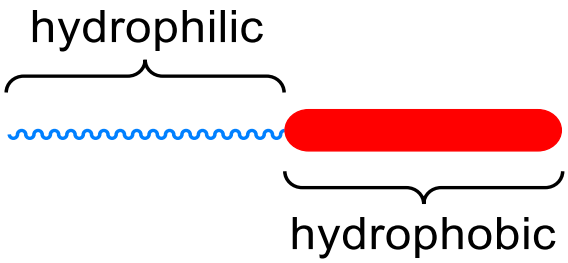

Scheme 4.3: Schematic representation of an amphiphilic block-co-polymer

This dual nature of the amphiphilic polymer coating can be advantageous since:

1. there are multiple contact points between the ligand and polymer coating, thus, reducing the desorption process[241]
2. the coating layer is not dependent on the nature of core material and ligand as the binding interactions are mostly hydrophobic interactions and van der Waals forces[241]

Also, the dual nature of the polymer shell helps to dissipate nano-assemblies in water, while the internal hydrophobic domain enables the entrapment of nanoparticles and organic molecules via ligand exchange (Figure 4.12).[264,265]

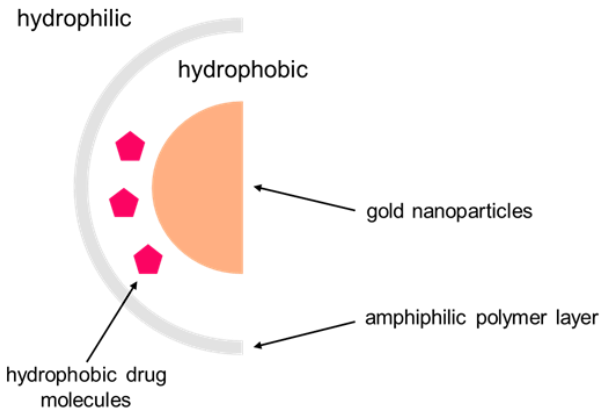

Figure 4.12: Amphiphilic polymer shell for encapsulation of gold nanoparticles and drug molecules that will utilize the photothermal effect of gold nanoparticles to release the desired drug

Wu *et al.* have successfully used a straightforward polymer encapsulation method to create numerous organic-inorganic hybrid systems based on upconverting nanoparticles and photoresponsive molecules without difficulty. The system neither required any synthetic modification of the photoresponsive molecules used nor was the ligand exchange on nanoparticles requisite.[265] While the use of such nano-assemblies based on upconverting nanoparticles has been reported for *in-vitro* and *in-vivo* bioimaging, drug delivery, and photodynamic therapy[266], there are not many examples of these nano-assemblies based on gold nanoparticles.[267,268]

In the following sections, we discuss the two different strategies of encapsulating biologically relevant molecules and gold nanoparticles. The release mechanism in both cases would be the retro-Diel-Alder reaction that is induced by the photothermal effect of the gold nanoparticles.

4.2. Strategy I – direct loading of the Diels-Alder adducts into the nano-assembly

This section provides a detailed description of the first strategy of encapsulation of biologically relevant molecules and gold nanoparticles by directly loading the Diels-Alder adduct of the desired molecule, in this case, Tyrphostin A8, into the polymer shell along with gold nanoparticles.

4.2.1. Graphical abstract

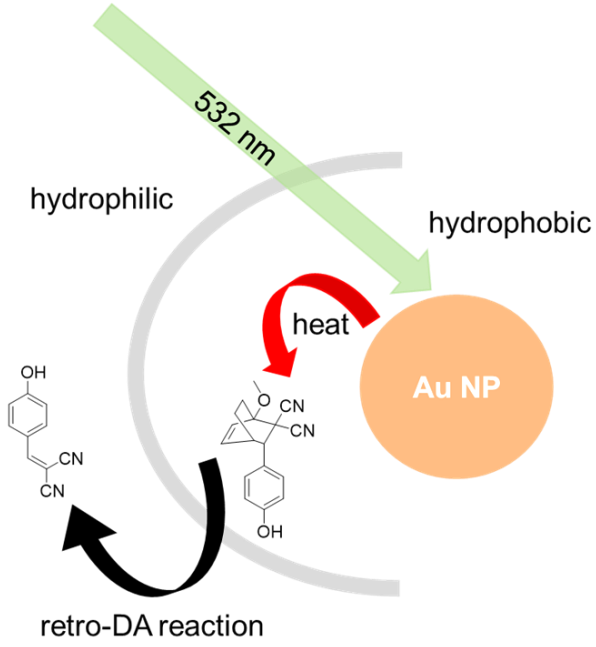

4.2.2. Tyrosine Kinase inhibitors

Tyrosine kinase inhibitors (TKIs) are defined as a class of small molecules that block the action of enzymes called tyrosine kinases.[269] Tyrosine kinases are the enzymes that are responsible for selective phosphorylation of tyrosine residues in different substrates using ATP.[270] These enzymes are classified into two categories: Receptor Tyrosine Kinases and Cytoplasmic/Non-receptor Tyrosine Kinases. Receptor Tyrosine Kinases (RTK) are part of multiple cell functions like cell growth, migration, division, and metabolism.[271] Activation of these enzymes is a highly controlled process, but, upon mutation, there is an unregulated cell growth leading to amplification of the entire cell-signalling pathway

(Figure 4.13).[272] This overexpression of the Epidermal Growth Factor receptor (EGFR) can lead to cancer, diseases in the nervous system, and injury.[273]

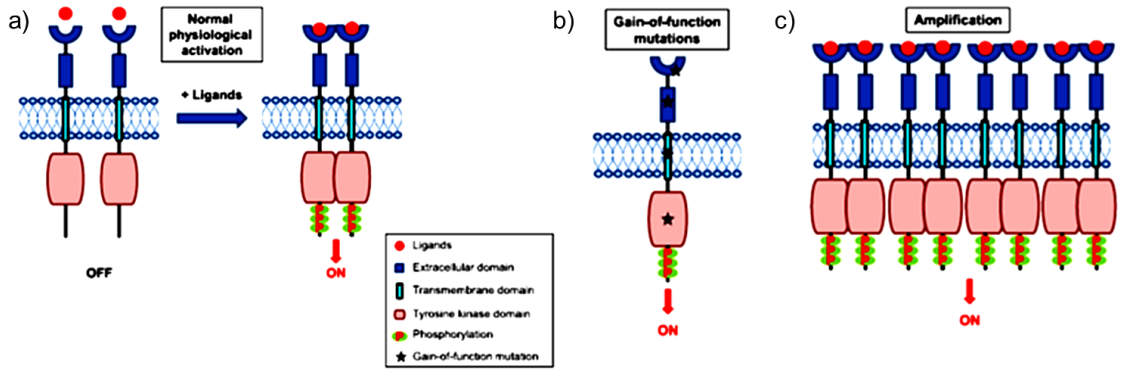

Figure 4.13: Schematic representation of: a) RTK activation in a normal cell; b) Potential mutations in various subdomains of RTK; c) overexpression of RTKs leading to malignancy. Reproduced with permission from ref. 271 © 2018 Springer Nature [271]

TKI molecules are designed to have a greater affinity toward the substrate site of the EGFR kinase domain and to block the autophosphorylation of the receptor that is dependent on EGF.[274] Naturally occurring compounds like erbstatin, quercetin, genistein, and lavendustin A, were recognized to inhibit the EGF receptor autophosphorylation in certain cancer cells in the early 1980s.[272,274] Early synthetic TKI molecules were based on the structure of benzylidene malononitrile core and closely resembled the structure of erbstatin and tyrosine (Scheme 4.4) and came to be known as “tyrphostins” (TYRosine PHOSphorylation Inhibitors).[274]

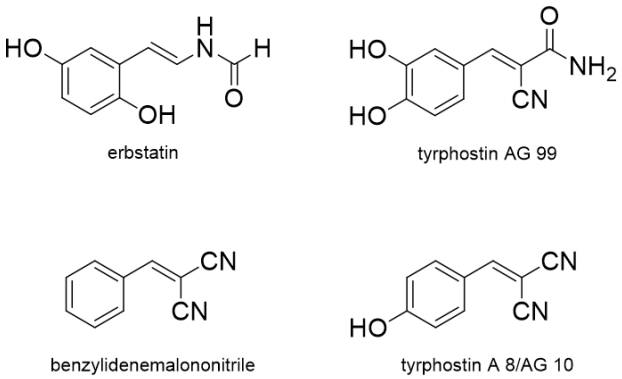

Scheme 4.4: Structures of some natural and synthetic TKIs

Tyrphostin A8/AG 10 is the simplest version of this class of chemotherapeutic agents. While, this class of therapeutics is highly effective as anti-cancer drugs, but they cause

significant toxic side effects. Moreover, due to their short circulation time in the bloodstream, there is a requirement for a controlled and targeted delivery system.[273,275]

4.2.3. Our system

Our concept is illustrated in Scheme 4.5 where three unique environments are depicted. The one on the far left represents the state of the nano-assembly prior to any treatment. In this case, the bicyclic compound (**1**) is trapped in the hydrophobic layer close to the nanoparticle. The middle 'cell' would be the result when the nano-assembly is exposed to visible light and the photothermal effect has generated enough heat to trigger the retro-Diels-Alder reaction producing Tyrphostin A8 and the cyclohexadiene. The far right 'cell' shows the ultimate outcome. Because the Tyrphostin A8 is less hydrophobic, it should be released from the nano-assembly where it can be effective. The cyclohexadiene retains its hydrophobic nature and should remain trapped in the nano-assembly. This last point is an additional advantage of our approach as it prevents any detrimental effect the by-products of the release event may cause.

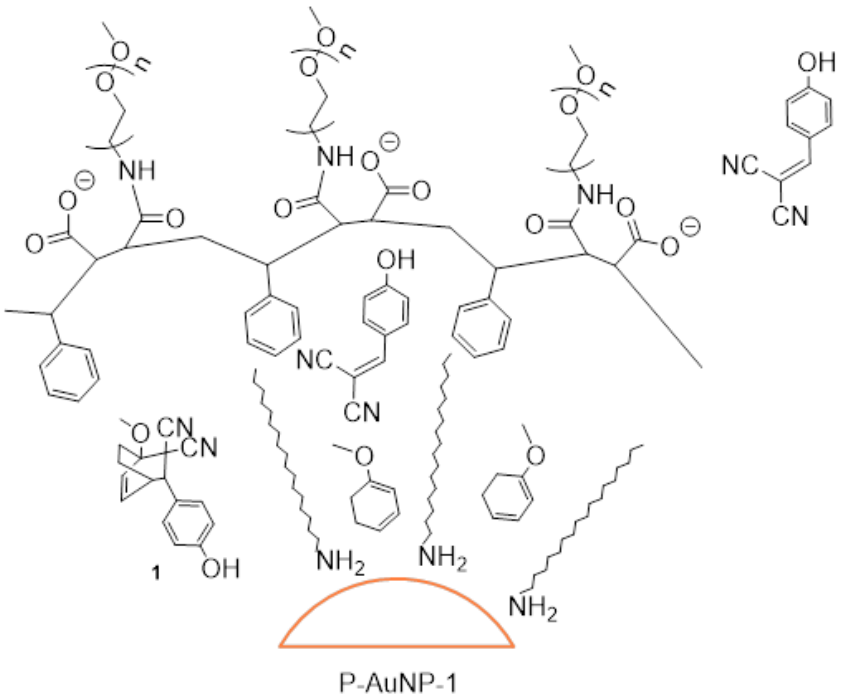

Scheme 4.5: Left cell: Bicyclic compound **1** trapped within the hydrophobic shell surrounding octadecylamine-coated gold nanoparticles; Middle cell: Retro-Diels-Alder reaction of bicyclic compound 1; Right cell: Release of Tyrphostin A8 ((4-hydroxybenzylidene)-malonitrile) and entrapment of 1-methoxy-1,3-cyclohexadiene

4.2.4. Results and Discussion

4.2.4.1. Synthesis

The bicyclic Diels-Alder adduct (**1**) was synthesized in modest yield by a single step Diels-Alder reaction between the commercially available Tyrphostin A8 ((4-hydroxybenzylidene)-malononitrile) and 1-methoxy-1,3-cyclohexadiene in 1,4-dioxane (Scheme 4.6). The final product structure was confirmed by ^{1}H-NMR spectroscopy with the appearance of new peaks in the region of δ: 1-2 ppm for the bridging methylene protons and the appearance of the protons of the C=C bond at δ = 6.50 ppm (d, 1H) and δ = 6.90 ppm (dd, 1H) of the 6-membered adduct ring. The structure was further confirmed by NMR couplings and X-ray crystallography data that was obtained for a similar adduct. Experimental details and characterizations of **1** are provided in Section 4.5.

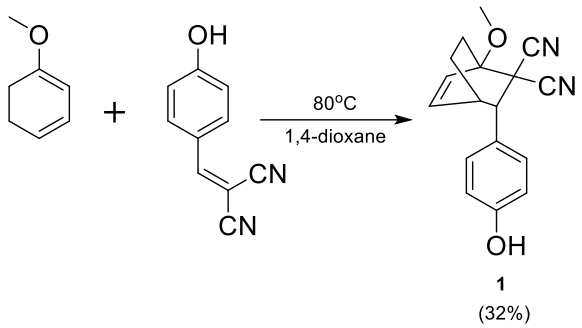

Scheme 4.6: Synthesis of bicyclic Diels-Alder adduct (**1**)

Synthesis of the amphiphilic polymer shell (**P**) was conducted in a single step by ring-opening of poly(styrene-*co*-maleic anhydride) (PSMA) with O-(2-aminopropyl)-O′-(2-methoxyethyl)polypropylene glycol (JeffAmine® M-2070), both of which were commercially obtained (Scheme 4.7). Polymeric systems PSMA and JeffAmine® M-2070 were chosen to ensure that the final nano-assemblies had good water dispersibility while maintaining a lipid-like core structure to trap hydrophobic molecules. The presence of IR bands at $\bar{\upsilon}$ = 3000 cm^{-1} for amide N-H stretching, $\bar{\upsilon}$ = 2865 cm^{-1} for styrene C-H stretching and $\bar{\upsilon}$ = 1090 cm^{-1} for PEG C-O stretching indicate the opening of the anhydride ring and attachment of the desired PEG chains to make the polymer shell amphiphilic. Experimental details and characterizations of **P** are provided in Section 4.5.

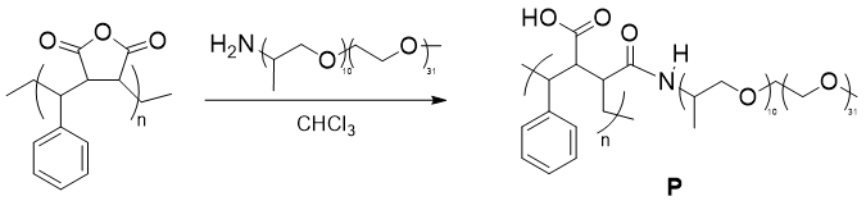

Scheme 4.7: Synthesis of amphiphilic polymer shell (**P**)

Gold nanoparticles (**AuNP**) were prepared in an aqueous solution using the literature procedure[276] using sodium citrate as the reducing and capping agent. The produced gold nanoparticles had an average diameter of 11.2 nm ± 1.2 nm as obtained from TEM. The UV-visible Absorption spectrum of the citrate-coated gold nanoparticles showed its sharp characteristic surface plasmon resonance (SPR) band centred at 519 nm (Figure 4.14 a) red line). The monodisperse nature of the citrate-coated gold nanoparticles was determined by TEM imaging (Figure 4.14b)) and Particle Size Analysis (PSA) by DLS measurements (Section 4.5.7). To create the desired hydrophobic environment around the gold nanoparticles, the citrate-coated gold nanoparticles were transferred into the organic phase (chloroform) by the procedure of ligand exchange with octadecylamine (ODA).[277] The absorption spectrum for octadecylamine coated gold nanoparticles in chloroform (Figure 4.14 a) green line) was similar to that obtained for citrate coated gold nanoparticles in water with a small bathochromic shift in the λ_{max} from 519 nm in water to 526 nm in chloroform (difference = 7 nm), indicating that the organic dispersions of octadecylamine coated gold nanoparticles were stable under ambient conditions.

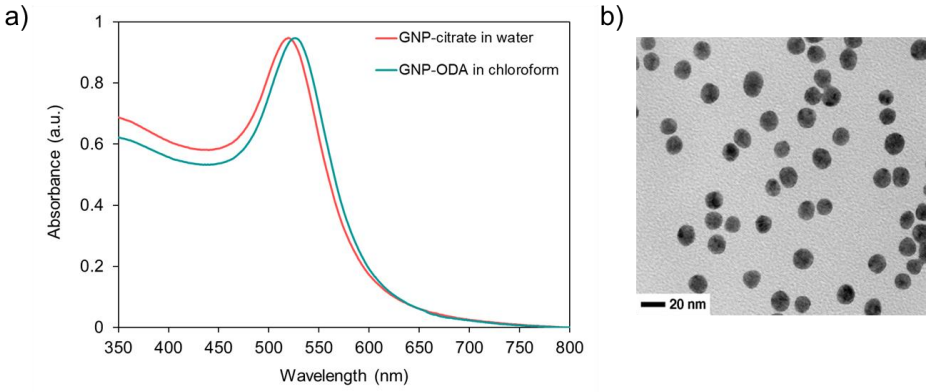

Figure 4.14: a) Normalized UV-vis absorption spectra of dispersions of citrate-coated gold nanoparticles (GNP) in water (2.55 mg/mL) (red line) and ODA-coated gold nanoparticles (GNP) in chloroform (0.39 mg/mL) (green line); b) TEM image of water dispersion of citrate-coated gold nanoparticles (2.55 mg/mL, 11.2 ± 1.2 nm)

The final nano-assembly (**P-AuNP-1**) was prepared in the organic phase by sequential addition of the amphiphilic polymer (**P**) followed by the solution of bicyclic Diels-Alder adduct (**1**) in chloroform. After stirring the mixture for 18 h, the organic solvent was removed, and the self-assembled nanostructure was dispersed in water (Scheme 4.8).

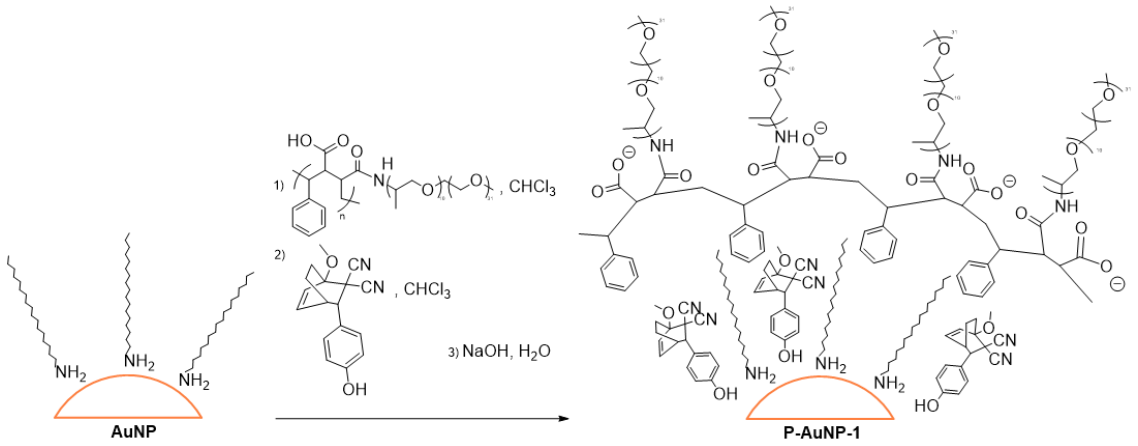

Scheme 4.8: Synthesis of the nano-assembly, **P-AuNP-1**

The UV-visible Absorption spectrum of the aqueous solution **P-AuNP-1** shows a bathochromic shift in the SPR band which was now centred at 524 nm (Figure 4.15 a)). This shift of λ_{max} towards longer wavelengths can be attributed to the ligand exchange from citrate to octadecylamine which may lead to the redistribution of charge on the nanoparticle surface.[278] The average diameter of the **P-AuNP-1** nano-assembly was determined using TEM and was obtained to be 10.68 nm ± 0.58 nm (Figure 4.15 b)). After encapsulation, the average size of the particles measured by TEM was similar to that of the original citrate-coated nanoparticles (11.2 nm ± 1.2 nm), but, the DLS measurements (Section 4.5.7), which provide an estimated size of the entire nano-assembly including the organic layer around the inorganic core, determined the average diameter of the nano-assembly to be 21.34 nm. The difference in size measurements from TEM and DLS for the nano-assembly is due to the solvation effect of the fully extended polyethylene glycol chains.

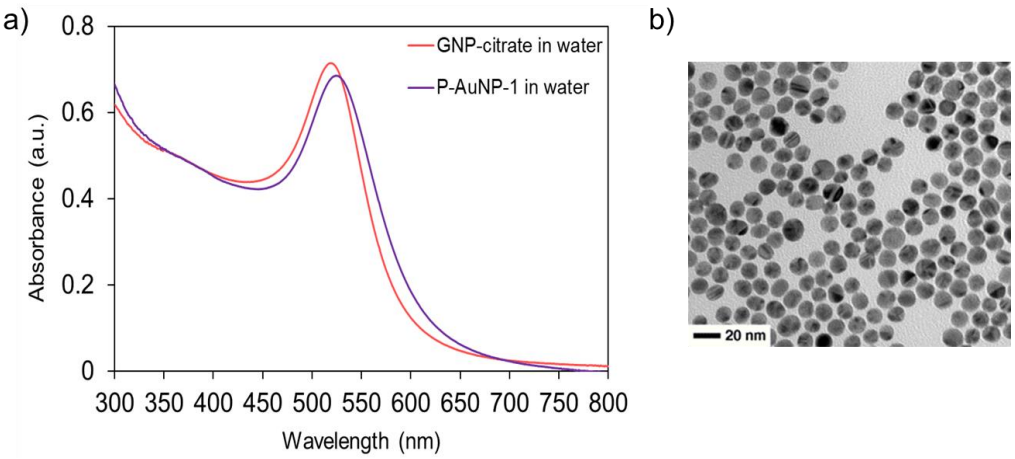

Figure 4.15: a) Normalized UV-vis absorption spectra of dispersions of citrate-coated gold nanoparticles (GNP) in water (2.55 mg/mL) (red line) and **P-AuNP-1** in water (2.66 mg/mL) (purple line); b) TEM image of water dispersion of **P-AuNP-1** (2.66 mg/mL, 10.68 ± 0.58 nm)

The loading of the adduct **1** within the nanoassembly **P-AuNP-1** was determined using the UV-visible absorption spectroscopy and was estimated by determining the concentration of released Tyrphostin A8 in the flow-through filtrate after the photothermolysis and spin-filtering and comparing it to the amount of adduct **1** based on a 1:1 reaction ratio. The number of molecules of adduct **1** per nanoparticle is approximately 92 (see Table 4.5 in Section 4.5.7).

4.2.4.2. Thermolysis of bicyclic Diels-Alder adduct 1

To understand the thermal behaviour of the novel bicyclic compound (**1**), a heat-induced retro-Diels-Alder reaction of the bicyclic compound (**1**) was conducted by heating the solution of **1** (4.10 x 10^{-3} M) in 40% DMSO in a water mixture at 90 °C (Scheme 4.9). The goal of this study was to determine whether any retro-Diels-Alder reaction is triggered at high temperatures and to provide the basis for the subsequent photothermal release experiment.

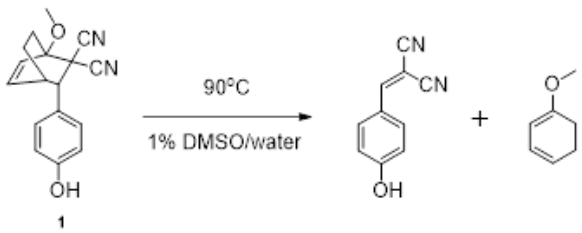

Scheme 4.9: Retro-Diels-Alder reaction of **1**

The reaction progress was evaluated using UV-visible absorption spectroscopy by removing 0.02 mL aliquots at every measurement time interval and immediately quenched with ice-cold DMSO/water solution. The aliquot solutions were diluted to a final concentration of 8.20 x 10^{-5} M in 1% DMSO in water for all UV-visible absorption measurements (Figure 4.16 a)). After acquiring an initial spectrum for **1**, the reaction was heated at 90°C and the spectra were recorded every 30 seconds for the first 5-minute reaction interval. During this time a small band centred at 415 nm began to appear. After 10 minutes of heating, the band at 415 nm became stronger in intensity. The band at 415 nm continued to increase in intensity up to 60 minutes of heating. At the 30-minute heating interval, a new band began to appear at 330 nm. The band at 330 nm continued to increase in intensity upon further heating (Figure 4.16 b)). The results obtained from the initial thermolysis experiment suggest that Tyrphostin A8 may not be released in the form suggested in Scheme 4.9 and that the released molecule undergoes some chemical transformation upon extended heating.

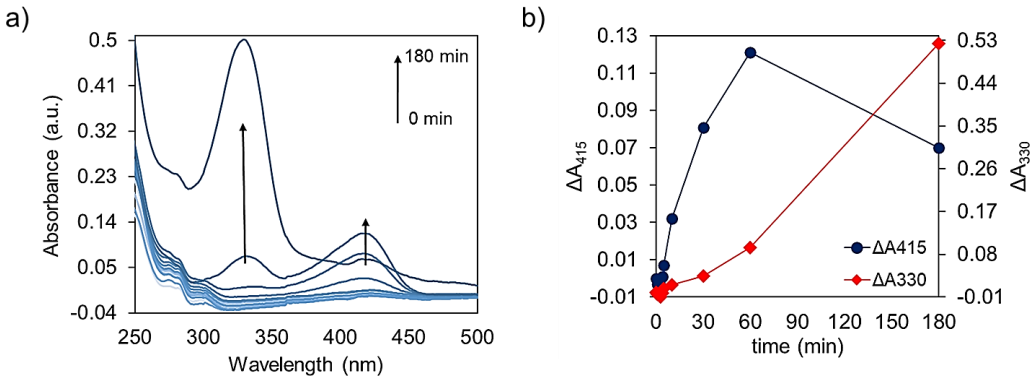

Figure 4.16: a) Changes in the UV-vis absorption spectrum when a solution of **1** (8.2 x 10^{-5} M) in 1% DMSO in water was heated at 90 °C for a total of 180 minutes; b) Kinetic plot summarizing the changes in the absorbance values at λ_{max} = 330 nm and λ_{max} = 415 nm upon heating the adduct **1** over time

The Tyrphostin A8 molecule can exist in both phenolic and phenoxide forms. The proton transfer between the phenol and the phenoxide form of Tyrphostin A8 is a highly solvent specific phenomenon and is known to occur in solvents like DMSO and water due to the strong solute-solvent interactions occurring in these solvents.[279] Additionally, the presence of electron-withdrawing dicyanovinyl group at the *para* position to the OH group of the phenol results in a strong through-resonance interaction between the oxygen and the dicyanovinyl group in the structure that results in the better stabilization of the phenoxide

form of (4-hydroxybenzylidene)malononitrile (Tyrphostin A8).[280] The net result is a strong intramolecular charge transfer (ICT) band observed at λ_{max} = 415 nm in our spectrum (Figure 4.16 a)).[279]

Moreover, the Tyrphostin A8 belongs to the class of compounds called arylmethylenemalononitriles that tend to undergo facile hydrolysis under aqueous conditions to form their corresponding aldehydes along with the removal of malononitrile.[281,282] The possible mechanism for the retro-Diels-Alder reaction of **1** to release Tyrphostin A8 and its hydrolysis to form p-hydroxybenzaldehyde is shown in Scheme 4.10.

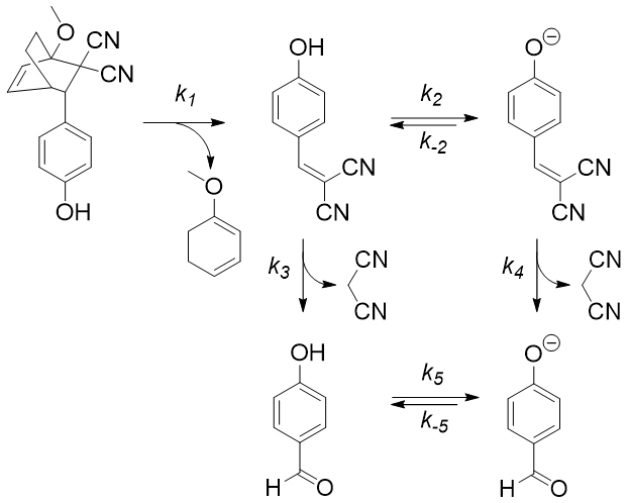

Scheme 4.10: The retro-Diels-Alder reaction of compound **1** releasing Tyrphostin A8, which can deprotonate and/or hydrolyze to benzaldehyde. The retro-Diels-Alder and hydrolysis reactions are portrayed as irreversible given the dilute condition of all components.

To further review the products of thermolysis of **1**, *i.e.*, the bands at 330 nm and 415 nm, authentic solutions of Tyrphostin A8 and its hydrolysis product p-hydroxybenzaldehyde were prepared (1.00 x 10^{-5} M, water with 40% DMSO) and analyzed using UV-visible absorption spectroscopy. The initial measurement showed λ_{max} at 353 nm for Tyrphostin A8 and 285 nm for the aldehyde (Figure 4.17 a)). The solutions were then gently heated in a water bath at 50°C for a total of 5 minutes. Upon acquiring the spectra after 5 minutes, the band for Tyrphostin A8 at 353 nm completely shifted towards 430 nm. A similar bathochromic shift in the absorbance for the aldehyde to 337 nm was also observed (Figure 4.17 b)). This shift in λ_{max} towards longer wavelengths has been described as a result of the solvation of the phenolic molecules and is brought on by heating and/or by

changes in pH.[279] Additionally, this solvation is highly sensitive to the solvent ratio as λ_{max} of Tyrphostin A8 shifts from 415 nm in water with 1% DMSO to 430 nm in water with 40% DMSO. Nonetheless, the results of the thermolysis experiment do suggest that authentic Tyrphostin A8 was released into the solution. However, it also indicates that hydrolysis to the benzaldehyde occurs before the release of Tyrphostin A8 was complete as the peak corresponding to the aldehyde appeared to be significantly higher in intensity from 1 to 3 hours. Because the extinction coefficients are of a similar magnitude (Figure 4.17 a) was shown at equimolar concentrations) release of Tyrphostin A8 continued after 1 hour and was not complete before the first appearance of benzaldehyde. The appearance of benzaldehyde must therefore be from the hydrolysis of (4-hydroxybenzylidene)malononitrile as compound **1** has no aldehyde present in the structure nor would the retro-Diels Alder be capable of preparing such a molecule.

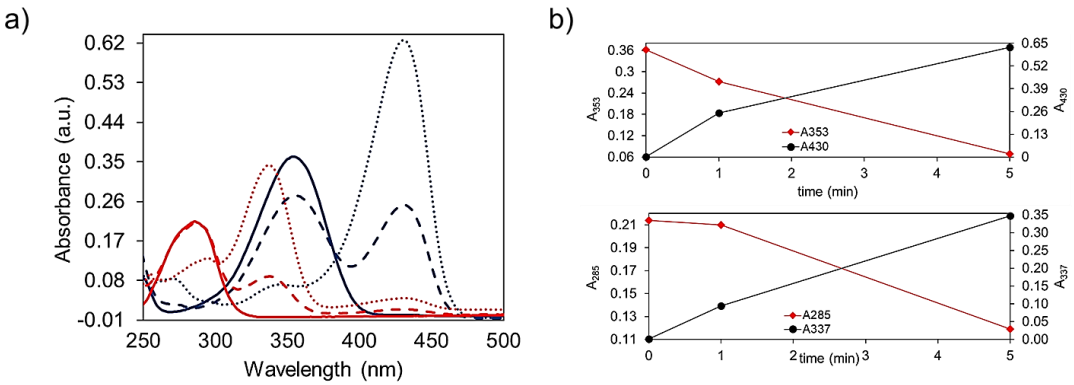

Figure 4.17: a) UV-vis absorption spectra of a 1.00 x 10^{-5} M solution of Tyrphostin A8 in 60% DMSO in water (blue lines) and a 1.00 x 10^{-5} M solution of benzaldehyde in 40% DMSO in water (red lines) upon heating at 50°C for 0 min (solid lines), 1 min (dashed lines), and 5 min (dotted lines); b) Kinetic plot summarizing the changes in the absorbance values for Tyrphostin A8 at λ_{max} = 353 nm and λ_{max} = 430 nm (top) and *p*-hydroxybenzaldehyde at λ_{max} = 285 nm and λ_{max} = 337 nm (bottom) upon heating over time

The results for the thermolysis experiment were further corroborated by analyzing the reaction progress by ^{1}H NMR spectroscopy. After obtaining the initial ^{1}H NMR spectrum for **1** (6 x 10^{-5} g in 1% DMSO-d_6 in D_2O), the tube was heated at 90°C for 4.5 h with ^{1}H NMR spectra being recorded every hour. After 1 h of heating, the peaks for the protons of the C=C bond at δ = 6.50 ppm (d, 1H) and δ = 6.90 ppm (dd, 1H) of the 6-membered

adduct ring disappeared completely. While the aromatic protons corresponding to Tyrphostin A8 ((4-hydroxybenzylidene)-malononitrile) appear at δ = 7.45 ppm, the peak for the alkene proton connected to the nitrile groups is not observed. Instead, a sharp singlet is seen at δ = 9.70 ppm in the region of resonance of aldehyde protons (Figure 4.18).

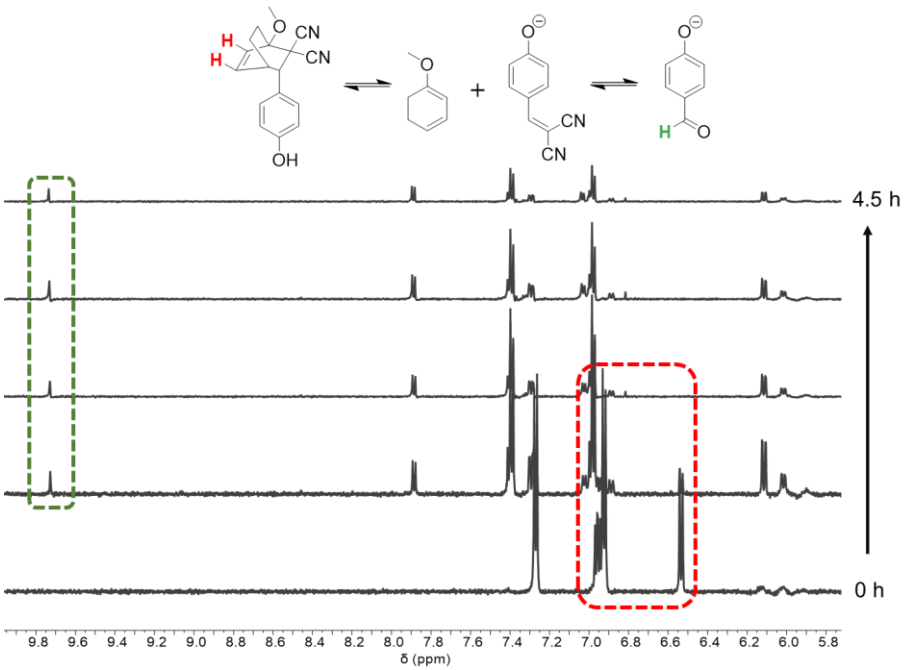

Figure 4.18: Changes in the ^{1}H NMR spectrum when a solution of **1** (6 x 10^{-5} g) in 1% DMSO-d_6 in D_2O was heated at 90 °C; after 1 h of heating the alkene protons of the adduct (red dashed box) disappear indicating the occurrence of retro-Diels-Alder reaction followed by further hydrolysis of the released Tyrphostin A8 to yield 4-hydroxybenzaldehyde indicated by the appearance of aldehyde proton at δ = 9.70 ppm (green dashed box)

Therefore, the thermolysis of adduct **1** under aqueous conditions led to the formation of hydrolyzed products instead of retro-Diels-Alder products.

4.2.4.3. Photothermolysis of nano-assembly P-AuNP-1

The photothermal release of Tyrphostin A8 triggered by the retro-Diels-Alder reaction of **1** encapsulated in the nano-assembly **P-AuNP-1** was also assessed using UV-visible absorption spectroscopy. The minimum power of the 532 nm nanosecond pulsed laser that is required to trigger the retro-Diels-Alder reaction to release Tyrphostin A8 was

determined by irradiating the **P-AuNP-1** nano-assembly with different laser powers for a time interval of 1 minute. Upon acquiring an initial spectrum for **P-AuNP-1**, the aqueous dispersion of **P-AuNP-1** (2.66 mg/mL) was irradiated with a 532 nm nanosecond pulsed laser (10 Hz, 5 mJ/pulse, 10 ns) at 100 mW/cm^2 for 1 minute followed by increasing the power density by 100 mW/cm^2, and the spectra of the solution being acquired after each power density increment until no further change in the spectrum were observed. No change in the spectrum was observed upon increasing the power density up to 700 mW/cm^2. A new peak in the region of 380-440 nm, corresponding to released Tyrphostin A8, began to appear at the power density of 800 mW/cm^2 and continued to increase upon increasing the power to 1 W/cm^{2}after which no change in the spectrum was observed.

In a similar experiment, the photothermal release of Tyrphostin A8 from the nanoassembly, **P-AuNP-1**, was observed by irradiating an aqueous dispersion of **P-AuNP-1** (2.66 mg/mL) with a nanosecond pulsed laser (10 ns, 532 nm) at 800 mW/cm^2 (Not all of the light is absorbed by the sample. The absorbed power is 230 mW/cm^2. The remainder of the light is transmitted or absorbed by the cuvette. See Table 4.8 in section 4.5.7) in 1-minute intervals. After acquiring an initial spectrum for **P-AuNP-1**, an immediate increase in the intensity of the band centred at 415 nm was observed upon irradiation (Figure 4.19a)). This band corresponds to the phenoxide form of Tyrphostin A8 released from bicyclic compound **1** through a retro-Diels-Alder reaction like the results illustrated in the thermolysis experiments. The retro-Diels-Alder reaction assisted by the photothermal effect of the gold nanoparticles was shown to be a quick process, with the completion of the retro-Diels-Alder reaction in 5 minutes possibly due to the migration of the adduct closer to the gold nanoparticle core within the polymeric shell.[283] Additionally, no bands for hydrolyzed products were observed upon photothermolysis indicating that even though the nano-assembly was dispersed in water, the local interior environment where the adduct resided within the amphiphilic nanoassembly, consisting of the hydrophobic chains of the amphiphilic polymer and the ODA ligands coating the gold nanoparticles, lacked enough water for the hydrolysis reaction to occur.[265, 283, 284] Furthermore, the released product was almost entirely obtained in the flow-through (supernatant) after centrifugation and filtration of the nanoassembly as no peak for the released Tyrphostin A8 at 415 nm was observed for the redispersed pellet. Mass spectrometry analysis of the flow-through confirmed the presence of Tyrphostin A8 (Figure 4.19 d)). Notably, the stability of the nano-assembly was mostly retained after irradiation with the 532 nm pulsed laser as

observed from the TEM images before and after irradiation (Figure 4.19 b), c)). Moreover, the SPR band for gold nanoparticles was seen to shift from 524 nm to 517 nm after the irradiation without any peak broadening. This shift towards shorter wavelengths can be attributed to possible fragmentation and vaporization of gold nanoparticles, which is a direct consequence of the fact that the gold nanoparticles absorb laser energy leading to high temperatures inside them with low heat transfer to the surrounding solvent.[285,286,287]

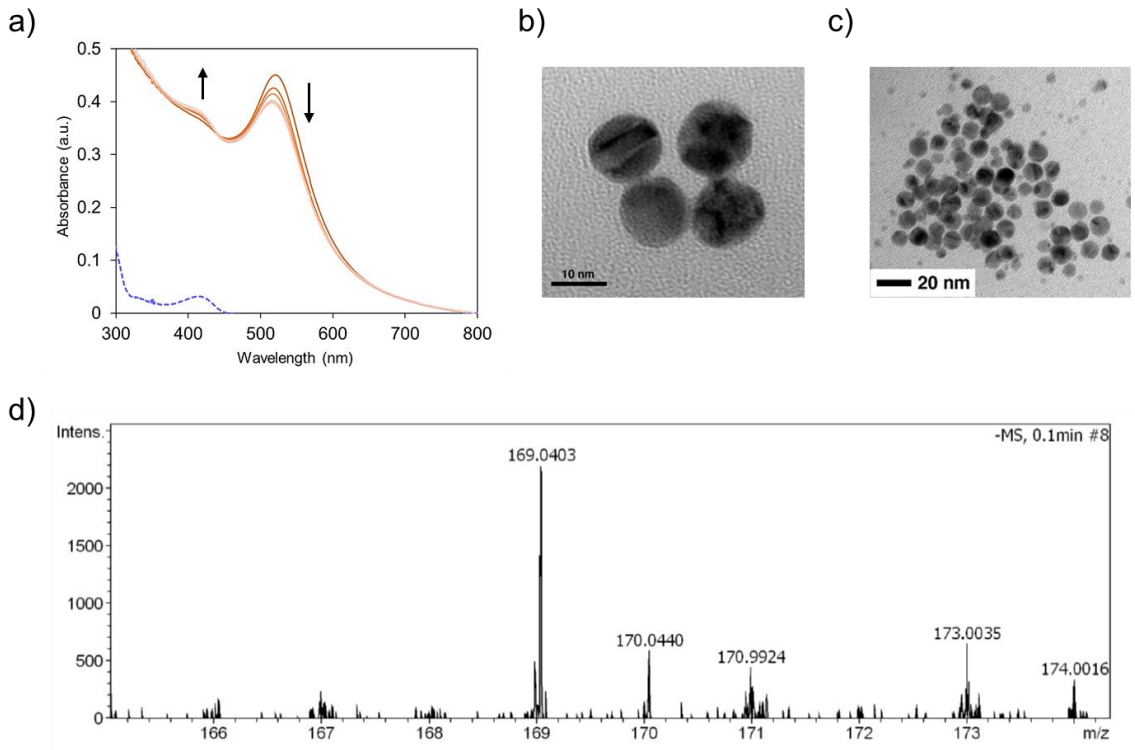

Figure 4.19: a) Changes in the UV-vis absorption spectrum when an aqueous solution of **P-AuNP-1** is irradiated with a nanosecond pulse laser (10 ns, 532 nm) at 800 mW/cm^2. The dotted line corresponds to released Tyrphostin A8 in the supernatant after centrifugation; b) TEM image of an aqueous dispersion of **P-AuNP-1** before irradiation with 532 nm pulsed laser light (10 Hz, 5 mJ/pulse, 10ns); c) TEM image of an aqueous solution of **P-AuNP-1** after irradiation with 532 nm pulsed laser light (10 Hz, 5 mJ/pulse, 10 ns) for a total of 5 min; d) High-resolution mass spectrum analysis of the flow-through confirms the presence of Tyrphostin A8. ESI-MS: m/z 169.0403 (M-H) Calc. $C_{10}H_5N_2O^-$ 169.0407.

4.2.5. Conclusion summary

In this section, the creation of hybrid organic-inorganic nano-assembly based on gold nanoparticles, **P-AuNP-1**, using hydrophobic bicyclic Diels-Alder adduct, **1**, was successfully demonstrated. It was illustrated that upon exposure to 532 nm pulsed laser,

1 encapsulated inside the nano-assembly underwent a retro-Diels-Alder reaction to release Tyrphostin A8, a simple chemotherapeutic drug, via the photothermal heating process. The ability of the amphiphilic polymer shell to create water dispersibility while retaining local hydrophobicity can make this method optimal to design systems that can be used in biological conditions.

4.3. Strategy II – tethering of the Diels-Alder adducts onto the amphiphilic polymer

In this section, a detailed discussion on the unique second strategy is provided, which is a proof-of-concept, for encapsulation of biologically relevant molecules and gold nanoparticles by covalently tethering the Diels-Alder adducts of the desired molecule, in our case, N-ethylmaleimide, onto the polymer shell and then wrapping this modified amphiphilic polymer assembly onto the gold nanoparticles to create nanoassemblies that are stable in aqueous environments.

4.3.1. Graphical abstract

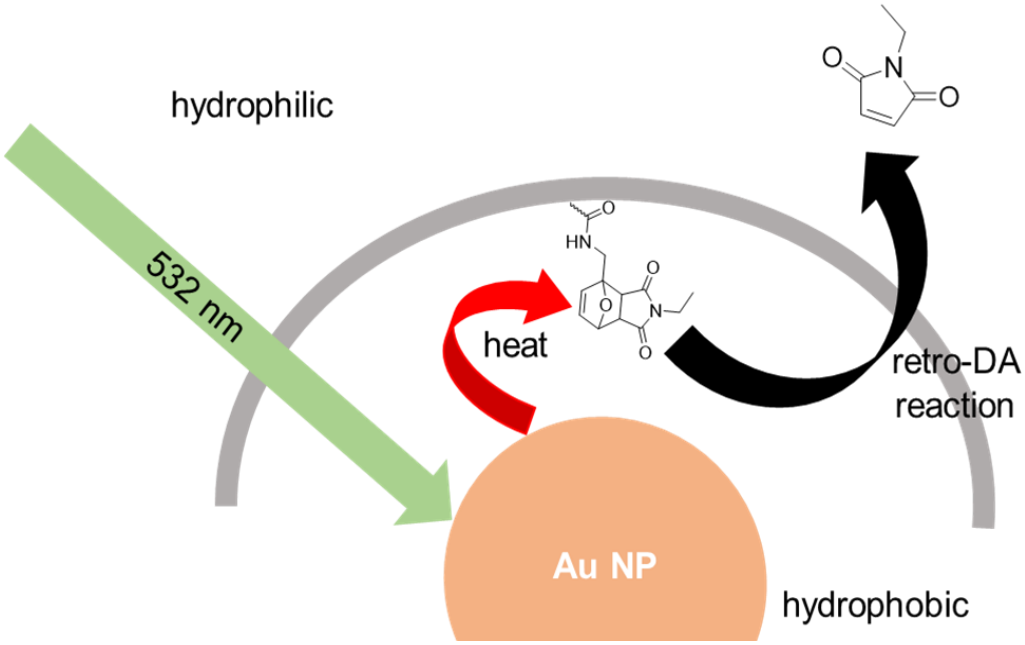

4.3.2. Polymeric systems for Drug delivery

Diels-Alder based “click chemistry”[288] has gained much attention recently, for the development of drug delivery systems and biomaterials. Hydrogels and polymeric nanoparticles based on amphiphilic polymers have been developed for biomedical applications.[289] Some of the key advantages of Diels-Alder chemistry include:

1. ease of access to suitable diene-dienophile pairs[289]
2. facile functionalization of molecules of interest with reactive groups[289]
3. free from side reactions and by-products[259]
4. readily proceeds in water[290,291]
5. can proceed under mild conditions, but, at a slower reaction rate[292,293]

Araújo *et al.* have successfully incorporated Diels-Alder chemistry for ligation reactions of peptides and proteins using a peptide-based on hexadienyl ester and another peptide-functionalized with maleimide group (Figure 4.20).[294]

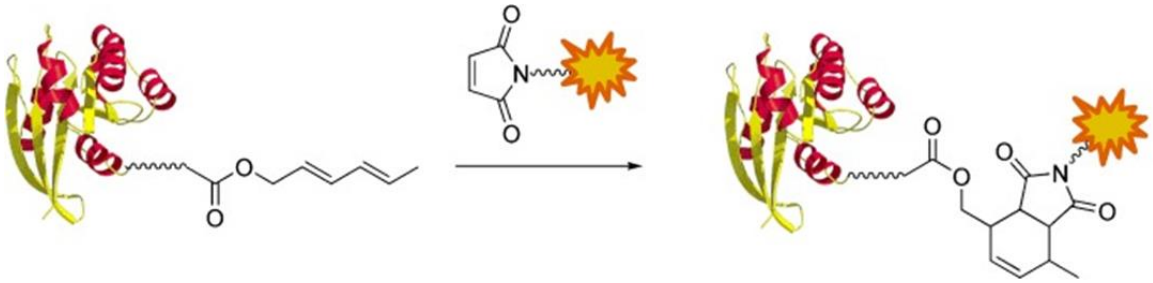

Figure 4.20: Diels-Alder cycloaddition for ligation of peptides at room temperature in water. Reproduced with permission from ref. 294 © 2006 WILEY-VCH Verlag GmbH & Co. KGaA [294]

Self-assembled amphiphilic polymer nanoparticles as delivery payloads have the benefit of having higher drug loading and composition that allows for functionalization. Shoichet *et al.* have synthesized furan-functionalized co-polymers[295] and have successfully employed them as self-assembled polymer nanoparticles for targeted delivery of antibodies[296] and chemotherapeutic drugs[297] (Figure 4.21).

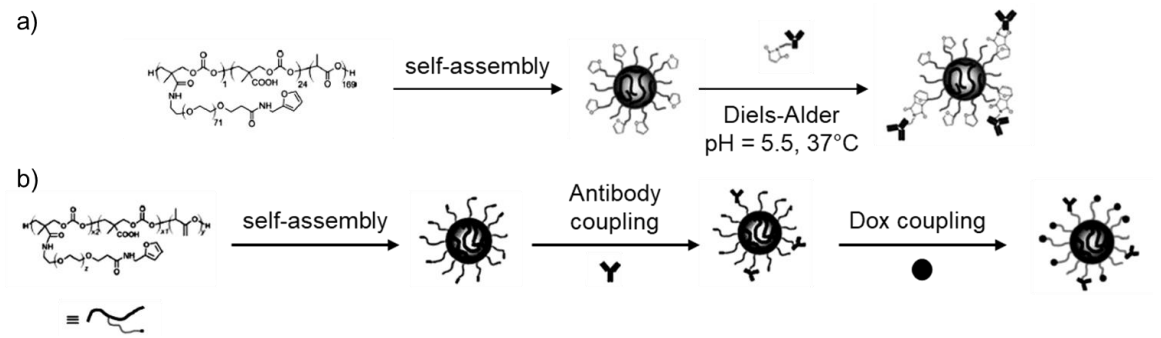

Figure 4.21: Schematic representation of the self-assembly of furan-functionalized co-polymer into micellar nanoparticles and Diels-Alder reaction between the nanoparticles: a) maleimide-functionalized antibodies. Reproduced with permission from ref. 296 © 2007 WILEY-VCH Verlag GmbH & Co. KGaA [296]; b) maleimide-functionalized Doxorubicin (Dox). Reproduced with permission from ref. 297 © 2009 WILEY-VCH Verlag GmbH & Co. KGaA [297]

Nimmo *et al.* have been able to efficiently crosslink hydrogels based on hyaluronic acid by employing furan and maleimide based Diels-Alder reaction that can be employed in applications based on Tissue engineering (Figure 4.22).[298]

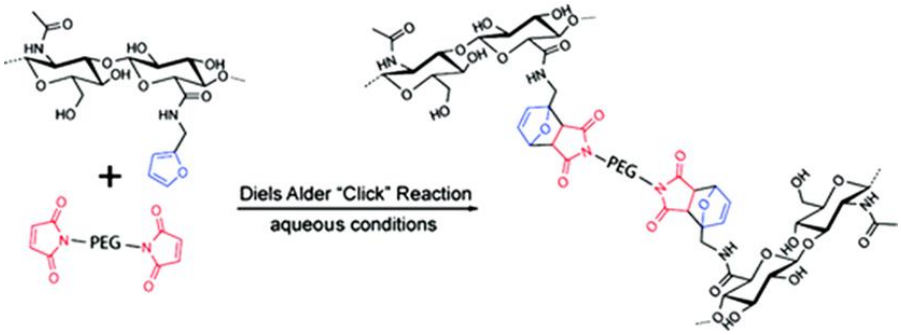

Figure 4.22: Diels-Alder reaction-based crosslinking of hyaluronic acid to form hydrogels. Reproduced with permission from ref. 298 © 2011 American Chemical Society [298]

While the covalent attachment of drug molecules onto polymer shells is a promising technique, much of the current systems are susceptible to premature drug release, which can have toxic and adverse effects.[289] Moreover, such polymeric systems have not been explored in combination with inorganic nanoparticles. We believe that the use of inorganic nanoparticles can resolve some of these issues.

4.3.3. Our system

We represent our proof-of-concept in Scheme 4.11 where three distinct domains are depicted. Domain one on the far left represents the state of the nano-assembly prior to any treatment. In this case, the bicyclic Diels-Alder adduct (**2**) is covalently attached via an amide linkage to the amphiphilic polymer shell creating the hydrophobic layer, with the adduct close to the gold nanoparticle. The middle 'cell' would be the result when the nano-assembly is exposed to visible light and the photothermal effect has generated enough heat to trigger the retro-Diels-Alder reaction releasing a functionalized maleimide, in this case, N-ethylmaleimide. The far right 'cell' shows the ultimate outcome. Because maleimide is less hydrophobic, it should be released from the nano-assembly where it can be effective. Furan remains attached to the polymer backbone and should remain trapped in the nano-assembly. This latter aspect is an additional advantage of our approach as it prevents any detrimental effect the by-products of the release event may cause. Furthermore, tethering an 'on-command' release system onto a polymer shell would create systems that contain defined loading proportions. For our system prototype, the choice of furan as the diene and N-ethylmaleimide as the dienophile components is of particular interest as the retro-Diels-Alder temperature of the Diels-Alder adduct of furan-maleimide systems is well above the body temperature,~100°C, so that the reaction does not occur spontaneously but is low enough to be achieved by external stimuli.[259]

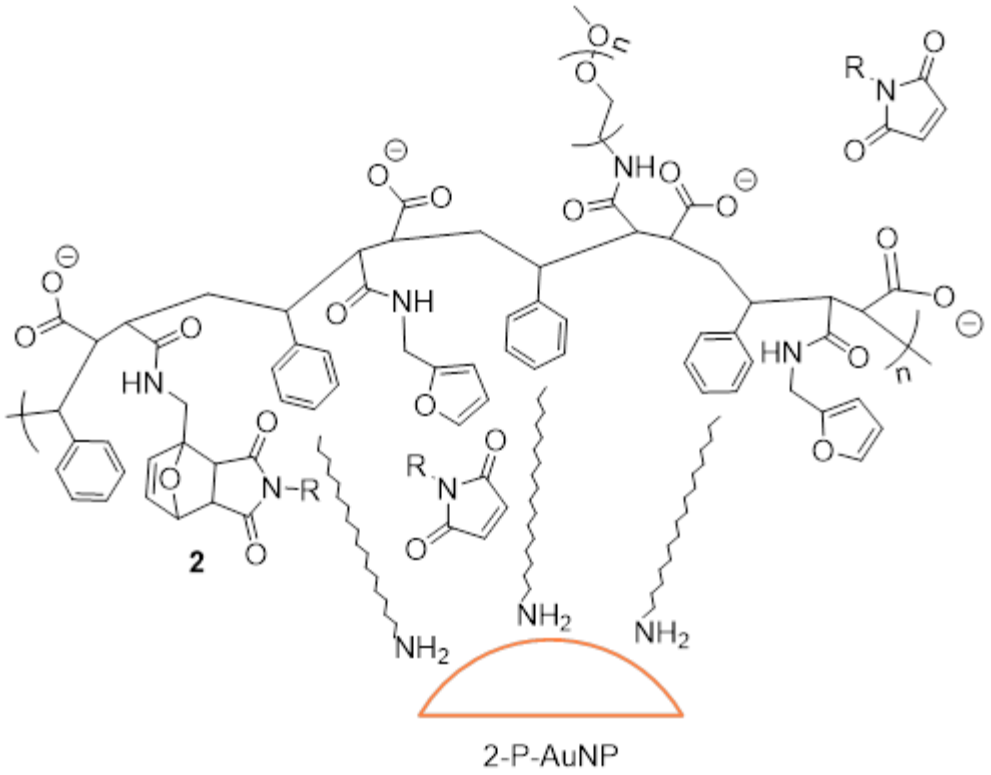

Scheme 4.11: Left cell: Bicyclic Diels-Alder adduct **2** tethered to the polymer backbone creating the hydrophobic shell surrounding octadecylamine-coated gold nanoparticles; Middle cell: Retro-Diels-Alder reaction of bicyclic Diels-Alder adduct **2**; Right cell: Release of functionalized maleimide while the furan remains attached to the polymer backbone [R = $-C_2H_5$]

4.3.4. Results and Discussion

4.3.4.1. Synthesis

The synthesis of the amphiphilic polymer shell grafted with the Diels-Alder adduct, **2-P**, was carried out in three steps starting with commercially available poly(styrene-*co*-maleic anhydride) (PSMA) (Scheme 4.12). Starting with poly(styrene-*co*-maleic anhydride) (PSMA), the pendent furan functionality is appended via ring-opening reaction of the maleic anhydride groups on the polymer chain with 2-aminomethylfuran in chloroform in a 1:3 equivalent ratio (relative to the maleic anhydride moiety on PSMA) to yield **I**. A subsequent Diels-Alder reaction of **I** with N-ethylmaleimide in toluene formed **II**. The final addition of JeffAmine® M-2070 to a solution of **II** in chloroform yielded the desired Diels-Alder adduct grafted amphiphilic polymer shell, **2-P**. The presence of IR bands at $\bar{\upsilon}$ = 3000 cm^{-1} for amide N-H stretching, $\bar{\upsilon}$ = 2865 cm^{-1} for styrene C-H stretching, $\bar{\upsilon}$ = 1697 cm^{-1} for C=O stretching of N-ethylmaleimide and $\bar{\upsilon}$ = 1090 cm^{-1} for PEG C-O stretching indicate

the opening of the anhydride ring and attachment of the Diels-Alder adduct **2** and desired PEG chains to make the polymer shell amphiphilic. Further experimental details and characterizations of compounds are provided in Section 4.5.

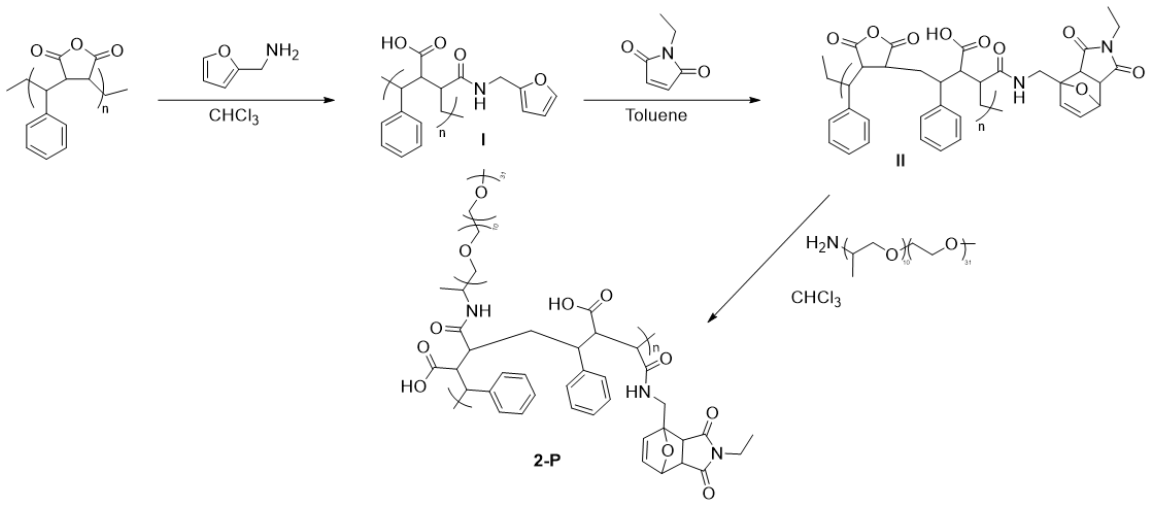

Scheme 4.12: Synthesis of Diels-Alder (2) adduct grafted polymer system, **2-P**

The thermal stability of **2-P** and physical and chemical transitions taking place in **2-P** upon heating from 25°C to 650°C were explored using thermogravimetric analysis (TGA) (Figure 4.23). 6.09 x 10^{-3} g of **2-P** was dissolved in a minimum amount of chloroform and carefully deposited in the sample pan and was air-dried to remove the solvent.

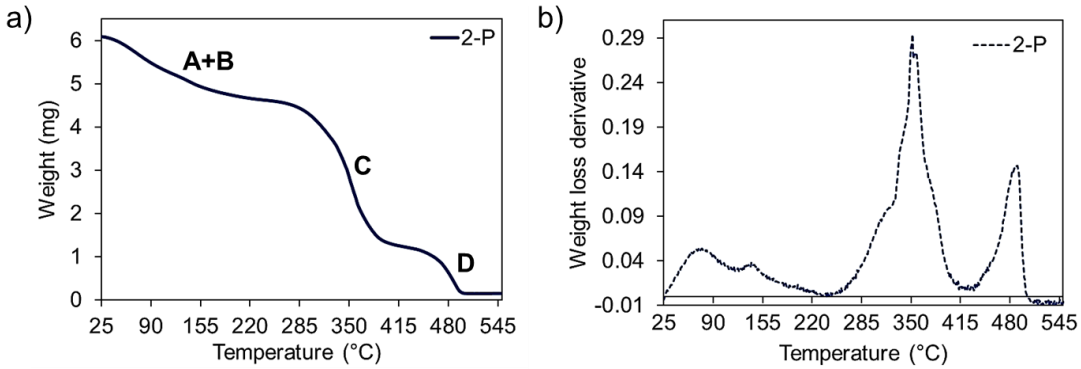

Figure 4.23: Thermogravimetric analysis (TGA) of **2-P** (6.09 x 10^{-3} g) a) curve for weight loss of **2-P** vs heating temperature at a constant heating rate of 5°C/min under inert atmosphere; b) the corresponding curve for weight loss derivative (1st) of **2-P** as a function of heating temperature with peak maxima representing maximum decomposition rate temperatures (inflection points) for each transition

The TGA curve for **2-P** displayed a four-step degradation process with transitions A & B occurring consecutively. Initial weight loss corresponding to transition A begins to occur immediately upon heating and is primarily attributed to the loss of volatile organics and residual water. Total weight loss % for transition A was determined to be 11 % with a maximum decomposition occurring at 72°C and was attributed to the loss of residual chloroform. A concurrent transition B was seen from 125°C to 270°C with a weight loss % of 9.5%. This transition was assigned to the possible retro-Diels-Alder reaction of N-ethylmaleimide and furan-attached to the polymer backbone.[247,299,300,301] Similar transition temperature range was observed for the TGA curve of the Diels-Alder adduct **2** (see section 4.5.6). Major weight loss % of about 56% was observed for transition C where most of the poly(styrene-*co*-carboxylate) backbone decomposed. Finally, transition D was consistent with the region of degradation of PEG chains.[302,303] Table 4.1 below provides a summary of the thermal transitions observed for **2-P**.

Transition	Onset temperature	Inflection point	% wt. loss
A	25°C	72°C	11%
B	125°C	143°C	9.5%
C	275°C	352°C	56%
D	420°C	490°C	14%

Table 4.1: Summary of thermal properties of **2-P**

The loading of the tethered bicyclic compound **2** onto the amphiphilic polymer **P** was determined using the thermogravimetric analysis and was estimated by determining the % weight loss for N-ethylmaleimide by retro-Diels-Alder reaction and comparing its theoretical contribution in **2-P**. Based on the theoretical calculations and TGA data, the expected loading of the adduct **2** was determined to be approximately 8.6% per chain. (see Table 4.3 in section 4.5.6)

Gold nanoparticles (**AuNP**) were prepared in an aqueous solution using the literature procedure[276] using sodium citrate as the reducing and capping agent. The produced gold nanoparticles had an average diameter of 11.2 nm ± 1.2 nm as obtained from TEM. The UV-visible Absorption spectrum of the citrate-coated gold nanoparticles showed its sharp characteristic surface plasmon resonance (SPR) band centred at 519 nm (Figure 4.24 a)). The monodisperse nature of the citrate-coated gold nanoparticles was determined by TEM imaging (Figure 4.24b)) and Particle Size Analysis (PSA) by DLS measurements. To create the desired hydrophobic environment around the gold nanoparticles, the citrate-

coated gold nanoparticles were transferred into the organic phase (chloroform) by the procedure of ligand exchange with octadecylamine (ODA).[277]

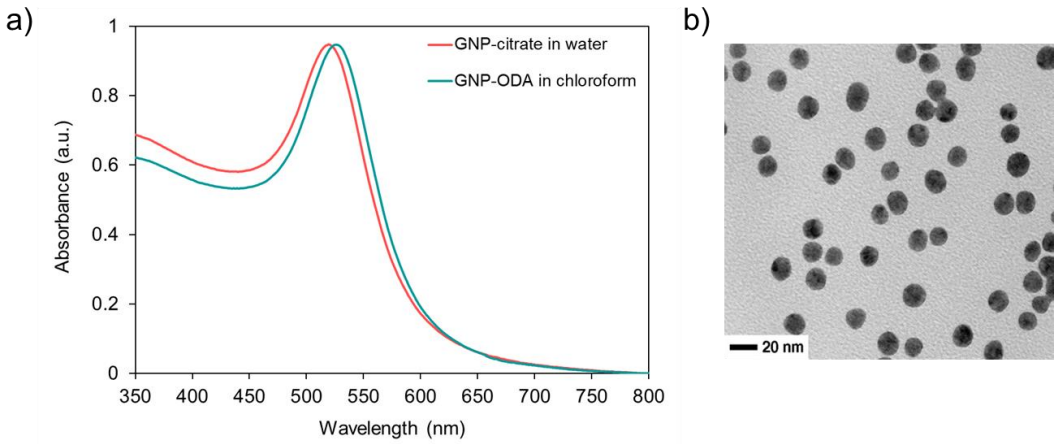

Figure 4.24: a) Normalized UV-vis absorption spectra of dispersions of citrate-coated gold nanoparticles (GNP) in water (2.55 mg/mL) (red line) and ODA-coated gold nanoparticles (GNP) in chloroform (0.39 mg/mL) (green line); b) TEM image of water dispersion of citrate-coated gold nanoparticles (2.55 mg/mL, 11.2 ± 1.2 nm)

The final nano-assembly (**2-P-AuNP**) was prepared in the organic phase by the addition of the Diels-Alder adduct grafted amphiphilic polymer (**2-P**) in chloroform. After stirring the mixture for 18 h, the organic solvent was removed, and the self-assembled nanostructure was dispersed in water (Scheme 4.13).

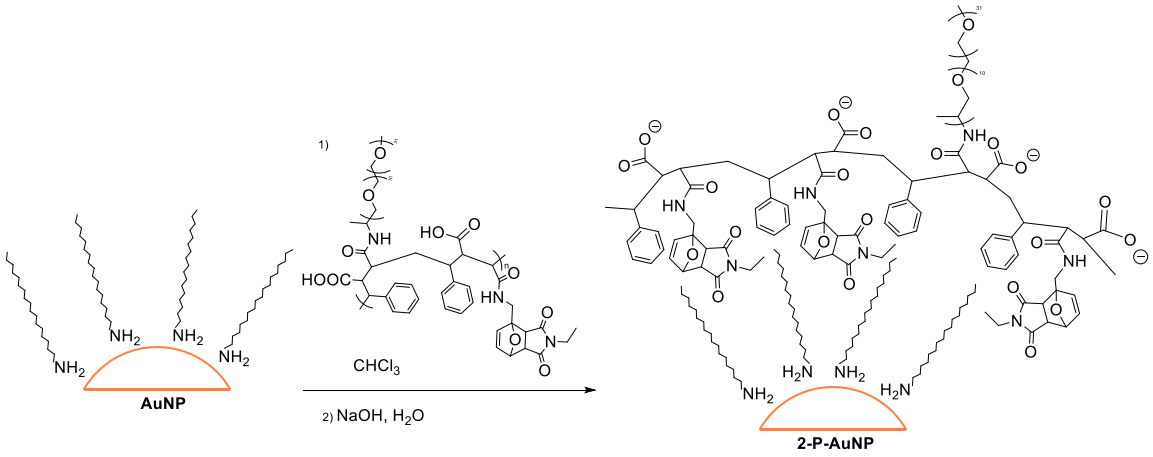

Scheme 4.13: Synthesis of the nano-assembly, **2-P-AuNP**

The UV-visible Absorption spectrum of the aqueous solution **2-P-AuNP** shows a bathochromic shift in the SPR band which was now centred at 532 nm (Figure 4.25 a)).

This shift of λ_{max} towards longer wavelengths can be attributed to the ligand exchange from citrate to octadecylamine which may lead to the redistribution of charge on the nanoparticle surface.[278] The average diameter of the **2-P-AuNP** nano-assembly was determined using TEM and was obtained to be 11.60 nm ± 1.50 nm (Figure 4.25 b)). After encapsulation, the average size of the particles measured by TEM was similar to that of the original citrate-coated nanoparticles (11.20 nm ± 1.20 nm), but, the DLS measurements (Section 4.5.7), which provide an estimated size of the entire nano-assembly including the organic layer around the inorganic core, determined the average diameter of the nano-assembly to be 21.04 nm. The difference in size measurements from TEM and DLS for the nano-assembly is attributed to the solvation effect of the fully extended polyethylene glycol chains. The loading of the tethered bicyclic compound **2** onto the amphiphilic polymer **P** within the nanoassembly was determined using the UV-visible absorption spectroscopy and was estimated by determining the concentration of released N-ethylmaleimide after Photothermolysis and spin-filtering and comparing it to the amount of adduct **2** based on 1:1 reaction ratio. The number of molecules of adduct **2** tethered onto the polymer **P** per nanoparticle is approximately 532 (see Table 4.7 in Section 4.5.7).

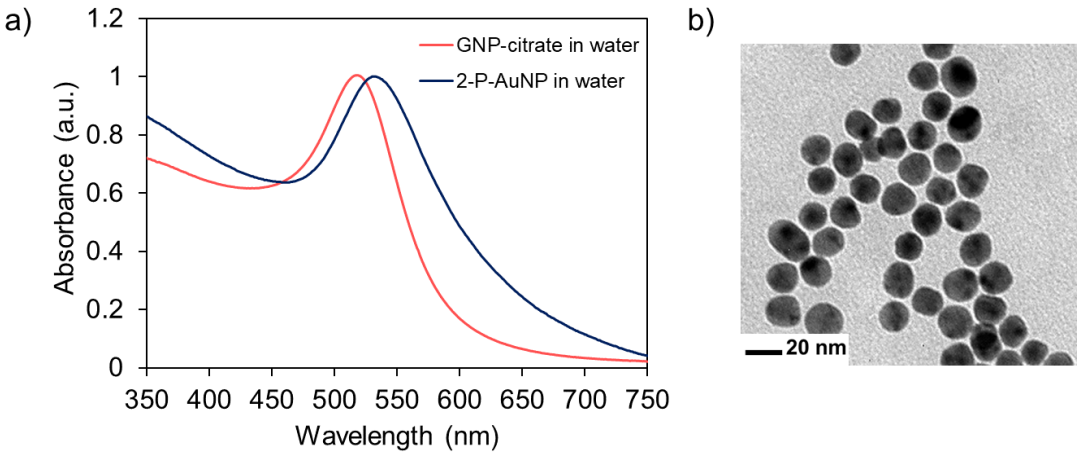

Figure 4.25: a) Normalized UV-vis absorption spectra of dispersions of citrate-coated gold nanoparticles (GNP) in water (2.55 mg/mL) (red line) and **2-P-AuNP** in water (0.48 mg/mL) (blue line); b) TEM image of water dispersion of **2-P-AuNP** (0.48 mg/mL, 11.6 ± 1.5 nm)

4.3.4.2. Thermolysis of Diels-Alder adduct grafted amphiphilic polymer 2-P

To determine the thermal behaviour of the Diels-Alder adduct grafted polymer (**2-P**), a heat-induced retro-Diels-Alder reaction of the Diels-Alder adduct grafted amphiphilic polymer **2-P** was evaluated by heating a solution of **2-P** in DMSO at 110°C (Scheme 4.14).

^{1}H NMR spectroscopy and UV-visible absorption spectroscopy were employed to analyze the reaction progress. The objective of this analysis was to determine whether high temperatures could initiate any retro-Diels-Alder reaction without any degradation of the polymer itself and to provide the rationale for the subsequent photothermal release experiment.

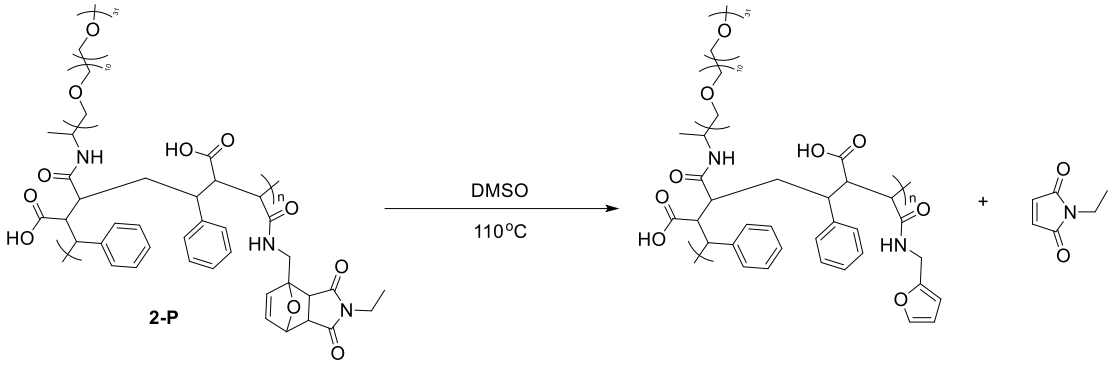

Scheme 4.14: Retro-Diels-Alder reaction of **2-P**

After acquiring an immediate ^{1}H NMR spectrum of a solution of **2-P** in DMSO-d_6 (1.00 x 10^{-3} M), the tube was heated at 110°C for 3h with ^{1}H NMR spectra being recorded every hour. The initial ^{1}H NMR spectrum for **2-P** showed a broad peak in the δ = 7.00 – 7.50 ppm region corresponding to the styrene protons on the polymer backbone, a large singlet at δ = 3.50 ppm for the methoxy protons of the PEG chains, a weak multiplet in the δ =3.40 – 3.46 ppm region due to the overlap of methylene protons of -CONH- linker and the maleimide ring, a sharp singlet at δ = 3.32 ppm for the methylene groups in the backbone. The broadness of the styrene proton peaks for the polymer **2-P** is due to the overlapping of the resonance signals from the repeating units which, in turn, is the result of weak molecular rotation across the backbone and repeating units being situated in only slightly different chemical environments.[304,305,306] After 1 h of heating, a singlet appears at δ = 7.00 ppm corresponding to HC=CH protons for N-ethylmaleimide while no change in the signals for the polymer are observed (Figure 4.26, marked as **a**). Further heating of the solution led to no further changes in the spectra of N-ethylmaleimide. However, a new peak was observed at δ = 2.08 ppm possibly due to slight degradation of the polymer that led to cleavage of the end-groups from polymer. The results obtained from the initial thermolysis experiment suggest that the retro-Diels-Alder reaction to release N-ethylmaleimide occurs within 1 h of heating of the **2-P** solution without any visible polymer degradation.

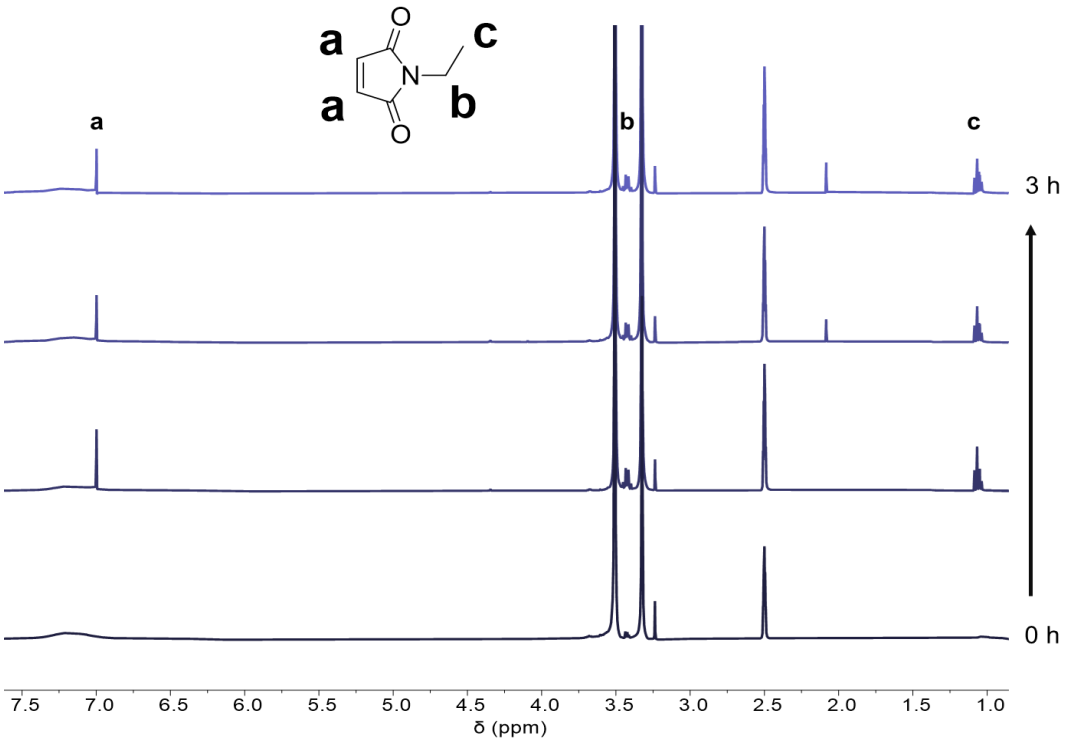

Figure 4.26: Changes in ^{1}H NMR spectrum corresponding to N-ethylmaleimide proton **a** (δ = 7.00 ppm) when a solution **2-P** in DMSO-d_6 (1.00 x 10^{-3} M) is heated at 110°C for 3h

Similarly, upon acquiring an initial UV-visible absorption spectrum of a solution of **2-P** in DMSO (2.3 x 10^{-3} M), the solution was heated at 110°C, and spectra were acquired every 20 minutes for 1.00 mL aliquot of the sample for a total of 3 h. After 20 minutes of heating, a broad band centred at 305 nm began to appear. This band can be attributed to free N-ethylmaleimide and it continued to increase in intensity upon further heating. No further changes in the spectrum were observed after 3h of heating (Figure 4.27). Thus, the thermolysis of **2-P** under aqueous conditions led to a complete retro-Diels-Alder reaction with the desired release of N-ethylmaleimide.

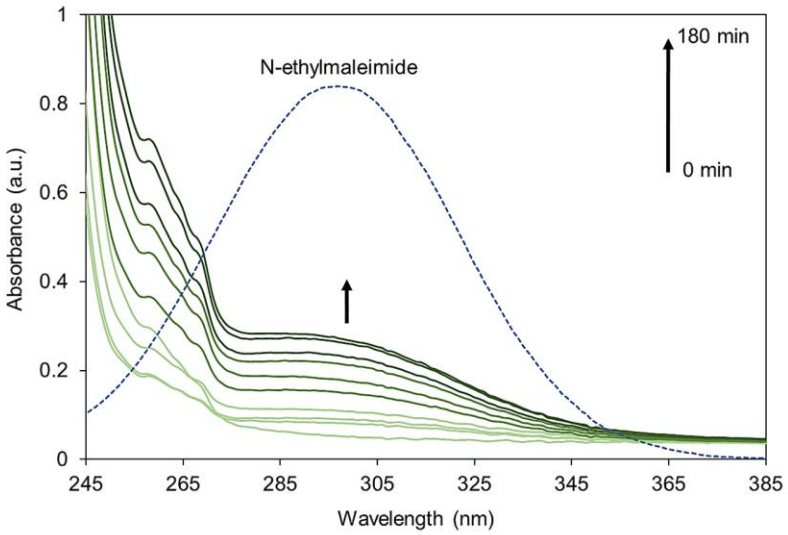

Figure 4.27: Changes in the UV-vis absorption spectrum when a solution of **2-P** in DMSO (2.30 x 10^{-3} M, stock) was heated at 110 °C, 5.00 x 10^{-3} M solution of N-ethylmaleimide in DMSO was used for comparison (dotted line)

4.3.4.3. Photothermolysis of the nano-assembly 2-P-AuNP

The minimum power of the 532 nm nanosecond pulsed laser that is required to trigger the retro-Diels-Alder reaction to release N-ethyl maleimide was determined by irradiating the **2-P-AuNP** nano-assembly with different laser powers for a time interval of 1 minute. The release was monitored by UV-visible Absorption spectroscopy. Upon acquiring an initial spectrum for **2-P-AuNP**, the aqueous dispersion of **2-P-AuNP** (0.48 mg/mL) was irradiated with a 532 nm nanosecond pulsed laser (10 Hz, 5 mJ/pulse, 10 ns) at 100 mW/cm^2 for 1 minute followed by increasing the power density by 100 mW/cm^2, and the spectra of the solution being acquired after each power density increment until no further change in the spectrum were observed (Figure 4.28 a)). After a minute of exposure of **2-P-AuNP** with 100 mW/cm^2 pulsed laser, the broad band for gold nanoparticles SPR at 532 nm became sharper and shifted towards a shorter wavelength centred at 526 nm. At the same time, a new peak in the region of 270-310 nm. This band corresponds to N-ethyl maleimide released from **2-P** through a retro-Diels-Alder reaction as illustrated in our thermolysis experiments. The intensity of the peak in the 270-310 nm region continues to increase upon increasing the power to 400 mW/cm^2 after which no change in the spectrum was observed.

In a similar experiment, the retro-Diels-Alder reaction triggered release of N-ethylmaleimide from the nanoassembly, **2-P-AuNP**, was observed in 10 minutes, after

which no changes in the spectrum were observed, when the aqueous dispersion of **2-P-AuNP** (0.48 mg/mL) was irradiated with a nanosecond pulsed laser (10 ns, 532 nm) at 200 mW/cm^2 (Not all of the light is absorbed by the sample. The absorbed power is 58 mW/cm^2. The remainder of the light is transmitted or absorbed by the cuvette. Details in section 4.5.7) in 1-minute intervals. A corresponding shift in the gold nanoparticle SPR band was also observed from 532 nm to 520 nm without any peak broadening. The retro-Diels-Alder reaction assisted by the photothermal effect of the gold nanoparticles took more time in the case of **2-P-AuNP** as compared to **P-AuNP-1**, possibly due to the covalent attachment of the adduct onto the hydrophobic chains of the polymer resulting in a lack of migration of the adduct closer to the gold nanoparticle core within the polymeric shell.[283] Additionally, the lower laser power used for **2-P-AuNP** suggests that fewer photons will be absorbed by the gold nanoparticles in case of **2-P-AuNP** that would lead to a different localized temperature than in case of **P-AuNP-1**.

Furthermore, the released product was almost entirely obtained in the flow-through (supernatant) after centrifugation and filtration of the nanoassembly as no peak for the released N-ethylmaleimide in the region of 270-310 nm was observed for the redispersed pellet. Mass spectrometry analysis of the flow-through confirmed the presence of N-ethylmaleimide (Figure 4.28 d)). Notably, the present nanoassembly also retained its stability after irradiation with the 532 nm pulsed laser, similar to the results in the case of release of Tyrphostin A8 from the nanoassembly, as observed from the TEM images before and after irradiation (Figure 4.28 b), c)).

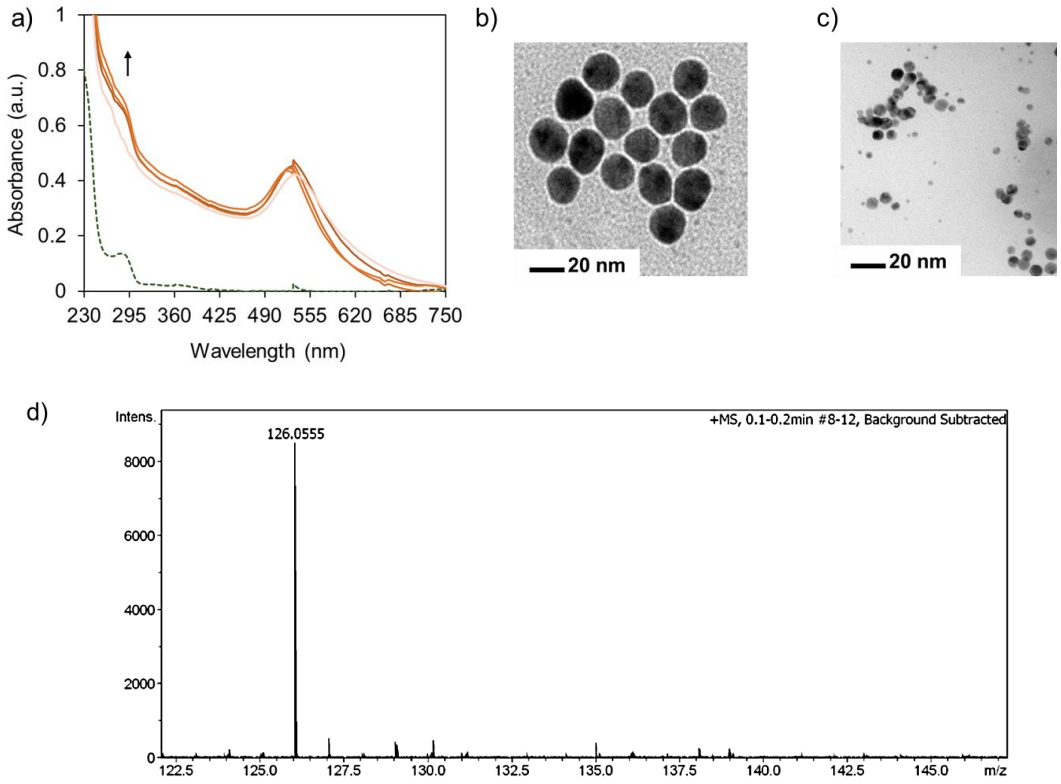

Figure 4.28: a) Changes in the UV-vis absorption spectrum when an aqueous solution of **2-P-AuNP** is irradiated with a nanosecond pulse laser (10 ns, 532 nm) for 1 min; The dotted line corresponds to released N-ethylmaleimide in the supernatant after centrifugation; b) TEM image of an aqueous dispersion of **2-P-AuNP** before irradiation with 532 nm pulsed laser light (10 Hz, 5 mJ/pulse, 10ns); c) TEM image of an aqueous solution of **2-P-AuNP** after irradiation with 532 nm pulsed laser light (10 Hz, 5 mJ/pulse, 10 ns) for a total of 10 min; d) High-resolution mass spectrum analysis of the flow-through confirms the presence of N-ethylmaleimide. ESI-MS: m/z 126.05549 (M+H) Calc. $C_6H_8NO_2$ 126.04768.

4.3.5. Conclusion summary

Herein, a successful demonstration of the construction of a modified amphiphilic polymer shell with covalently attached N-ethylmaleimide-based Diels-Alder adduct, **2-P**, capable of releasing N-ethylmaleimide upon heating was reported. This amphiphilic polymer shell was employed for wrapping the gold nanoparticles to create an aqueous stable nanoassembly, **2-P-AuNP**. It was demonstrated that upon exposure to 532 nm pulsed laser, **2**, tethered as a pendent group, inside the nano-assembly underwent a retro-Diels-Alder reaction to release N-ethylmaleimide, a standard biomarker for sulfhydryl groups, via the photothermal heating process. Our amphiphilic polymer, **2-P**, can act as a

prototype to create polymer systems that are tailor-made for desired biomedical applications.

4.4. Future prospects

The release approaches described in this chapter aim to work as a foundation to build targeted carrier systems that can be placed in active sites inside cell membranes and release 'on-command' the therapeutic drug. Such a delivery mechanism can help circumvent the potentially fatal side effects of the most common chemotherapeutic drugs like Doxorubicin. Aldoxorubicin is being tested as a potential anti-cancer drug and has proven to address the limitations of Doxorubicin. Aldoxorubicin consists of a maleimide-terminated hydrazide linkage that is acid sensitive (Figure 4.29).[307] Maleimide group can act as a dienophile for Diels-Alder reaction with the furan modified PSMA polymer **I**. The process of releasing the active drug would involve a retro-Diels-Alder reaction induced by the photothermal effect of the gold nanoparticles followed by the cleavage of the hydrazide in the acidic environment of the tumour.

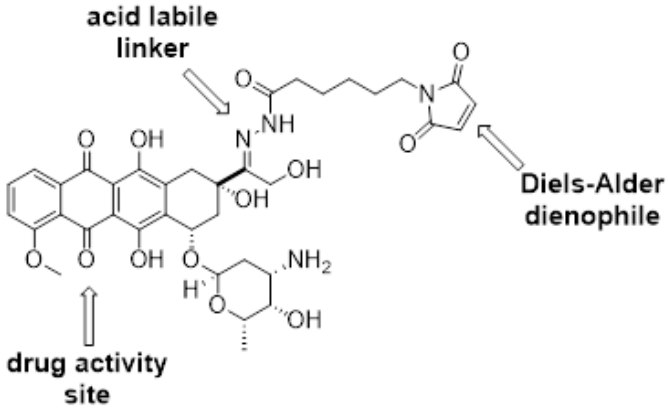

Figure 4.29: Structure of Aldoxorubicin which is a maleimide-terminated hydrazide of Doxorubicin

Similarly, maleimide derivatized fluorophores can be encapsulated as Diels-Alder adduct with simple furfuryl amine or the furan modified polymer inside the gold nanoassembly. The Diels-Alder adduct would remain non-fluorescent until the retro-Diels-Alder reaction triggered by the photothermal effect of gold nanoparticles occurs (Scheme 4.15). Such systems can be employed for the detection and imaging of thiol-containing biomolecules.

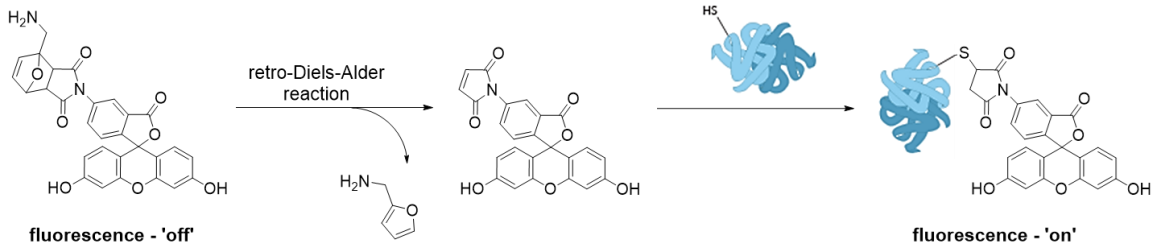

Scheme 4.15: Schematic fluorescent imaging using maleimide modified fluorophore like fluorescein

One of our systems uses high laser power of 800 mW/cm^2 to generate the heat required for the retro-Diels-Alder reaction which is induced by the photothermal effect of gold nanoparticles. Such high powers are considered detrimental for living cells and thus too high for use in biological conditions. To develop systems that can operate at lower laser powers, we need to consider:

1. how far the heat is conducted from the gold nanoparticle surface inside the hydrophobic pocket
2. the heat generated is enough to drive the chemical reaction

Nanoassemblies of gold nanoparticles capped with alkylamines of varying chain length (n) that have terminally attached furan-maleimide-based Diels-Alder adduct and encapsulated in amphiphilic polymer **P** can be employed to potentially determine the extent of heat conduction from the gold nanoparticle surface inside the hydrophobic pocket (Scheme 4.16). Theoretically, capping agents with shorter chain lengths should undergo retro-Diels-Alder reaction faster than those with longer chain lengths. As a result, the total exposure time to laser for complete release would be further reduced.

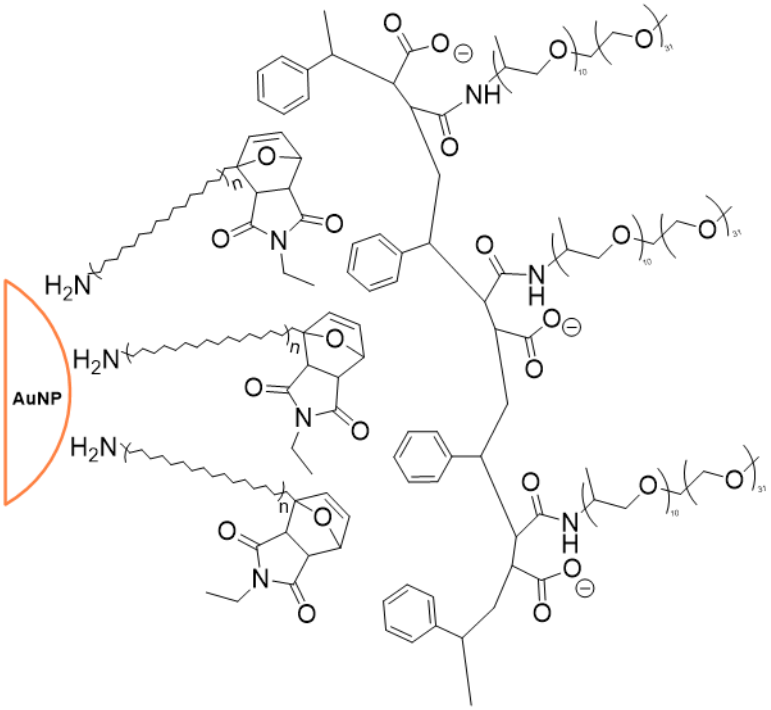

Scheme 4.16: Schematic representation of nanoassemblies with alkylamine-based capping agents that have varying chain length (n) and are terminated with furan-maleimide Diels-Alder adduct

Alternatively, changing the diene-dienophile pair would result in modifying the temperature of the retro-Diels-Alder reaction. Incorporation of such systems could also enable the use of lower powers of the laser. Moreover, creating nanoassemblies based on gold nanorods instead of nanoparticles would shift the absorption in the near-IR regions resulting in deeper tissue penetration which is desired for biomedical applications.

4.5. Experimental

4.5.1. General

All reagents and solvents, unless otherwise stated, were from MilliporeSigma, Alfa Aesar (Thermo Fisher Scientific), or ACP Chemical Inc. and were used as received. Solvents for NMR analysis were purchased from Cambridge Isotope Laboratories and used as received. Poly(styrene-co-maleic anhydride) (PSMA), average M_n ~ 1700 Da, was obtained from MilliporeSigma. Poly(propylene glycol)bis(2-aminopropyl ether) (Jeffamine® M-2070) was procured from Huntsman International LLC. Column chromatography was performed using silica gel 60 (230–400 mesh) from Silicycle Inc.

4.5.2. Instrumentation

^{1}H NMR and ^{13}C NMR characterizations were performed on the Bruker Avance-400 instrument with a 5 mm inverse probe operating at 400.13 MHz for ^{1}H NMR and 100.61 MHz for ^{13}C NMR. ^{1}H NMR and ^{13}C NMR characterization of bicyclic compound **1** were performed on a Bruker QNP 600 cryoprobe working at 600.13 MHz for ^{1}H and 150.92 MHz for ^{13}C. Chemical shifts (δ) are reported in parts per million (ppm) relative to tetramethylsilane using the residual solvent peak as a reference. Coupling constants (J) are reported in Hertz. Multiplicities are reported as: s = singlet, d = double, t = triplet, q = quartet, m = multiplet. UV–visible absorption spectroscopy was performed using a Varian Cary 300 Bio spectrophotometer. IR spectroscopy measurements were conducted on a PerkinElmer Spectrum Two™ IR spectrometer equipped with a universal ATR accessory with a 9-bounce diamond top-plate. Mass Spectroscopy (HRMS) measurements were performed using an Agilent 6210 TOF LC/MS in ESI-(+) mode. The thermo-gravimetric analysis was performed using a Shimadzu TGA50 instrument. The weight loss was analyzed by heating the samples from room temperature to 650°C at the rate of 5°C/min under an inert (N_2) atmosphere. Melting points were measured using a Gallenkamp melting point apparatus and are uncorrected.

4.5.3. Transmission Electron Microscopy (TEM)

TEM images were obtained using a Hitachi 8100 Scanning Transmission Electron Microscope operating at 200 keV. Dilute colloids of the AuNPs (approximately 0.1 wt-%) dispersed in water (0.01 mL) were placed on thin, carbon formvar-coated copper grids held by anti-capillary tweezers (Ted Pella, Part # 501-4). The grids were slowly dried under reduced pressure in a vacuum desiccator. The shape and size of the gold nanoparticles and nanoassemblies were evaluated from the collected TEM images. The size of the nanoparticles was calculated from over 100 particles located in different areas of the TEM grid.

4.5.4. Dynamic Light Scattering (DLS)

DLS measurements were carried out using a Malvern Zetasizer Nano-ZS. The colloidal samples were held in a 1 cm path length square glass cuvette (Starna Cells, Part 76 #

23/G/10). A nanoparticle concentration of ~0.6 mg/mL was employed for the measurements. All DLS measurements were conducted at 25 °C.

4.5.5. Photolysis

All photolysis experiments were carried out using a nanosecond pulse laser (10 ns, 532 nm) with a tuneable power. A power setting of 200 and 800 mW/cm^2 was used for the photothermal release experiments. Aqueous suspensions of citrate-coated nanoparticles or the nanoassemblies (**P-AuNP-1**, **2-P-AuNP**) were irradiated in a quartz cuvette with a path length of 1 cm. Nanoparticles were irradiated in one-minute intervals for the duration of time specified.

4.5.6. Synthesis

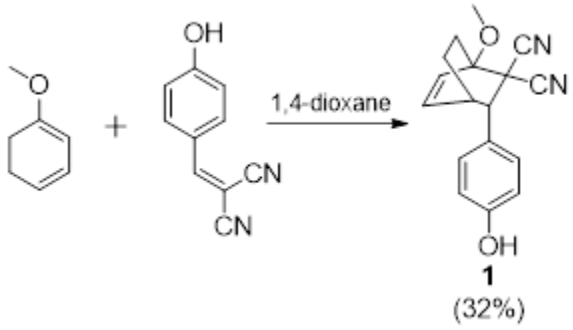

Synthesis of bicyclic compound 1. A suspension of Tyrphostin A8 ((4-hydroxybenzylidene)-malononitrile) (0.25 g, 0.00147 mol) in 1,4-dioxane (0.75 mL) was treated with 1-methoxy-1,3-cyclohexadiene (0.696 g, 0.00411 mol), and heated at 80 °C for 16 h. The solvent was removed under vacuum and the residue was purified by column chromatography on silica gel (25–30% ethyl acetate/hexanes) to yield a yellow solid, which was further recrystallized in warm $CHCl_3$ to afford 0.133 g (32% yield) of compound **1** as a white solid.

m.p: 153-157.5 °C (decomposed)

^{1}H NMR (600 MHz, DMSO-d_6) δ 7.05 – 7.02 (m, 2H), 6.90 (dd, J = 8.8, 6.5 Hz, 1H), 6.77 – 6.73 (m, 2H), 6.50 (d, J = 8.8 Hz, 1H), 3.81 (s, 1H), 3.46 (s, 3H), 2.84 (dt, J = 6.4, 2.7 Hz, 1H), 2.01 (ddd, J = 12.6, 9.8, 2.9 Hz, 1H), 1.98 – 1.92 (m, 1H), 1.79 – 1.73 (m, 1H), 1.36 (tdd, J = 12.3, 5.9, 2.5 Hz, 1H).

^{13}C NMR (151 MHz, DMSO-d_6) δ 157.53, 137.00, 130.18, 129.66, 129.10, 117.01, 115.92, 114.67, 81.69, 53.61, 52.71, 33.98, 26.34, 21.80.

ESI-MS: m/z (M+Na) calculated for $C_{17}H_{16}N_2O_2Na$: 303.1104, found: 303.1112.

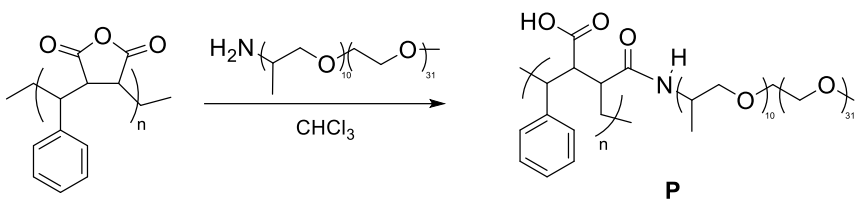

Synthesis of amphiphilic polymer P. A solution of poly(propylene glycol)bis(2-aminopropyl ether) (Jeffamine® M-2070) (1.300 g, 6.5 x 10^{-4} mol) and poly(styrene-co-maleic anhydride) (PSMA) (0.194 g, 1.14 x 10^{-4} mol) in 20 mL of chloroform was stirred at 25°C for 16 h.

^{1}H NMR (400, DMSO-d_6) δ 8.31 (s from the aromatic group of PSMA), 3.51 (s from OCH_2 of Jeffamine® M-2070), 3.24 (s from CH_2 of PSMA), 1.05 - 1.03 (s from CH_3 of Jeffamine® M-2070)

FT-IR (diamond ATR): $\tilde{\upsilon}$ (cm^{-1}) 3000 cm^{-1} (N-H stretch), 2865 cm^{-1} (C-H stretch, aromatic), 1090 cm^{-1} (C-O stretch), 747 cm^{-1} (C-H bend, oop)

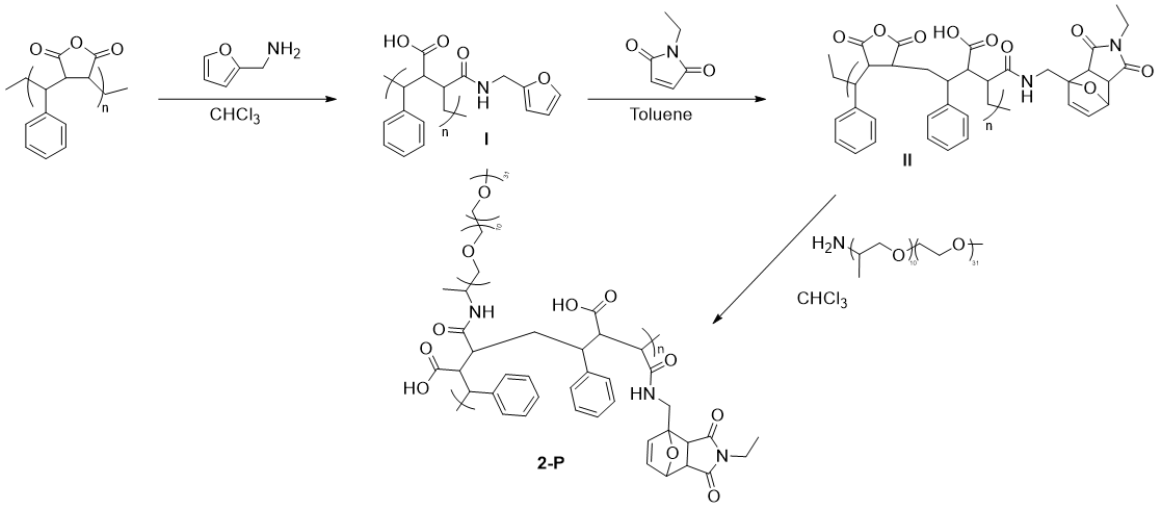

Synthesis of Diels-Alder adduct grafted amphiphilic polymer 2-P. A solution of poly(styrene-co-maleic anhydride) (PSMA) (0.499 g, 2.94 x 10^{-4} mol) in chloroform was treated with 2-aminomethylfuran (0.08566 g, 8.82 x 10^{-4} mol) and the resulting mixture

was refluxed for 16 h. The reaction mixture was cooled to room temperature and the solvent was removed under reduced pressure. The residue **I** was re-dissolved in toluene and was treated with N-ethylmaleimide (0.11 g, 8.82 x 10^{-4} mol). The mixture was heated at 75°C for 16 h in a temperature-controlled oil bath. The reaction mixture was cooled to room temperature and the solvent was evaporated under reduced pressure. The residue **II** was re-dissolved in chloroform and was charged with poly(propylene glycol)bis(2-aminopropyl ether) (Jeffamine® M-2070) (0.588 g, 2.94 x 10^{-4} mol). The resulting mixture was stirred at room temperature for 16 h followed by evaporation of the solvent. The resulting polymer was purified by dialysis.

^{1}H NMR (500, DMSO-d_6) δ 7.50 - 7.00 (bs from the aromatic group of PSMA), 3.50 (s from OCH_2 of Jeffamine® M-2070), 3.46 – 3.40 (bm from CH_2 connected to -CONH- linker and CH_2 of N-ethylmaleimide) 3.32 (s from CH_2 of PSMA), 1.30 (s for CH_3 of N-ethylmaleimide) 1.05 - 1.03 (bm from CH_3 of Jeffamine® M-2070)

FT-IR (diamond ATR): $\bar{\upsilon}$ (cm^{-1}) 3000 cm^{-1} (N-H stretch), 2865 cm^{-1} (C-H stretch, aromatic), 1697 cm^{-1} (C=O stretch), 1090 cm^{-1} (C-O stretch), 699 cm^{-1} (C-H bend, oop)

Estimating the stoichiometry of components of 2-P

The results of the theoretical calculations to determine the ratio of all components on the amphiphilic polymer **2-P** suggest that each polymer chain contains furan: Jeffamine: unreacted maleic anhydride in the ratio of 3:1:1.5.

MW of PSMA (g/mol)	~ 1700	
MW of styrene (g/mol)	= 104.15	
MW of maleic anhydride (g/mol)	= 98.06	
Ratio of styrene:maleic anhydride in PSMA‡	= (0.68)/(0.32)†	= 2.1:1
Average MW of repeat unit	= (2.1)*(104.15)+(98.06)	= 316.78
Number of repeat units per polymer	= (1700)/(316.78)	= 5.36
Moles of PSMA used (mol)	= 2.94 x 10^{-4}	
Moles of maleic anhydride present (mol)	= (5.36)*(2.94 x 10^{-4})	1.57 x 10^{-3}
Moles of 2-aminofuran used (mol)	= 8.82 x 10^{-4}	
Moles of Jeffamine® M-2070 used (mol)	= 2.94 x 10^{-4}	

Table 4.2: Calculation of stoichiometry of components of polymer **2-P**

‡vendor designation of 68 % styrene and 32% maleic anhydride

According to the theoretical calculation for weight %, N-ethylmaleimide was estimated to approximately make up 8.6% of the total weight % of the polymer **2-P** This was similar to the % wt. loss observed in the region of the retro-Diels-Alder reaction of 9.5%.

Mass of PSMA used (g)	= 0.499	
Mass of 2-aminofuran used (g)	= 0.086	
Mass of N-ethylmaleimide used (g)	= 0.110	
Mass of Jeffamine® M-2070 used (g)	= 0.588	
Total mass (g)	= (0.499)+(0.086)+(0.110)+(0.588)	= 1.283
Wt. % of N-ethylmaleimide	= [(0.110)/(1.283)]*100	= 8.6

Table 4.3: Estimation of wt. % of N-ethylmaleimide with respect to polymer **2-P**

IR spectra of amphiphilic polymer shells

FT-IR spectra of amphiphilic polymer **P** (top) and Diels-Alder adduct grafted amphiphilic polymer **2-P** (bottom).

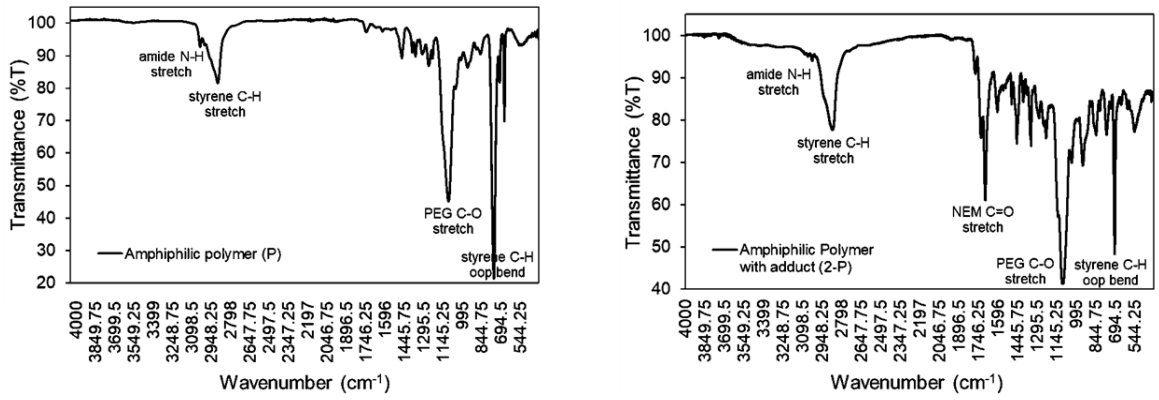

TGA data of N-(2-furylmethyl)acetamide and N-ethylmaleimide Diels-Alder adduct (2)

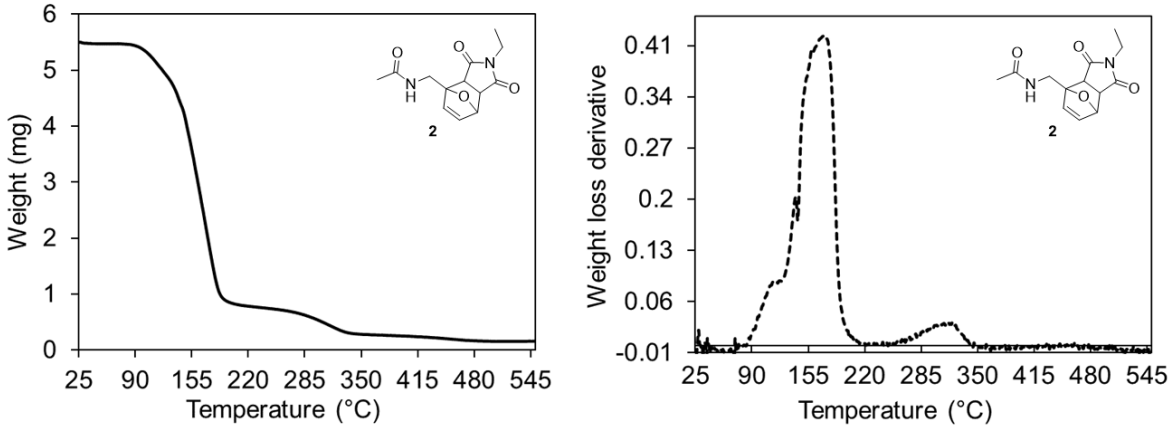

4.5.7. Preparation of gold nanoparticles and nano-assemblies

Synthesis of citrate-coated gold nanoparticles. The citrate-coated gold nanoparticles were synthesized according to the literature.[277] A solution of $HAuCl_4 \bullet (H_2O)_3$ (1.00×10^{-3} M in ultrapure water) was heated to reflux in a 250 mL round-bottom flask. At this temperature, the solution was treated with warm aqueous sodium citrate (1% w/v in ultrapure water, 80 °C) with vigorous stirring. The resulting mixture was heated at reflux for 10 min to obtain a deep red coloured solution. This solution was allowed to cool to room temperature. This dispersion was stored and used without any further purification. The UV-visible absorption spectrum of citrate-coated gold nanoparticles showed an intense absorption band centred at 519 nm. The TEM images of these nanoparticles showed that they have an average size of 11.20 ± 1.20 nm. The concentration of citrate-coated gold nanoparticles was estimated by drying 1.00 mL of the nanoparticle solution under a high vacuum and weighing the residue. This afforded a value of 2.55 mg/mL.

Synthesis of octadecylamine (ODA)-coated gold nanoparticles. The citrate-coated gold nanoparticles were transferred from the aqueous phase to the organic phase according to the literature procedure.[277] Briefly, the aqueous solution of citrate-coated gold nanoparticles (2.00 mL) was cautiously layered over a solution of 7.50×10^{-4} M octadecylamine solution in chloroform (4.00 mL) in a centrifuge tube, followed by the addition of ultrapure water (2.00 mL). The two-phase mixture was mixed vigorously for 3 min using a vortex. The organic layer was carefully removed, and its volume reduced to

half using a rotary evaporator. This solution of octadecylamine-coated gold nanoparticles was used without any further purification. The UV-vis spectrum of this chloroform solution showed an intense absorption band centred at 525 nm. The TEM images of these nanoparticles showed that they have an average size of 14.60 ± 0.90 nm. The concentration of octadecylamine-coated gold nanoparticles was estimated by drying 1.00 mL of the nanoparticle solution under a high vacuum and weighing the residue. This afforded a value of 0.39 mg/mL.

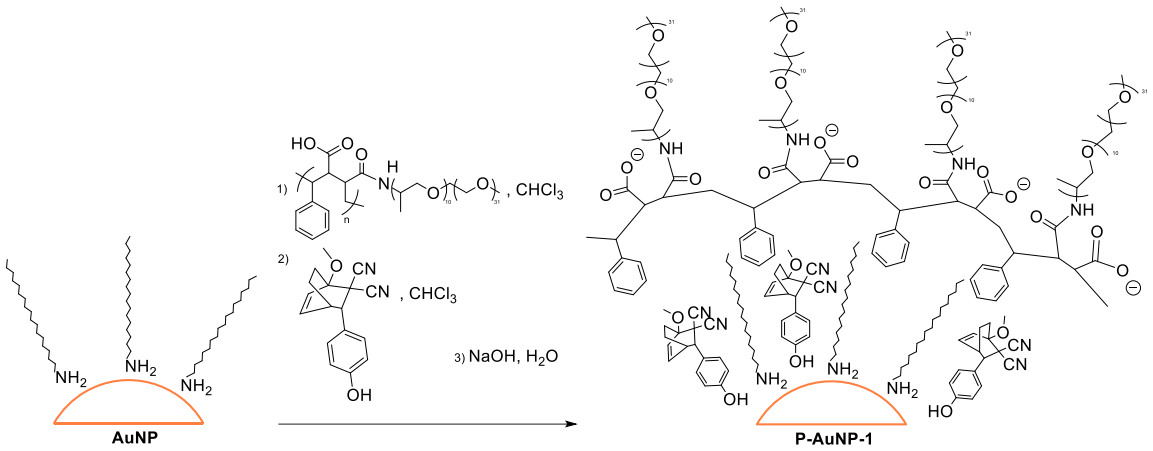

Synthesis of nano-assembly P-AuNP-1. A stirring solution of 2 mL of octadecylamine-coated gold nanoparticles was treated with 2 mL of the solution of polymer **P** over 1 min, followed by the bicyclic compound **1** (0.001 g, 3.50 x 10^{-6} mol) dissolved in 1.00 mL of chloroform. The resulting mixture was stirred for 18 h at ambient temperature (22 °C), at which time the solvent was removed under vacuum until a red viscous residue was obtained. This residue was treated with alkaline water (1.00 mL, pH 13, adjusted with 0.1 M aqueous NaOH), and the resulting mixture was sonicated for approximately 30 s. The volume of the red emulsion was reduced using a rotary vacuum until a clear colloid formed. The colloid was centrifuged at 20600 rpm for 20 min and the flow-through was discarded. The remaining pellet was re-dispersed in 2.00 mL of ultrapure water to obtain a final stock solution of **P-AuNP-1** for further use.

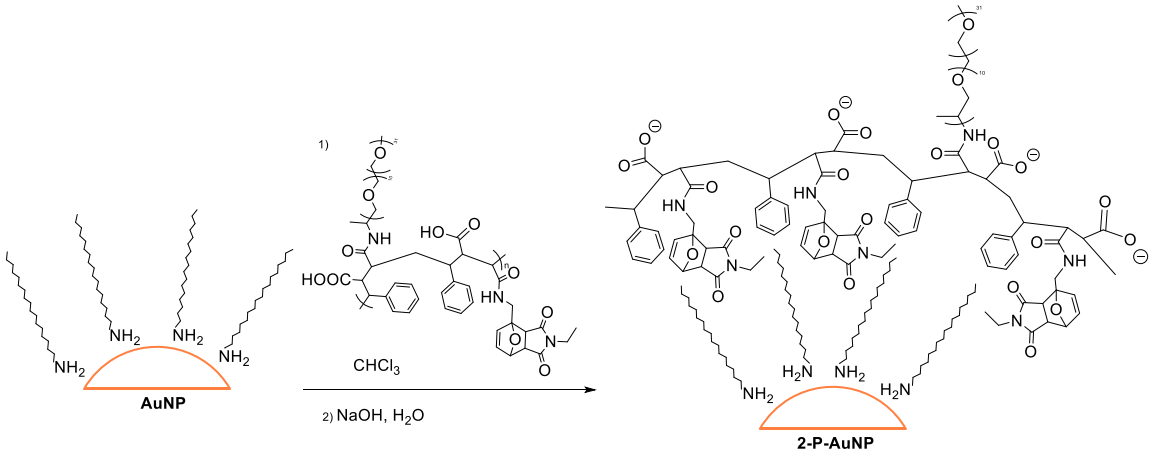

Synthesis of nano-assembly 2-P-AuNP. A stirring solution of 2.00 mL of octadecylamine-coated gold nanoparticles was treated with the solution of Diels-Alder adduct grafted amphiphilic polymer **2-P** (0.0031 g) in 1.00 mL of chloroform. The resulting mixture was stirred for 18 h at ambient temperature (22 °C), at which time the solvent was removed under vacuum until a red viscous residue was obtained. This residue was treated with alkaline water (1.00 mL, pH 13, adjusted with 0.1 M aqueous NaOH), and the resulting mixture was sonicated for approximately 30 s. The volume of the red emulsion was reduced using a rotary vacuum until a clear colloid formed. The colloid was centrifuged at 20600 rpm for 20 min and the flow-through was discarded. The remaining pellet was re-dispersed in 2.00 mL of ultrapure water to obtain a final stock solution of **2-P-AuNP** for further use.

Particle Size Analysis (PSA) of nanoassemblies

Size distribution of **AuNP** in water (a) (average size 11.70 nm); **AuNP** in chloroform (b) (average size = 4.85 nm); **2-P-AuNP** (c) (average size = 21.04 nm); **P-AuNP-1** (d) (21.34 nm). The Average size values were obtained directly from the DLS instrument using Malvern General Purpose & Multiple Narrow Mode NNLS (non-negative least squares) algorithm to treat the autocorrelation equation of the intensity trace describing sample intensity fluctuation recorded during the experiment.

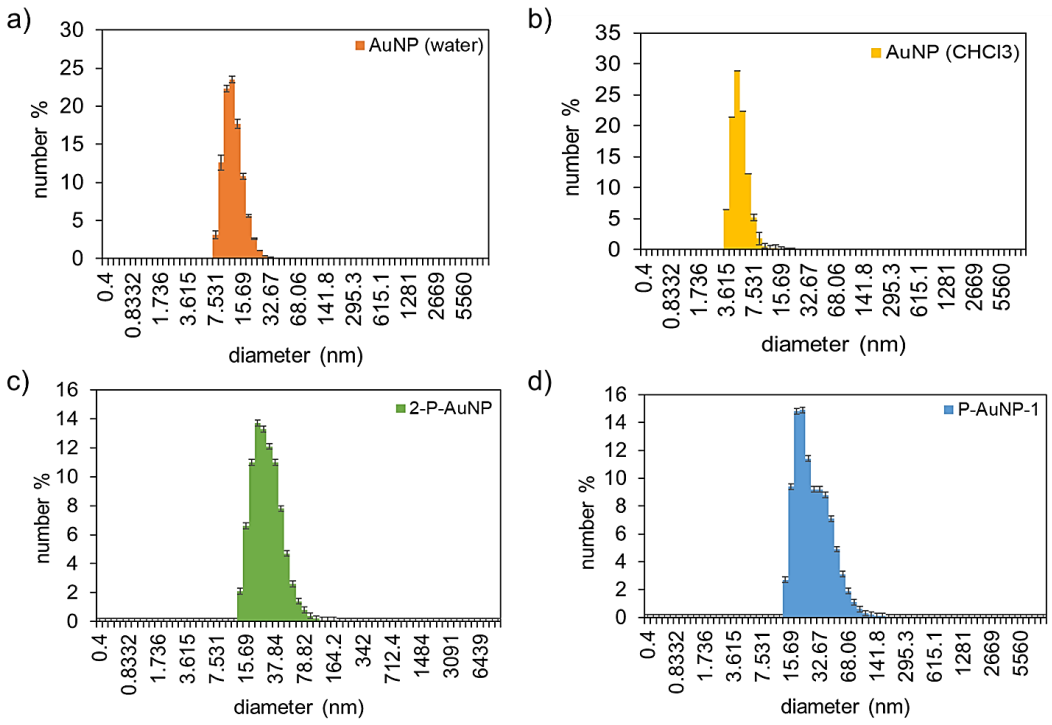

Estimating the loading of bicyclic compound 1 in P-AuNP-1

Quantification of the bicyclic compound **1** that was encapsulated inside the amphiphilic nanoassembly **P-AuNP-1** was achieved by determining the concentration of released Tyrphostin A8 in the flow-through filtrate after the photothermolysis and spin-filtering using UV-vis absorption spectroscopy. The assumption is that all Tyrphostin A8 is released from the nano-assembly. The mass of a single gold nanoparticle was calculated using the size determined by TEM and assuming that the nanoparticles are perfectly spherical.

Average radius of one particle (cm)	= 5.6×10^{-7}	
Volume of a particle, $V = 4/3\pi r^3$ (cm^3)	= $4/3*(3.14)*(5.6 \times 10^{-7})^3$	= 7.35×10^{-19}
Density of gold (g/cm^3)	= 19.30	
Mass of a single particle (g)	= $(19.30)*(7.35 \times 10^{-19})$	= 1.42×10^{-17}
Weight of residue of P-AuNP-1 (g)	= 8.4×10^{-5}	
Number of AuNP in 1 mL of P-AuNP-1	= $(8.4 \times 10^{-5})/(1.42 \times 10^{-17})$	= 5.92×10^{12}

Table 4.4: Calculated molecules of gold nanoparticles in 1 mL of **P-AuNP-1**

Concentration of P-AuNP-1 (μg/μL) in water	2.66×10^{-6}	
A_{Tyr} (415 nm)	3.2×10^{-2}	
ε of released Tyrphostin (415 nm) ($M^{-1}cm^{-1}$)	3.5×10^{4}	
Volume of sample (L)	1×10^{-3}	
Concentration of released Tyrphostin (M)	$= (3.2 \times 10^{-2})/(3.5 \times 10^{4})$	$= 9.14 \times 10^{-7}$
Moles of released Tyrphostin	$= (9.14 \times 10^{-7})*(1 \times 10^{-3})$	$= 9.14 \times 10^{-10}$
Molecules of released Tyrphostin	$= (9.14 \times 10^{-10})*(6.022 \times 10^{23})$	$= 5.5 \times 10^{14}$
Molecules of Adduct 1 in the sample, based on 1:1 reaction ratio	$= 5.5 \times 10^{14}$	
Loading of Adduct 1 per particle	$= (5.5 \times 10^{14})/(5.92 \times 10^{12})$	$= 92$

Table 4.5: Calculated loading of adduct **1** in 1 mL of **P-AuNP-1**

Estimating the loading of Diels-Alder adduct 2 in 2-P-AuNP

Determination of the bicyclic compound **2** that was tethered onto the amphiphilic polymer **P** for the nanoassembly **2-P-AuNP** was done by determining the concentration of released N-ethylmaleimide after Photothermolysis and spin-filtering using UV-vis absorption spectroscopy. The assumption is that all N-ethylmaleimide is released from the nano-assembly. The mass of a single gold nanoparticle was calculated using the size determined by TEM and assuming that the nanoparticles are perfectly spherical.

Average radius of one particle (cm)	$= 5.6 \times 10^{-7}$	
Volume of a particle, $V = 4/3\pi r^3$ (cm^3)	$= 4/3*(3.14)*(5.6 \times 10^{-7})^3$	$= 7.352 \times 10^{-19}$
Density of gold (g/cm^3)	$= 19.30$	
Mass of a single particle (g)	$= (19.30)*(7.352 \times 10^{-19})$	$= 1.42 \times 10^{-17}$
Weight of residue of 2-P-AuNP (g)	$= 1.3 \times 10^{-2}$	
Number of AuNP in the sample	$= (1.3 \times 10^{-2})/(1.42 \times 10^{-17})$	$= 9.1 \times 10^{14}$

Table 4.6: Calculated molecules of gold nanoparticles in 1 mL **2-P-AuNP**

Concentration of 2-P-AuNP (mg/mL) in water	0.48×10^{-3}	
A_{NEM} (298 nm)	1.36×10^{-1}	
ε of released NEM (298 nm) ($M^{-1}cm^{-1}$)	1.68×10^{2}	
Volume of sample (L)	1×10^{-3}	
Concentration of released N-ethylmaleimide (M)	$= (1.36 \times 10^{-1})/(1.68 \times 10^{2})$	$= 8.09 \times 10^{-4}$
Moles of released N-ethylmaleimide	$= (8.09 \times 10^{-4})*(1 \times 10^{-3})$	$= 8.09 \times 10^{-7}$
Molecules of released N-ethylmaleimide	$= (8.09 \times 10^{-7})*(6.022 \times 10^{23})$	$= 4.87 \times 10^{17}$
Molecules of Adduct 2 in the sample, based on 1:1 reaction ratio	$= 4.87 \times 10^{17}$	
Loading of Adduct 2 per particle	$= (4.87 \times 10^{17})/(9.1 \times 10^{14})$	= 532

Table 4.7: Calculated loading of tethered adduct **2** in 1 mL **2-P-AuNP**

Verification of Tyrphostin A8 and N-ethyl maleimide in the supernatant liquid

To verify that compound had been released and liberated from the nanoparticles it was essential to separate the nanoparticles from the solution. The sample after photolysis experiments was centrifuged using Amicron® Ultra-0.5 centrifugal filter devices (10 kDa) as per the recommendations of the manufacturer. The resulting supernatants were extracted and analyzed via UV-vis spectroscopy and mass spectrometry.

Determination of absorbed power by nanoassemblies

To verify the net absorbed power by the nanoassembly, power measurements were conducted and compared with the power transmitted by the empty quartz narrow channel cuvette used for UV-visible absorption measurements and power transmitted by the cuvette containing the nanoparticle solution.

	P-AuNP-1	**2-P-AuNP**
Incident power (mW)	800	200
Power transmitted by the empty cuvette (mW)	680	170
Power transmitted by 1 mL of solution (mW)	450	112
Net power absorbed (mW)	230	58

Table 4.8: Calculated net absorbed power by nanoassemblies

Chapter 5.

Conclusion

The growth and development of technologies that can provide superior control over material properties have led to the rise in popularity of novel smart materials which are responsive towards the light. The applicability of light as the external stimulus is further advantageous as it offers superior spatial and temporal control, together with its non-invasive nature and the ability to control its magnitude, and effect. Therefore, molecular systems that respond to light are finding a better scope of application in the areas ranging from biochemistry, medicine, bioimaging, to data storage, chemical synthesis, and polymer science. These photoresponsive systems could dramatically influence chemical reactivity by improving the efficiency of the reaction or reducing the formation of undesired side-products. Nonetheless, designing intelligent systems that are capable of controlling a chemical process requires effective communication of the photoresponsive moiety with light and is potentially challenging, as these systems are required to efficiently absorb specific wavelengths of light and undergo excited-state deactivation *via* a preferred pathway. The dithienylethene-based molecular switches are especially suitable to minimize these constraints as they have well-behaved photoresponsive properties as well as the better thermal stability of both isomers compared to other systems. The electronic and structural differences of the two isomers of DTEs can influence and regulate their chemical reactivity. Alternatively, the modification of geometric and electronic configuration, the presence or absence of competing mechanisms, or the creation or destruction of the photoresponsive architecture by the means of secondary chemical reactions or interactions can allow for control of their photochromic properties.

This thesis illustrated and discussed, by providing examples, multiple strategies that can be employed to integrate chemical reactivity and light either directly, by using small photoresponsive dithienylethenes (DTEs), or indirectly, by the means of metal-based nano-assemblies. The applicability of this *gated reactivity* approach was demonstrated in the areas of catalysis and on-command drug delivery. The photoresponsive dithienylethene framework was destroyed upon interaction with reactive chemical reagents. The DTE-based detectors for hydrazine and other toxic industrial chemicals with

this modified 1,3,5-hexatriene system and turned “off” photochromism were used to present the *gated photochemistry* approach.

The concept of direct *gating* of chemical reactivity using light was introduced in *Chapter 2*. A carefully constructed and modified DTE system including an electron-deficient alkene in the main 1,3,5-hexatriene motif was presented and tested to act as a light-initiated trigger for the inhibition of the catalytic activity of Karstedt’s catalyst. It was demonstrated that light of appropriate wavelength resulted in a rearrangement of the central 1,3,5-hexatriene system that induced variations in the electronic properties of the DTE-based photoresponsive inhibitor. Furthermore, it was shown that these changes in electronic properties directly led to alterations in the inhibitor’s coordination ability towards the metal centre of the catalyst. The differences in the binding strength of the two photoisomers were shown to vary the kinetics of a simple hydrosilylation reaction catalyzed by Karstedt’s catalyst. While the presented system was limited by its moderate photostationary state, the fundamental structure of the inhibitor, the inhibition mechanism, and the inhibition detection methodology offered, provide the necessary foundation towards redesigning the photoresponsive inhibitor scaffold to create fully *gated* “on-off” catalytic systems.

In *Chapter 3*, the concept of *reactivity-gated photochromism* was discussed to create a molecular system that can act as a multi-processing detector upon interaction with external chemical reagents. The presented nitrile functionalized DTE system freely underwent bidirectional transformation upon exposure to light of specific wavelengths. The nitrile functionality of the system displayed reactivity towards hydrazine in both solution and vapour phases that resulted in the permanent quenching of the photoresponsive activity of the molecule due to the destruction of the 1,3,5-hexatriene structure. The irreversible structural change in the DTE motif in the presence of hydrazine led to a change in the molecule’s optical response. Furthermore, it was presented that the system served as a dual-mode detector (both colour and emission) for detecting and entrapping hydrazine. The concept of the modification of DTE design in the presence of external chemicals generating a paired output signal could lead to the development of simple detection systems.

The approach of *gating* chemical reactivity with light was further explored in *Chapter 4*, described by employing gold-nanoparticle-based nanoassemblies for potential drug delivery applications. The described nanoassemblies that were created consisted of a gold

nanoparticle core and an amphiphilic polymer shell and were shown to be stable under aqueous conditions. Simple thermoresponsive Diels-Alder adducts were either loaded inside the amphiphilic polymer shell or were covalently attached as a pendent group onto the shell itself. It was further demonstrated that the photothermal effect of the gold nanoparticles generated enough heat in the vicinity of the nanoparticles and caused a retro-Diels-Alder reaction that resulted in the rapid release of the dienophiles outside the shell. The nanoassemblies were shown to be stable under the LASER conditions and no release of by-product diene was observed. These systems can be regarded as prototypes of photogated reactivity whereby light triggers the generation of heat inside the nano-system that results in the initiation of a chemical reaction and represents a novel strategy for the development of photorelease technologies. In addition, visible light is used to activate the release reaction which is doubly advantageous as there would be minimal biological damage and an increased penetration depth. The presented study provides appropriate details for modification of the thermoresponsive systems that are incorporated for the development of controlled-release applications that allow for the release of complex therapeutic reagents on demand.

In summary, this thesis exemplified the integration of light and chemical reactivity in molecular systems based on dithienylethenes and gold nanoparticles. The creation of a functionalized DTE structure was shown to efficiently *gate* the chemical reactivity of the two isomers towards external chemical species by altering their electronics. Alternatively, the DTE structure could be modified structurally in the presence of external chemical species such that the photochromism and emission of the system were modulated effectively. In addition, elaborate nanoassemblies based on gold nanoparticles represented systems that displayed conversion of light energy to heat to facilitate and bring about chemical reactions inside nanoreactors. Overall, the integration of light and chemical reactivity using molecular systems presents promising approaches for the development of functional materials for usage in controlling the chemical process, drug delivery applications, and chemical detection. Several strategies have already been presented at the end of each chapter to mitigate these limitations.

References

1 National Research Council, *Opportunities in Chemistry*, The National Academies Press, Washington, DC, 1985.

2 F. A. Leibfarth, K. M. Mattson, B. P. Fors, H. A. Collins and C. J. Hawker, *Angew. Chemie - Int. Ed.*, 2013, **52**, 199–210.

3 N. Corrigan and C. Boyer, *ACS Macro Lett.*, 2019, **8**, 812–818.

4 M. Zhu, X. Z. Song, S. Y. Song, S. N. Zhao, X. Meng, L. L. Wu, C. Wang and H. J. Zhang, *Adv. Sci.*, 2015, **2**, 1–6.

5 A. E. Enciso, L. Fu, A. J. Russell and K. Matyjaszewski, *Angew. Chemie - Int. Ed.*, 2018, **57**, 933–936.

6 S. Angelos, Y. Yang, K. Patel, J. F. Stoddart and J. I. Zink, *Angew. Chemie - Int. Ed.*, 2008, **47**, 2222–2226.

7 E. M. Broderick, N. Guo, C. S. Vogel, C. Xu, J. Sutter, J. T. Miller, K. Meyer, P. Mehrkhodavandi and P. L. Diaconescu, *J. Am. Chem. Soc.*, 2011, **133**, 9278–9281.

8 V. Balzani, A. Credi and M. Venturi, *Molecular Devices and Machines: Concepts and Perspectives for the Nanoworld*, Wiley-VCH Verlag GmbH, Weinheim, 2nd Editio., 2008.

9 R. S. Stoll and S. Hecht, *Angew. Chemie - Int. Ed.*, 2010, **49**, 5054–5075.

10 R. Göstl, A. Senf and S. Hecht, in *Photochromic Materials: Preparation, Properties and Applications*, eds. H. Tian and J. Zhang, Wiley-VCH Verlag GmbH & Co. KGaA, Weinheim, First., 2016, pp. 167–194.

11 W. Zhou, S. M. Kuebler, K. L. Braun, T. Yu, J. K. Cammack, C. K. Ober, J. W. Perry and S. R. Marder, *Science*, 2002, **296**, 1106–1109.

12 L. Ionov and S. Diez, *J. Am. Chem. Soc.*, 2009, **131**, 13315–13319.

13 M. M. Russew and S. Hecht, *Adv. Mater.*, 2010, **22**, 3348–3360.

14 A. D. McNaught and A. Wilkinson, *IUPAC. Compendium of Chemical Terminology (the 'Gold Book')*, Blackwell Scientific Publications, Oxford, 2nd edn., 1997.

15 H. Dürr and H. Bouas-Laurent, Eds., *Photochromism molecules and systems*, Elsevier B.V., Amsterdam, Revised., 2003.

16 K. Nakatani, J. Piard, P. Yu and R. Métivier, in *Photochromic Materials*, eds. H. Tian and J. Zhang, Wiley-VCH Verlag GmbH & Co. KGaA, Weinheim, 2016, pp. 1–46.

17 S. Shinkai, T. Nakaji, Y. Nishida, T. Ogawa and O. Manabe, *J. Am. Chem. Soc.*, 1980, **1**, 5860–5865.

18 D. Sud, T. B. Norsten and N. R. Branda, *Angew. Chemie - Int. Ed.*, 2005, **44**, 2019–2021.

19 M. Ishikawa, T. Ohzono, T. Yamaguchi and Y. Norikane, *Sci. Rep.*, 2017, **7**, 3–8.

20 K. Arai and Y. Kawabata, *Macromol. Rapid Commun.*, 1995, **16**, 875–880.

21 M. S. Kim, H. Maruyama, T. Kawai and M. Irie, *Chem. Mater.*, 2003, **15**, 4539–4543.

22 C. Bertarelli, A. Bianco, F. D'Amore, M. C. Gallazzi and G. Zerbi, *Adv. Funct. Mater.*, 2004, **14**, 357–363.

23 G. Callierotti, A. Bianco, C. Castiglioni, C. Bertarelli and G. Zerbi, *J. Phys. Chem. A*, 2008, **112**, 7473–7480.

24 T. Kawai, Y. Nakashima and M. Irie, *Adv. Mater.*, 2005, **17**, 309–314.

25 H. Choi, H. Lee, Y. Kang, E. Kim, S. O. Kang and J. Ko, *J. Org. Chem.*, 2005, **70**, 8291–8297.

26 M. N. Roberts, C. J. Carling, J. K. Nagle, N. R. Branda and M. O. Wolf, *J. Am. Chem. Soc.*, 2009, **131**, 16644–16645.

27 M. Morimoto and M. Irie, *Chem. Commun.*, 2011, **47**, 4186–4188.

28 X.-D. Huang, G.-H. Wen, S.-S. Bao, J.-G. Jia and L.-M. Zheng, *Chem. Sci.*, 2021, **12**, 929–937.

29 M. Irie, S. Kobatake and M. Horichi, *Science*, 2001, **291**, 1769–1772.

30 M. Irie, *Bull. Chem. Soc. Jpn.*, 2008, **81**, 917–926.

31 J. C. Crano and R. J. Guglielmetti, Eds., *Organic Photochromic and Thermochromic Compounds volume 1*, Springer, Boston, MA, 2002.

32 J. García-Amorós and D. Velasco, *Beilstein J. Org. Chem.*, 2012, **8**, 1003–1017.

33 F. Hamon, F. Djedaini-Pilard, F. Barbot and C. Len, *Tetrahedron*, 2009, **65**, 10105–10123.

34 S. Shinkai, T. Minami, Y. Kusano and O. Manabe, *J. Am. Chem. Soc.*, 1983, **105**, 1851–1856.

35 V. I. Minkin, in *Molecular Switches volume 1*, eds. B. L. Feringa and W. R. Browne, Wiley-VCH Verlag GmbH & Co. KGaA, Weinheim, second., 2011, pp. 37–80.

36 S. Helmy, F. A. Leibfarth, S. Oh, J. E. Poelma, C. J. Hawker and J. R. De Alaniz, *J. Am. Chem. Soc.*, 2014, **136**, 8169–8172.

37 B. L. Feringa, Ed., *Molecular switches*, Wiley-VCH Verlag GmbH, Weinheim, 2001.

38 Y. Yokoyama, T. Gushiken and T. Ubukata, in *Molecular Switches volume 1*, eds. B. L. Feringa and W. R. Browne, Wiley-VCH Verlag GmbH & Co. KGaA, Weinheim, second., 2011, pp. 81–95.

39 Y. Yokoyama, *Chem. Rev.*, 2000, **100**, 1717–1739.

40 C. C. Warford, V. Lemieux and N. R. Branda, in *Molecular Switches volume 1*, eds. B. L. Feringa and W. R. Browne, Wiley-VCH Verlag GmbH & Co. KGaA, Weinheim, second., 2011, pp. 1–35.

41 M. Irie, in *Organic Photochromic and Thermochromic Compounds Main Photochromic Families*, eds. J. C. Crano and R. J. Guglielmetti, Springer US, New York, 2002, pp. 207–222.

42 M. Irie, *Chem. Rev.*, 2000, **100**, 1685–1716.

43 H. Tian and S. Yang, *Chem. Soc. Rev.*, 2004, **33**, 85–97.

44 M. Irie and M. Mohri, *J. Org. Chem.*, 1988, **53**, 803–808.

45 R. M. Kellogg, M. B. Groen and H. Wynberg, *J. Org. Chem.*, 1967, **32**, 3093–3100.

46 S. Nakamura and M. Irie, *J. Org. Chem.*, 1988, **53**, 6136–6138.

47 R. Hoffmann and R. B. Woodward, *The conservation of orbital symmetry*, Verlag Chemie GmbH, Weinheim, 1971.

48 J. Clayden, N. Greeves and S. Warren, in *Organic chemistry*, Oxford University Press, New York, Second., 2012, pp. 922–927.

49 M. Irie, T. Lifka, S. Kobatake and N. Kato, *J. Am. Chem. Soc.*, 2000, **122**, 4871–4876.

50 S. L. Gilat, S. H. Kawai and J. -M Lehn, *Chem. – A Eur. J.*, 1995, **1**, 275–284.

51 D. Wilson and N. R. Branda, *Angew. Chemie - Int. Ed.*, 2012, **51**, 5431–5434.

52 H. Taniguchi, A. Shinpo, T. Okazaki, F. Matsui and M. Irie, *Nippon Kagaku Kaishi*, 1992, 1138–1140.

53 M. Irie, T. Lifka, K. Uchida, S. Kobatake and Y. Shindo, *Chem. Commun.*, 1999, 747–748.

54 K. Higashiguchi, K. Matsuda, S. Kobatake, T. Yamada, T. Kawai and M. Irie, *Bull. Chem. Soc. Jpn.*, 2000, **73**, 2389–2394.

55 M. Irie and K. Uchida, *Bull. Chem. Soc. Jpn.*, 1998, 71, 985–996.

56 K. Higashiguchi, K. Matsuda, S. Kobatake, T. Yamada, T. Kawai and M. Irie, *Bull. Chem. Soc. Jpn.*, 2000, **73**, 2389–2394.

57 M. Irie and M. Morimoto, *Bull. Chem. Soc. Jpn.*, 2018, **91**, 237–250.

58 T. Fukaminato, T. Hirose, T. Doi, M. Hazama, K. Matsuda and M. Irie, *J. Am. Chem. Soc.*, 2014, **136**, 17145–17154.

59 M. Irie, K. Sakemura, M. Okinaka and K. Uchida, *J. Org. Chem.*, 1995, **60**, 8305–8309.

60 B. Lasorne, A. Fihey, D. Mendive-Tapia and D. Jacquemin, *Chem. Sci.*, 2015, **6**, 5695–5702.

61 M. Herder, B. M. Schmidt, L. Grubert, M. Pätzel, J. Schwarz and S. Hecht, *J. Am. Chem. Soc.*, 2015, **137**, 2738–2747.

62 S. Chen, W. Li and W.-H. Zhu, in *Photon-Working Switches*, eds. Y. Yokoyama and K. Nakatani, Springer Japan, Tokyo, 2017, pp. 37–68.

63 K. Matsuda and M. Irie, *Chem. Lett.*, 2006, **35**, 1204–1209.

64 H. Tian and S. Wang, *Chem. Commun.*, 2007, 781–792.

65 M. Takeshita, K. Uchida and M. Irie, *Chem. Commun.*, 1996, 1807–1808.

66 M. Takeshita, C. F. Soong and M. Irie, *Tetrahedron Lett.*, 1998, **39**, 7717–7720.

67 M. Takeshita and M. Irie, *Tetrahedron Lett.*, 1998, **39**, 613–616.

68 M. Takeshita and M. Irie, *J. Org. Chem.*, 1998, **63**, 6643–6649.

69 S. H. Kawai, *Tetrahedron Lett.*, 1998, **39**, 4445–4448.

70 D. Vomasta, C. Högner, N. R. Branda and B. König, *Angew. Chemie - Int. Ed.*, 2008, **47**, 7644–7647.

71 S. H. Kawai, S. L. Gilat and J.-M. Lehn, *Eur. J. Org. Chem.*, 1999, 2359–2366.

72 Y. Odo, K. Matsuda and M. Irie, *Chem. Eur. J.*, 2006, **12**, 4283–4288.

73 J. P. Malval, I. Gosse, J. P. Morand and R. Lapouyade, *J. Am. Chem. Soc.*, 2002, **124**, 904–905.

74 D. Sud, T. J. Wigglesworth and N. R. Branda, *Angew. Chemie - Int. Ed.*, 2007, **46**, 8017–8019.

75 H. D. Samachetty, V. Lemieux and N. R. Branda, *Tetrahedron*, 2008, **64**, 8292–8300.

76 V. Lemieux, M. D. Spantulescu, K. K. Baldridge and N. R. Branda, *Angew. Chemie - Int. Ed.*, 2008, **47**, 5034–5037.

77 C. C. Warford, C. J. Carling and N. R. Branda, *Chem. Commun.*, 2015, **51**, 7039–7042.

78 M. Irie, O. Miyatake, K. Uchida and T. Eriguchi, *J. Am. Chem. Soc.*, 1994, **116**, 9894–9900.

79 J. Zhang, W. Tan, X. Meng and H. Tian, *J. Mater. Chem.*, 2009, **19**, 5726–5729.

80 K. Liu, Y. Wen, T. Shi, Y. Li, F. Li, Y. L. Zhao, C. Huang and T. Yi, *Chem. Commun.*, 2014, **50**, 9141–9144.

81 S. H. Kawai, S. L. Gilat and J. M. Lehn, *J. Chem. Soc. Chem. Commun.*, 1994, 1011–1013.

82 S. H. Kawai, S. L. Gilat, R. Ponsinet and J. -M Lehn, *Chem. – A Eur. J.*, 1995, **1**, 285–293.

83 N. A. Simeth, A. C. Kneuttinger, R. Sterner and B. König, *Chem. Sci.*, 2017, **8**, 6474–6483.

84 M. Ohsumi, T. Fukaminato and M. Irie, *Chem. Commun.*, 2005, 3921–3923.

85 F. Nourmohammadian, T. Wu and N. R. Branda, *Chem. Commun.*, 2011, **47**, 10954–10956.

86 Z. H. Chen, S. M. Zhao, Z. Y. Li, Z. Zhang and F. S. Zhang, *Sci. China, Ser. B Chem.*, 2007, **50**, 581–586.

87 K. Uchida, T. Matsuoka, S. Kobatake, T. Yamaguchi and M. Irie, *Tetrahedron*,

2001, **57**, 4559–4565.

88 J. Kühni and P. Belser, *Org. Lett.*, 2007, **9**, 1915–1918.

89 A. Peters, C. Vitols, R. McDonald and N. R. Branda, *Org. Lett.*, 2003, **5**, 1183–1186.

90 B. Wüstenberg and N. R. Branda, *Adv. Mater.*, 2005, **17**, 2134–2138.

91 H. D. Samachetty and N. R. Branda, *Pure Appl. Chem.*, 2006, **78**, 2351–2359.

92 V. Lemieux and N. R. Branda, *Org. Lett.*, 2005, **7**, 2969–2972.

93 V. Lemieux, S. Gauthier and N. R. Branda, *Angew. Chemie - Int. Ed.*, 2006, **45**, 6820–6824.

94 A. M. Asadirad, S. Boutault, Z. Erno and N. R. Branda, *J. Am. Chem. Soc.*, 2014, **136**, 3024–3027.

95 B. Kaur, R. Raza, M. J. Stashick and N. R. Branda, *Org. Chem. Front.*, 2019, **6**, 1253–1256.

96 V. W. Yam, J. K. Lee, C. Ko and N. Zhu, *J. Am. Chem. Soc.*, 2009, **131**, *3*, 912–913.

97 M. V. Peters, R. S. Stoll, A. Kühn and S. Hecht, *Angew. Chemie - Int. Ed.*, 2008, **47**, 5968–5972.

98 F. Würthner and J. Rebek, *J. Chem. Soc. Perkin Trans. 2*, 1995, 1727–1734.

99 J. . Mark, H. . Allcock and R. West, *Inorganic polymers*, Oxford University Press, New York, 2005.

100 A. . Tracton, *Coating materials and surface coatings*, CRC Press Taylor & Francis Group, Boca Raton, 2006.

101 R. De Jaeger and M. Gleria, Eds., *Silicon-Based Inorganic Polymers*, Nova Science Publishers, New York, 2008.

102 http://www.tullisrussell.com/userfiles/images/Labelstock/Labelstock-Diagram.jpg%0A.

103 A. More, Silicone Coating Market 2019, https://www.marketwatch.com/press-release/silicone-coating-market-2019-global-industry-analysis-by-trends-size-share-company-overview-growth-and-forecast-by-2025-latest-research-report-by-research-reports-world-2019-04-24.

104 G. Odian, *Principles of Polymerization*, John Wiley & Sons, Inc., New Jersey,

Fourth Edi., 2004.

105 L. N. Lewis, J. Stein, Y. Gao, R. E. Colborn and G. Hutchins, *Platin. Met. Rev.*, 1997, **41**, 66–75.

106 T. K. Meister, K. Riener, P. Gigler, J. Stohrer, W. A. Herrmann and F. E. Kühn, *ACS Catal.*, 2016, **6**, 1274–1284.

107 T. Hayashi, in *Comprehensive Asymmetric Catalysis*, eds. E. . Jacobsen, A. Pflatz and H. Yamamoto, Springer, Berlin, volume 1., 1999.

108 F. Faglioni, M. Blanco, W. A. Goddard and D. Saunders, *J. Phys. Chem. B*, 2002, **106**, 1714–1721.

109 L. N. Lewis, J. Stein, R. E. Colborn, Y. Gao and J. Dong, *J. Organomet. Chem.*, 1996, **521**, 221–227.

110 A. G. Bejenariu, J. Ø. Poulsen, A. L. Skov and L. C. Henriksen, *Annu. Trans. Nord. Rheol. Soc.*, 2009, **17**, 269–276.

111 I. Kownacki, B. Marciniec, H. Steinberger, M. Kubicki, M. Hoffmann, A. Ziarko, K. Szubert, M. Majchrzak and S. Rubinsztajn, *Appl. Catal. A Gen.*, 2009, **362**, 106–114.

112 A. Hopf and K. H. Dötz, *J. Mol. Catal. A Chem.*, 2000, **164**, 191–194.

113 P. Steffanut, J. A. Osborn, A. DeCian and J. Fisher, *Chem. - A Eur. J.*, 1998, **4**, 2008–2017.

114 R. van Asselt, C. J. Elsevier, W. J. J. Smeets and A. L. Spek, *Inorg. Chem.*, 1994, **33**, 1521–1531.

115 J. Salmone, *Concise Polymeric Materials Encyclopedia*, CRC Press Taylor & Francis Group, 1998.

116 Radtech-Europe, UV/EB Brochure, https://www.radtech-europe.com/sites/default/files/rte_uveb_brochure_2018_0.pdf.

117 S. Wadge, Simon Fraser University, 2009 (M.Sc. Thesis).

118 S. Lee, Y. You, K. Ohkubo, S. Fukuzumi and W. Nam, *Chem. Sci.*, 2014, **5**, 1463–1474.

119 D. Sud, T. J. Wigglesworth and N. R. Branda, *Angew. Chemie*, 2007, **119**, 8163–8165.

120 M. D'Auria, A. De Mico, F. D'Onofrio and G. Piancatelli, *J. Org. Chem.*, 1987, **52**, 5243–5247.

121 K. Uchida, Y. Kido, T. Yamaguchi and M. Irie, *Bull. Chem. Soc. Jpn.*, 1998, **71**, 1101–1108.

122 B. Marcinie and J. Chojnowski, Eds., *Progress in Organosilicon Chemistry*, Gordon and Breach Science Publishers S.A., Basel, 1995.

123 S. Fantasia, J. L. Petersen, H. Jacobsen, L. Cavallo and S. P. Nolan, *Organometallics*, 2007, **26**, 5880–5889.

124 W. Levason and D. Pletcher, *Platin. Met. Rev.*, 1993, 17–23.

125 US Patent 3383356, 1968.

126 J. Stein, L. N. Lewis, Y. Gao and R. A. Scott, *J. Am. Chem. Soc.*, 1999, **121**, *15*, 3693–3703.

127 M. A. Taige, S. Ahrens and T. Strassner, *J. Organomet. Chem.*, 2011, **696**, 2918–2927.

128 L. N. Lewis, *J. Am. Chem. Soc.*, 1990, **112**, 5998.

129 Q. Luo, Y. Liu, X. Li and H. Tian, *Photochem. Photobiol. Sci.*, 2010, **9**, 234–238.

130 J. Wickham, S. Stehman, L. Gass, J. Dewitz, D. Sorenson, B. Granneman, R. Ross and L. Baer, *Environ. Int.*, 2018, **116**, 286–299.

131 J. Plautz, *Bloom. CityLab*, 2018.

132 P. M. J. Byrnes, M. E., King, D. A. & Tierno, *Nuclear, Chemical, and Biological Terrorism – Emergency Response and Public Protection*, CRC Press, 2003, vol. 53.

133 R. Fletcher-Wood, Magnificent molecules: Hydrazine, https://edu.rsc.org/magnificent-molecules/hydrazine/2000023.article.

134 L. Cui, C. Ji, Z. Peng, L. Zhong, C. Zhou, L. Yan, S. Qu, S. Zhang, C. Huang, X. Qian and Y. Xu, *Anal. Chem.*, 2014, **86**, 4611–4617.

135 B. Roy and S. Bandyopadhyay, *Anal. Methods*, 2018, **10**, 1117–1139.

136 K. H. Nguyen, Y. Hao, W. Chen, Y. Zhang, M. Xu, M. Yang and Y. N. Liu, *Luminescence*, 2018, **33**, 816–836.

137 A. More, *360 Res. Reports*, 2019.

138 S. Satsangi, Hydrazine Market by Application (Pharmaceuticals, Water Treatment, Blowing Agents, Agrochemicals, and Others) - Global Opportunity Analysis and Industry Forecast, 2014-2022, https://www.alliedmarketresearch.com/hydrazine-

market, (accessed 13 April 2021).

139 Hydrazine Market Size, Share & Trends Analysis Report By Application, Regional Outlook, Competitive Strategies, And Segment Forecasts, 2019 To 2025, https://www.grandviewresearch.com/industry-analysis/hydrazine-market, (accessed 13 April 2021).

140 U. S. E. P. Agency, *Hydrazine*, 2016.

141 U. D. of H. and H. Services, *Occupational safety and health guideline for hydrazine potential human carcinogen*, 1988.

142 D. P. Elder, D. Snodin and A. Teasdale, *J. Pharm. Biomed. Anal.*, 2011, **54**, 900–910.

143 A. Carlin, N. Gregory and J. Simmons, *J. Pharm. Biomed. Anal.*, 1998, **17**, 885–890.

144 B. Handwerk, *Bacteria Eat Human Sewage, Produce Rocket Fuel*, 2005.

145 M. Byers and C. Byers, *Polar Rec. (Gr. Brit).*, 2017, **53**, 580–591.

146 S. Parodi, S. De Flora, M. Cavanna, A. Pino, L. Robbiano, C. Bennicelli and G. Brambilla, *Cancer Res.*, 1981, **41**, 1469–1482.

147 M. J. Zeilmaker, M. J. Horsfall, J. B. van Helten, B. W. Glickman and G. R. Mohn, *Mol. Carcinog.*, 1991, **4**, 180–188.

148 J. R. Stetter, K. F. Blurton, A. M. Valentine and K. A. Tellefsen, *J. Electrochem. Soc.*, 1978, **125**, 1804–1807.

149 J. Liu, W. Zhou, T. You, F. Li, E. Wang and S. Dong, *Anal. Chem.*, 1996, **68**, 3350–3353.

150 C. Batchelor-McAuley, C. E. Banks, A. O. Simm, T. G. J. Jones and R. G. Compton, *Analyst*, 2006, **131**, 106–110.

151 A. Umar, M. M. Rahman, S. H. Kim and Y. B. Hahn, *Chem. Commun.*, 2008, **7345**, 166–168.

152 J. Liu, Y. Li, J. Jiang and X. Huang, *Dalton Trans.*, 2010, **39**, 8693–8697.

153 T. Kean, J. H. M. B. Miller, G. G. Skellern and D. Snodin, *Pharmeur. Sci. Notes*, 2006, **2006**, 23–33.

154 M. Sun, L. Bai and D. Q. Liu, *J. Pharm. Biomed. Anal.*, 2009, **49**, 529–533.

155 H. Lingeman, HOW TO SELECT A TECHNIQUE,

http://www.chromedia.org/chromedia?waxtrapp=gzgegDsHqnOxmOlIEcCbCsF&subNav=yarwnEsHqnOxmOlIEcCxBWT, (accessed 13 March 2021).

156 A. D. Smolenkov, I. A. Rodin and O. A. Shpigun, *J. Anal. Chem.*, 2012, **67**, 98–113.

157 J. Ma, J. Fan, H. Li, Q. Yao, J. Xia, J. Wang and X. Peng, *Dye. Pigment.*, 2017, **138**, 39–46.

158 W. Xu, X. Li, J. Yin, M. Han, W. Liu, Y. Yang and W. Li, *J. Photochem. Photobiol. A Chem.*, 2020, **390**, 112262.

159 X. Jin, C. Liu, X. Wang, H. Huang, X. Zhang and H. Zhu, *Sensors Actuators, B Chem.*, 2015, **216**, 141–149.

160 J. Fan, W. Sun, M. Hu, J. Cao, G. Cheng, H. Dong, K. Song, Y. Liu, S. Sun and X. Peng, *Chem. Commun.*, 2012, **48**, 8117–8119.

161 S. Goswami, S. Paul and A. Manna, *RSC Adv.*, 2013, **3**, 18872–18877.

162 H. Xu, Z. Huang, Y. Li, B. Gu, Z. Zhou, R. Xie, X. Pang, H. Li and Y. Zhang, *Analyst*, 2018, **143**, 4354–4358.

163 Y. Jung, I. G. Ju, Y. H. Choe, Y. Kim, S. Park, Y. M. Hyun, M. S. Oh and D. Kim, *ACS Sensors*, 2019, **4**, 441–449.

164 M. H. Lee, B. Yoon, J. S. Kim and J. L. Sessler, *Chem. Sci.*, 2013, **4**, 4121–4126.

165 B. Roy, S. Halder, A. Guha and S. Bandyopadhyay, *Anal. Chem.*, 2017, **89**, 10625–10636.

166 S. W. Thomas and T. M. Swager, *Adv. Mater.*, 2006, **18**, 1047–1050.

167 K. Vijay, C. Nandi and S. D. Samant, *RSC Adv.*, 2014, **4**, 30712–30717.

168 M. Qin, Y. Huang, F. Li and Y. Song, *J. Mater. Chem. C*, 2015, **3**, 9265–9275.

169 J. Liu, T. Li, S. Wang, Q. Qi, H. Song, Z. Li, L. Yang and W. Huang, *RSC Adv.*, 2020, **10**, 5572–5578.

170 C. L. Dickinson, J. K. Williams and B. C. McKusic, *J. Org. Chem.*, 1964, **29**, 1915–1919.

171 T. B. Norsten and N. R. Branda, *J. Am. Chem. Soc.*, 2001, **123**, 1784–1785.

172 T. Kawai, T. Koshido, Y. Kaneuchi and K. Yoshino, *Thin Solid Films*, 1996, **273**, 195–198.

173 M. Irie, T. Fukaminato, K. Matsuda and S. Kobatake, *Chem. Rev.*, 2014, **114**, 12174–12277.

174 K. Kasatani, S. Kambe and M. Irie, *J. Photochem. Photobiol. A Chem.*, 1999, **122**, 11–15.

175 K. Matsuda and M. Irie, *J. Photochem. Photobiol. C Photochem. Rev.*, 2004, **5**, 169–182.

176 M. M. Krayushkin, B. V. Lichitskii, A. P. Mikhalev, B. V. Nabatov, A. A. Dudinov and S. N. Ivanov, *Russ J Org Chem*, 2006, **42**, 860–864.

177 P. J. Hasnip, K. Refson, M. I. J. Probert, J. R. Yates, S. J. Clark and C. J. Pickard, *Philos. Trans. R. Soc. A Math. Phys. Eng. Sci.*, , DOI:10.1098/rsta.2013.0270.

178 M. J. Frisch, G. W. Trucks, H. B. Schlegel, G. E. Scuseria, M. A. Robb, J. R. Cheeseman, G. Scalmani, V. Barone, G. A. Petersson, H. Nakatsuji, X. Li, M. Caricato and A. Marenich, 2016.

179 Density Functional (DFT) Methods, https://gaussian.com/dft/, (accessed 14 May 2020).

180 Basis Sets, https://gaussian.com/basissets/, (accessed 14 May 2020).

181 C. T. Poon, W. H. Lam and V. W. W. Yam, *Chem. - A Eur. J.*, 2013, **19**, 3467–3476.

182 D. L. Lichtenberger, COMMON CONVERSION FACTORS IN COMPUTATIONAL CHEMISTRY, http://u.arizona.edu/~stefanb/linkpages/conversions.html, (accessed 15 May 2020).

183 A. R. Katritzky, C. Dennis Hall, B. E. D. M. El-Gendy and B. Draghici, *J. Comput. Aided. Mol. Des.*, 2010, **24**, 475–484.

184 A. Secrieru, P. M. O'Neill and M. L. S. Cristiano, *Molecules*, 2020, **25**, 1–28.

185 I. Alkorta, J. Elguero and J. F. Liebman, *Struct. Chem.*, 2006, **17**, 439–444.

186 M. Jarończyk, J. C. Dobrowolski and A. P. Mazurek, *J. Mol. Struct. THEOCHEM*, 2004, 673, 17–28.

187 S. M. Hecht, D. Werner, D. Traficante, M. Sundaralingam, P. Prusiner, T. Ito and T. Sakurai, *J. Org. Chem.*, 1975, **40**, 1815–1822.

188 D. S. Noyce, E. Ryder and B. H. Walker, *J. Org. Chem.*, 1955, **20**, 1681–1686.

189 W. Jacek, M. Szczęśniak and D. Shugar, *Zeitschrift fur Naturforsch. - Sect. C J. Biosci.*, 1980, **35**, 878–889.

190 C. Lee, W. Yang and R. G. Parr, *Phys. Rev. B*, 1988, **37**, 785–789.

191 A.-S. S. H. Elgazwy, *Org. Chem. Curr. Res.*, , DOI:10.4172/2161-0401.1000117.

192 Y. Juillet, S. Le Moullec, A. Bégos and B. Bellier, *Analyst*, 2005, **130**, 977–982.

193 F. Halet, A. R. Yeddou, A. Chergui, S. Chergui, B. Nadjemi and A. Ould-Dris, *J. Dispers. Sci. Technol.*, 2015, **36**, 1736–1741.

194 D. Sicilia, S. Rubio, D. Pérez-Bendito, N. Maniasso and E. A. G. Zagatto, *Analyst*, 1999, **124**, 615–620.

195 IR Spectrum Table & Chart, https://www.sigmaaldrich.com/technical-documents/articles/biology/ir-spectrum-table.html, (accessed 25 August 2020).

196 V. Valderrey, A. Bonasera, S. Fredrich and S. Hecht, *Angew. Chemie - Int. Ed.*, 2017, **56**, 1914–1918.

197 G. L. Long and J. D. Winefordner, *Anal. Chem.*, 1983, **55**, 712–724.

198 *Guidance for Industry Q2B Validation of Analytical Procedures: Methodology*, 1996, vol. 20857.

199 J. Ripp, *ANALYTICAL DETECTION LIMIT GUIDANCE & Laboratory Guide for Determining Method Detection Limits*, Madison, 1996.

200 *Definition and procedure for the determination of the method detection limit—Revision 1.11*, Washington, DC, 2016.

201 M. Shortreed, R. Kopelnan, M. Kuhn and B. Hoyland, *Anal. Chem.*, 1996, **68**, 1414–1418.

202 W. Lin, L. Yuan, Z. Cao, Y. Feng and L. Long, *Chem. - A Eur. J.*, 2009, **15**, 5096–5103.

203 A. Caballero, R. Martínez, V. Lloveras, I. Ratera, J. Vidal-Gancedo, K. Wurst, A. Tárraga, P. Molina and J. Veciana, *J. Am. Chem. Soc.*, 2005, **127**, 15666–15667.

204 N. (National T. Program), *Report on Carcinogens*, Research Triangle Park, NC, 2016.

205 National Research Council, *Acute Exposure Guideline Levels for Selected Airborne Chemicals: Volume 8*, Washington, DC, 2010.

206 C. Alvarez-Lorenzo, L. Bromberg and A. Concheiro, *Photochem. Photobiol.*, 2009, **85**, 848–860.

207 Y. Tao, H. F. Chan, B. Shi, M. Li and K. W. Leong, *Adv. Funct. Mater.*, 2020, **30**,

1–28.

208 Controlled Release Drug Delivery Market Worth $69.8 Billion By 2027, https://www.grandviewresearch.com/press-release/global-controlled-release-drug-delivery-market.

209 J. R. Robinson and L. J. Gauger, *J. Allergy Clin. Immunol,* 1986, **78**, 676–681.

210 G. F. Paciotti, L. Myer, D. Weinreich, D. Goia, N. Pavel, R. E. McLaughlin and L. Tamarkin, *Drug Deliv. J. Deliv. Target. Ther. Agents*, 2004, **11**, 169–183.

211 E. E. Connor, J. Mwamuka, A. Gole, C. J. Murphy and M. D. Wyatt, *Small*, 2005, **1**, 325–327.

212 A. L. Bailly, F. Correard, A. Popov, G. Tselikov, F. Chaspoul, R. Appay, A. Al-Kattan, A. V. Kabashin, D. Braguer and M. A. Esteve, *Sci. Rep.*, 2019, **9**, 1–12.

213 Drug delivery, https://www.nature.com/subjects/drug-delivery.

214 J. T. Santini, A. C. Richards, R. Scheidt, M. J. Cima and R. Langer, *Angew. Chemie - Int. Ed.*, 2000, **39**, 2396–2407.

215 J. Siepmann, R. A. Siegel and M. J. Rathbone, *Fundam. Appl. Control. Release Drug Deliv.*, 2012, 1–594.

216 K. Park, *J. Control. Release*, 2014, **190**, 3–8.

217 P. I. Lee and J. Li, in *Oral Controlled Release Formulation Design and Drug Delivery*, eds. H. Wen and K. Park, John Wiley & Sons, Inc., Hoboken, 1st edn., 2010, pp. 21–31.

218 S. M. Henry, M. E. H. El-Sayed, C. M. Pirie, A. S. Hoffman and P. S. Stayton, *Biomacromolecules*, 2006, **7**, 2407–2414.

219 B. Aktan, L. Chambre, R. Sanyal and A. Sanyal, *Biomacromolecules*, 2017, **18**, 490–497.

220 Y. Suzuki, M. Tanihara, Y. Nishimura, K. Suzuki, Y. Kakimaru and Y. Shimizu, *J. Biomed. Mater. Res.*, 1998, **42**, 112–116.

221 F. Fischel-Ghodsian, L. Brown, E. Mathiowitz, D. Brandenburg and R. Langer, *Proc. Natl. Acad. Sci. U. S. A.*, 1988, **85**, 2403–2406.

222 J. Kost, K. Leong and R. Langer, *Proc. Natl. Acad. Sci. U. S. A.*, 1989, **86**, 7663–7666.

223 E. Mathiowitz and M. . Cohen, *J. Memb. Sci.*, 1989, **40**, 67–86.

224 A. K. Bajpai, S. K. Shukla, S. Bhanu and S. Kankane, *Prog. Polym. Sci.*, 2008, **33**, 1088–1118.

225 Z. S. Al-Ahmady, W. T. Al-Jamal, BosscheJ.V., T. T. Bui, A. F. Drake, A. J. Mason and K. Kostarelos, *ACS Nano*, 2012, **6**, 9335–9346.

226 E. Koren, A. Apte, A. Jani and V. P. Torchilin, *J. Control. Release*, 2012, **160**, 264–273.

227 Z. Xiao, C. Ji, J. Shi, E. M. Pridgen, J. Frieder, J. Wu and O. C. Farokhzad, *Angew. Chemie - Int. Ed.*, 2012, **51**, 11853–11857.

228 N. Y. Rapoport, A. M. Kennedy, J. E. Shea, C. L. Scaife and K.-H. Nam, *J. Control. Release*, 2009, **138**, 268–276.

229 Q. Yan, J. Yuan, Z. Cai, Y. Xin, Y. Kang and Y. Yin, *J. Am. Chem. Soc.*, 2010, **132**, 9268–9270.

230 C. R. Thomas, D. P. Ferris, J.-H. Lee, M. H. Cho, E. S. Kim, J. F. Stoddart, J.-S. Shin, J. Cheon and J. I. Zink, *J. Am. Chem. Soc.*, 2010, **132**, 10623–10625.

231 R. Liang, M. Wei, D. G. Evans and X. Duan, *Chem. Commun.*, 2014, **50**, 14071–14081.

232 M. Cerro-Lopez and M. A. Méndez-Rojas, in *Ecopharmacovigilance*, ed. L. M. Gómez-Oliván, Springer International Publishing, New York, 1st edn., 2019, pp. 201–219.

233 J. K. Patra, G. Das, L. F. Fraceto, E. V. R. Campos, M. D. P. Rodriguez-Torres, L. S. Acosta-Torres, L. A. Diaz-Torres, R. Grillo, M. K. Swamy, S. Sharma, S. Habtemariam and H. S. Shin, *J. Nanobiotechnology*, 2018, **16**, 1–33.

234 L. Gasman, *Nanotechnology applications and markets*, Artech House, Boston, 2006.

235 R. C. Scott, D. Crabbe, B. Krynska, R. Ansari and M. F. Kiani, *Expert Opin. Drug Deliv.*, 2008, **5**, 459–470.

236 S. Mura, J. Nicolas and P. Couvreur, *Nat. Mater.*, 2013, **12**, 991–1003.

237 D. Lombardo, M. A. Kiselev and M. T. Caccamo, *J. Nanomater.*, , DOI:10.1155/2019/3702518.

238 E. Abbasi, S. F. Aval, A. Akbarzadeh, M. Milani, H. T. Nasrabadi, S. W. Joo, Y. Hanifehpour, K. Nejati-Koshki and R. Pashaei-Asl, *Nanoscale Res. Lett.*, 2014, **9**, 1–10.

239 G. S. Kwon and K. Kataoka, *Adv. Drug Deliv. Rev.*, 2012, **64**, 237–245.

240 O. M. Koo, I. Rubenstein and H. Onyuksel, *Nanomedicine*, 2005, **1**, 193–212.

241 R. A. Sperling and W. J. Parak, *Philos. Trans. R. Soc. A Math. Phys. Eng. Sci.*, 2010, **368**, 1333–1383.

242 A. Gharatape and R. Salehi, *Eur. J. Med. Chem.*, 2017, **138**, 221–233.

243 C. Abbruzzese, P. Fornari, R. Massidda, F. Vegliò and S. Ubaldini, *Hydrometallurgy*, 1995, **39**, 265–276.

244 I. Fratoddi, I. Venditti, C. Cametti and M. V. Russo, *J. Mater. Chem. B*, 2014, **2**, 4204–4220.

245 O. S. Muddineti, B. Ghosh and S. Biswas, *Int. J. Pharm.*, 2015, **484**, 252–267.

246 E. E. Conner, J. Mwamuka, A. Gole, C. J. Murphy and M. D. Wyatt, *Small*, 2005, **1**, 325–327.

247 A. B. S. Bakhtiari, D. Hsiao, G. Jin, B. D. Gates and N. R. Branda, *Angew. Chemie - Int. Ed.*, 2009, **48**, 4166–4169.

248 J. Turkevich, P. C. Stevenson and J. Hillier, *Discuss. Faraday Soc.*, 1951, **11**, 55–75.

249 G. Frens, *Nat. Phys. Sci.*, 1973, **241**, 20–22.

250 M. C. Daniel and D. Astruc, *Chem. Rev.*, 2004, **104**, 293–346.

251 E. C. Cho, Y. Liu and Y. Xia, *Angew. Chemie - Int. Ed.*, 2010, **49**, 1976–1980.

252 H. Wang, D. W. Brandl, P. Nordlander and N. J. Halas, *Acc. Chem. Res.*, 2007, **40**, 53–62.

253 Y. S. Zhang, Y. Wang, L. Wang, Y. Wang, X. Cai, C. Zhang, L. V. Wang and Y. Xia, *Theranostics*, 2013, **3**, 532–543.

254 C. M. Cobley, J. Chen, E. C. Cho, L. V. Wang and Y. Xia, *Chem. Soc. Rev.*, 2011, **40**, 44–56.

255 A. R. Guerrero, N. Hassan, C. A. Escobar, F. Albericio, M. J. Kogan and E. Araya, *Nanomedicine*, 2014, **9**, 2023–2039.

256 X. Xu and M. B. Cortie, *Adv. Funct. Mater.*, 2006, **16**, 2170–2176.

257 S. Yamashita, H. Fukushima, Y. Niidome, T. Mori, Y. Katayama and T. Niidome, *Langmuir*, 2011, **27**, 14621–14626.

258 E. P. Furlani, I. H. Karampelas and Q. Xie, *Lab Chip*, 2012, **12**, 3707–3719.

259 A. Gandini, *Prog. Polym. Sci.*, 2013, **38**, 1–29.

260 A. M. Asadirad and N. R. Branda, *J. Am. Chem. Soc.*, 2015, **137**, *8*, 2824–2827.

261 D. Döllefeld, K. Hoppe, J. Kolny, K. Schilling, H. Weller and A. Eychmüller, *Phys. Chem. Chem. Phys.*, 2002, **4**, 4747–4753.

262 L. Poon, W. Zandberg, D. Hsiao, Z. Erno, D. Sen, B. D. Gates and N. R. Branda, *ACS Nano*, 2010, **4**, 6395–6403.

263 D. Lombardo, M. A. Kiselev, S. Magazù and P. Calandra, *Adv. Condens. Matter Phys.*, , DOI:10.1155/2015/151683.

264 I. Yildiz, S. Impellizzeri, E. Deniz, B. McCaughan, J. F. Callan and F. I. M. Raymo, *J. Am. Chem. Soc.*, 2011, **133**, 871–879.

265 T. Wu, J. C. Boyer, M. Barker, D. Wilson and N. R. Branda, *Chem. Mater.*, 2013, **25**, 2495–2502.

266 S. Gai, C. Li, P. Yang and J. Lin, *Chem. Rev.*, 2014, **114**, 2343–2389.

267 D. Hühn, K. Kantner, C. Geidel, S. Brandholt, I. De Cock, S. J. H. Soenen, P. Riveragil, J. M. Montenegro, K. Braeckmans, K. Müllen, G. U. Nienhaus, M. Klapper and W. J. Parak, *ACS Nano*, 2013, **7**, 3253–3263.

268 W. G. Kreyling, A. M. Abdelmonem, Z. Ali, F. Alves, M. Geiser, N. Haberl, R. Hartmann, S. Hirn, D. J. De Aberasturi, K. Kantner, G. Khadem-Saba, J. M. Montenegro, J. Rejman, T. Rojo, I. R. De Larramendi, R. Ufartes, A. Wenk and W. J. Parak, *Nat. Nanotechnol.*, 2015, **10**, 619–623.

269 NCI Dictionary of Cancer Terms, https://www.cancer.gov/publications/dictionaries/cancer-terms/def/tyrosine-kinase-inhibitor.

270 M. K. Paul and A. K. Mukhopadhyay, *Int. J. Med. Sci.*, 2012, **1**, 101–115.

271 Z. Du and C. M. Lovly, *Mol. Cancer*, 2018, **17**, 1–13.

272 A. Levitzki and E. Mishani, *Annu. Rev. Biochem.*, 2006, **75**, 93–109.

273 R. Robinson, J. P. Bertram, J. L. Reiter and E. B. Lavik, *J. Microencapsul.*, 2010, **27**, 263–271.

274 A. Gazit, P. Yaish, C. Gilon and A. Levitzki, *J. Med. Chem.*, 1989, **32**, 2344–2352.

275 M. Chorny, I. Fishbein, H. D. Danenberg and G. Golomb, *J. Control. Release*,

2002, **83**, 401–414.

276 J. Turkevich; P.C. Stevenson; J. Hiller, *Discuss. Faraday Soc.*, 1951, **11**, 55–75.

277 L. Polavarapu and Q. H. Xu, *Nanotechnology*, , DOI:10.1088/0957-4484/20/18/185606.

278 S. K. Ghosh, S. Nath, S. Kundu, K. Esumi and T. Pal, *J. Phys. Chem. B*, 2004, **108**, 13963–13971.

279 S. K. Panja, *J. Mol. Liq.*, 2020, **299**, 112194.

280 M. Haeberlein and T. Brinck, *J. Phys. Chem.*, 1996, **100**, 10116–10120.

281 S. Patai and Z. Rappoport, *J. Chem. Soc.*, 1962, 383–391.

282 C. F. Bernasconi, K. A. Howard and A. Kanavarioti, *J. Am. Chem. Soc.*, 1984, **106**, 6827–6835.

283 T. Wu, J. Oake, Z. Liu, C. Bohne and N. R. Branda, *ACS Omega*, 2018, **3**, 7673–7680.

284 T. Wu, D. Wilson and N. R. Branda, *Chem. Mater.*, 2014, **26**, 4313–4320.

285 A. Takami, H. Kurita and S. Koda, *J. Phys. Chem. B*, 1999, **103**, 1226–1232.

286 S. Inasawa, M. Sugiyama and Y. Yamaguchi, *J. Phys. Chem. B*, 2005, **109**, 9404–9410.

287 M. Maciulevičius, A. Vinčiunas, M. Brikas, A. Butsen, N. Tarasenka, N. Tarasenko and G. Račiukaitis, *Appl. Phys. A Mater. Sci. Process.*, 2013, **111**, 289–295.

288 H. C. Kolb, M. G. Finn and K. B. Sharpless, *Angew. Chemie - Int. Ed.*, 2001, **40**, 2004–2021.

289 M. Gregoritza and F. P. Brandl, *Eur. J. Pharm. Biopharm.*, 2015, **97**, 438–453.

290 R. Breslow, U. Maitra and D. Rideout, *Tetrahedron Lett.*, 1983, **24**, 1901–1904.

291 W. Blokzijl, M. J. Blandamer and J. B. F. N. Engberts, *J. Am. Chem. Soc.*, 1991, **113**, 4241–4246.

292 B. J. Adzima, H. A. Aguirre, C. J. Kloxin, T. F. Scott and C. N. Bowman, *Macromolecules*, 2008, **41**, 9112–9117.

293 G. Scheltjens, M. M. Diaz, J. Brancart, G. Van Assche and B. Van Mele, *React. Funct. Polym.*, 2013, **73**, 413–420.

294 A. D. De Araújo, J. M. Palomo, J. Cramer, M. Köhn, H. Schröder, R. Wacker, C. Niemeyer, K. Alexandrov and H. Waldmann, *Angew. Chemie - Int. Ed.*, 2005, **45**, 296–301.

295 M. Shi and M. S. Shoichet, *J. Biomater. Sci. Polym. Ed.*, 2008, **19**, 1143–1157.

296 M. Shi, J. H. Wosnick, K. Ho, A. Keating and M. S. Shoichet, *Angwandte Chemie International Edition*, 2007, **46**, 6126–6131.

297 M. Shi, K. Ho, A. Keating and M. S. Shoichet, *Adv. Funct. Mater.*, 2009, **19**, 1689–1696.

298 C. M. Nimmo, S. C. Owen and M. S. Shoichet, *Biomacromolecules*, 2011, **12**, 824–830.

299 A. Gandini, *Polímeros Ciência e Tecnol.*, 2005, **15**, 95–101.

300 E. Dolci, G. Michaud, F. Simon, B. Boutevin, S. Fouquay and S. Caillol, *Polym. Chem.*, 2015, **6**, 7851–7861.

301 N. Iglesias, E. Galbis, L. Romero-Azogil, E. Benito, M. J. Díaz-Blanco, M. G. García-Martín and M. V. De-Paz, *Polym. Chem.*, 2019, **10**, 5473–5486.

302 G. D. Guerra, N. Barbani, M. L. Coluccio and C. Cristallini, *J. Appl. Biomater. Biomech.*, 2006, **4**, 97–101.

303 A. Sarı, A. Biçer and C. Alkan, *Sol. Energy Mater. Sol. Cells*, 2017, **161**, 219–225.

304 F. A. Bovey, F. P. Hoodht, E. W. Andeeson and L. C. Snydee, *J. Chem. Phys.*, 1965, **42**, 3900–3910.

305 A. S. Brar, A. K. Goyal and S. Hooda, *Pure Appl. Chem.*, 2009, **81**, 389–415.

306 K. Saalwächter, in *NMR Methods for Characterization of Synthetic and Natural Polymers*, eds. R. Zhang, T. Miyoshi and P. Sun, Royal Society of Chemistry, 2019, pp. 1–22.

307 C. Corporation, ALDOXORUBICIN – A NEW APPROACH TO CANCER TREATMENT, http://www.cytrx.com/aldoxorubicin/, (accessed 23 May 2020).

Appendix.

NMR spectra of compounds

Compounds from Chapter 2

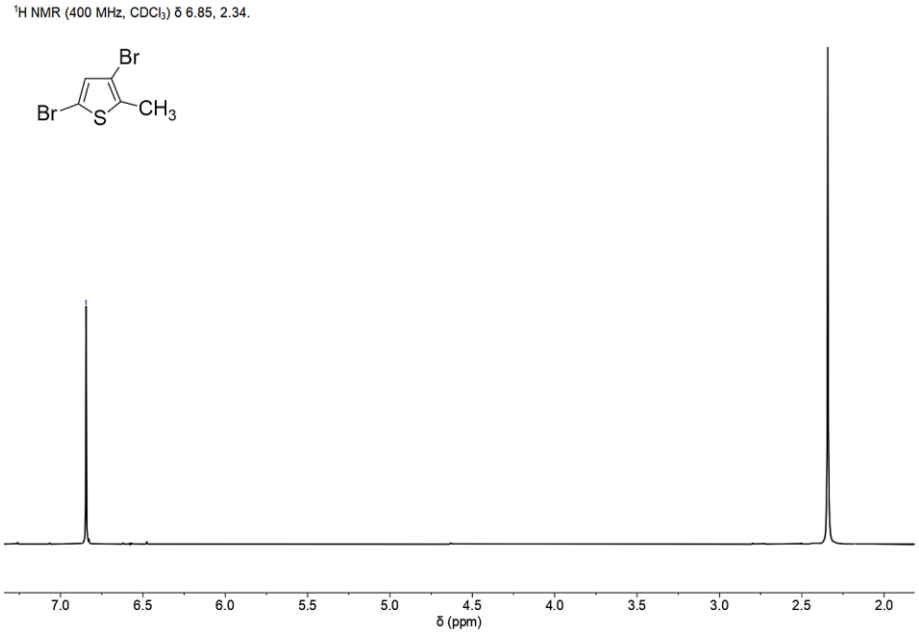

Figure A 1: ^{1}H NMR spectrum (400 MHz) of 3,5-dibromo-2-methylthiophene in $CDCl_3$

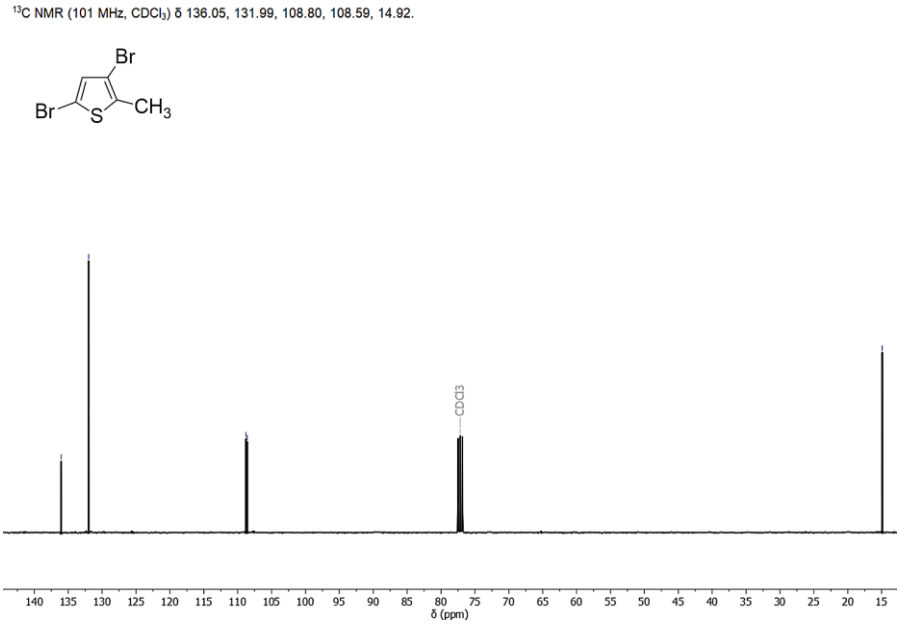

Figure A 2: ^{13}C NMR spectrum (101 MHz) of 3,5-dibromo-2-methylthiophene in $CDCl_3$

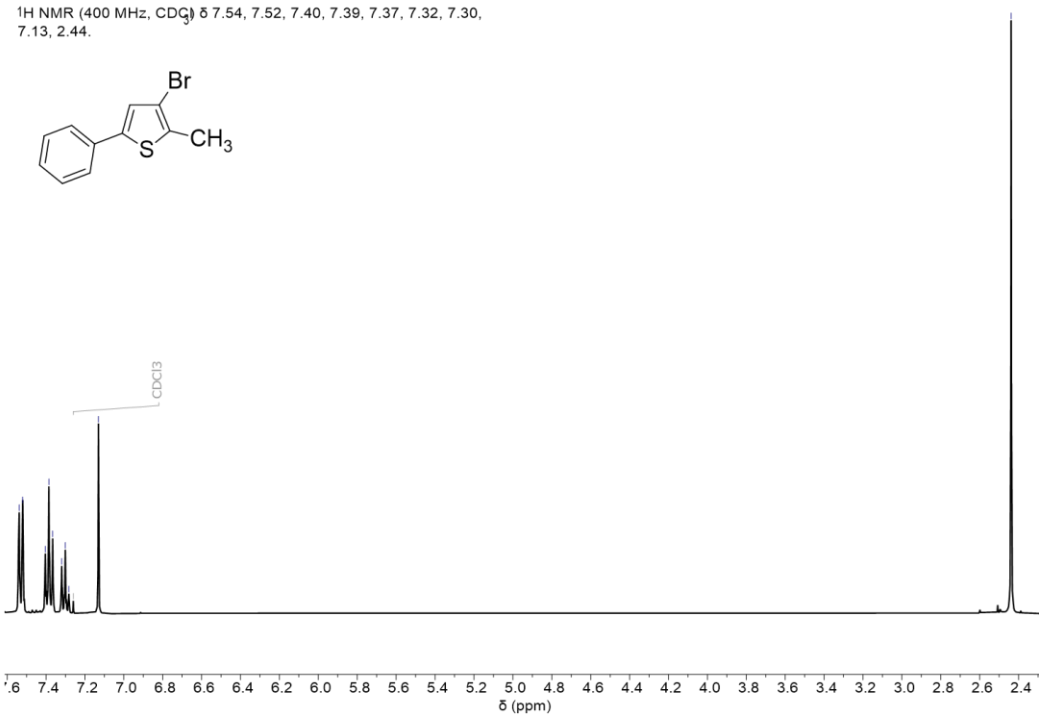

Figure A 3: ^{1}H NMR spectrum (400 MHz) of 3-bromo-2-methyl-5-phenylthiophene in $CDCl_3$

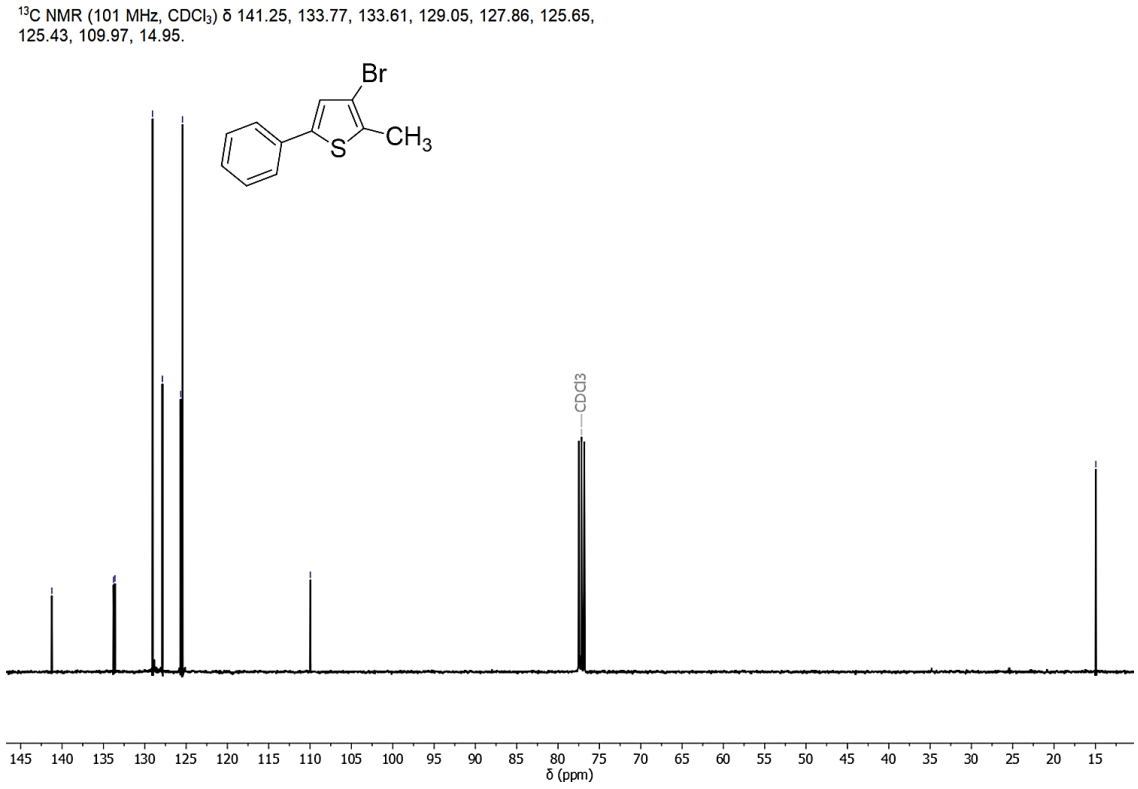

Figure A 4: ^{13}C NMR spectrum (101 MHz) of 3-bromo-2-methyl-5-phenylthiophene in $CDCl_3$

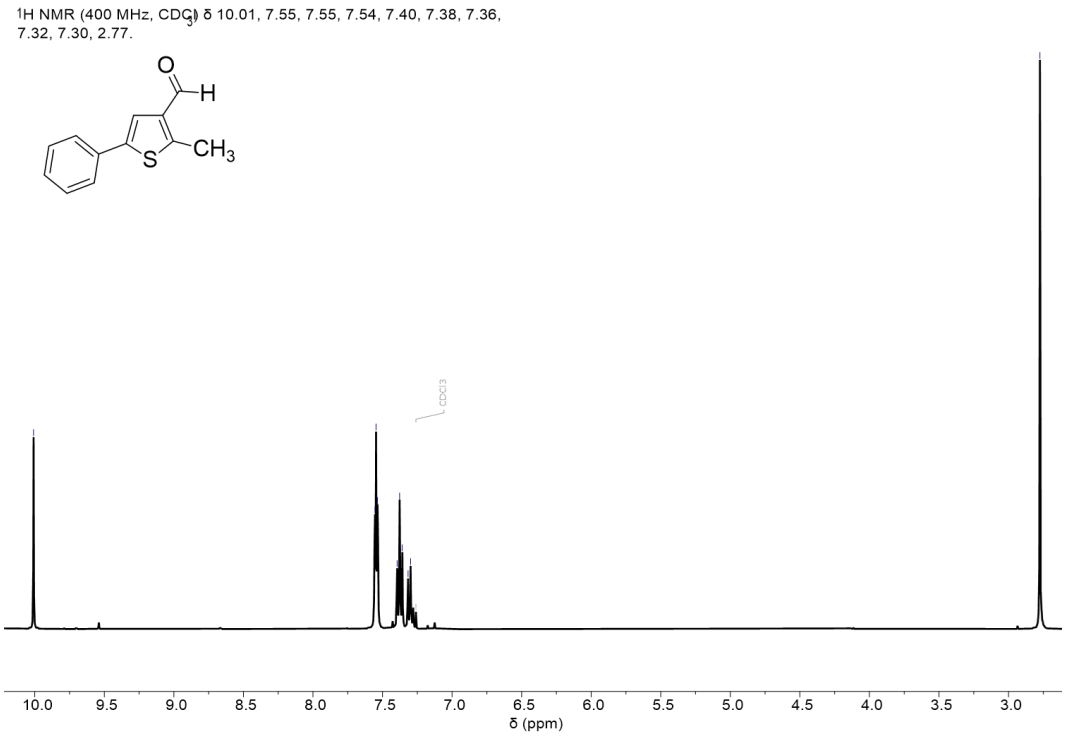

Figure A 5: ^{1}H NMR spectrum (400 MHz) of 2-methyl-5-phenylthiophene-3-carbaldehyde in $CDCl_3$

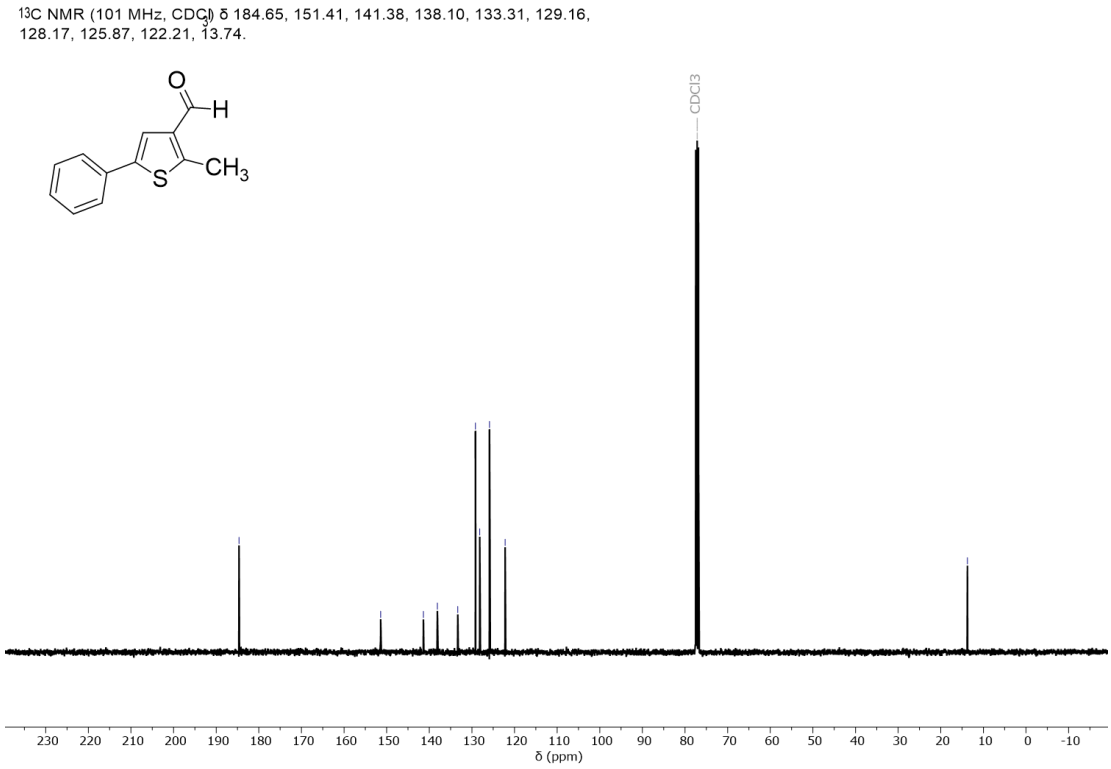

Figure A 6: ^{13}C NMR spectrum (101 MHz) of 2-methyl-5-phenylthiophene-3-carbaldehyde in $CDCl_3$

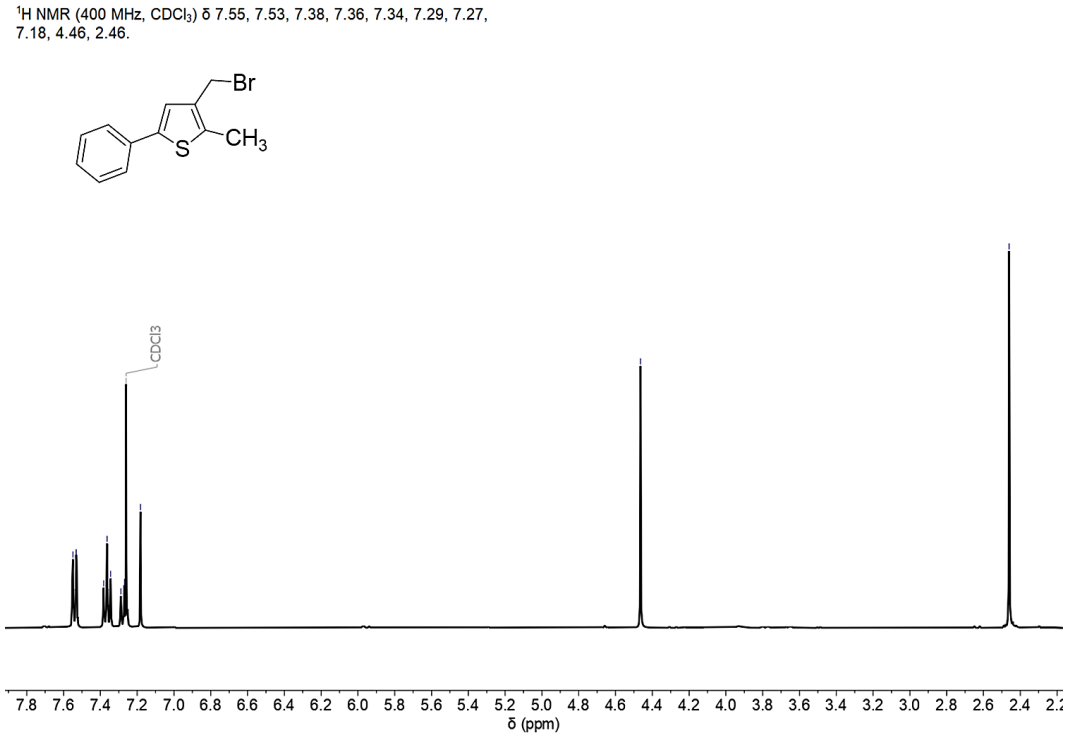

Figure A 7: ^{1}H NMR spectrum (400 MHz) of 3-(bromomethyl)-2-methyl-5-phenylthiophene in $CDCl_3$

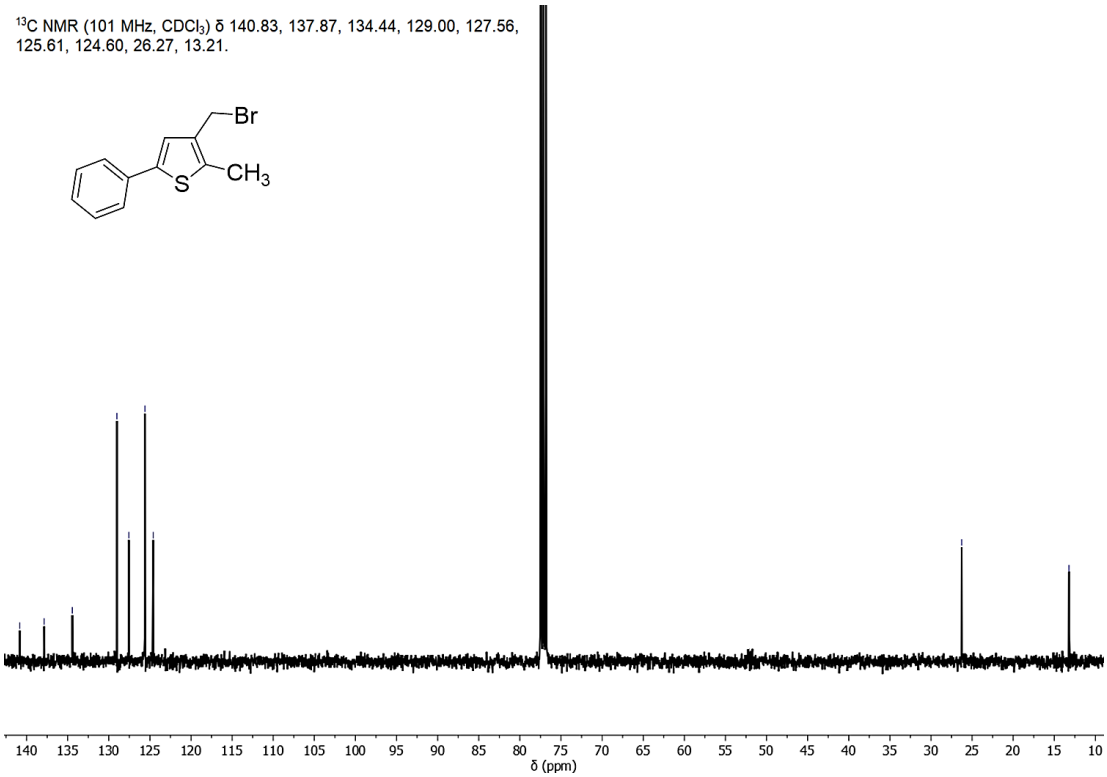

Figure A 8: ^{13}C NMR spectrum (101 MHz) of 3-(bromomethyl)-2-methyl-5-phenylthiophene in $CDCl_3$

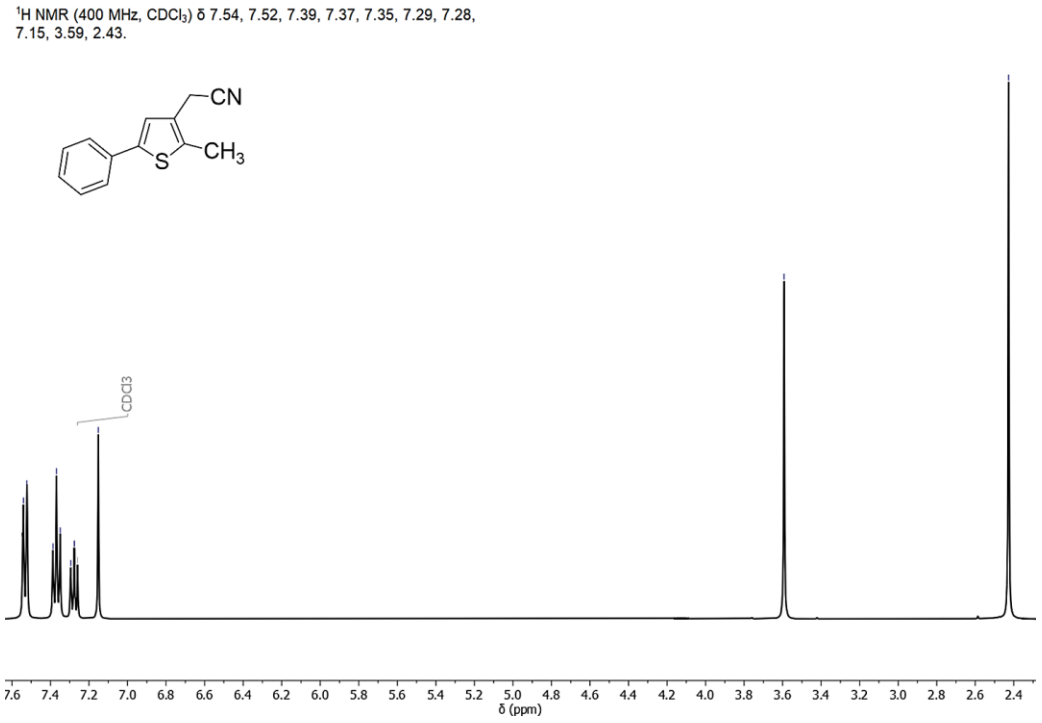

Figure A 9: ^{1}H NMR spectrum (400 MHz) of 2-(2-methyl-5-phenylthiophen-3-yl) acetonitrile in $CDCl_3$

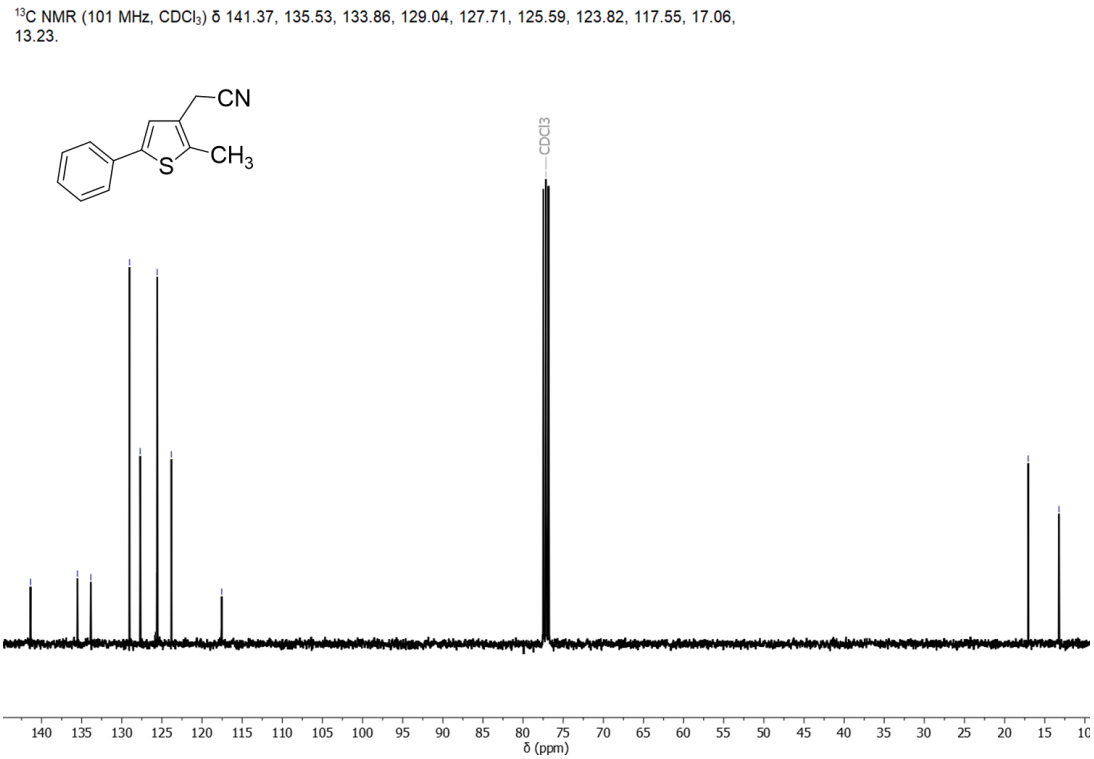

Figure A 10: ^{13}C NMR spectrum (101 MHz) of 2-(2-methyl-5-phenylthiophen-3-yl) acetonitrile in $CDCl_3$

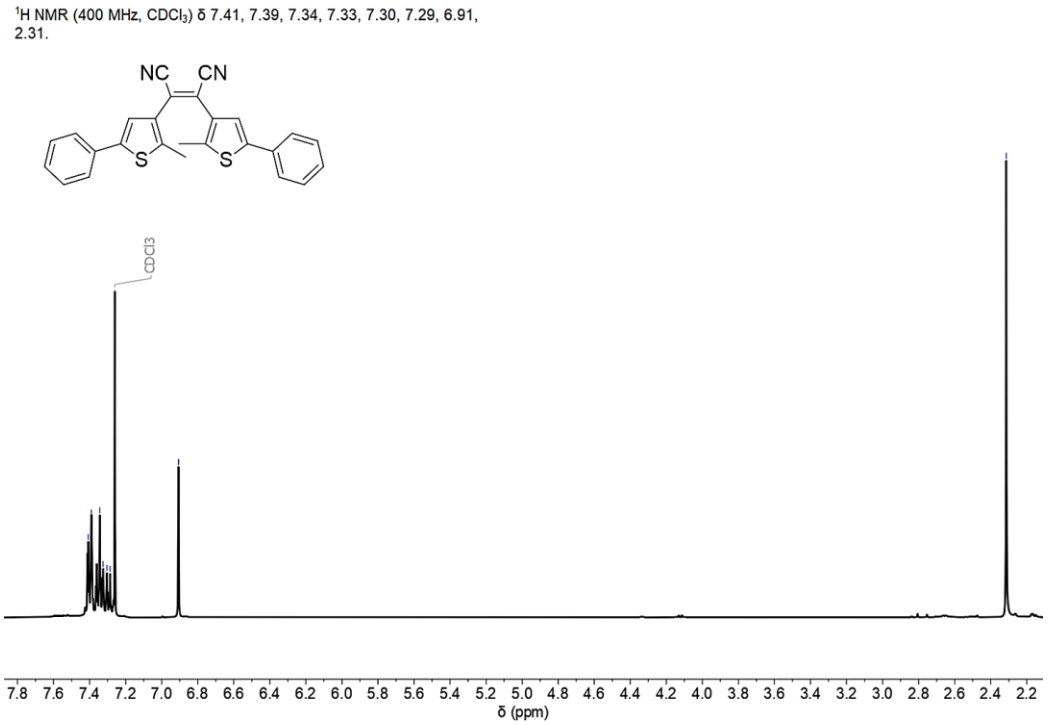

Figure A 11: ^{1}H NMR spectrum (400 MHz) of 2,3-bis(2-methyl-5-phenylthiophen-3-yl) maleonitrile (ring-open isomer) in $CDCl_3$

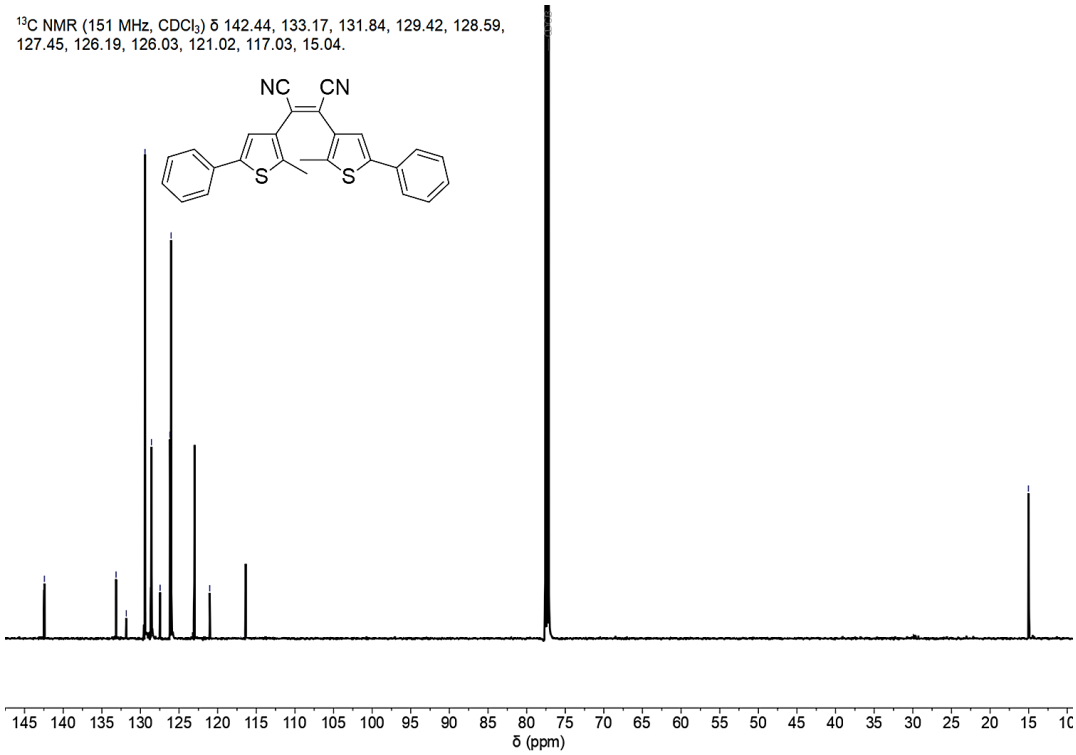

Figure A 12: ^{13}C NMR spectrum (101 MHz) of 2,3-bis(2-methyl-5-phenylthiophen-3-yl) maleonitrile (ring-open isomer) in $CDCl_3$

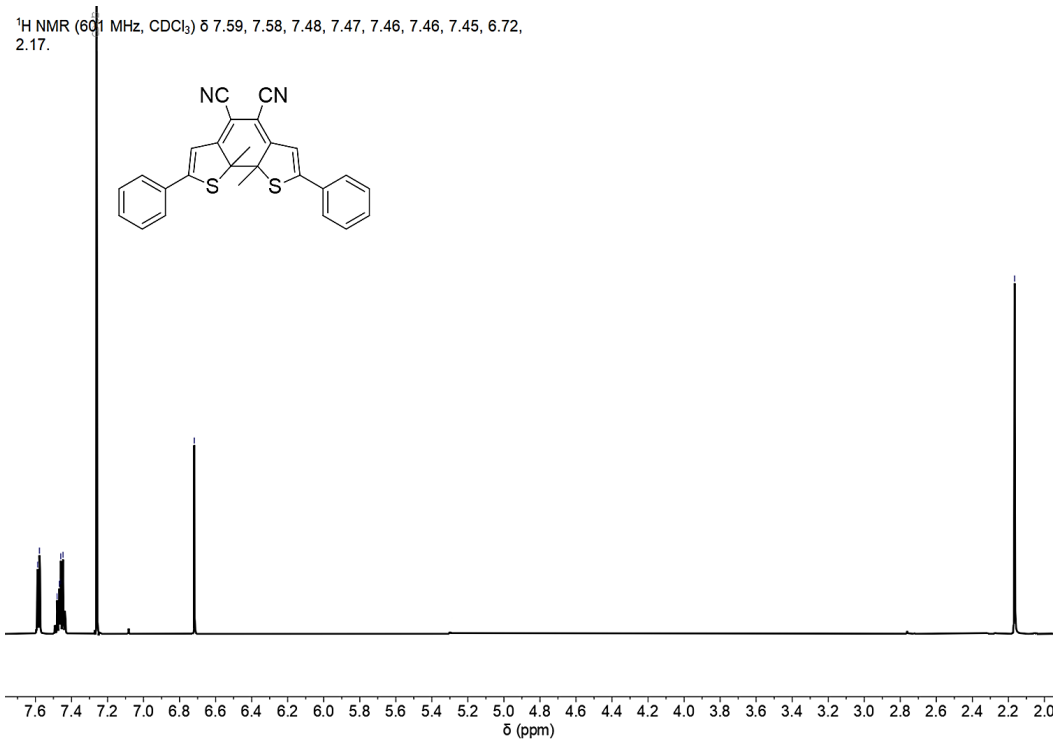

Figure A 13: ^{1}H NMR spectrum (400 MHz) of 2,3-bis(2-methyl-5-phenylthiophen-3-yl) maleonitrile (ring-closed isomer) in $CDCl_3$

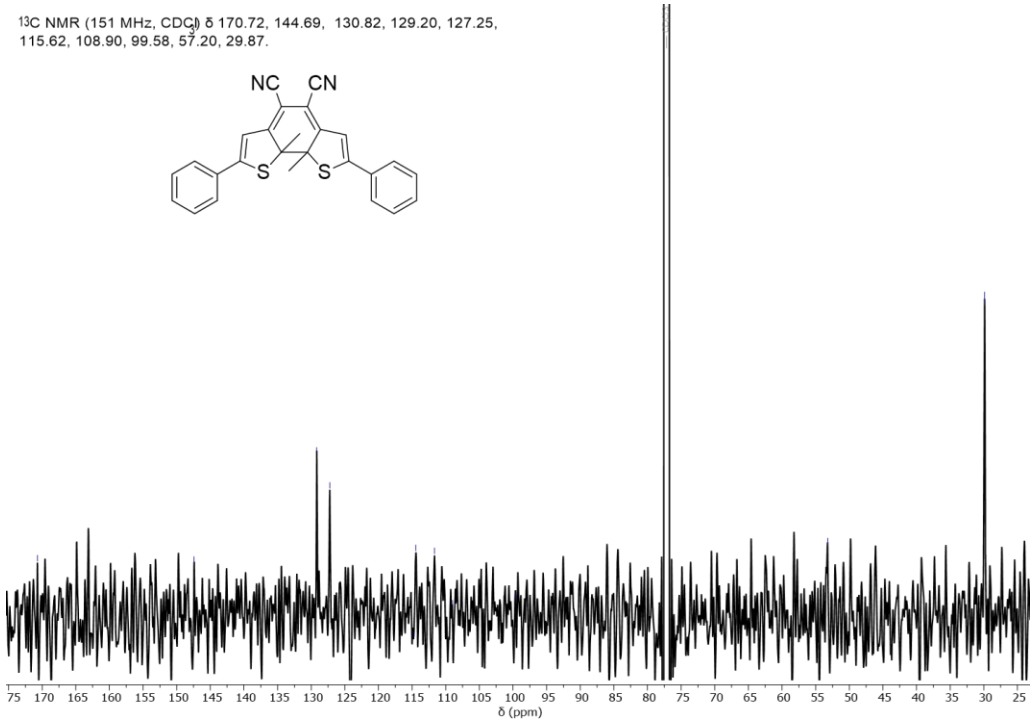

Figure A 14: ^{13}C NMR spectrum (101 MHz) of 2,3-bis(2-methyl-5-phenylthiophen-3-yl) maleonitrile (ring-closed isomer) in $CDCl_3$

Compounds from Chapter 3

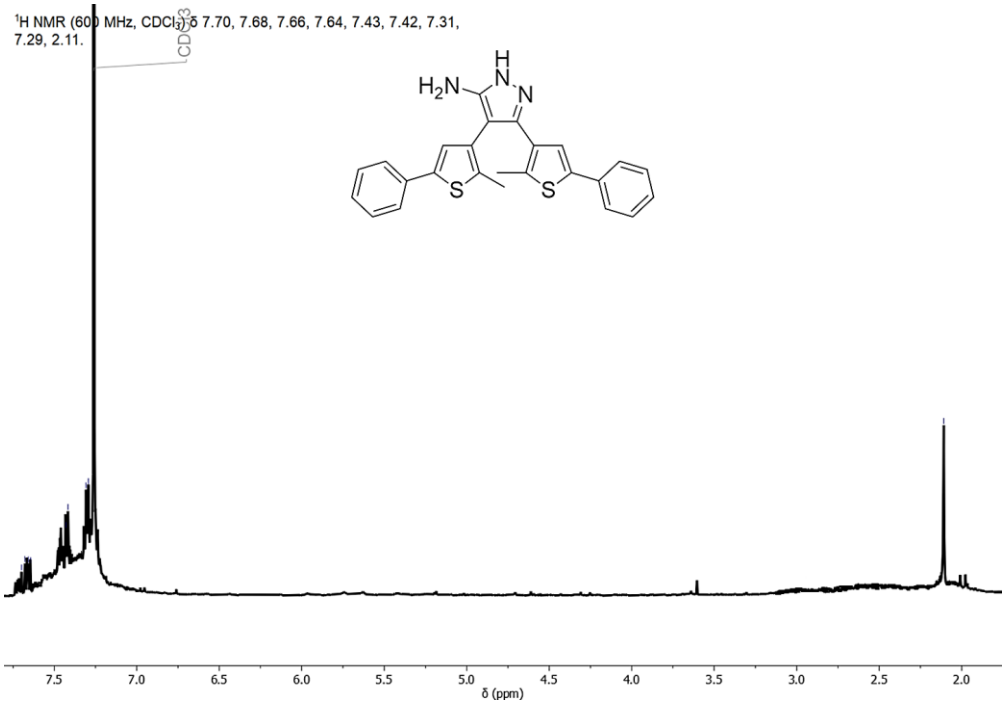

Figure A 15: ^{1}H NMR spectrum (600 MHz) of 3,4-bis(2-methyl-5-phenylthiophen-3-yl)-1H-pyrazol-5-amine in $CDCl_3$

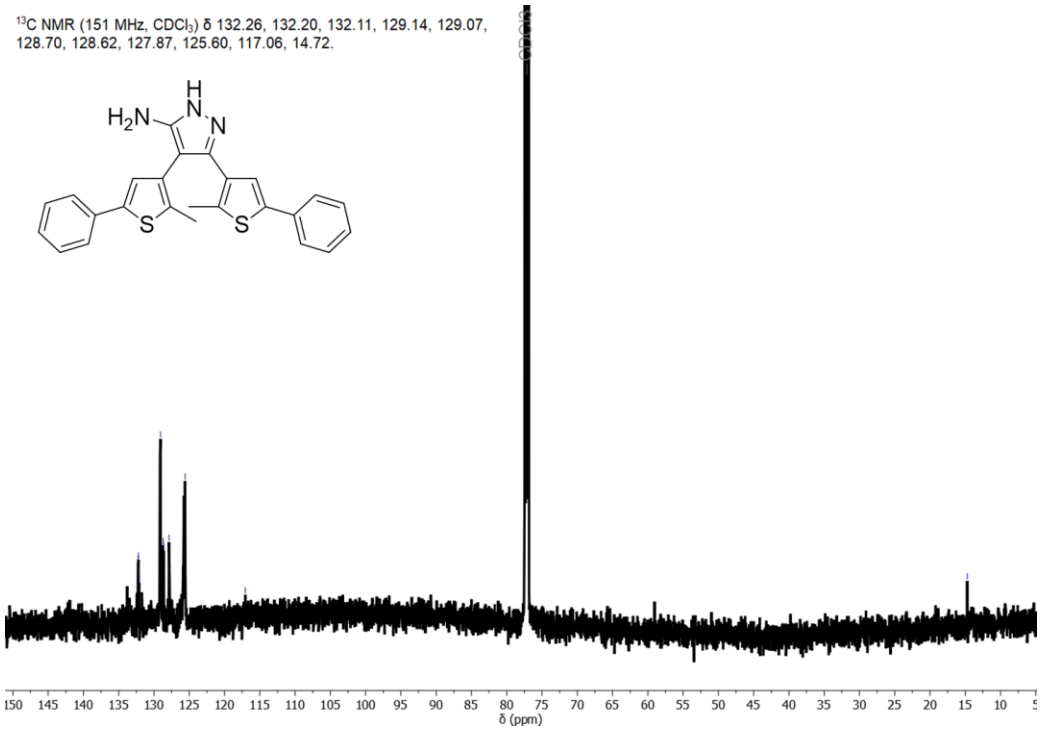

Figure A 16: ^{13}C NMR spectrum (151 MHz) of 3,4-bis(2-methyl-5-phenylthiophen-3-yl)-1H-pyrazol-5-amine in $CDCl_3$

Compounds from Chapter 4

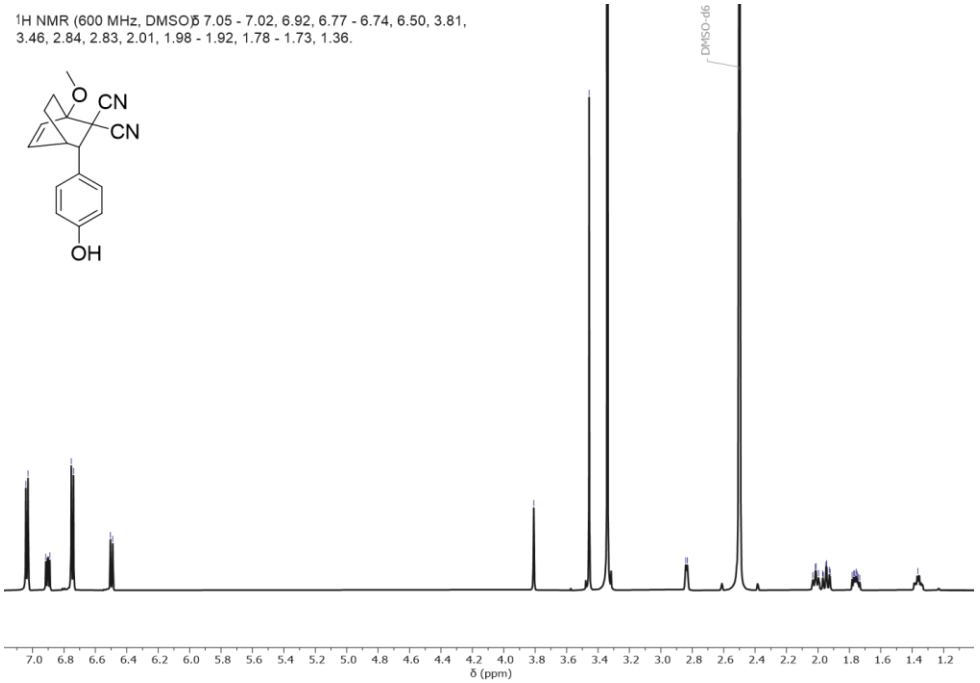

Figure A 17: ^{1}H NMR spectrum (600 MHz) of (1S,3S,4S)-3-(4-hydroxyphenyl)-1-methoxybicyclo[2.2.2]oct-5-ene-2,2-dicarbonitrile in DMSO-d_6

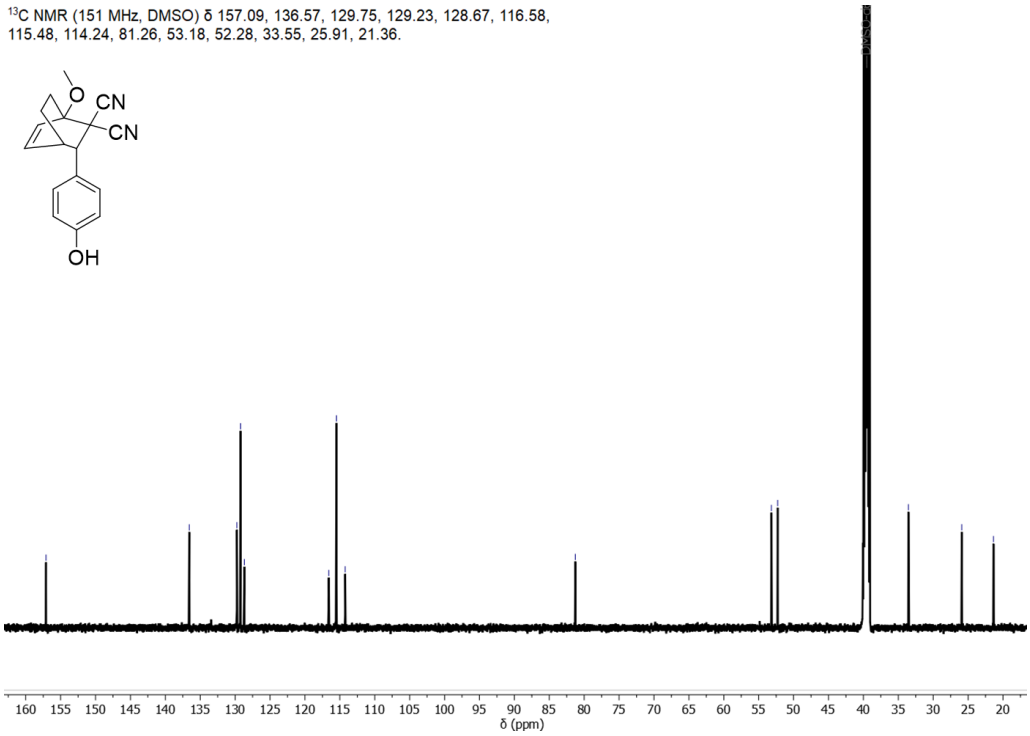

Figure A 18: ^{13}C NMR spectrum (151 MHz) of (1S,3S,4S)-3-(4-hydroxyphenyl)-1-methoxybicyclo[2.2.2]oct-5-ene-2,2-dicarbonitrile in DMSO-d_6

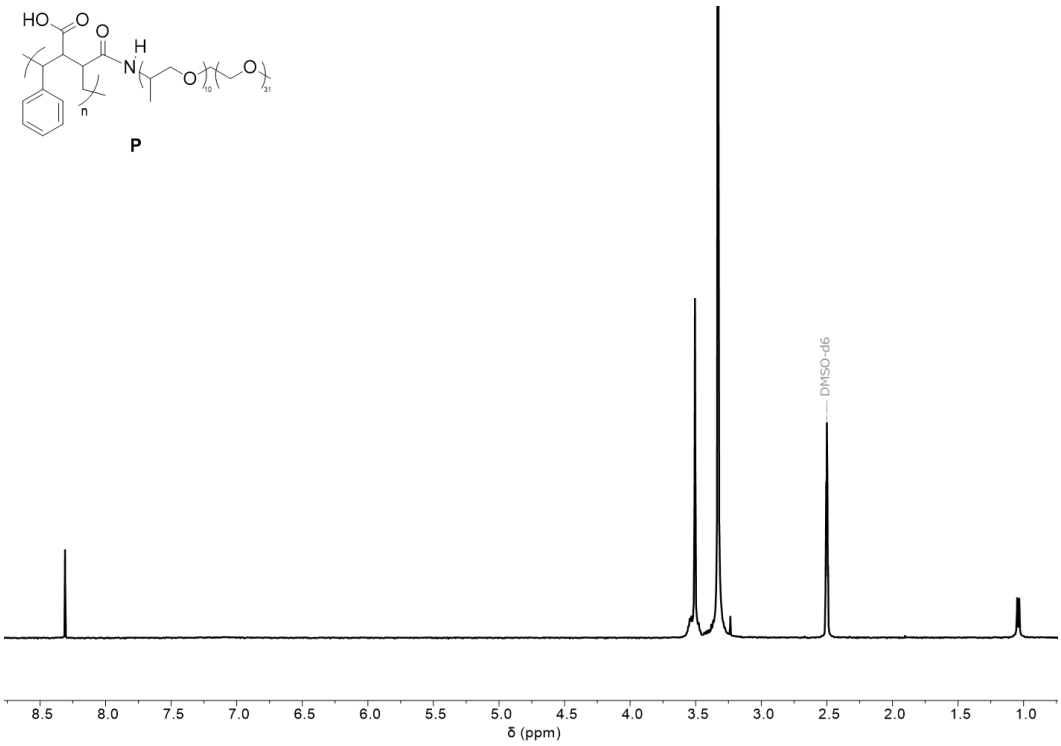

Figure A 19: ^{1}H NMR spectrum (400 MHz) of amphiphilic polymer (**P**) in DMSO-d_6

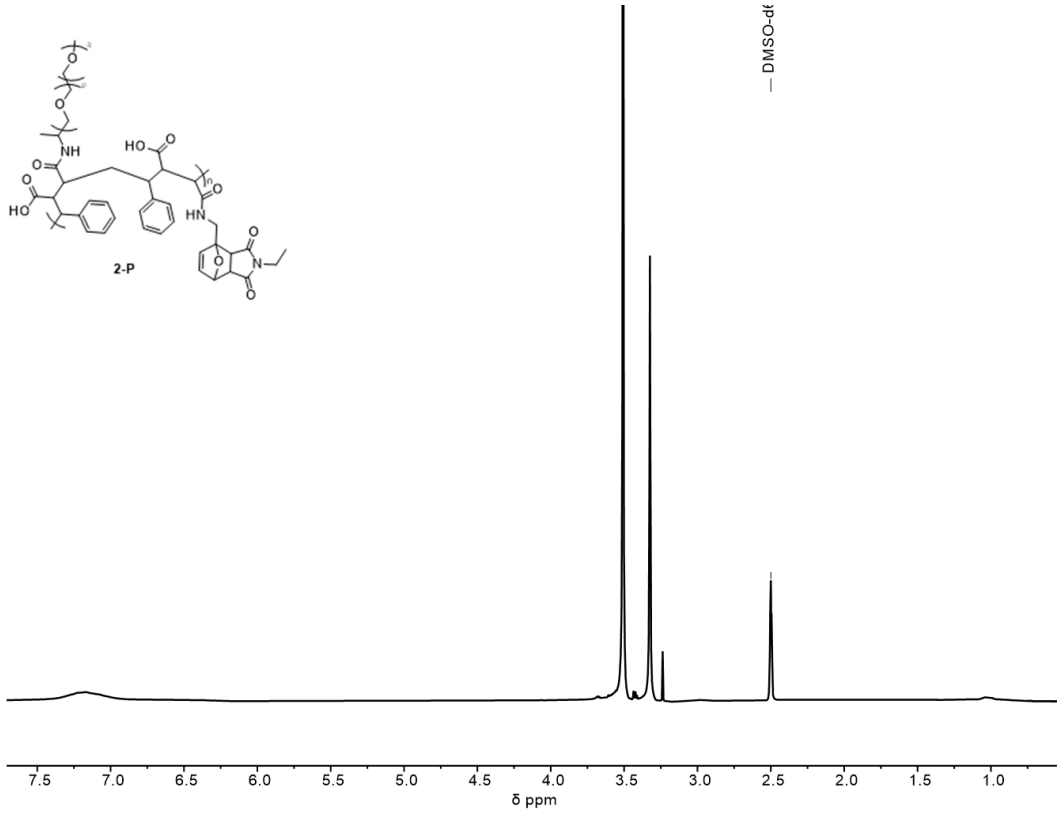

Figure A 20: ^{1}H NMR spectrum (500 MHz) of Diels-Alder adduct tethered amphiphilic polymer (**2-P**) in DMSO-d_6